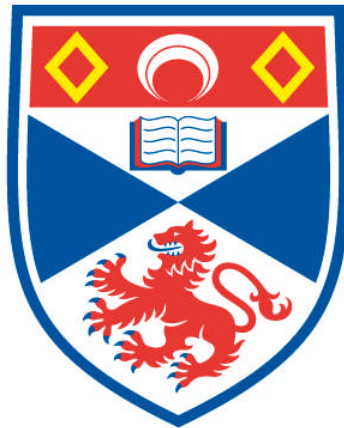


RESONANTLY ENHANCED THERMAL EMITTERS BASED ON NANOPHOTONIC STRUCTURES

Bryan J. O'Regan

A Thesis Submitted for the Degree of PhD
at the
University of St Andrews



2015

Full metadata for this item is available in
Research@StAndrews:FullText
at:

<http://research-repository.st-andrews.ac.uk/>

Please use this identifier to cite or link to this item:

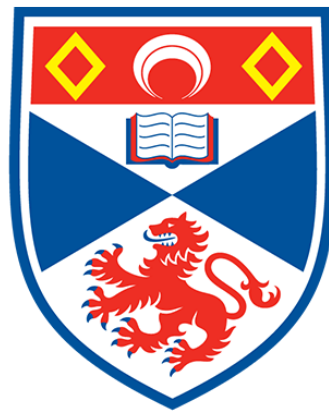
<http://hdl.handle.net/10023/7801>

This item is protected by original copyright

This item is licensed under a
Creative Commons Licence

Resonantly Enhanced Thermal Emitters Based on Nanophotonic Structures

Bryan J. O'Regan



University of
St Andrews

A thesis presented for the degree of Doctor of Philosophy
at the
University of St Andrews

October 2015

To my family.

Declaration

I, Bryan J. O'Regan, hereby certify that this thesis, which is approximately 56,000 words in length, has been written by me, and that it is the record of work carried out by me and that it has not been submitted in any previous application for a higher degree.

I was admitted as a research student in September 2011 and as a candidate for the degree of Doctor of Philosophy in September 2011; the higher study for which this is a record was carried out in the University of St Andrews and the University of York between 2011 and 2015.

Date: Signature of Candidate

I hereby certify that the candidate has fulfilled the conditions of the Resolution and Regulations appropriate for the degree of Doctor of Philosophy in the University of St Andrews and that the candidate is qualified to submit this thesis in application for that degree.

Date: Signature of Supervisor

In submitting this thesis to the University of St Andrews I understand that I am giving permission for it to be made available for use in accordance with the regulations of the University Library for the time being in force, subject to any copyright vested in the work not being affected thereby. I also understand that the title and the abstract will be published, and that a copy of the work may be made and supplied to any bona fide library or research worker, that my thesis will be electronically accessible for personal or research use unless exempt by award of an embargo as requested below, and that the library has the right

to migrate my thesis into new electronic forms as required to ensure continued access to the thesis. I have obtained any third-party copyright permissions that may be required in order to allow such access and migration, or have requested the appropriate embargo below.

The following is an agreed request by candidate and supervisor regarding the electronic publication of this thesis:

Access to printed copy and electronic publication of thesis through the University of St Andrews.

Date:

Signature of Candidate:

Signature of Supervisor:

Acknowledgements

I wish to express my deepest gratitude to those who made this thesis possible. First of all, I would like to thank my supervisor Prof. Thomas Krauss for giving me the opportunity to work in his research group and for his friendly guidance and continuous support throughout my research. He always found time for discussion and did not spare on words of encouragement. Secondly, I would also like to thank Dr. Andrea Di Falco, as my second supervisor, for his patience and instruction at the beginning of the PhD.

I would like to thank all my colleagues and friends from the Microphotonics Research Group at St Andrews and those from the new Photonics group at the University of York, who made my time during the PhD enjoyable and rewarding. It was a pleasure to work with you all during the last four years. In particular, from St Andrews, I would like to thank Pedro Damas, Mina Yeşilyurt, Dr. Sebastian Kosmeier, Christian Reimer, Dr. Kapil Debnath and Dr. Emiliano Rezende Martins. A special thanks goes to Callum Smith for his help inside the cleanroom and his friendship outside of it. At York, my appreciation goes to José (Pepe) Juan Colás, Daan Stellinga, Graham Triggs, Dr. Annett Fischer, Dr. Matthias Fischer and Dr. Mark Scullion. A very special thank you goes to Dr. Yue Wang and Dr. Christopher Reardon for their support and encouragement.

Finally, I would like to thank all my friends and especially my family, my parents Jimmy and Catherine and siblings Patrick, James and Rachel, for their belief in me and continuous support. Lastly, I express my special gratitude to Ashling for her care and never ending patience.

List of Publications

Journal papers

- **B. J. O'Regan**, Y. Wang and T. F. Krauss, “Silicon photonic crystal thermal emitter at near-infrared wavelengths,” *Scientific Reports* **5**, 13415; doi: 10.1038/srep13415 (2015).
- R. Faggiani, A. Baron, X. Zang, L. Lalouat, S. A. Schulz, K. Vynck, **B. O'Regan**, B. Cluzel, F. de Fornel, T. F. Krauss, and P. Lalanne, “Ultimate limits of light confinement in randomly-perturbed periodic structures”. arXiv:1505.03472 (2015). - Not related to this work.

Conferences attended

- **B. J. O'Regan**, Y. Wang and T. F. Krauss, “Silicon photonic crystal thermal emitter at near-infrared wavelengths,” *Silicon Photonics Summer School*, Ghent, July 2014. - Poster presentation.
- **B. J. O'Regan**, Y. Wang and T. F. Krauss, “Silicon photonic crystal thermal emitter at near-infrared wavelengths,” *Postgraduate Research on Photonics as an Enabling Technology (PROPHET) Conference*, Cork, June 2014. - Invited talk.
- **B. J. O'Regan**, Y. Wang and T. F. Krauss, “Silicon photonic crystal thermal emitter at near-infrared wavelengths,” *The 11th International Symposium on Photonic and Electromagnetic Crystal Structures (PECS)*, Shanghai, May 2014. - Poster presentation with prize for best poster.
- **B. J. O'Regan**, Y. Wang and T. F. Krauss, “Silicon photonic crystal thermal emitter at near-infrared wavelengths,” *Semiconductor and Integrated Optoelectronics (SIOE) Conference*, Cardiff, Apr 2014. - Contributed talk.

Abstract

The manipulation of photons, especially the control of spontaneous emission, has become a core area of photonics research in the 21st century. One of the key challenges is the control of the broadband emission profile of thermal emitters. Recently, attention has focused on resonant nanophotonic structures to control the thermal emission with most of the work concentrating on the mid-infrared wavelength range and/or based on metallic nanostructures. However, the realisation of a high temperature, single wavelength, narrowband and efficient thermal source, remains a challenge.

In this project, four individual nanophotonic resonant structures are presented for the control of thermal emission, all operating in the near-infrared ($\approx 1.5 \mu\text{m}$) wavelength range. The work is split over two different emission materials; gold and doped silicon. While I present two successful designs of narrowband thermal emitters from gold, the main backbone of the research is concentrated on doped silicon as the emission material. By combining the weak broadband absorption of doped silicon with a photonic crystal resonator, resonantly enhanced narrowband absorption is achieved. Using Kirchhoffs law of thermal radiation which equates the absorptivity and emissivity, narrowband absorption leads to narrowband emission, which is the underlying principle used throughout the work presented in this thesis to achieve narrowband thermal emission.

One common oversight in many of the presented thermal emitter designs is the angular emission dependence, i.e. how the emission wavelength behaves away from surface normal. Typically, since the majority of the devices are based on periodic structures, the resonant emission wavelength changes with emission angle, which is not ideal. Here, the angular sensitivity is considered and addressed, by constructing a device that is based on localised confined resonances and not on propagating resonances, it is possible to achieve a truly monochromatic source i.e. one with the same emission wavelength in all directions, all the way up to an angle of 90° .

Finally, the devices presented here demonstrate that weak absorption together with photonic resonances can be used as a wavelength-selection mechanism for thermal emitters, both for the enhancement and the suppression of emission away from the resonant wavelength.

Contents

Declaration	v
Acknowledgements	vii
List of Publications	ix
Abstract	xi
1 Thermal Emitters: Introduction and Background	1
1.1 Introduction and Motivation	1
1.2 Aim and Preview of the Thesis	5
1.3 Theory of Photonic Crystals	7
1.3.1 From Maxwell's Equations to Photonic Crystals	8
1.3.1.1 1D Photonic Crystal Band Gap	9
1.3.1.2 2D Photonic Crystal Band Gap	11
1.4 Fundamentals of Thermal Emission	12
1.4.1 Radiative Properties	13
1.4.1.1 Planck's Radiation Law	13
1.4.1.2 Kirchhoff's Radiation Law	15
1.5 Review of Selected Devices	16
1.5.1 Organ Pipe Radiant Modes of Periodic Micromachined Silicon Surfaces	17
1.5.2 Sharp Thermal Emission and Absorption from Conformally Coated Metallic Photonic Crystal with Triangular Lattice	18
1.5.3 Conversion of Broadband to Narrowband Thermal Emission Through Energy Recycling	19
2 Fabrication and Measurement Techniques	23
2.1 Introduction	23
2.2 Lithography	24
2.2.1 Electron Beam Lithography	24
2.2.1.1 Electron Beam Resists	27
2.2.2 Photolithography	30
2.3 Reactive Ion Etching	30
2.4 Lift-off and Metal Evaporation	32
2.5 SU-8 Polymer Waveguides	33
2.6 Optical Characterisation	36
2.6.1 Coupling Light into a Multimode Fibre	36
2.6.2 Optical Setup	39

3	Photonic Crystal Based Thermal Emitter	43
3.1	Introduction	43
3.2	Two Dimensional Photonic Crystal Slabs	44
3.2.1	Photonic Crystal Slab Modes	45
3.2.2	Introducing Absorption - Doped Photonic Crystal Slab	50
3.3	Temporal Coupled Mode Theory	52
3.3.1	Symmetric Photonic Crystal Slab	53
3.3.2	Symmetric Photonic Crystal Slab with Absorption	56
3.3.3	Q-matching Doped Photonic Crystal Slab	57
3.3.4	Vertically Asymmetric Photonic Crystal Slab with Absorption	60
3.4	Device Fabrication	63
3.4.1	N-type (Phosphorus) Diffusion Doping	64
3.4.2	Fabrication of Photonic Crystal	66
3.4.3	Aluminium Contact Pads	67
3.4.4	Photonic Crystal Membrane	69
3.5	Device Characterisation	77
3.5.1	Passive Characterisation - Reflection	78
3.5.2	Temperature Estimation Procedure	82
3.5.3	Active Characterisation - Thermal Emission	85
4	Metallic Thermal Emitter	89
4.1	Introduction	89
4.2	Metal-Insulator-Metal	91
4.2.1	Introduction	91
4.2.2	Metal-Insulator-Metal Fabrication	94
4.3	Binary Biharmonic Gold Grating	100
4.3.1	Introduction	100
4.3.2	Fundamentals of Surface Plasmon Polaritons	101
4.3.2.1	Surface Plasmon Polariton Dispersion Relation	102
4.3.2.2	Excitation of Surface Plasmon Polaritons	105
4.3.3	Binary Biharmonic Grating Structure	107
4.3.4	Optical Characterisation of the Binary Biharmonic Structure	112
5	Coupled Cavity Array Thermal Emitter	119
5.1	Introduction	119
5.2	Defect Modes Inside the Band Gap	121
5.2.1	Single Point Defect	121
5.2.2	Two Dimensional Defect Array	121
5.2.3	Coupled Cavity Array Slab	124
5.3	Coupled Cavity Array Slab with Absorption	126
6	Conclusions and Outlook	131
	Bibliography	135

Chapter 1

Thermal Emitters: Introduction and Background

1.1 Introduction and Motivation

Thermal emitters radiate electromagnetic energy and generally exhibit a broad emission spectrum characterised by Planck's radiation law [1]. The power emitted and the peak emission wavelength are directly and inversely proportional to the temperature, respectively. For example, sunlight with peak emission wavelength in the visible is produced from hot plasma in the sun at temperatures around 5500 °C. Animals, on the other hand, are much cooler bodies (37 °C), therefore, emit less power and have a peak emission wavelength in the infrared wavelength range at almost 10 μm . This peak-wavelength temperature dependence has been exploited by blacksmiths for centuries to determine the temperature of hot glowing metal.

The broadband nature of thermal emitters is not always advantageous and in many circumstances results in poor energy efficiency. For example, the Joule heating of a tungsten filament in an incandescent light bulb produces broadband thermal radiation. However, tungsten filaments typically only radiate around 12% of light in the visible wavelength range [2]. If somehow the filament was redesigned such that all the emission took place in the visible band of the spectrum, with all the other emission wavelengths suppressed, the efficiency of the light bulb would increase. The light bulb is one example where the tailoring and optimisation of thermal emission would be hugely beneficial.

Recently, there has been an extensive effort aimed at controlling and manipulating the thermal emission spectrum of emitters, mostly in the visible and infrared wavelength ranges. In general, there are two ways to control the thermal emission; (1) chose a material that has a desired emission spectrum such as rare earth oxides or (2) modify the structure of the emitter at the wavelength and sub-wavelength scale.

Rare earth oxides such as Yb_2O_3 and Er_2O_3 present sharp emission peaks when heated, at 0.980 μm and 1.550 μm , respectively [3, 4]. These materials have very high melting points and have very good thermal stability. However, there are some disadvantages, as this approach does not allow any control over the emission wavelength, with only very discrete wavelength ranges covered by the oxide emitters being available, and no control over the emission bandwidth.

An alternative approach that has recently received attention is to control the thermal emission using photonic resonant structures. The addition of a photonic resonance enhances the absorption of the material over a specific and narrow wavelength range. The enhanced absorption results in enhanced emission, according to Kirchhoff's radiation law [5], which equates the absorptivity (α) and emissivity (ϵ) $\alpha(\lambda) = \epsilon(\lambda)$, when the structure is heated. Metallic [6–11], metallo-dielectric [12–15] and all dielectric [16–19] thermal emission devices have been investigated, all exhibiting a controlled narrow emission profile. The devices cover the complete wavelength range from visible up to the mid-infrared. A review of a select number of these devices is presented in Section 1.5.

Other than scientific interest, there are many applications for narrowband thermal emitters, for example as light sources in the mid-infrared wavelength range. The world of mid-infrared sources (operating in the 3-5 μm range) can be divided into two categories: thermal emitters and active devices such as lasers and light emitting diodes (LEDs). Quantum cascade lasers [20] and interband cascade lasers [21] are high power continuous wave sources, capable of covering the complete mid-infrared wavelength range. For example, commercial interband cascade lasers (Thorlabs) have efficiency values around 1.85% at 3.55 μm . Quantum cascade lasers (Thorlabs) exhibit similar behaviour with efficiency values in the range of 1.25% at 4.05 μm . These efficiency values are larger than typical LED devices and the lasers have a narrower emission bandwidth of 50-100 nm. However, due to their expense and large size, they are not in the same league as the smaller, cheaper sources such as thermal emitters and LEDs.

LED sources for the mid-infrared range are typically based on antimonide compounds [22]. The main drawback is their poor energy efficiency. Typical commercially available devices (Boston Electronic Corporation and Roithner Lasertechnik) exhibit efficiency values in the region of 0.4% at 3.4 μm wavelength. Furthermore, the emission bandwidth of these devices is rather wide in the range of 400-800 nm. However, the broad emission of these LEDs remains much narrower than the alternative blackbody-like broadband thermal emitters (e.g. a hot filament), making the LEDs an attractive light source despite the poor efficiency.

However, with the introduction of nanophotonic structures as thermal emitters, narrow linewidth thermal sources are now an option and LEDs may no longer be the go-to light source. While it is difficult to give an accurate estimate of the expected efficiency of a typical narrowband thermal emitter, because of the difficulty in determining the heat conduction losses, what can be expected is a significant increase in the efficiency when compared to the broadband blackbody thermal emitters. By narrowing the emission profile, greater efficiency is achieved by forcing more of the input energy to emit at the desired, resonant, wavelength. In reference [23] for example, the efficiency of the narrowband thermal source is improved by a factor of 10 compared to the equivalent blackbody thermal emitter. This increase is achieved through a method described as photon recycling, where the energy that is suppressed at the off-resonant wavelengths is re-emitted at the desired narrow emission peak and therefore, more light is emitted in that wavelength range. A summary of this device is presented in Section 1.5.3.

A schematic of a very simple gas detection system, non-dispersive infrared

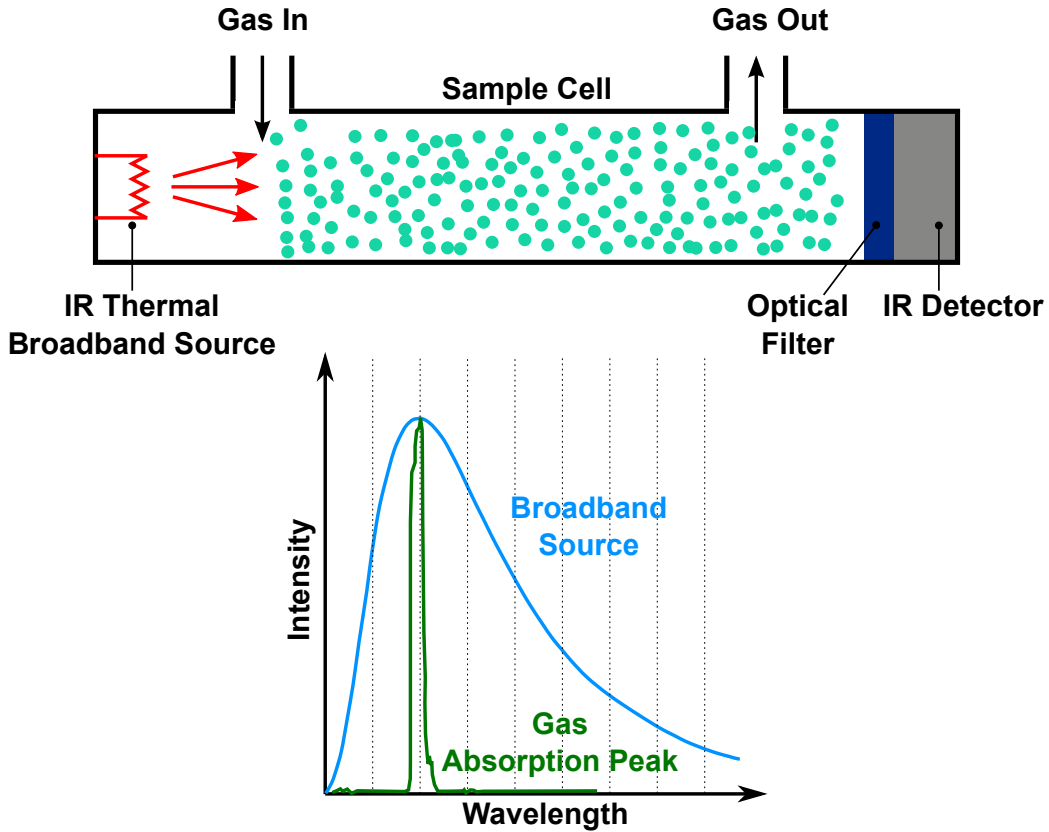


Figure 1.1: A schematic of a very simple NDIR (non-dispersive infrared sensor) including a typical broadband thermal emission profile overlaid onto a typical narrow gas absorption peak.

(NDIR) gas sensing [24], is presented in Fig. 1.1. The system typically uses a hot filament as a broadband light source with narrowband optical filters placed over the detector. The pass bands of the filters overlap with the absorption lines of the target gases. However, these gas absorption resonances are typically very narrow, like the example shown in Fig. 1.1, and cover the entire mid-infrared wavelength range [25]. Schematically comparing this absorption line to the overlaid blackbody spectrum of a typical thermal emitter, it is easy to see that this system wastes the vast majority of the light produced. The aim of the research is to replace mid-infrared light sources like these, with narrowband emission sources which are specifically tailored for the application. There would no longer be a requirement for optical filters and the power consumption of the whole system would dramatically reduce. Due to the wavelength scalable nature of many photonic structures, it is possible to design a thermal source to operate at any wavelength across the entire mid-infrared range and therefore overlap with many of the absorption lines of the target gases.

A second application area where controlled thermal emission is advantageous is thermophotovoltaics, i.e. the conversion of thermal energy to electrical energy [26]. Generally, heat from solar radiation or industrial waste heat is used to increase the temperature of an object, Fig. 1.2. It is important to realise that this object (labelled as thermal emitter in Fig. 1.2) has a different structure at each side. The side facing the light/heat source behaves as a broadband absorber, on the other hand, the side facing the photovoltaic (PV) cell contains

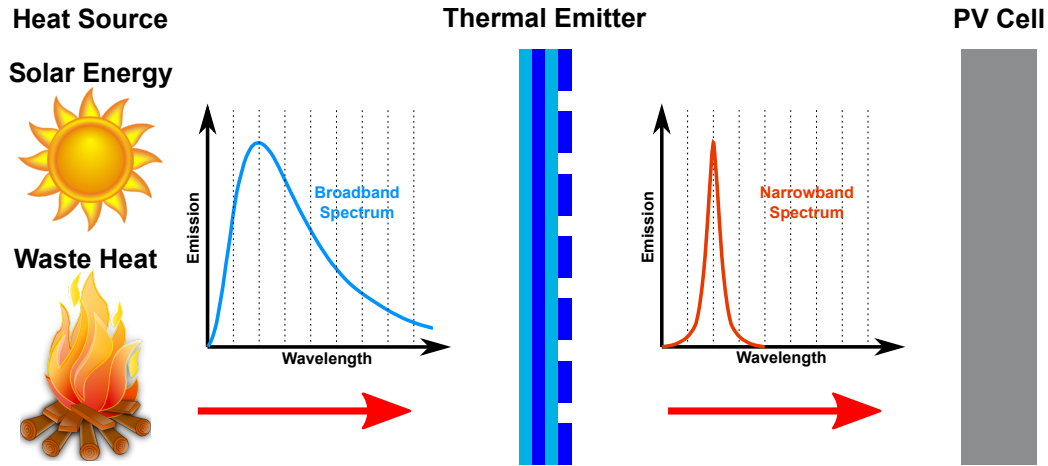


Figure 1.2: A schematic representation of a thermophotovoltaic power generation system. The thermal emitter object is heated by absorbing solar radiation (broad band emission) or waste heat energy (e.g. nuclear reactor). The heated thermal emitter re-radiates the energy in a narrow wavelength range only, which matches the photovoltaic (PV) cell.

a nanophotonic structure engineered to have a very narrow absorption profile.

The input energy is represented as the blue broadband spectrum in Fig. 1.2. Ideally, all of the input energy is absorbed by the thermal emitter, therefore, the energy of the photons at every wavelength (and incident angle) contribute to raising the temperature of the thermal emitter. To achieve such a broadband absorption, the side of the thermal emitter facing the source needs to be a perfect absorber i.e. it needs to be a blackbody, where an absorptivity of 1 is achieved at every wavelength and incident angle.

The temperature of the thermal emitter will increase and at equilibrium, it will re-emit light according to Kirchhoff’s radiation law [5], where the emissivity is equal to the absorptivity. Considering the broadband absorption side, the thermal emission spectrum will be the same as the input absorbed spectrum, i.e. light absorbed at each wavelength and at each angle is re-emitted at that wavelength and emission angle. The side with the nanophotonic structure is designed to absorb light differently to a blackbody, for example, lets say it absorbs light over a narrow wavelength range and at normal incident only. Again, according to Kirchhoff, it will only emit light over that wavelength range and normal to the surface, see the narrow red emission plot in Fig. 1.2. Light at every other wavelength and emission angle is suppressed.

Typically, the PV cell is a p-n junction which has an electronic energy gap and only the wavelength band of light that corresponds to this energy gap is converted efficiently to an electric current. Therefore, by using Kirchhoff’s law we are able to design an object that at one side can absorb (and emit) a broadband spectrum, while the other side is designed to emit only over a narrow wavelength range. The narrow emission wavelength band is designed to overlap with the high efficiency absorption band of the PV cell. This approach potentially allows for greater energy efficiency, because the energy of every incident photon, whether it be within the absorption band of the PV cell or well outside it, is utilised and converted to an electric current [27].

Therefore, the motivation to realise narrowband thermal emission devices is

strong. Devices that can be scaled and operate at a large range of wavelengths, with high emissivity at the target wavelength are desired. In order to realize a narrowband thermal emission spectrum, we have to maximize the absorptivity of the emitter at a target wavelength while minimizing it at all other wavelengths, Kirchhoff’s radiation law [5]. Nanophotonic structures are the way to achieve these requirements. Through correct Q-matching of the optical resonance and the optical loss of the material, high emissivity values can be achieved.

1.2 Aim and Preview of the Thesis

In this thesis, I present my work on the development of four different nanophotonic structures for narrowband thermal emission. The development process includes the initial designing, all simulation and computational work, complete fabrication and experimental measurements of the devices. Each is based on a different photonic resonant structure. Two of the designs are based on doped silicon as the thermal emission material; photonic crystal square hole array (PhC) Fig. 1.3a and the photonic crystal coupled cavity array (CCA) Fig. 1.3b, while the other two use gold as the emission material; metal-insulator-metal resonator (MIM) Fig. 1.3c and the binary biharmonic grating structure (BBS) Fig. 1.3d.

Gold is a very popular choice as a thermal emission material because of its natural broadband absorption properties. It has been used extensively throughout the literature for various metallic thermal emission devices. The MIM structure presented here consists of a thick metal ground plane and an array of metallic resonators which is separated from the ground plane by a dielectric insulator layer. MIM devices have shown to be near perfect absorbers of radiation, particularly at longer wavelengths in the THz frequency regime. When designing a thermal emitter, the description “perfect absorber” is a very attractive quality because, in theory, heating such a device will lead to “perfect emission”, i.e. an emissivity of 1. The MIM device presented here is based on a similar structure which originally operated as a THz absorber. The structure parameters were scaled down and redesigned to operate in the near-infrared wavelength range. Since the device operates by exciting localised, almost point like resonances, the absorption is omnidirectional in nature i.e. the resonant wavelength is independent of the incident (emission) angle.

The BBS is the second device based on gold as the emission material. Unlike the MIM device, which is based on localised resonances, this device is based on propagating surface plasmon polaritons (SPPs). The structure consists of two combined grating components. The shorter period harmonic creates a band gap which prohibits the propagation of a range of SPP frequencies, while the second, larger period harmonic, couples the modes at the band gap edge to radiative free space photons. The width of this band gap is proportional to the relative amplitude ratio of the two grating components and also to the grating groove depth. By correctly tuning both parameters of the structure, a completely flat resonance dispersion band is achieved where, like the MIM device, the resonance wavelength does not change as the incident angle goes from normal to 90°. As with all SPP structures, it is polarisation dependent, achieving such a flat dispersion band from a periodic structure is truly remarkable.

However, there are some drawbacks with using gold; very broad optical res-

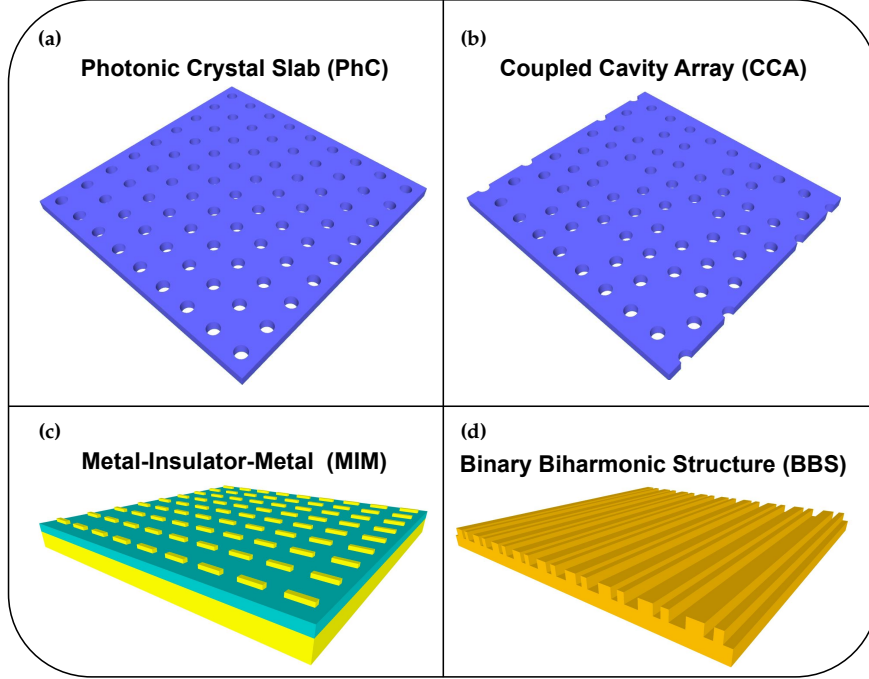


Figure 1.3: Diagram of the four photonic resonant structures studied within the thesis; (a) photonic crystal square hole array (PhC), (b) photonic crystal coupled cavity array (CCA), (c) metal-insulator-metal resonator and (d) binary biharmonic grating structure (BBS).

onances ($Q < 10$) and undesired emission over a wide wavelength range, both due to the strong free carrier absorption of the metal. More importantly, the melting point is too low for practical, long-term use. Therefore, an all-dielectric thermal emitter is a promising alternative to achieving high Q emission with relatively low background. The primary focus of this thesis is on doped silicon photonic crystal thermal emitters. Silicon was chosen as the emission material for a number of reasons. Firstly, in the world of photonics silicon, commonly in the form of SOI (silicon-on-insulator), is becoming a very popular platform for both active and passive devices. Its high refractive index (≈ 3.5) enables strong light confinement, and by etching an array of holes into the top silicon layer of a SOI wafer, it is possible to achieve very sharp optical resonances. An issue for thermal emitters, however, is that silicon is almost completely transparent in the near-infrared wavelength range. To increase its absorption properties, silicon was heavily doped with phosphorous. By controlling the doping concentration it is possible to “ Q -match” the absorption Q -factor of the material with the Q -factor of the optical resonance in the photonic crystal slab. To achieve “ Q -matching” the values of the absorption and radiation Q -factors need to be equal. At this optimal condition, the maximum emission intensity is achieved with the narrowest possible linewidth. Under-couple (doping density too low), the emission linewidth is narrow but the emission intensity is low; over-couple (doping density too high), the maximum emission intensity is achieved but the resonance is unnecessarily broad. At this optimal or “critical coupling” condition, the absorptivity is optimally maximised and narrowband thermal emission is demonstrated.

A common oversight in a large portion of the published research work on

thermal emitters are the angular, off-normal, emission properties of the device. The primary reasons for ignoring this behaviour is, that it is more difficult to measure and secondly, it is not very desirable. If one considers a periodic structure, its response is typically strongly dependent on the angle [28]. This means that when the structure is heated, the emission wavelength changes as one moves away from the surface normal. This is not an attractive quality as one would like to have a monochromatic source with only the desired wavelength emitted into any angle.

In this thesis there is a strong emphasis on examining the angular emission properties of all the developed devices. The MIM and BBS structures, discussed in Chapter 4, demonstrates very favourable angular emission properties. The MIM structure was fabricated and tested but unfortunately did not perform as expected and the BBS structure was not experimentally fabricated due to the very high aspect ratios required and is based on simulation results only. The complication with the fabrication of the metallic devices is based on the etching difficulty of gold.

On the other hand, the silicon photonic crystal slab was successfully fabricated on SOI and experimentally demonstrated narrowband thermal emission, however, the emission behaviour is not angularly independent. To improve on the design which is so successful as a thermal emitter, the CCA photonic crystal was examined. This structure is also based on doped SOI with a triangular lattice of holes instead of square. The array of cavities is created by removing every third hole from the lattice. The dispersion of the cavities is completely flat with no angular dependence on the resonance wavelength. These structures show a very promising behaviour as monochromatic thermal emission devices, but was not realised experimentally due to lack of time and are based on simulation results only.

A significant part of the work was to design an optical characterisation setup to measure the reflection and thermal emission properties of the fabricated devices. I would also like to point out that all the work presented in this thesis is based on designing the thermal emitters to operate in the near-infrared wavelength range at $\approx 1.5 \mu\text{m}$. Of course, the wavelength range of interest for many applications is predominately in the mid-infrared. The reason for carrying out the investigations at $1.5 \mu\text{m}$ is that the experimental equipment available to me operates in this range. In principle, this should not matter, as all the work here involves new designs and devices and is largely proof-of-concept work, not for finalised devices. Therefore, as with all photonic crystal structures, they are scalable and it is relatively straightforward to increase the structural parameters in order to shift the operating wavelength into the mid-infrared wavelength range.

1.3 Theory of Photonic Crystals

Two key publications in 1987 by Yablonovitch [29] and John [30] on the optical properties of three dimensional (3D) photonic crystals triggered huge interest in the control and manipulation of light and photons. Along with many other applications, this emergence of the photonic crystal generated new possibilities to control spontaneous emission that did not exist before and is the main reason for such a large interest in thermal emission in the past two decades. This

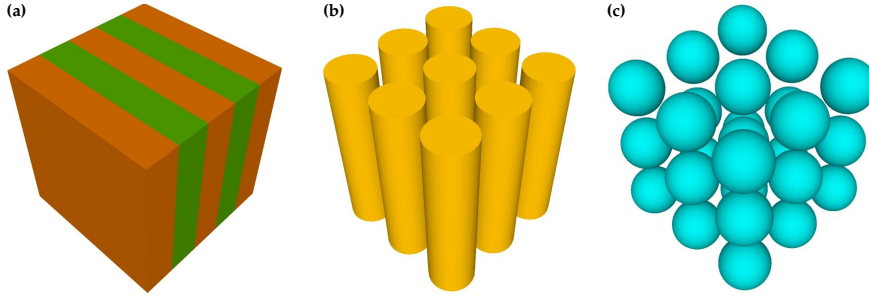


Figure 1.4: Schematic of (a) one-, (b) two-, and (c) three-dimensional photonic crystals. (a) A multilayer film. (b) A square lattice of dielectric columns. (c) An opal crystal

new class of periodic materials affect light propagation in a similar way as a potential in a semiconductor crystal affects the motion of electrons [28]. Since the size of this periodic permittivity variation is on the scale of the wavelength of light, photonic band gaps can be formed where no electromagnetic radiation with frequency within the band gap is allowed to propagate [31, 32].

Of course, the properties of optical periodic structures have been well known for over a 100 years. Prior to the work presented by Yablonovitch on 3D structures, Lord Rayleigh in 1887 demonstrated the prohibition of light propagating through a 1D crystal lattice [33]. And through the twentieth century, 1D multilayer structures were extensively studied and used as mirrors and filters [34]. It was Yablonovitch who introduced the electronic crystal concepts from solid state physics to describe light propagating through a periodic structure and with his new findings aroused enormous interest in theoretical and experimental studies of photonic crystals.

There are several different geometries of photonic crystals but generally, they can be broken down into three categories with the periodically varying refractive index oriented in one-, two- and three dimensions. An example of each is presented in Fig. 1.4. All the work in this thesis focuses on 1D and 2D photonic crystal structures.

1.3.1 From Maxwell's Equations to Photonic Crystals

The material and analysis in the following section has been partially extracted from [28]. This section discusses how to start from Maxwell's equations and then create a photonic band gap for a simple 1D photonic crystal. To begin, we assume an isotropic material where the electric permittivity (ϵ) and the magnetic permeability (μ) are scalar quantities. We also assume that we are dealing with non-magnetic ($\mu = \mu_0$, vacuum permeability) and non-electric (both the electrical charge density and electrical conductivity are zero) media. Therefore, Maxwell's equations for light propagating in such a medium are

$$\nabla \cdot E = 0 \tag{1.1}$$

$$\nabla \cdot H = 0 \tag{1.2}$$

$$\nabla \times E = -\mu_0 \frac{\partial H}{\partial t} \tag{1.3}$$

$$\nabla \times H = \epsilon \frac{\partial E}{\partial t} \quad (1.4)$$

where E and H are the vector electric and magnetic fields, respectively, and ϵ is the free space permittivity, ϵ_0 , times the dielectric function $\epsilon(r)$. Eqs. 1.1 and 1.2 imply that they are no point sources but always closed loops of the fields while Eqs. 1.3 and 1.4 show that to create an electrical field one requires an oscillating magnetic field and vice versa. Combining all four equations leads to the fundamental electromagnetic wave equation, shown here for the electric field case

$$\nabla^2 E = \mu_0 \epsilon_0 \frac{\partial^2 E}{\partial t^2} \quad (1.5)$$

The equation is also valid for the magnetic field. It shows that the field replicates itself through its own second derivative. Solutions of the equation must be in the form of a linear superposition of sinusoidal frequencies, therefore the radiation propagates as a wave.

1.3.1.1 1D Photonic Crystal Band Gap

Eq. 1.5 describes how radiation propagates through a homogeneous medium, but this changes when light propagates through a photonic crystal i.e. a periodically changing medium. The simplest 1D photonic crystal consists of alternating layers of different dielectric constants, see Fig. 1.5a where the periodicity is in the z -direction and the stack is homogeneous in the xy plane. The periodic dielectric function is $\epsilon(z) = \epsilon(z + la)$, where a is the lattice vector characterising the periodic properties of the 1D photonic crystal, and l is an integer. The wave vector of the propagating wave is in the z -direction, k_z .

Since we are dealing with a periodic structure, we can apply the Floquet-Bloch theorem [35] which tells us that the solutions to any eigenvalue problem can be chosen to have the form of a plane wave times the periodicity of the lattice. Therefore, for the multilayer stack the optical modes can be expressed as Bloch waves in the form of

$$H(z) = u_{k_z}(z) e^{-ik_z z} \quad (1.6)$$

where H represents the magnetic field vector (but it is equally accurate to consider the electric field) with wave vector k_z and $u_{k_z}(z)$ is the periodic function with the periodicity of the lattice a .

$$u_{k_z}(z) = u_{k_z}(z + R) \quad (1.7)$$

where $R = la$, which is simply an integer multiple of the period. The Bloch theorem can be expressed in an alternative form by combining Eqs. 1.6 and 1.7.

$$H(z + R) = H(z) e^{-ik_z R} \quad (1.8)$$

The Bloch mode with wave vector k_z is identical to the Bloch mode with wave vector $k_z + l2\pi/a$.

By setting the permittivity of the two alternating layers to be the same, the dispersion relation is that of a homogeneous media $\omega = ck$, represented by the solid blue lines in Fig. 1.5b. Due to the periodicity, the dispersion relation

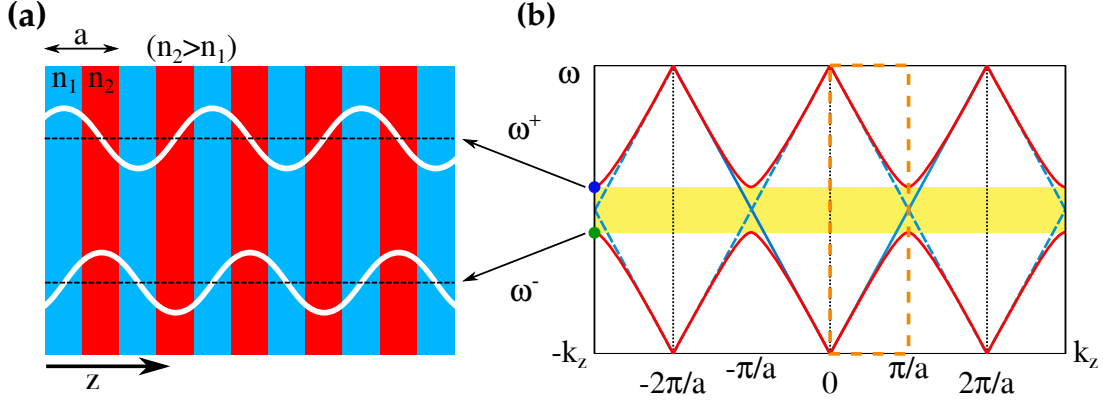


Figure 1.5: (a) 1D periodic dielectric stack, in the z -direction with high (n_2) and low (n_1) refractive indices. The field intensity of the two standing wave solutions is shown in blue (ω^+) and green (ω^-). (b) Band diagram of the 1D dielectric stack as in (a). The band gap is highlighted in yellow and the irreducible Brillouin zone is highlighted with a dotted orange box.

replicates itself at every $k_z = k_g$ point, where $k_g = 2\pi/a$ is the reciprocal lattice vector or grating vector, dashed blue line in Fig. 1.5b. At each cross point of the dispersion lines at $k_z = \pm\pi/a$, there is a degeneracy, with two possible solutions both with frequency $\omega = c\pi/a$. If we now set the permittivity of the alternating layers to be different, the degeneracy is broken and it splits to two separate frequency values for the same k_z value. Due to periodic nature of the structure and using simple symmetry arguments, there are only two possible solutions for arranging such modes within the stack. The nodes of the standing wave solutions must lie at the centre of the high-index or low-index regions. The high index material is analogous of the lower potential in solid state physics, therefore, the lower frequency mode (ω^-) sits with the majority of the mode within the high index region, and conversely, the high frequency mode (ω^+) has the majority of its field in the low index layers, see Fig. 1.5a where the relative field amplitude is shown. As a result, a frequency range is created where no modes exist, called the photonic band gap, see yellow band in Fig. 1.5b. When light impinges on the photonic crystal in the direction along the stack, with a frequency within the band gap, it will be totally reflected because there are no electromagnetic modes within the structure to couple to. The size of this band gap is directly proportional to the index contrast.

Because the structure is periodic, the region $k_z = \pm\pi/a$ of k -space replicates itself periodically, so the solutions for all modes can be completely characterised by looking at their behaviour in this region of k -space only, known as the first Brillouin zone. As k_z repeats itself outside the Brillouin zone, the mode folds back on itself when it reaches the edge at $\pm\pi/a$. For convenience, the dispersion relation can be restricted to the first Brillouin zone and this construction is called the reduced zone scheme. Furthermore, within the Brillouin zone, the modes have mirror symmetry about $k_z = 0$, hence the Brillouin zone can be reduced to the primitive unit cell named the irreducible Brillouin zone, which is marked by the orange dotted box in Fig. 1.5b. The irreducible Brillouin zone is not unique to the 1D case but extends to 2D and 3D structures as well. It simplifies the k -space domain by only looking at a few high symmetry k -directions.

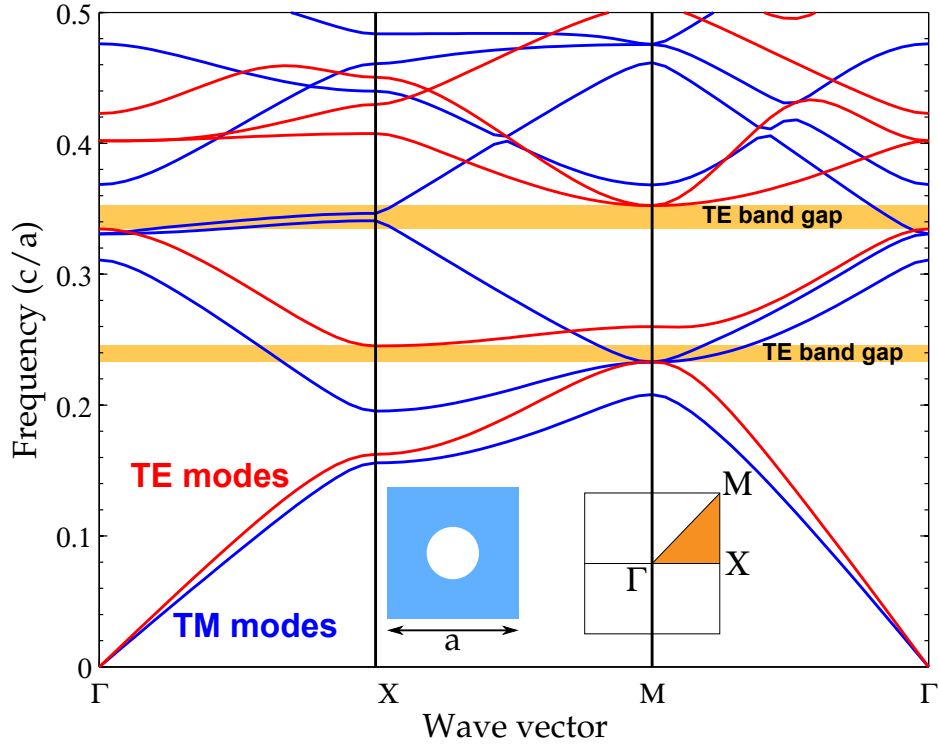


Figure 1.6: Two dimensional photonic band diagram for a square array of holes in silicon ($n=3.5$) with period a hole radius of $0.35a$. The left inset shows a cross-sectional view of the unit cell. The right inset show the first Brillouin zone, with the irreducible Brillouin zone highlighted in orange.

The binary biharmonic structure presented in Chapter 4 is based on a 1D grating profile. The material is metal, so instead of propagating electromagnetic modes, we deal with SPP modes. However, the same analysis as for the 1D dielectric structure can be applied and band gaps are formed in the same way. More information about the formation of these band gaps for propagating SPP on metal gratings is given in Chapter 4.

1.3.1.2 2D Photonic Crystal Band Gap

After the 1D multilayer stack, the most common photonic structure used in planar silicon photonics is the 2D lattice of air holes. It typically consists of an array of air holes in either a square or triangular format in a high index dielectric, such as silicon. It has periodicity in two directions while being continuous and homogeneous in the third. A band diagram for a typical square hole array photonic crystal is presented in Fig. 1.6. The left inset shows a segment of the square hole array lattice of period a (hole radius is $0.35a$) and index of the dielectric set to $n=3.5$. It is important to note that this is not a slab structure, and that it is infinite in the vertical direction. The modes are strictly divided into two polarisations; TM (transverse magnetic) where the electric field is perpendicular to the plane of the periodicity and the magnetic fields are parallel, and TE (transverse electric) where the electric field is parallel to the plane periodicity and the magnetic fields are perpendicular [28]. The band diagram shows modes for both polarisations.

The band structure is calculated numerically using the plane wave expansion

method, where the periodic structure is transformed into a series of sines and cosines, using a very popular free simulation tool - MIT Photonic-Bands package - known as MPB. The band diagram shows the frequency of modes for each wave vector. The right inset in Fig. 1.5 shows the first Brillouin zone for the square lattice with the irreducible Brillouin zone shaded in orange. Here the band diagram is only calculated along the wave vectors which lie on the edge of the irreducible Brillouin zone i.e. Γ -X-M- Γ . These are called the key symmetry points and the band diagram is calculated along these points because most of the time the band gap forms between two of the high symmetry points. In the 2D case, a complete band gap may be achieved in the plane i.e. no propagation of light in any direction within the crystal. The band diagram shown here has two complete band gaps for TE modes (red lines), but there are no band gaps for the TM modes (blue lines). By increasing the hole radius, a complete band gap is possible for both polarisations. It is easier to achieve a band gap in a triangular lattice than in a square lattice because of higher symmetry i.e. the triangular lattice has a six-fold symmetry whereas the square array only a four-fold symmetry.

In this thesis, square hole array photonic crystal slabs are used as the resonant photonic structure for thermal emission control. The band diagram for the slab structure is different to the one for the pure 2D case and it is very important to realise the difference. For the slab crystal the light line plays a key role. Any modes below the light line are fully confined and guided within the structure, whereas (most) modes above the light line (within the light cone) are leaky and weakly guided modes with a finite decay time. The energy in the lossy modes couples out to the surrounding environment.

Many silicon photonic crystal devices are used for in-plane applications, here the confined modes are crucial. In this work, however, we are interested in the vertical out-of-plane emission and so modes that lie within the light cone. The primary interest is in normal emission, which takes place at the Γ -point of the band diagram for both the photonic crystal slab in Chapter 3 and the CCA in Chapter 5.

1.4 Fundamentals of Thermal Emission

It is well known that thermal radiation is wavelength and temperature dependent. Radiation is created within matter through phonon relaxation mechanisms, such as molecular vibrations in gases or electron and lattice vibrations in solids and this radiation is emitted from the surface of the object. The emitted electromagnetic waves have different frequencies and wave vector values.

So far we have looked at the dispersion relation of 1D and 2D structures and developed the relation from Maxwell's equations. These equations determine how the light propagates through the material and structure, whether it be homogeneous or periodic. The dispersion or band diagrams allows us to see the spectral position of the resonances, but how does this affect the emission properties of the structure across the full wavelength range. What does the reflection (transmission) spectrum look like? In the next section some of the properties of radiative light emission are presented and I demonstrate how a photonic resonance can enhance the emission properties of a material.

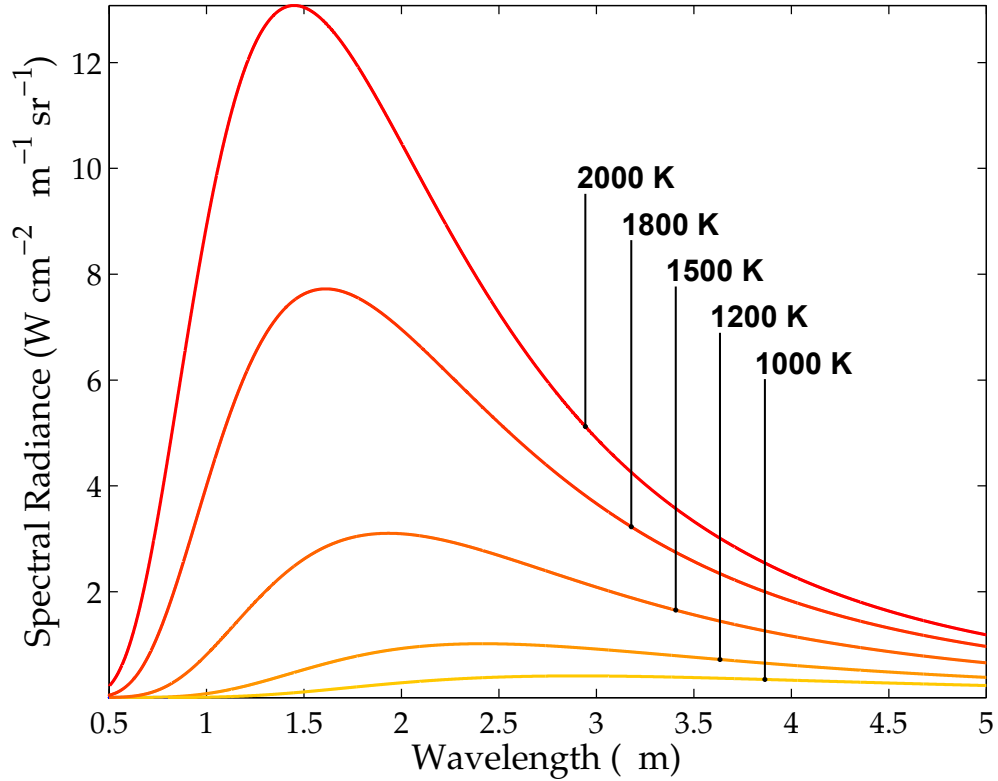


Figure 1.7: Blackbody thermal emission spectrum for various temperatures; 1000 K, 1200 K, 1500 K, 1800 K and 2000 K.

1.4.1 Radiative Properties

Lets begin by considering a wave incident from air onto a homogeneous medium with no patterning or any sort of periodic modulation. Generally, that wave will be partially reflected, partially transmitted and partially absorbed. These three fundamental radiative properties are reflection (R), transmission (T) and absorption (A) are defined as follows

$$R = \frac{\text{Reflected Power}}{\text{Total Incoming Power}} \quad (1.9)$$

$$T = \frac{\text{Transmitted Power}}{\text{Total Incoming Power}} \quad (1.10)$$

$$A = \frac{\text{Absorbed Power}}{\text{Total Incoming Power}} \quad (1.11)$$

These radiative properties are non-dimensional and all the radiation is either reflected, transmitted or absorbed, therefore $R + T + A = 1$.

1.4.1.1 Planck's Radiation Law

If all the incident radiation, at every wavelength, on the medium is absorbed with no transmission or reflection, that body is called a blackbody and is described as a perfect absorber of all radiation (regardless of polarisation and angle). In theory, no such body exists, however, materials like carbon black, platinum black and silicon carbide do approach behaviour that is close to a blackbody.

In thermal equilibrium, if a material is a perfect absorber it is also a perfect emitter of radiation. Therefore, for a given temperature, the maximum thermal radiation can be emitted from a blackbody. To determine the spectral behaviour and the temperature dependence of the blackbody emission, the quantum theory developed by Max Planck must be considered [36]. The spectral radiance of a black body, E_{BB} , is described by Planck's radiation law [1]

$$E_{BB}(\lambda, T) = \frac{2hc^2}{\lambda^2} \frac{1}{e^{\frac{hc}{\lambda k_B T}} - 1} \quad (1.12)$$

where k_B is the Boltzmann constant ($\approx 1.38 \times 10^{-23}$ J/K), h the Planck constant ($\approx 6.626 \times 10^{-34}$ J s) and c the speed of light in vacuum ($\approx 2.998 \times 10^8$ m/s). The law describes the amount of radiation given off at a given wavelength (λ) for a given temperature (T). The power emitted is per unit area, per unit solid angle and per unit wavelength. The SI units of the emission is $\text{W sr}^{-1} \text{m}^{-3}$. The emission spectrum of a blackbody for different temperatures is presented in Fig. 1.7.

From Fig. 1.7, we note that the peak power emission wavelength shifts to shorter wavelengths as the temperature of the blackbody increases. Wien's displacement law explains this behaviour and specifies the maximum emission wavelength (λ_{max}) at each temperature with

$$\lambda_{max} = \frac{b}{T} \quad (1.13)$$

where b is constant of proportionality called Wien's displacement constant, with a value of 2.8977721×10^{-3} m K.

The total emitted power, i.e. the integral of the area under the curve, increases with temperature. For a blackbody, the overall radiated power (P) from a given area (A) is calculated according to the Stefan-Boltzmann law

$$P(T) = A\sigma T^4 \quad (1.14)$$

where σ is the Stefan-Boltzmann constant 5.670373×10^{-8} $\text{W m}^{-2} \text{K}^{-4}$.

From this discussion, we can define another non-dimensional radiative property called emissivity ϵ . It is defined as the ratio of energy emitted by the surface of a greybody (non-ideal blackbody) to the emitted energy of an ideal blackbody surface, it varies between 0 and 1, with 1 corresponding to a perfect blackbody emitter. The maximum spectral emission is E_{BB} and at the same temperature a real emitting surface will emit a lower power E_{GB} (greybody)

$$\epsilon(\theta, \phi, \lambda, T) = \frac{\text{Emitted Power Greybody}}{\text{Emitted Power Blackbody}} = \frac{E_{GB}(\theta, \phi, \lambda, T)}{E_{BB}(\theta, \phi, \lambda, T)} \quad (1.15)$$

It is important to point out that the emissivity is wavelength dependent and we should redefine the the Stefan-Boltzmann definition for a real grey body by including the emissivity value

$$P(T, \lambda) = A\epsilon(\lambda)\sigma T^4 \quad (1.16)$$

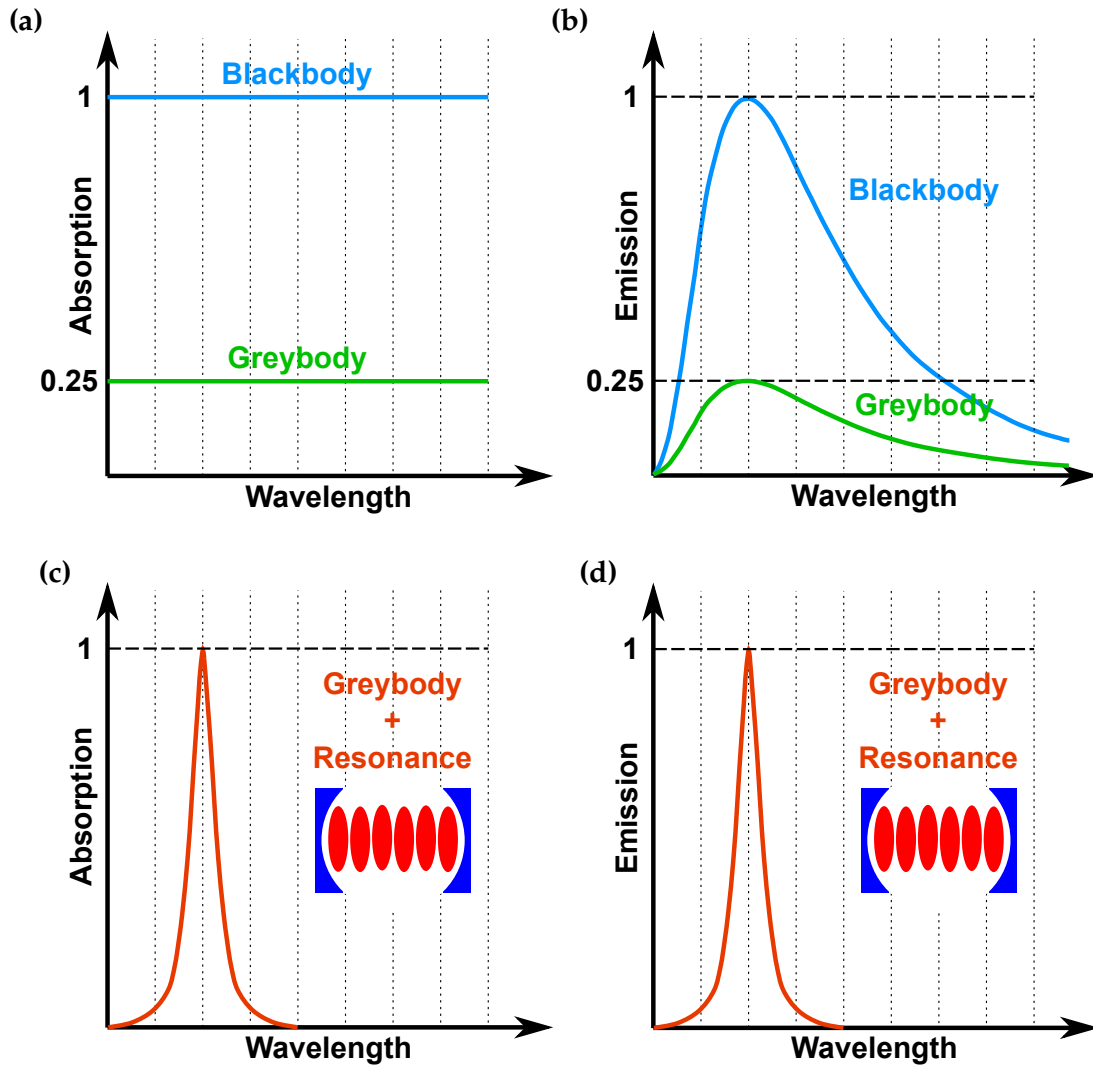


Figure 1.8: Schematic of resonantly enhanced thermal emission. Typical absorption of a grey body is less than 1 which produces low emission spectrum (b). With the addition of an optical resonance the absorption is enhanced at the resonate wavelength (c) and when heated resonantly enhanced emission is observed (d).

1.4.1.2 Kirchhoff's Radiation Law

One of the fundamental principles of thermal emission is Kirchhoff's law of thermal radiation [5]. Derived by Gustav Kirchhoff in 1859, it states that

For a body of any arbitrary material, emitting and absorbing thermal electromagnetic radiation at every wavelength in thermodynamic equilibrium, the ratio of its emissive power to its dimensionless coefficient of absorption is equal to a universal function only of radiative wavelength and temperature. That universal function describes the perfect black-body emissive power.

Consider a body within an enclosure at equilibrium. The body has finite absorption and the dimensions of the body are assumed to be large compared to the wavelength of the radiation. For the body to be truly in equilibrium, the energy i.e. the temperature of the body must not change. Therefore, if a

finite amount of radiation is incident on the body, it will absorb a fraction of this energy. It then must re-emit the exact same amount of energy in order to remain at the same fixed temperature. Hence, the power absorbed by the body is equal to the power emitted by the body.

This is not a proof of Kirchhoff's law, but is a very simple argument for it. Kirchhoff used a series of carefully thought out experiments and fundamental thermodynamic laws to prove the theory and, in summary, deduced that the emissivity (ϵ) of a body is equal to its absorptivity (α) (absorption)

$$\epsilon(\theta, \phi, \lambda) = \alpha(\theta, \phi, \lambda) \quad (1.17)$$

Both quantities are a function of wavelength λ , polarisation and incident angle. A simple corollary of this relationship is that the emissivity cannot exceed unity because the absorptivity cannot exceed it. And therefore, it is not possible to radiate more energy than a theoretical blackbody at equilibrium.

This relationship tells us that in order to control the emission properties of a body one needs to control its absorption properties. A typical material such as gold or doped silicon absorbs light but only weakly [37, 38]. They behave like a greybody with low broadband absorption, schematically shown in Fig. 1.8a, which corresponds to low broadband emission when compared to a blackbody Fig. 1.8b. However, if we include an optical resonance, we can increase the light-matter interaction and therefore, increase the absorption at the resonant wavelength, thereby creating a narrowband absorber, Fig. 1.8c. According to Kirchhoff's law, the resonantly enhanced narrowband absorption leads to enhanced narrowband emission, Fig. 1.8d.

Kirchhoff's thermal emission law is the foundation of the entire thesis. I present a range of optical resonant structures, each of which resonantly enhances the absorption of the material. Throughout the work, I will talk equivalently about a material's emissivity and absorptivity. This equivalence allows all the design considerations and computational work to focus on the absorption properties of the structure and there is no need to compute the emission behaviour, which makes computation much easier.

1.5 Review of Selected Devices

The aim of the work is to achieve narrowband thermal emission in the near-infrared wavelength range. I will now review a selection of three different thermal emitters from the literature. For each, I will describe the device, including; materials, structure parameters, wavelength and temperature ranges, and focus mainly on thermal spectral emission properties achieved by each. The list is not exhaustive, because there are a large number of thermal emitters described in the literature. The three examples summarised here are somewhat related to the devices I have designed. Therefore, they are a good bench mark to compare my work against.

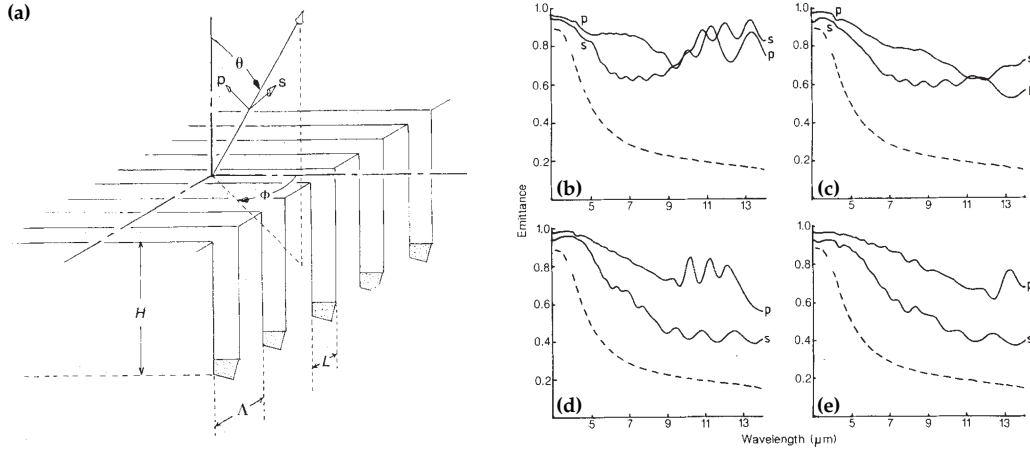


Figure 1.9: (a) Schematic drawing of the grating. Λ , period; L , slot width; H , depth; s- and p-polarisation vectors; θ , polar angle and Φ , azimuthal angle. (b)-(e) Normal polarised, spectral emittance as a function of wavelength for s- and p-polarisations at $T=400^\circ\text{C}$. The emittance of the smooth surface is shown as the dashed line in each. Grating depth is $\approx 45 \pm 2 \mu\text{m}$ with (b) $\Lambda=10 \mu\text{m}$; $L= 7.3 \mu\text{m}$, (c) $\Lambda=14 \mu\text{m}$; $L= 8.4 \mu\text{m}$, (d) $\Lambda=18 \mu\text{m}$; $L= 12.6 \mu\text{m}$ and (e) $\Lambda=22 \mu\text{m}$; $L= 14 \mu\text{m}$. Reprinted with permission from [39].

1.5.1 Organ Pipe Radiant Modes of Periodic Micromachined Silicon Surfaces

This publication (published in 1986) studies normal thermal emission from deep linear gratings, which are wet etched into bulk doped silicon [39]. A schematic of the structure is shown in Fig. 1.9a. Grating structures with four different periods (Λ); 10, 14, 18 and 22 μm , all with a depth of 45 μm were examined. The silicon was doped with phosphorous to a concentration in the range of $4\text{-}6 \times 10^{19} \text{cm}^{-3}$. All the emission measurements were taken at 400°C over the wavelength range 3 μm to 14 μm .

The thermal emission results are presented in Fig. 1.9b. The emission measurements were taken normal ($\theta = 0^\circ$) to the surface for both s- and p-polarisation states with the azimuthal angle $\Phi = 90^\circ$ with the s-polarisation vector parallel to the slots while the p-polarisation vector perpendicular. The results show the emittance, where the emission spectrum has been normalised to the measured emission of a blackbody at the same temperature. The dotted curve in each plot is the emissivity for a smooth doped silicon surface with no patterning.

Overall, the structured silicon emissivity is increased by up to a factor of 5 compared to that of the unpatterned silicon case. Also, and more importantly, there are emissivity oscillations in the spectrum of each of the four grating periods for both polarisations, which are not present in the smooth silicon curve. Their presence suggests that there is some kind of optical resonant enhancement occurring. The authors propose that these pronounced oscillations are explained by the presence of standing waves within the deep grating grooves. They developed an analysis where the wave number of each of the oscillation maxima is fitted to a mode number. This mode number corresponds to a standing wave mode that fits within the air groove. These standing waves have two orientations; one where the nodes occur at the surface and the bottom of the groove and

one where a node is at the surface with an anti-node at the base of the groove. Very good agreement with the fit is achieved.

Therefore, the enhanced emission properties are the result of an optical resonance. If we consider light incident on the same structure, it will result in an enhancement of the absorption due to the presence of these “organ pipe” type optical modes. Therefore, these modes lead to an enhancement in the emission properties at the same wavelength.

These results are a very early demonstration of resonant thermal emission enhancement. It is important to bear in mind that this letter was published the year before Yablonovitch [29] and John [30] published their pioneering results on photonic crystals. The enhanced emission is shown to be independent of the grating period, so the behaviour is not dependent on a periodic structure. However, there is an optical resonance and this has led to an enhancement of the emission properties. This letter is of particular interest because it uses doped silicon as the emission material which is the material I use (see Chapter 3), although not in bulk but in thin membranes, but with a very similar doping density of phosphorus.

1.5.2 Sharp Thermal Emission and Absorption from Conformally Coated Metallic Photonic Crystal with Triangular Lattice

As previously mentioned, gold is a very popular material for thermal emission control. Here I present an example of a very simple thermal emitter fabricated from gold. This device consists of a metallic photonic crystal with a triangular lattice of holes which are first etched into silicon and then coated in a uniform layer of gold, see SEM images in Fig. 1.10a [11]. The period of the lattice is $3.75 \mu\text{m}$. The hole radius, after the metallic coating, is $0.94 \mu\text{m}$ and the hole depth is $2.5 \mu\text{m}$. As the gold layer is thicker than the skin depth, it is accurate to assume that the structure is an array of holes etched into bulk metal. The wavelength range of interest is the mid-infrared i.e. 2 to $7 \mu\text{m}$.

Figure 1.10b shows the simulated normal reflection spectrum of the structure. A very strong reflection minimum is observed at $3.5 \mu\text{m}$. As there are no transmission components, all of the coupled light is absorbed by the gold photonic crystal lattice, see plot in Fig. 1.10b. In Fig. 1.10c, using emissivity is equal to absorptivity, the simulated absorption resonance is compared to a blackbody emission at 260°C . Also included in the plot is the emission (absorption) for an angle of 12° degrees to normal. The resonance peak has shifted to a longer wavelength and decreased in strength. This angular dependence of the resonant wavelength is typical for periodic structures and is a concern that I address in Chapter 4 and 5.

Figure 1.10d shows the measured experimental emission spectrum at 260°C . The emitted light has been collected over a 12° cone around normal with the peak emission at $3.85 \mu\text{m}$. While this is a fine example of how resonantly enhanced absorption by a photonic crystal can lead to narrowband thermal emission, the emission properties are not ideal. Firstly, the emission peak is very broad, with a Q-factor in the range of about 10 and secondly, the off-normal angular emission behaviour is not optimal i.e. the emission wavelength changes as the angle from

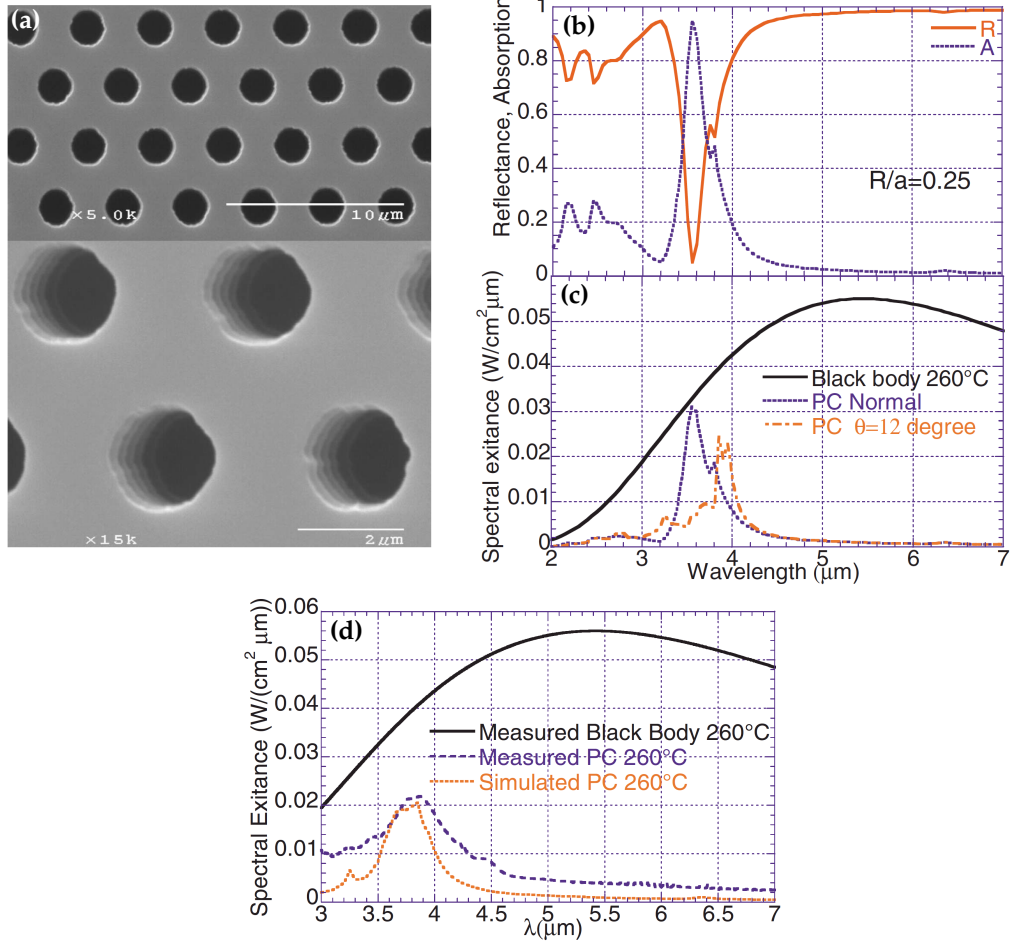


Figure 1.10: (a) SEM images of a 2D triangular lattice of holes fabricated from gold with period $a=3.75 \mu\text{m}$, radius $R=0.95 \mu\text{m}$. (b) Simulated reflection and absorption spectrum for the metallic photonic crystal. (c) Simulated spectral emission at 260°C for the normal direction and 12° from normal, compared to a black body at the same temperature. (d) Measured emission spectrum within a cone (-7.5° - 12°) around normal at 260°C , compared to the measured blackbody emission at the same temperature. Reprinted with permission from [11].

normal increases. The broad resonance is largely due to the material loss, which is why we choose doped silicon, which facilitates the realisation of higher Q resonances.

1.5.3 Conversion of Broadband to Narrowband Thermal Emission Through Energy Recycling

This device [23], and its related structures described in other publications [40–42], highlights the state-of-the-art in thermal emitter designs. It consists of a triangular array of holes etched into a multi quantum well (MQW) layer structure. Intersubband transitions in the MQWs produce a narrowband Lorentzian absorption profile. Unlike the two previous papers, where the gold and doped silicon exhibit broad band absorption properties, the MQW structure produces a narrowband absorption peak. Therefore, by directly heating the MQW structure

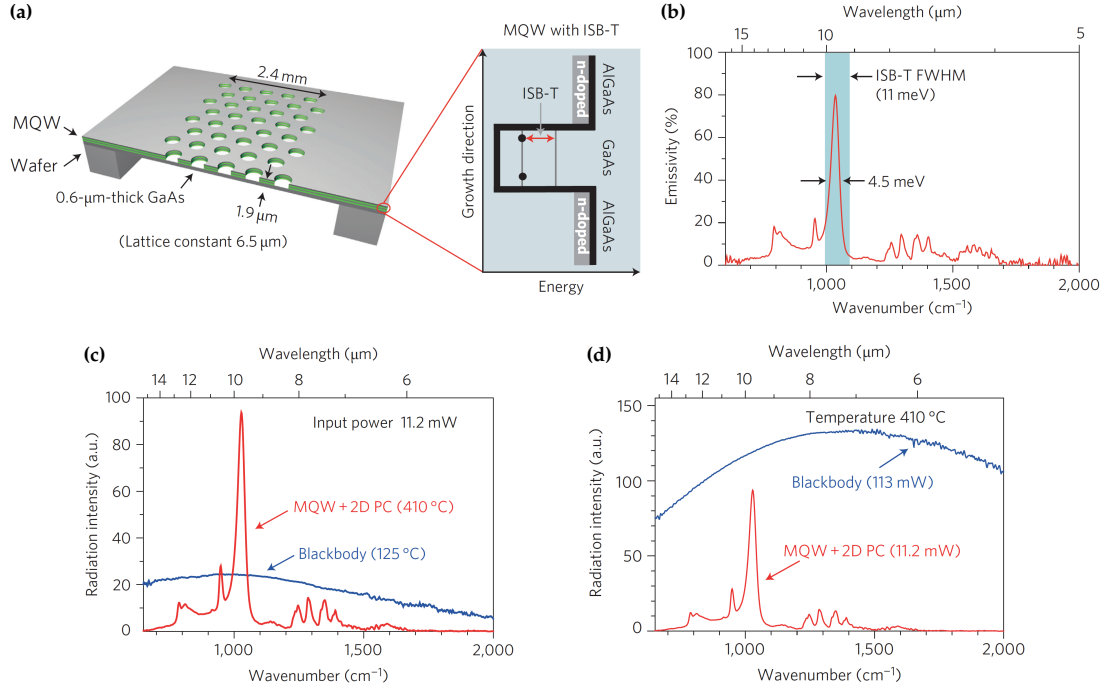


Figure 1.11: (a) Schematic of device, consisting of a MQW layer and a photonic crystal with lattice constant of $6.5 \mu\text{m}$. (b) Emissivity spectrum of the MQW and photonic crystal device at $150 \text{ }^\circ\text{C}$ from the surface-normal direction. (c) Thermal emission spectra of the narrow band thermal source and the reference blackbody in the surface-normal direction for the same input power of 11.2 mW . (d) Thermal emission spectra of the same two samples as in (c) with both now at $410 \text{ }^\circ\text{C}$. Reprinted with permission from [23].

(without the photonic crystal) narrow band thermal emission is “automatically” achieved without the need for a photonic resonance. However, the light is emitted at the edge of the structure. The addition of the triangular lattice of holes etched directly into the MQW layers is then required to couple the narrowband thermal light vertically out of the device. The photonic crystal also plays a role in further narrowing the emission peak and increasing its emissivity.

A diagram of the device is shown in Fig. 1.11a. The MQW structure consists of 63 periods of 6.8 nm GaAs QW and 13 nm $\text{Al}_{0.3}\text{Ga}_{0.7}\text{As}$ as barriers with a total thickness of $1.25 \mu\text{m}$, all on a GaAs substrate. The intersubband transition wavelength for this structure is $9.7 \mu\text{m}$. The introduced lattice of holes has a period of $6.5 \mu\text{m}$ and was designed so that the frequency of one of its band edge modes at the Γ -point (vertical (normal) emission) would overlap with the peak of the absorption profile. Figure 1.11b shows the emissivity curve for the photonic crystal-MQW structure for surface-normal emission at $150 \text{ }^\circ\text{C}$, with an emissivity value of $\approx 80\%$. Such high emissivity in the vertical direction was achieved because the structure itself is asymmetric in the vertical direction due to the GaAs substrate layer, and this directed the emission to the top surface. I will present an asymmetric device in Chapter 3, with the same goal of increasing the emission from the top surface of a photonic crystal slab.

However, the key message from this letter [23] is not the use of MQWs as a narrowband thermal emission material but its investigation into the phenomenon of energy-recycling. The device is redesigned so that it can be resistively heated

by passing a current through it, which allows for greater control and accuracy of the input power. A similar device, of the same size, as a reference blackbody sample was prepared (GaAs wafer coated with black paint). Both devices were electrically pumped with 11.2 mW of power with the measured emission spectrum for each presented in Fig. 1.11c. The peak emission intensity for the MQW narrowband thermal emitter is more than four times stronger than the reference blackbody sample. Furthermore, the narrowband thermal emitter reached a temperature of 410°C while the reference sample only achieved 125°C for the same input power.

To explain this difference, the authors invoke photon-recycling. By producing a narrowband thermal emitter, they limit the radiative channels out of the material. In other words, radiative cooling is suppressed. The energy that would usually be emitted at the wavelengths on either side of the enhanced peak remains within the material, i.e. it has no escape route, and is therefore recycled by being reabsorbed and increasing the temperature of the material.

The concept of energy-recycling was further demonstrated by heating the blackbody reference device to 410°C like the narrowband emitter. It required 113 mW of power i.e. more than 10 times the electrical power needed for the narrowband device, see Fig. 1.11d. In the introduction to this thesis I explained the need for lower power and better efficient thermal light sources. This paper provides a very good demonstration of the possible efficiency improvements that can be achieved with narrowband thermal emitters. The photon-recycling concept is not just accountable for MQW structures, but can be applied generally across all thermal emission devices.

The drawback of the device is its limited operating wavelength and its relatively low operating temperature i.e. these materials are not stable at temperatures >600 °C. That said, a narrowband emitter with the same MQW structure but with a different photonic crystal pattern, operating at the same wavelength, was successfully used as a narrowband light source in a filter free NDIR gas measuring system [42], again another demonstration of the effectiveness of this structure.

Chapter 2

Fabrication and Measurement Techniques

2.1 Introduction

This chapter gives an overview of the nano fabrication tools and techniques used to realise the thermal emission devices presented in this thesis. The fundamentals of each technique are presented along with information about the equipment itself. Details about the various fabrication recipes and the recipe development are included.

The research work was carried out at two different universities. The early part of the work was done at the University of St Andrews. There, I focused mainly on the fabrication of metallic thermal emitters with particular attention to the etching of gold and platinum structures. The remaining, and larger portion, of the fabrication work was completed at the University of York after new cleanroom facilities were constructed. There, I mainly focused on the fabrication of dielectric (doped silicon) based thermal emission devices.

Since the equipment varied between the two facilities, the fabrication recipes had to be changed and adapted. The tools for etching and metal deposition were similar, although the new tools still required setting up and full calibration. The main difference, however, was the electron beam lithography tool. With the group's relocation to the University of York, a state-of-the-art electron beam lithography system was purchased. This system has a higher acceleration voltage (50 kV instead of 30 kV) and larger beam currents compared to the St Andrews system. Hence, new lithography recipes were developed to take full advantage of the machine's capabilities.

This chapter also describes the design and construction of a completely new optical measurement setup to facilitate the characterisation of the fabricated devices. The setup illuminates and accurately measures the reflection spectrum of the resonant structures. The same setup is also used to measure the thermal emission spectrum radiating from the heated structures.

My personal contribution to the fabrication development is split over both facilities. At St Andrews, I developed the reactive ion etching recipes for platinum and gold. I designed the fabrication procedure to expose and etch the 2D gold dipole array. At York, the majority of the equipment was new, therefore, a lot of recipe development work was required. For the new electron beam lithog-

raphy system, completely new recipes were designed from scratch for each resist, the work was carried out by all members of the group. My contribution was to the development of the photonic crystal pattern (2D array of holes) written in ARP resist. I designed the metal lift-off process to achieve thick ($600\ \mu\text{m}$) aluminium contact pads using three layers of PMMA electron beam resist. Finally, I developed the recipe to write the SU-8 polymer waveguides using a graded line-dose exposure technique. Lastly, I fully designed and constructed the optical measurement setup to characterise the fabricated devices.

2.2 Lithography

Lithography is the technique of defining or transferring a given pattern into a material, it originates from the Greek “lithos” meaning stone and “graphein” meaning to write. Here, the main lithography technique is electron beam lithography with some photolithography also being used for larger, less critical, work. The principle of operation of both techniques is quite similar and is summarised in Fig. 2.1. In both cases a resist, which is either sensitive to electrons (e-beam resist) or electromagnetic radiation (photo-resist), and in some cases both, is coated onto the substrate of the sample (Fig. 2.1a). Under exposure, the resist is chemically changed (Fig. 2.1b). Depending on the type of resist, the exposed (non-exposed) areas can be dissolved in a suitable solvent for a positive (negative) resist (Fig. 2.1c). This process is called development and is analogous to the development of photographic films. The pattern defined in the resist layer can then be transferred to the substrate material via either a wet or dry etching procedure (Fig. 2.1d). Of course the resist may not always be used as an etch mask. For example, polymer waveguides, may directly be defined in the resist by the writing process, in which case after development no further steps are required.

2.2.1 Electron Beam Lithography

The essential fabrication technique used through out all of my research work is electron beam lithography (EBL). EBL was used to define all the photonic crystal patterns, both 1D gratings and 2D arrays of holes, on top of metallic and dielectric substrates. EBL is a fundamental technique of nano fabrication and capable of high resolution lithography, with feature sizes down to 10s of nm. Basically, the system consists of a focused beam of electrons which are used to define a custom pattern into an electron-sensitive polymer film, known as e-beam resist. The beam of electrons is controlled and guided across the resist using electromagnetic lenses and electrostatic deflection plates. By exposing the e-beam resist, its solubility changes and allows selective removal of either the exposed area (positive e-beam resist) or the non-exposed area (negative e-beam resist) in a suitable solvent.

The primary advantage of EBL, along with the high accuracy and high resolution, is its versatility. The exposed pattern can be readily changed or adjusted; this is in contrast to photolithography which requires a different physical mask each time a different pattern or a change in the parameters is required. This versatility makes EBL an ideal fabrication technique for research and development

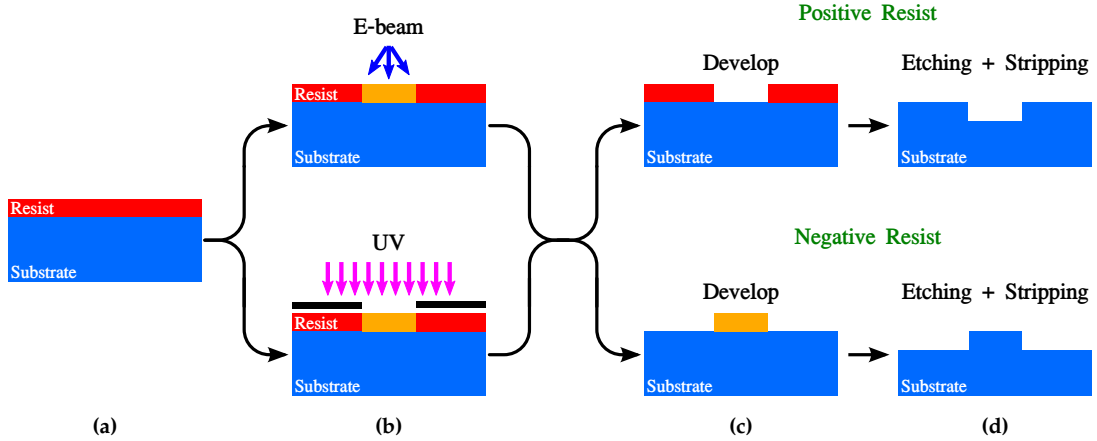


Figure 2.1: Generic lithography process flow. (a) The e-beam resist (or photo-resist) is spin-coated onto the substrate. (b) The exposure of the desired pattern is carried out using EBL or photolithography with a hard mask. (c) Development; for positive resist the exposed area is removed where for a negative resist the exposed area remains. (d) The pattern is then transferred to the substrate layer using either a wet or dry etching technique.

work, as many different designs, with many different structure patterns (e.g. hole radius), can be easily written and optimised with low overhead.

The exposure of the e-beam patterns was carried out using two EBL systems. Initially, the EBL tool at the University of St Andrews (LEO Gemini 1530 SEM/Raith Elphy Plus), which has an acceleration voltage of 30 kV, was used in the development of metallic thermal emitters. The new system (Raith, Voyager) at the University of York has an acceleration voltage of 50 kV and a maximum write field size of $500 \times 500 \mu\text{m}$, larger than the St Andrews system of $200 \times 200 \mu\text{m}$. Along with larger beam currents and faster writing speeds, the new Voyager system is superior to the old machine.

The write field defines the largest area that the e-beam can write by deflecting the electron beam only. To write a larger pattern, the computer divides the area up into multiple write fields. After writing the first, the stage itself is moved and repositioned to allow the beam to write the next write field pattern. This stage repositioning leads to errors in the written pattern at the write field boundaries, known as stitching errors. In this work, the majority of the devices are based on 1D and 2D arrays and operate out-of-plane, i.e. vertical emission. Therefore, stitching errors do not have as severe an impact as they have for in-plane applications such as waveguides. For the in-plane applications like waveguides, stitching errors can lead to large scattering losses of confined light. For the out-of-plane emitters, a stitch error is relatively a very small area of the total device, something like 10-40 nm over an area in the order of a few $100 \times 100 \mu\text{m}$ and so they do not impact the overall performance. Comparing the two systems, the Gemini-Elphy hybrid EBL machine has more stitch errors due to the increased number of write fields because of their smaller size, and each of its individual stitch errors is larger than the new Voyager EBL. The new system has increased accuracy and alignment with significantly reduced stitching errors.

As the electrons propagate through the resist and substrate, they experience scattering where the electrons exchange energy with the molecules in the resist

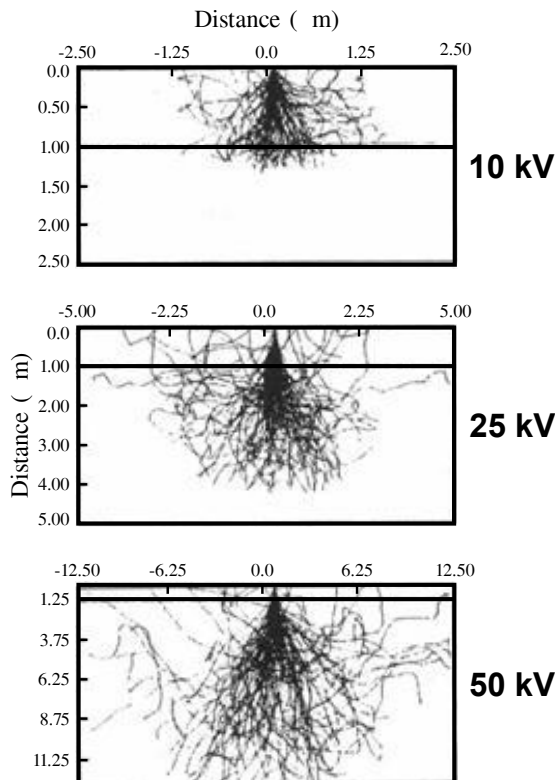


Figure 2.2: Monte Carlo simulation of electron trajectories propagating through a $1\ \mu\text{m}$ thick resist layer on a silicon substrate for three different acceleration voltages; (a) 10 kV, (b) 25 kV and (c) 50 kV.

and expose it. As they penetrate through the resist, they experience a large number of small angle scattering events called forward scattering. The forward scattering broadens the beam and so also the exposed area. The thicker the resist, the more forward scattering and the broader the exposed area will be. Therefore, it is important to keep the resist as thin as possible. The chosen resist thickness is based on what dry etch process is going to be used and how deep the pattern will be etched. It is important that the resist comfortably survives the complete etch process. Regarding the target hole size, we find that the holes turn out to be slightly larger than designed. Therefore, the radius of each written hole is designed 10 nm smaller than the required size.

Figure 2.2 shows Monte Carlo simulations of electron trajectories through a $1\ \mu\text{m}$ thick resist layer on silicon for three different acceleration voltages, 10 kV (Fig. 2.2a), 25 kV (Fig. 2.2b) and 50 kV (Fig. 2.2c). The forward scattering reduces as the acceleration voltage increases. When the electrons penetrate into the substrate, they occasionally undergo larger angle scattering, where the scattering angle is greater than 90° , known as backscattering. An increase in the acceleration voltage increases this backscattering effect (Fig. 2.2c). These backscattered, lower energy, electrons lead to exposure in areas around the initially exposed area and also exposure of areas that are some distance away. This additional exposure is known as the electron beam proximity effect.

This proximity effect leads to areas in the written pattern with an incorrect structure size, which in turn will effect the resonance wavelength at that position. Figure 2.3 shows SEM images of two examples of how this proximity effect man-

ifests itself when writing periodic patterns. Figure 2.3a shows a square array of pillars after development, which were written in a e-beam resist known as ZEP. To note, since ZEP is a positive resist, it is the area around the dipoles and not the dipoles themselves that is exposed. This image shows many features of the proximity effect:

1. The centre region of the pattern has been completely washed away, suggesting substantial over exposure
2. A ring of dipoles have collapsed, again a sign of over exposure, as the pillar is too narrow to support itself and collapses.
3. The remainder of the pattern towards the edge of the array is securely standing although the difference in the diameter from the centre outwards is obvious.

The second image (Fig. 2.3b) shows the corner of a square array of dipoles and illustrates similar behaviour. The reason for this gradient from the centre out to the edge is the proximity effect. The centre region of the resist receives a greater average exposure dose than the areas near the perimeter of the pattern since the structures near the perimeter have fewer neighbours.

To solve this issue one varies the dose across the pattern by taking into account the scattered electrons. Both EBL systems used have a built-in software tool called NanoPECS[®], Proximity Error Correction Software, that calculates the proximity effect for a given pattern and resist, and adjusts the exposure dose across the pattern accordingly.

However, for all the patterns presented in this work, no proximity error correction was carried out. The reason for not implementing this is because all of the crystal patterns for the thermal emitter devices are relatively large, with side lengths in the order of 100s μm . The proximity effect is really only a problem at the edges of these arrays, with a very uniform dose distribution in the centre region of the pattern. All spectral measurements for the characterisation of the fabricated devices, i.e. reflection and emission measurements, were taken from the central, uniform region of the crystal pattern, so the perturbed pattern at the edges can be easily ignored. The proximity error correction is more important for much smaller high Q-factor devices, for example photonic crystal waveguides and cavities where there are only around 20 to 30 rows of holes and where it is important that each hole is correctly reproduced.

2.2.1.1 Electron Beam Resists

Through out the research work I used two high resolution e-beam resists for the exposure of the metallic gratings and photonic crystal patterns. The first is Zeon Chemicals ZEP 520A resist (ZEP) and the second, which replaced ZEP as our high resolution resist, is ALLRESIST AR-P 6200.09 (ARP). They both are positive e-beam resists, i.e. the area that is exposed is removed during development, and have very similar properties, i.e. very high resolution, down to 10s of nm, and very good dry etch selectivity. This makes them ideal for writing small features and both resists are excellent dry-etch masks for transferring the pattern into a metallic or dielectric substrate.

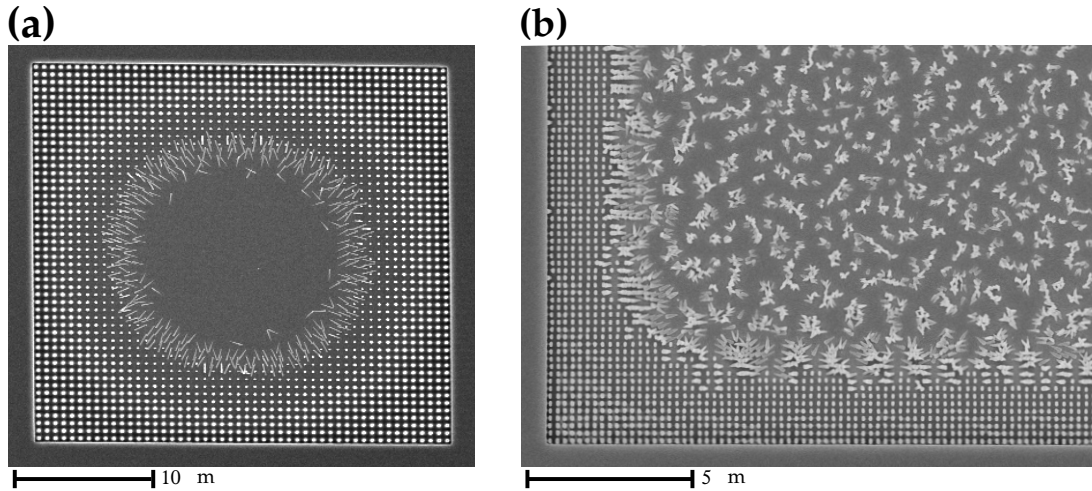


Figure 2.3: SEM images showing how the electron beam proximity effect manifests itself when writing periodic patterns. (a) and (b) show an array of dipole patterns written in the e-beam resist ZEP after development. The images show how the increase in total exposure from the centre out, because of the proximity effect, effects the pattern. It results in an over exposure of the pattern in the centre and a variation in the feature size from the centre out to the edge. It is Important to note that ZEP is a positive e-beam resist so in both images it is the area around the dipole and not the dipoles themselves that is exposed.

ZEP was primarily used to define the patterns for the metallic grating and dipole structures and also used for some silicon photonic crystal devices. ZEP was used to pattern the bottom (platinum) and top (gold) metal layers of the metal-insulator-metal thermal emitter structures in Chapter 4. In order to obtain the small dimensions of the gold dipole structure on top (75×350 nm), the ZEP was diluted with anisole 2:1, to thin down the resist layer and improve the resolution. ARP was the exclusive resist at the University of York and was implemented for the fabrication of all silicon photonic crystal structures. The reason for introducing ARP by the group is that it is 5-10 times cheaper than ZEP.

Another positive e-beam resist that was used in this work is Polymethyl Methacrylate (PMMA), MicroChem Inc.. In fact, two different types of PMMA resist were used, they are 495PMMA and 950PMMA. The difference between these two PMMA e-beam resists is their molecular weight (MW) and sensitivity with 495,000 and 950,000 MW, respectively. 950PMMA is slightly less sensitive, so when used in a bilayer, it forms an overhang over the 450PMMA layer. This overhang makes it very suitable for lift-off, because after metal deposition, this overhang ensures there is a clean break between the top layer of metal on the resist and the bottom layer on the substrate, ensuring a very good quality lift-off.

Two other e-beam resists, both of which are negative, are SU-8 MicroChem Inc. (two types; 2000.5 and 2050) and the other is FOx 15 (Flowable Oxide) which is a hydrogen silsesquioxane (commercially available as FOx15 from Dow Corning), with properties very similar to silicon dioxide. The SU-8 resists are used to fabricate thick polymer waveguides, see Section 2.5 for full details of the fabrication process. The FOx resist is used as the spacer (insulator) layer of the metal-insulator-metal thermal emitter structure. To achieve the necessary thick-

Table 2.1: Summary of all the resist and the fabrication recipes used.

Type	Resist	Notes	Spin Coating				Exposure				Development			Stripping		
			Speed (rpm)	Thickness (nm)	Temp. (°C)	Bake Time (min)	Line (pC/cm)	Dose Area ($\mu\text{C}/\text{cm}^2$)	Temp. (°C)	Time (min)	Solution	Time (s)	Rinse		Solvent	
E-beam	ZEP	-	3700	400	140	20	-	55	-	-	-	-	Xylene	45	IPA	1165
	ZEP	Anisole (1:1)	5000	180	180	20	-	55	-	-	-	-	Xylene	45	IPA	1165
	ARP	09	1500	350	180	10	-	150	-	-	-	-	XAR	90	H ₂ O	1165
	ARP	13	5000	350	180	2	-	150	-	-	-	-	XAR	90	H ₂ O	1165
	PMMA	495	2000	400	180	2	-	400	-	-	-	-	IPA:H ₂ O (7:3)	120	H ₂ O	Acc.
	PMMA	950	5000	100	180	5	-	400	-	-	-	-	IPA:H ₂ O (7:3)	120	H ₂ O	Acc.
	SU-8	2000.5: 2050 (1:1)	5000	2000	1) 65 2) 95	3 3	6	-	-	1) 65 2) 95	3 3	-	EC	120	IPA	-
	FOx	MIBK (1:2)	5000	180	5	-	-	300	-	-	-	-	TMAH	60	H ₂ O	HF
Photo	S1818	-	4000	3	100	2	-	150 mJ/cm ²	-	-	-	MF319	45	H ₂ O	Acc.	

ness (around 60 nm), the resist is diluted with methyl isobutyl ketone (MIBK) at a ratio of 1:2. Table 2.1 summarises the fabrication recipes for each of the resists.

Each resist requires a certain number of electrons per unit area to get exposed; this is known as the exposure dose. The exposure dose refers to the dose required to expose a layer of resist completely, hence is often referred to as the clearing dose. With the correct clearing dose, after development, the exposed resist will be completely removed from the substrate. It is important to have the dose high enough to ensure smooth and vertical side walls in the resist. The exact clearing dose is dependent on a number of factors; the resist, the thickness of the resist layer and the size of the pattern being exposed i.e. small diameter holes will require a different area dose than larger exposed areas. The determination of the correct clearing dose is achieved empirically by writing the required pattern over a range of doses and examining the fabrication results. This test was carried out for each of the e-beam resists with each associated pattern.

2.2.2 Photolithography

Unlike e-beam lithography, photolithography uses resists that are sensitive to electromagnetic radiation (ultraviolet (UV) light) rather than electrons. The pattern is exposed through a photo-mask, on which the required pattern is printed. The exposure is based on a photochemical reaction of the resist to the UV light where, for a positive resist, the exposed areas become soluble and for a negative resist the exposed areas are insoluble due to photo-induced cross-linking of the polymer chains. The entire pattern is exposed at the same time, which is why this system is much quicker than the e-beam where each pixel is individually exposed as the e-beam raster scans across the write field. Of course, it does not have the same level of accuracy or resolution as the e-beam system and so is used in situations where these two quantities are not critical.

For the work presented in this thesis the main application of UV photolithography was to fabricate hydrofluoric acid (HF) access windows for the undercutting of photonic crystal arrays. Using the photosensitive positive resist S1818 (Shipley), windows were opened over the fabricated photonic crystals. These windows allowed the oxide layer beneath the crystal to be wet etched while protecting the rest of the sample and the metal contact pads. The exposure was performed using a mask aligner system from Karl Süss (MJB-3) utilizing a UV-LED. The alignment tolerance of such a system is a few micrometers, which was more than enough to position the HF window mask above the photonic crystal arrays. Using the UV photolithography system to expose these HF windows avoids the need for the EBL system which saves on exposure time.

2.3 Reactive Ion Etching

After the exposure and development, the resist pattern is transferred to the substrate beneath (here: platinum, gold and intrinsic and doped silicon) using reactive ion etching (RIE) (Fig. 2.1d). The RIE system is, basically, a parallel plate capacitor in a vacuum chamber. The top plate of the capacitor contains a ring of small holes where the reactive gases are fed into the chamber. The sample

Table 2.2: RIE recipes for different substrates.

Material	Gas Mixture	Gas Ratio	Pressure (mBar)	RF Power (W)	DC Bias (V)	Etch Rate (nm/min)
Gold	Ar	-	5×10^{-2}	20	330	6
Platinum	Ar, SF ₆	3:1	5×10^{-2}	20	300	20
Silicon	CHF ₃ , SF ₆	1:1	4.2×10^{-2}	22	186	115

to be etched is placed on the bottom plate electrode, sample stage. When a strong radio frequency (RF) electromagnetic field is applied, the gas between the two plates of the capacitor is stripped of its electrons and ionised, forming a plasma. The table is the driven electrode, the chamber is ground. This DC component accelerates the positively charged ions down to the stage electrode, bombarding into the sample and etching it.

The RIE etching process is not just a mechanical sputtering process, there is a chemical etch component also. The accelerated ions provide the physical component which is very anisotropic i.e. etches vertically downwards. The gases used in the plasma are very reactive and add a chemical, isotropic, etch component to the process. The two etch processes are not independent, but strongly interlinked and depend on many parameters like; gas composition, etch pressure and RF power. For example, a change in the applied power changes the DC bias which in turn will change the plasma formation and effects the chemical component of the etch process. The balance between the two components is crucial to achieve smooth vertical side walls. Too much chemical etching results in a loss of directionality with under-cut and angled side walls. A strong physical component and the material is heavily sputtered and not removed, leading to angled side walls and re-deposition of the etched material.

The choice and mixture of the etching gases depends on the substrate to be etched. For silicon (intrinsic and doped), CHF₃ and SF₆ are used. The fluorine ions do the etching, while the H⁺ ions contributes to polymer passivation and protects it from further etching, which ensures smooth vertical side walls. For etching of gold, Ar gas is used, which is purely a mechanical sputtering process with no chemical component. The etching of platinum proved to be a lot more challenging than the etching of gold. The platinum is much harder and does not mechanically mill as easily. To etch the platinum a chemical component was included by adding SF₆ to the Ar gas mixture. The fluorine ions form platinum-fluoride components are very volatile and decompose from the surface, greatly increasing the etch rate. Table 2.2 summaries all the optimised etch recipes. Again, as with the EBL, the etching work was divided between two etching machines, all of the metal etching, gold and platinum, was carried out at the University of St Andrews, while all the silicon etching was done at the University of York.

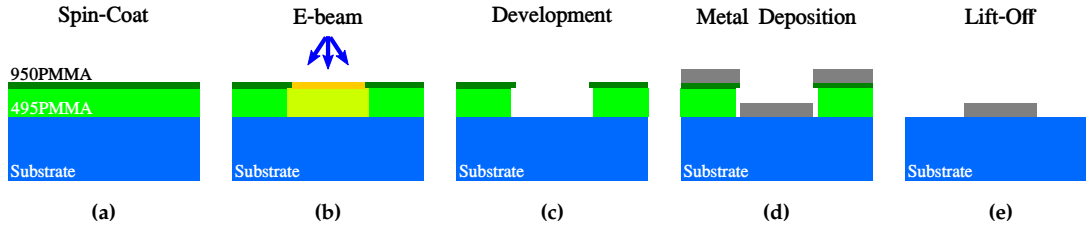


Figure 2.4: Illustration of the lift-off process. (a) A layer of 950PMMA (1:1 with xylene) is spin coated onto a layer of 450PMMA. (b) The required pattern is exposed by the EBL tool. (c) After development there is an undercut of the bottom resist layer. (d) Metal deposition, either gold or aluminium. (e) Finally, after the lift-off in acetone, a layer of metal remains on the substrate.

2.4 Lift-off and Metal Evaporation

The lift-off process is an alternative to etching and allows the patterning of materials that may otherwise be difficult to etch e.g. metals. In this work, the lift-off process is used for the patterning of large areas ($400 \times 400 \mu\text{m}$) of two different metals. The first is the patterning of a thin layer of gold ($\approx 40 \text{ nm}$) on top of FOx, for the top layer of the metal-insulator-metal thermal emitter. The second, and primary, function is the patterning of electrical contacts for the silicon-based thermal emitter devices using aluminium. Commonly, for such large area structures, photolithography is used to define the patterns. However, as high alignment accuracy was required, the EBL tool was also used to define these.

In the lift-off process (illustrated in Fig. 2.4), the sacrificial material is a bilayer of e-beam resist, 495PMMA and 950PMMA. As already mentioned in Section 2.2.1, the 950PMMA, diluted with xylene ratio 1:1, is spin coated on top of the 495PMMA layer (Fig. 2.4a). As a general rule of thumb, the thickness of the bottom (495PMMA) layer needs to be 2-3 times thicker than the required metal thickness to achieve a good quality lift-off. For the patterning of the gold (40 nm) a single layer of 495PMMA layer was sufficient, however for the thicker aluminium contacts (600 nm) two layers were spin-coated to increase the thickness.

Figure 2.4c shows the resist layers after exposure (Fig. 2.4b) and development. Due to the difference in MW between the two resists, the bottom layer is more sensitive and a larger area is exposed, which produces an overhang of the top resist layer. The overhang ensures a clean break between the bottom layer of metal and the top layer on the resist after the metal deposition. The lift-off is carried out in acetone and after 10 to 15 minutes, a clean layer of metal is achieved.

The deposition of the metals was carried out using two different types of evaporators. The gold and aluminium was deposited by a resistive thermal evaporation tool and the platinum (and some gold) by an electron beam evaporator. The resistive thermal evaporator is one of the most common and simple metal deposition tools. The heating is achieved by passing a large current through a tungsten (or similar material) boat or coil, in which the material to be evaporated is placed, this is known as in-direct thermal evaporation. When a sufficiently high temperature is reached, the material in the boat vaporises and re-condenses on

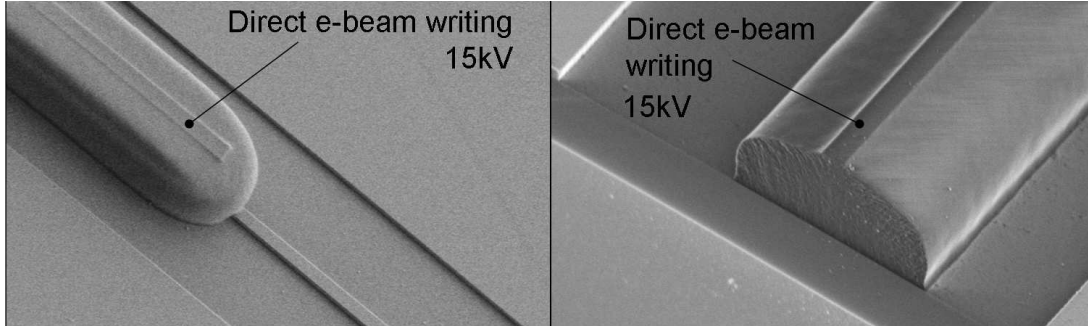


Figure 2.5: Two SEM images of SU-8 waveguides fabricated on SOI at the University of St Andrews using a 15 kV EBL system. Note the size of the directly written area ($1 \mu\text{m}$) compared to the final width ($6 \mu\text{m}$) of the polymer waveguide [44].

the cooler sample suspended overhead. This type of system works very well for metals with relatively low melting points such as gold ($1064 \text{ }^\circ\text{C}$) and aluminium ($660.3 \text{ }^\circ\text{C}$). However the evaporation of platinum ($1768 \text{ }^\circ\text{C}$) is more difficult due to its much higher melting point.

The electron beam evaporation tool is capable of reaching much higher temperatures compared to the resistively heated thermal evaporator. The difference is in the heating method; the e-beam tool focuses a beam of electrons into a crucible and on to the material to be evaporated directly heating it. This high density of electrons is directly absorbed by the material and is capable of driving high temperatures. A Mantis (Model) resistive thermal evaporator was used for the deposition of gold and aluminium (University of York). An Edwards Auto 306 FL 400 electron beam evaporator was used for the evaporation of gold and platinum (University of St Andrews). A quartz crystal monitor measured the thickness of the deposited layer in both machines.

2.5 SU-8 Polymer Waveguides

The work in this section is not related to this project but is my contribution to another project. The goal was, using the new EBL system, to develop a recipe to fabricate polymer waveguides to improve the coupling between on-chip devices and butt coupled single mode fibres and is based on work already published by the group [43].

For many photonic devices, and in particular silicon photonics, to successfully operate, the efficient coupling of light on-and-off the chip and to-and-from the optical device is crucial. The device or structure itself may have a very small footprint and so waveguides are used to transport light from an external source, e.g. via butt coupled single mode optical fibre, to the device. For standard silicon photonic devices operating at $1.5 \mu\text{m}$ in silicon-on-insulator wafers, the thickness of the device layer is typically 220 nm . Due to the difference in size between the single mode fibre core, typically $9 \mu\text{m}$ diameter, and this silicon layer, there is a large mode-size mismatch which will affect the coupling efficiency.

To optimise the coupling of light to the fabricated devices, inverse taper spot size converters have been used [45–48]. These consist of large polymer waveguides ($6 \times 2 \mu\text{m}$) fabricated on the chip, which couple to the optical fibre and

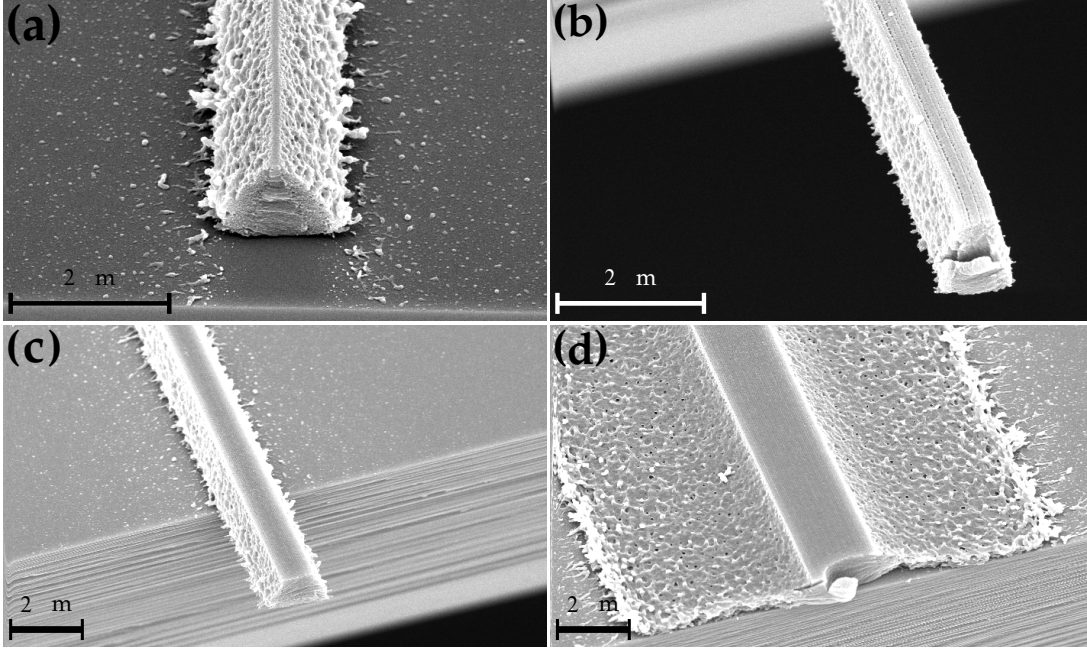


Figure 2.6: Four SEM images of the initial attempt at writing SU-8 waveguides at the University of York using the 50 kV EBL tool. The number of single pixel lines directly written across the waveguide is increased in each; (a) 3 lines, (b) 10 lines, (c) 20 lines and (d) 40 lines, each spaced at 50 nm.

transport the light along the chip to the device. At the device, the guided modes of the large polymer waveguide are slowly coupled into a, initially very narrow, tapered silicon waveguide and then into the device itself. As the high index silicon taper adiabatically widens, the light is progressively transferred into the silicon waveguide. This efficient method of coupling was previously developed in our group using the polymer resist SU-8 to define the large waveguides [44]. The low refractive index of SU-8 and the large cross section ensured high coupling efficiencies. Large polymer waveguides have also been fabricated directly over photonic crystal cavities and waveguides [49]. By tuning the height of the waveguide above the chip, a much improved coupling efficiency is achieved by verticality coupling to the cavity or waveguide structure.

The fabrication of the SU-8 polymer waveguides was optimised in the research group at the University of St Andrews [44]. SU-8 is the go-to material for the fabrication of these polymer waveguide structures because it is a negative resist and the waveguide structures can be directly written. It is possible to write very smooth, square-profile waveguides in SU-8 when the resist is exposed using an e-beam with high acceleration voltages (100 kV) [50].

At St Andrews the maximum acceleration voltage was much lower, 30 kV, which led to large amount of forward scattering in the resist and some back scattering from the silicon dioxide layer as the electrons didn't penetrate very far into the substrate. This relatively low acceleration voltage coupled with the high sensitivity of the resist, resulted in a very broad exposure, with large areas of excess exposed SU-8 at either side of the written area. To solve the problem, the acceleration voltage was reduce down to 15 kV and the written area was reduced to 1 μm wide which resulted in a 6 μm wide waveguide after the increased forward and backward scattering exposure. The 1 μm wide pattern

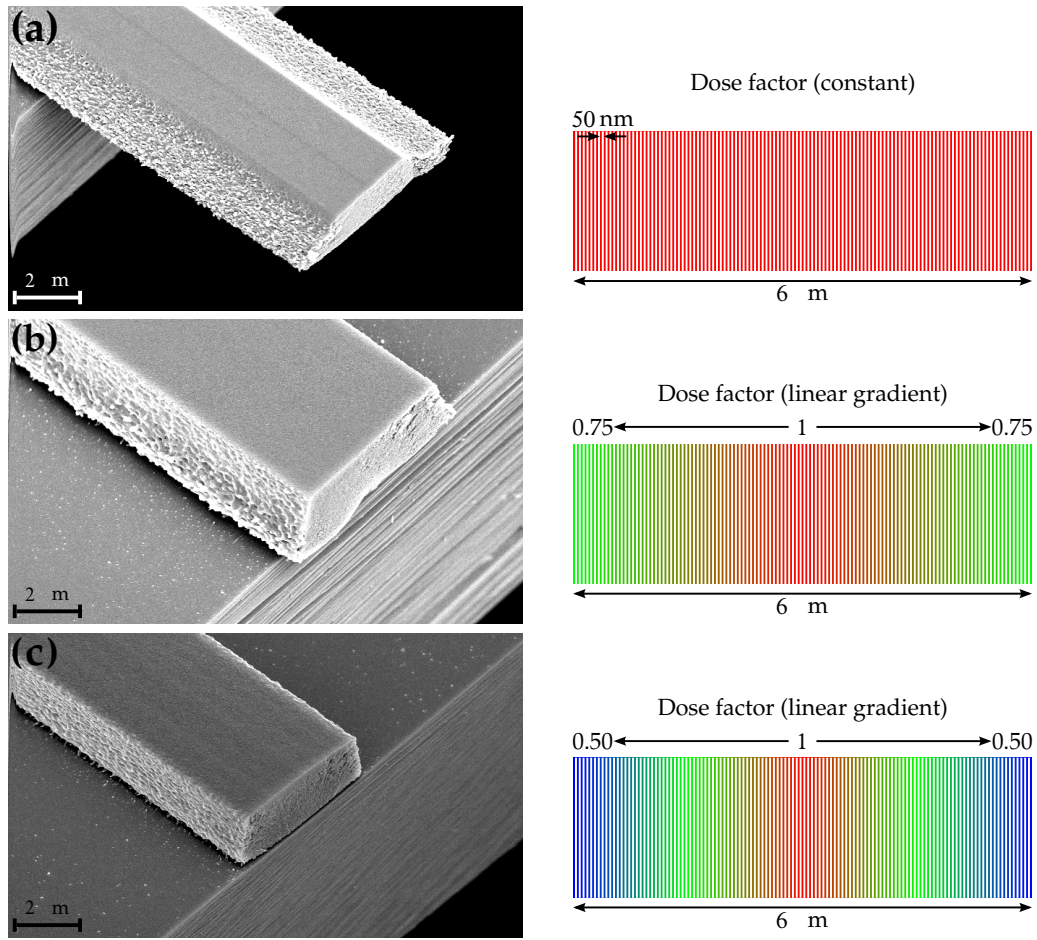


Figure 2.7: SEM images showing the fabricated SU-8 waveguides with the full $6 \mu\text{m}$ width of the waveguide written using single pixel lines. (a) Keeping the line dose the same across the waveguide, there is some over exposure at each side of the directly written region. (b) Introducing a dose factor gradient, 1 to 0.75, from the centre of the waveguide to the edges, greatly reduces the over exposure but there still remains a little bit. To remove the over exposed area completely, the dose factor range was reduced further to 0.5 at the edge (c), producing a waveguide with smooth vertical side walls. The line dose factor range across the waveguide is indicated at the side of each of the SEM images.

was not exposed as a complete area but was broken up into single pixel lines spaced 50 nm apart, which allowed very accurate control of the total exposure dose. The two SEM images in Fig. 2.5 show an example of a SU-8 waveguide written using this method [44]. The directly written area is clearly visible on top of the waveguide and the rounded cross-section is the resulted exposure form the scattered electrons.

To realise SU-8 polymer waveguides with the new 50 kV EBL system at the University of York the recipe required some changes. It was not possible to reduce the acceleration voltage of the new system, however, this high voltage should be more advantageous as it reduces the forward scattering and it increases the penetration depth of the electrons into the substrate. One would expect it should be easier to directly write the complete width of the waveguide with minimal excess exposure, this, however, was not the case.

A 1:1 ratio, by weight, of SU-8 2000.5 and SU-8 2050 was used, spun at 5000 rpm, it gives a resist thickness of approximately $2\ \mu\text{m}$. To begin, I used a similar exposure recipe, writing 50 nm spaced single pixel lines Fig. 2.6 shows SEM images of four SU-8 waveguides, each written with a different number of single pixel lines; 3 (Fig. 2.6a), 10 (Fig. 2.6b), 20 (Fig. 2.6c) and 40 (Fig. 2.6d). Examining the cross section in the first image (exposure with 3 pixel lines) it is interesting to see that the forward scattering exposure is visually obvious in the image and begins from the directly written area at the top and spreads out. The rougher outer skin must then be exposed by back scattered electrons. The 10 (500 nm wide) and 20 (1 μm wide) pixel line waveguides have a good shape although with some side roughness. Increasing the width by simply increasing the number of single pixel lines does not scale very well. As Fig. 2.6d clearly shows, where the number of single pixel lines is increased to 40 (2 μm wide), then double that in Fig. 2.6c, a much larger area is exposed, with very large areas of over exposure at each side of the waveguide.

To correct for this over exposure, the overall dose was reduced by reducing the single pixel line dose from 60 pC/cm to 6 pC/cm. The full width (6 μm) of the waveguide was written with single pixel lines spaced at 50 nm intervals. Fig. 2.7a shows an SEM image of the resulting polymer waveguide. The areas at the side of the waveguide are still a little over exposed. To reduce the total exposure dose even further a dose factor gradient was applied from the centre out to each side. Fig. 2.7b and Fig. 2.7c show an SEM image of the waveguide written with a dose factor gradient of 1-0.75 and 1-0.50 respectively, with the line dose profile shown beside each image. The dose factor gradient of 1-0.5 (Fig. 2.7(c)) shows a very nice rectangular profile waveguide with very little side roughness. The step down in dose factor from 0.75 to 0.50 was sufficient to remove the little bit of extra exposure at the edges and get vertical side walls.

2.6 Optical Characterisation

The optical properties of the photonic structures are characterised through reflection and emission measurements in the near-infrared (1 μm to 1.7 μm) wavelength range. The reflection measurements are taken at room temperature and the thermal emission is examined by directly measuring the samples' radiated light at various temperatures. In order to complete this characterisation, a completely new experimental setup was designed and built.

The measurement setup can perform two measurement tasks. Firstly, it can illuminate the sample (with a known light source), collect and couple the reflected light into a multimode fibre, which is connected to a spectrometer, and measure the spectrum. Secondly, the setup can collect the light directly emitted from the sample and, as with the reflected light, couple it to a spectrometer and examine the emission spectrum.

2.6.1 Coupling Light into a Multimode Fibre

The task of collecting thermally emitted light and reflected light from that same surface is essentially the same procedure. The difference is that the reflection behaviour is determined by how the surface is initially illuminated, but the task

of collecting this reflected light is the same as if it was directly emitted from the surface.

To simplify things, we will begin by assuming we have an extended diffuse light source. We want to collect the emitted light and couple it into a multimode fibre as efficiently as possible. By diffuse, I mean that the source emits light in all directions and is of the same intensity in all directions. This may not be case for all photonic crystal emitters, in fact for the devices in this work it clearly is not, as they have angularly dependent emission behaviour yet assuming diffuse emission is a good starting point.

The goal of the optical system is to maximise the amount of radiated power from the source to the detector, where the detector in our case is replaced with the facet of a multimode fibre, which is connected to a spectrometer.

Firstly, we consider a simple optical imaging system containing one lens and examine how an arbitrary optical ray propagates from the object h_1 at s_1 to the image h_2 at s_2 , Fig. 2.8a. The dotted line in the figure shows the ray from the object that has the maximum angle to the optical axis and is still within the aperture of the lens. This is the maximal ray and is very important for the design of an optical system. Assuming a thin lens and the paraxial approximation ($\sin(\theta) \approx \theta$), and after applying some basic geometry, we get

$$\theta_1 = \frac{R}{s_1}, \theta_2 = \frac{R}{s_2} \quad (2.1)$$

where θ_1 and θ_2 are the angles which the ray makes with the optical axis on the object and image side, respectively. R is the radius of the lens and s_1 and s_2 are the image and object distances from the lens. Using the definition of magnification ($h_2/h_1 = s_2/s_1$) and Eq. 2.1 we have

$$h_2\theta_2 = h_1\theta_1 \quad (2.2)$$

where h_1 and h_2 are the object and image height. This relationship is a fundamental law of optics, called the optical invariant, and is true for any ray through the system, not just the maximal as illustrated here. For any optical system of lenses, regardless of the number of lenses, the product of the image size and the ray angle is constant, which is called the *éntendu*. The optical invariant is a special case of the more general geometrical extent, where the product of the area and the solid angle is invariant. However, for systems that are rotationally symmetric (e.g. lenses and optical fibres), the 1D optical invariant is equally accurate.

In addition to the source (detector) and the entrance (exit) lenses, other elements may limit the optical invariant of a system. For example, internal apertures or some other physical restriction will limit the optical invariant. However, it is more often than not limited by the spectrometer or monochromator as these instruments have small entrance pupils and/or small detector areas and limited acceptance angles. Another possible limitation on the optical invariant is the use of fibre optics. The numerical aperture and the size of the fibre core can be the limiting factors and determine the best optical invariant achievable. It is important to understand the part of the system that limits the optical invariant of the system, fixes the maximum possible throughput since no amount of clever optical design can improve on this.

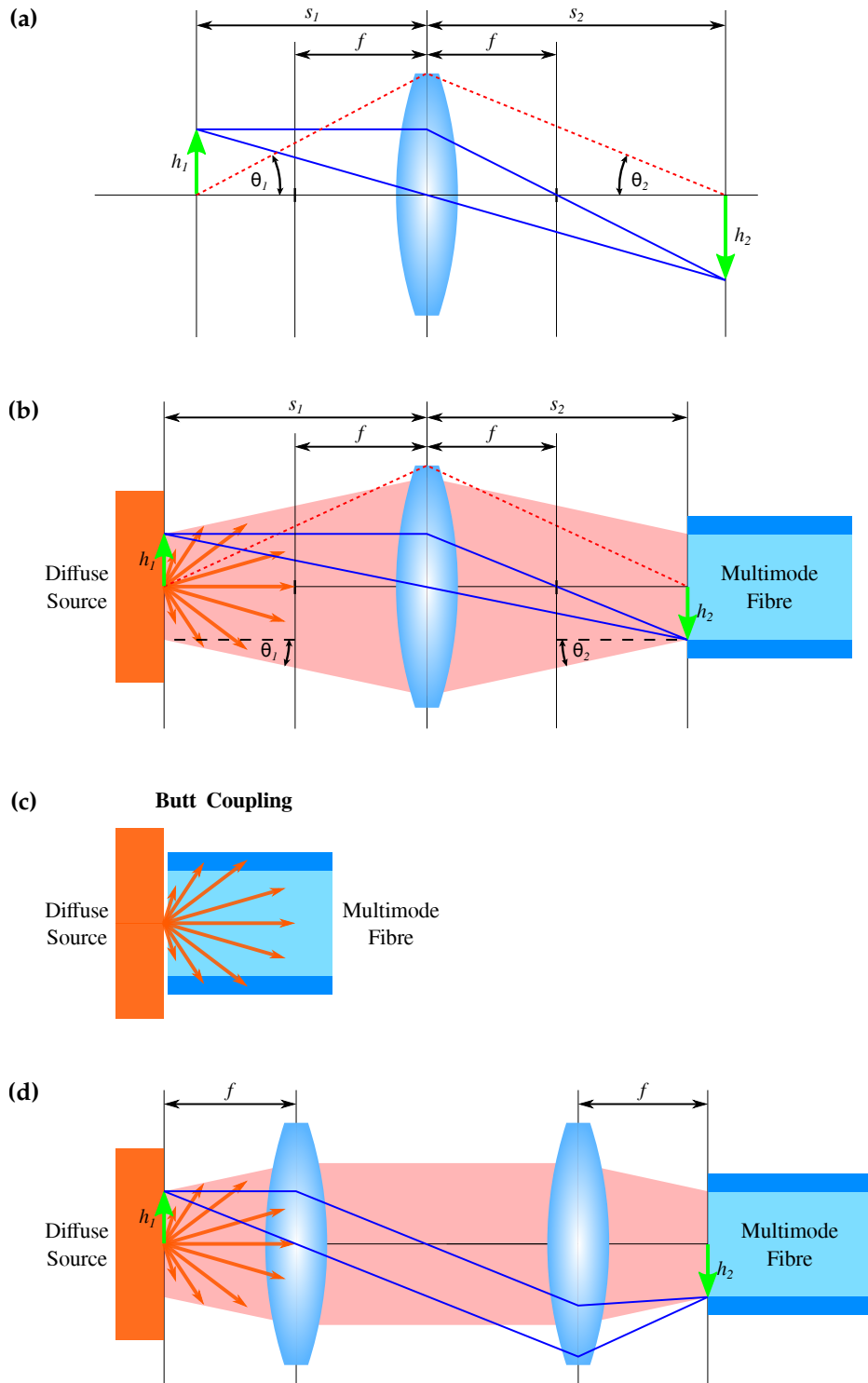


Figure 2.8: Four different optical imaging systems, each with the goal of efficiently coupling light from a diffuse source into a multimode fibre. (a) Simple optical imaging system illustrating the optical invariant by looking at an arbitrary ray propagating through the system. (b) Imaging of a diffuse light source onto the facet of a multimode fibre using a single lens with a 1:1 magnification. (c) Illustrating the butt coupling of a multimode fibre to a diffuse source. (d) Two lens coupling setup. Effectively the same coupling as (c) with the added advantage of the separation distance between the two lenses being more flexible which allows for easy integration of other optical components

Returning to our optical system design, Fig. 2.8b shows a possible system to couple light from a diffuse source into a multimode fibre. We must not forget that we are imaging an area of the source on to the facet of the fibre and in this case with a 1:1 magnification ratio. The source is placed at s_1 ($2f$), and its image is at s_2 ($2f$) at the other side of the lens (indicated with green arrows). The radius of the fibre core facet is h_2 , therefore the light is only collected from an area of radius h_1 at the source, (1:1 magnification). The largest possible angle coupled into the fibre is restricted by its own numerical aperture (NA, $\text{NA} = n\sin(\theta)$, where n is the refractive index (this case $n=1$) of the environment and θ is the maximum acceptable angle). In this case we let $\theta_2 = \text{NA}$, according to the paraxial approximation $\text{NA} \approx \theta$. Therefore, by the optical invariant, the maximum angle sampled from the source is θ_2 ($\theta_1 = \theta_2 = \text{NA}$). Thus, it is the fibre and not the lens that limits the coupling of the light assuming the lens has a sufficiently small $F/\#$ to overfill the acceptance cone of the collecting fibre. Using the paraxial approximation, the $F/\#$ of a lens can be defined as

$$F/\# \approx \frac{f}{D} \quad (2.3)$$

where f is the focal length and D is the diameter of the lens. The smaller the $F/\#$ the greater the radiant flux collected by the lens i.e. the larger the diameter or the smaller the focal length the better. Ideally, for this single lens 1:1 setup, require a $F/\# < 1/(2\text{NA})$.

Note that if we remove the lens and move the fibre directly over the source, effectively butt-coupling the fibre to the source, we will collect light from an area of h_2 , the radius of the fibre core, and collect light with an angle of NA (Fig. 2.8)c. This is what the lens and the 1:1 imaging system achieves, therefore any imaging system of lenses cannot collect more light than can be collected by simply butt coupling the fibre directly to the source.

In fact, this result is entirely general. If we try and use the multiple lenses to collect light from a much larger area and focus it down to the fibre facet, we will not gain anything. For example, by collecting light from a larger area, we will lose in collection angle.

In conclusion, the total light that is collected (area \times solid angle \times radiated power) is the same in each case. Therefore, the maximum efficiency that any lens system can achieve is to match that retrieved through butt coupling. A lens system makes it possible to place the fibre away from the source and get maximum coupling. To truly maximise the light throughput, a fibre with a large core diameter and a large NA is required.

2.6.2 Optical Setup

Next we apply this understanding of light collection and coupling to the design of an appropriate setup. Firstly, the fibre chosen for all measurements has a core diameter (h_2) of $105 \mu\text{m}$ and an NA of 0.22 (Throlabs, M18L01). Therefore, we need a lens with a $F/\#$ less than 2.27 which means we need a lens that has a diameter that is twice the focal length. However, this single lens coupling setup is a little restrictive and makes it difficult to insert other optical components (e.g. beam splitters) into the system. I therefore replaced this single lens coupling system with a two lens design (Fig. 2.8d).

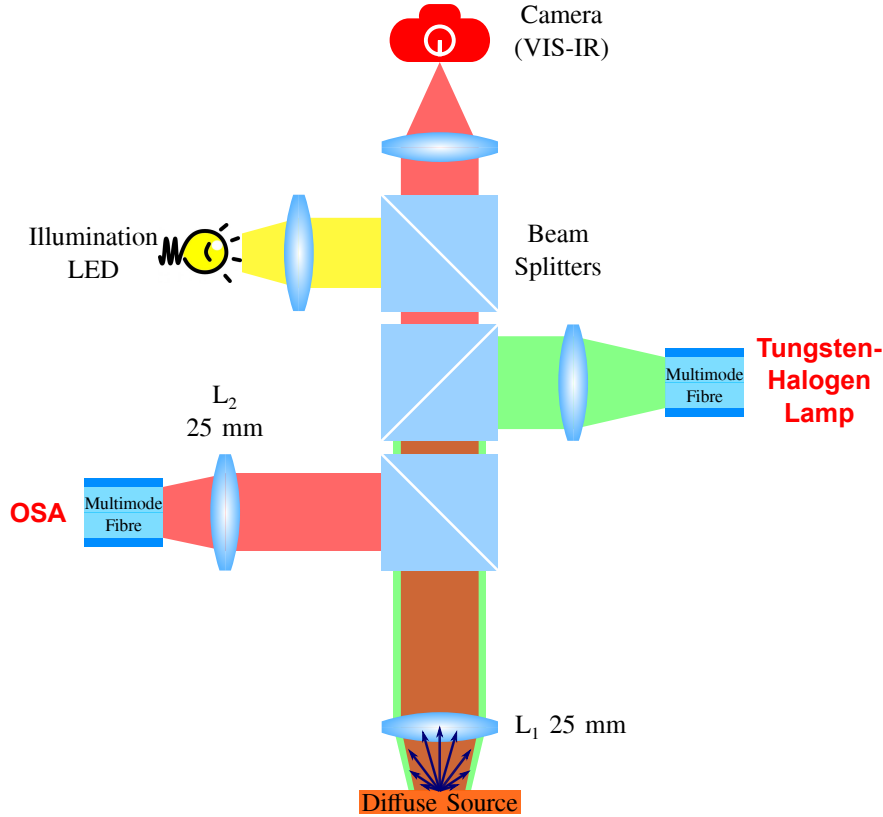


Figure 2.9: Measurement setup-A.

The system has the source and the fibre now at the focal point of each lens. The required $F/\#$ of each lens is half of the single lens system, as the distance between the source and the fibre from their respective lenses is reduced by a factor two. Therefore, we now need two lenses with a $F/\# < 1.135$, i.e roughly a lens with its diameter equal to its focal length. The two lenses are CaF lenses with a focal length of 25.4 mm and a diameter of 25 mm.

Having chosen the fibre and coupling lens, we can build the setup, shown in Fig. 2.9. As previously mentioned, this setup has two functions; it can characterise the fabricated structures through reflection measurements and can directly measure the thermal emission from the device. A tungsten lamp (Thorlabs SLS201/M) is fibre-coupled to the setup and is used to illuminate the structure, the illumination path is highlighted in green. The light from the source is collimated, it propagates through the beam splitters, and using the collection lens (L_1 ($f=25$ mm)) is focused down to the sample. The reflected light (highlighted in red) is then collected, collimated and imaged onto the facet of the collecting fibre using the second lens (L_2 ($f=25$ mm)) which is connected to the optical spectrum analyser (OSA) (Yokogawa). The illuminating fibre source has a much larger core ($600 \mu\text{m}$) and so a large area of the surface is illuminated, which ensures that the reflected light overfills the aperture of the collecting fibre and maximises the signal. The same setup can be used for the collection of thermal emission. In that case, there is no illumination and the light follows the highlighted red path directly to the fibre facet, with light emission collected from an area of $105 \mu\text{m}$ and an angle of 12.7° ($\text{NA} = 0.22$) around normal. This measurement setup is referred to as setup-A.

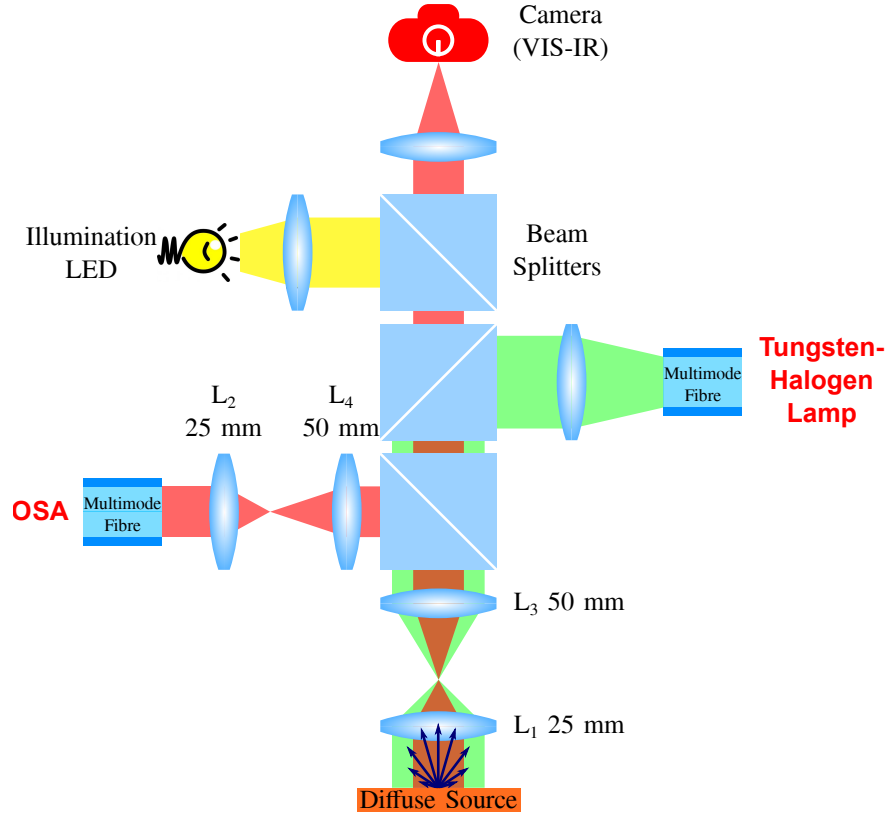


Figure 2.10: Measurement setup-B.

All of the devices presented in this thesis are designed using various simulation software tools. A common component between them is that the illumination of the photonic structure is via a plane wave light source. In the above setup, however, the structure is illuminated with curved wave fronts as the lens focuses the light on to the sample, which contains various plane wave components at different angles. This type of illumination makes it difficult to accurately compare real reflection measurements with simulation results.

Therefore, the setup was adjusted to obtain normal incidence plane wave illumination by including two extra CaF lens L_3 and L_4 , each with a focal length of 50 mm, see Fig. 2.10. The addition of L_3 to the incoming light pathway results in the sample being illuminated with horizontal plane waves of light. The distance between the lenses L_1 (L_2) and L_3 (L_4) is crucial for this to work and needs to be the sum of the two focal lengths, i.e. 75 mm. The collected reflected light follows the same pathway with the normal reflected light off the sample imaged on top the facet of the fibre. This measurement setup is referred to as setup-B.

Figure 2.11 shows a photograph of the constructed optical setup in the setup-B configuration. Each of the optical components are labelled. The inset shows a close up image of the sample with two electrical needle probes. The chip has a large range of devices with different lengths of photonic crystal structures. The green and purple colours are caused by light scattering off the photonic crystal pattern. The device between the two electrical needle probes is heated and emitting visible thermal radiation. Missing from the image of the setup is the tungsten light source (Thorlabs SLS201/M) and the OSA (optical spectrum

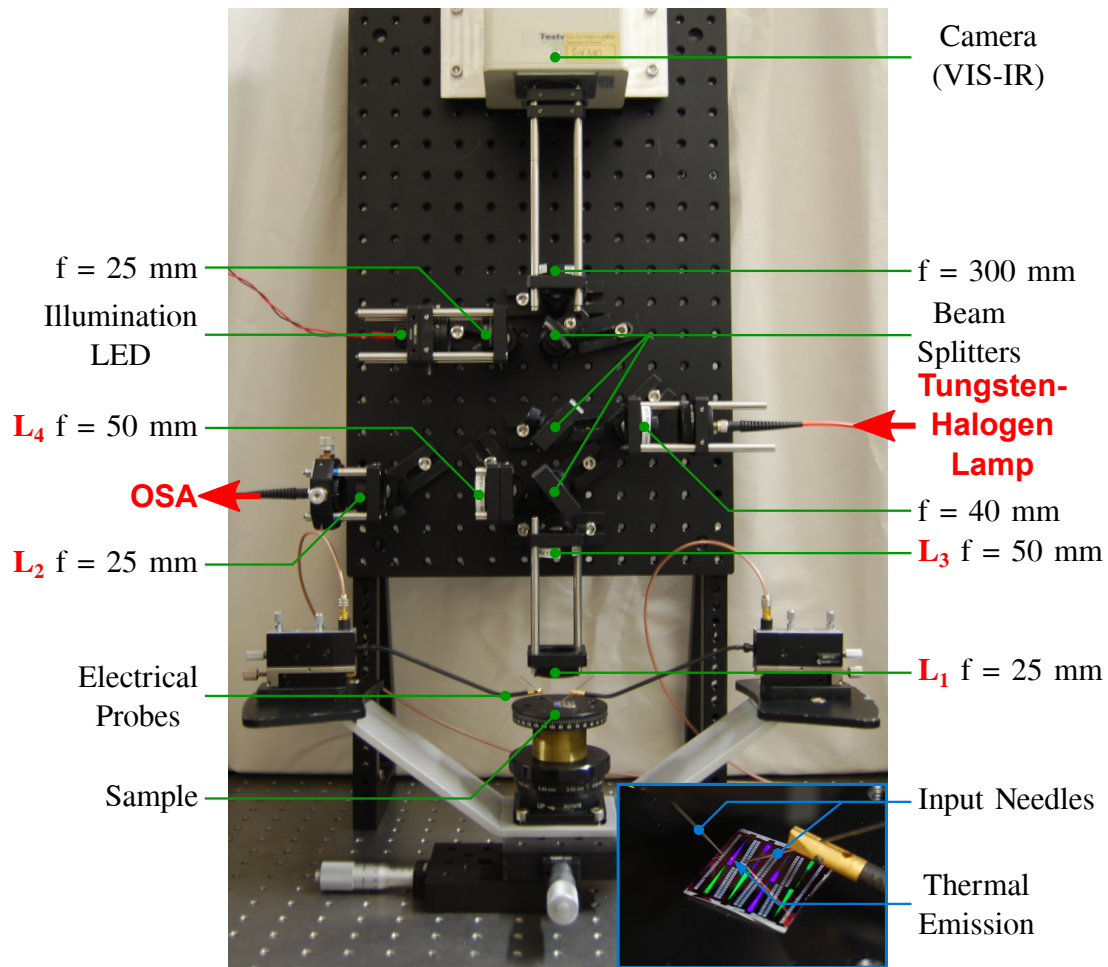


Figure 2.11: Photograph of the optical setup in the setup-B configuration. Each of the optical components and lenses are labelled. The inset in the bottom left shows a zoomed in image of the chip with the two needle probes at either side. Thermal light emission is visible from the device between the two probes. Please note that the purple and green colours are caused by room light scattering from the photonic structures. The bright metallic squares are the aluminium contact pads at each side of the photonic crystal pattern.

analyser), their corresponding input and output fibres are labelled accordingly. The main advantage of this setup is that all the optical components are above the chip, allowing the sample to be kept horizontal, which makes it easier to probe. The stage is designed so that the chip, along with the needle probes, can be moved together underneath all the optics facilitating easy alignment to each device.

Chapter 3

Photonic Crystal Based Thermal Emitter

3.1 Introduction

Controlling spontaneous emission is a topic that has fascinated generations of researchers. The area received a major boost with the introduction of photonic crystals, which enabled both the enhancement [51] and the suppression [52] of spontaneous emission, e.g. from III-V materials, by orders of magnitude. The key challenge we are now beginning to address is whether a much broader emission spectrum can be controlled in a similar way, in particular the very broadband emission profile of thermal emitters, as described by Planck's radiation law [1]. Initial work in this area has focused on metallic structures [8,9,11,53], but many of these tend to be unstable at elevated temperatures with the exception of refractory metals such as tantalum or tungsten that can reach stable temperatures greater than 1000 K [54,55]. Furthermore, any resonances in a metallic structure have a low Q-factor due to the strong free carrier absorption of the metal. For example, reference [11] reports a metallic gold structure with an emission peak at $3.85 \mu\text{m}$ with a Q-factor of approximately 10; reference [54] illustrates a three dimensional metallic photonic crystal with a peak emission at $1.5 \mu\text{m}$ but with a Q-factor around 1.7. Clearly, these examples highlight the utility of photonic resonances for thermal emission control, but for many applications, a narrower emission line is desirable.

In order to achieve a narrower emission line, one solution is to restrict the thermal emission by engineering materials with narrow absorption lines, such as intersubband transitions in doped semiconductor quantum wells [23]. Quantum well structures can be engineered to exhibit a narrow absorption profile over a wide wavelength range, from the visible all the way through the infrared and even up to 10s of microns in wavelength. Gallium arsenide and antimonide compounds are a popular material to cover the mid-infrared wavelength range. Reference [56] illustrates how these compounds are implemented to create a narrow absorption peak in the wavelength range of $2\text{-}4 \mu\text{m}$. However, these materials are not necessarily stable at high temperatures with doping migration within the material a problem at elevated temperatures.

Here, we propose and demonstrate the use of doped silicon as a thermal emission material. The advantages of doped silicon are low and controllable optical

loss, possibility to engineer high Q resonances and a higher heat stability than standard metals and other dielectrics. As introduced in Section(1.4), thermal emission is based on Kirchhoffs law of thermal radiation, which states that, for a body in a thermal equilibrium state, the emissivity (ϵ) (i.e. the ratio of the thermal emission intensity to that of a blackbody) is directly related to the absorptivity (α), $\epsilon(\omega, \theta, \phi) = \alpha(\omega, \theta, \phi)$ [5], for a given frequency, direction and polarisation. This fundamental principle is exploited to create a narrowband thermal source. By introducing a photonic crystal structure into a thin layer of doped silicon, the absorption is resonantly enhanced at the resonant photonic frequencies of the structure. When the structure is heated, the emission is therefore also resonantly enhanced at the same frequencies and suppressed at all others, thereby exercising broadband control over the thermal emission profile.

This chapter firstly introduces the concepts and behaviour of photonic crystal slabs for intrinsic silicon before introducing absorption into the material. Using temporal coupled mode theory, I examine the fundamental limitations of the photonic crystal structure and find the condition required to maximise the absorptivity (emissivity) and then look at a possible way of increasing it. A detailed fabrication procedure of the complete thermal emission device is presented and I experimentally demonstrate the narrowband thermal emission of a doped silicon photonic crystal slab operating at around 1100 K. A large portion of the results and discussions presented in this chapter have been published in the journal *Scientific Reports* under the title *Silicon photonic crystal thermal emitter at near-infrared wavelengths* [57].

A key point to note is the wavelength range of interest in this chapter which is between 1 μm and 1.7 μm . This range may appear to be a poor choice, as to have the peak intensity of the blackbody spectrum in this range, one would need to reach temperatures around 2000 K. It would be much better to work in the mid-infrared wavelength range where things don't have to be as hot and where there are more applications for narrowband thermal light sources such as, environmental gas sensing. The reason for operating at the shorter wavelength is simply that the equipment was readily available in the laboratory. Furthermore, the successful demonstration of a thermal emitter at 1.5 μm is an excellent proof-of-principal result and confirms that such emission control is possible. Due to the scalability of Maxwell's equations, the same concepts presented here and proven to work will also work in the mid-infrared wavelength range, simply by scaling the size of the photonic structure to operate at longer wavelengths.

3.2 Two Dimensional Photonic Crystal Slabs

One of the most commonly studied photonic crystal structures is the two dimensional photonic crystal slab. A large portion of the research work conducted with these photonic structures is concerned with the in-plane propagation of light along the crystal slab, such as photonic crystal waveguides [58, 59], slowlight behaviour [60, 61] and optical switches [62, 63]. However, here we are interested in the out-of-plane (perpendicular to the plane of periodicity) optical behaviour of the structures where they have already demonstrated a number of advantages as free space filters and mirrors [64, 65]. The major advantage is that a single dielectric photonic crystal slab layer can match and in many cases exceed the

response and behaviour traditionally achieved with a multilayer dielectric stack. The unique properties of photonic crystals can produce either high-Q resonances or broadband responses in both reflection and transmission. Photonic crystal slabs have also been used for semiconductor surface emitting lasers with very low threshold due to the high-Q resonances generated within the structure [66].

3.2.1 Photonic Crystal Slab Modes

The two main examples of photonic crystal slabs are illustrated in Fig. 3.1b and 3.1c and are the square and triangular hole array photonic crystal lattices respectively. These two lattices embody the two basic topologies of photonic crystal slabs and are characteristic of many possible structures. These slabs are similar to the two-dimensional photonic crystals discussed in Section (1.3), except that for the two-dimensional crystal case, the vertical z -direction is infinitely extruded. The modes of these pure two-dimensional structures correspond to states that have no wavevector component in the vertical z -direction and can be viewed as having strictly TE (transverse electric) and TM (transverse magnetic) polarisation states. Here, by restricting the vertical height of the crystal, the slab is finite in the vertical direction and the modes are no longer purely TE or TM but are still classified as TE-like (even) modes (electric field mostly parallel to the mirror symmetry plane ($z=0$) of the slab) and TM-like (odd) modes (electric field mostly perpendicular to the mirror symmetry plane ($z=0$) of the slab). This forces a new analysis of the system and the use of a full three dimensional model to accurately describe the behaviour as the finite slab introduces resonances that exist within the light cone that can propagate into the surrounding environment and are called quasi-guided modes.

The light cone is the feature that separates photonic crystal slabs from pure two dimensional photonic crystals. The light cone provides a continuum of modes in the region outside the slab and offers a set of radiation channels to the modes that are confined within the slab. A band diagram is the best way to understand and visualize these quasi-guided modes within the light cone. Figure 3.1 compares the band diagrams of an unpatterned dielectric slab with those of the square and triangular photonic crystal slabs. A full three dimensional computational model was implemented to accurately calculate the frequencies of the quasi-guided modes and to compute each off the band diagrams. The computation was done using the finite difference time domain (FDTD) software known as MEEP [67].

I give a more general description of what information a band diagram contains, focusing on the band diagram for the square hole array photonic crystal slab, Fig. 3.1e. The x -axis of the band diagram is the value of the wavevector component parallel to the slab structure, with the y -axis representing the frequency value for the mode. The band diagram looks at the wavevector component in two directions; along the Γ -X direction, along the rows of holes, and along the Γ -M direction, diagonally along the rows of holes. As previously described, any mode above the light-line (red line in the band diagrams) is quasi-guided and its energy will slowly leak into the surrounding environment. We are interested in the out-of-plane thermal emission from the photonic crystal slab and so not concerned about the modes that are fully confined, i.e. below the light line. Therefore, we

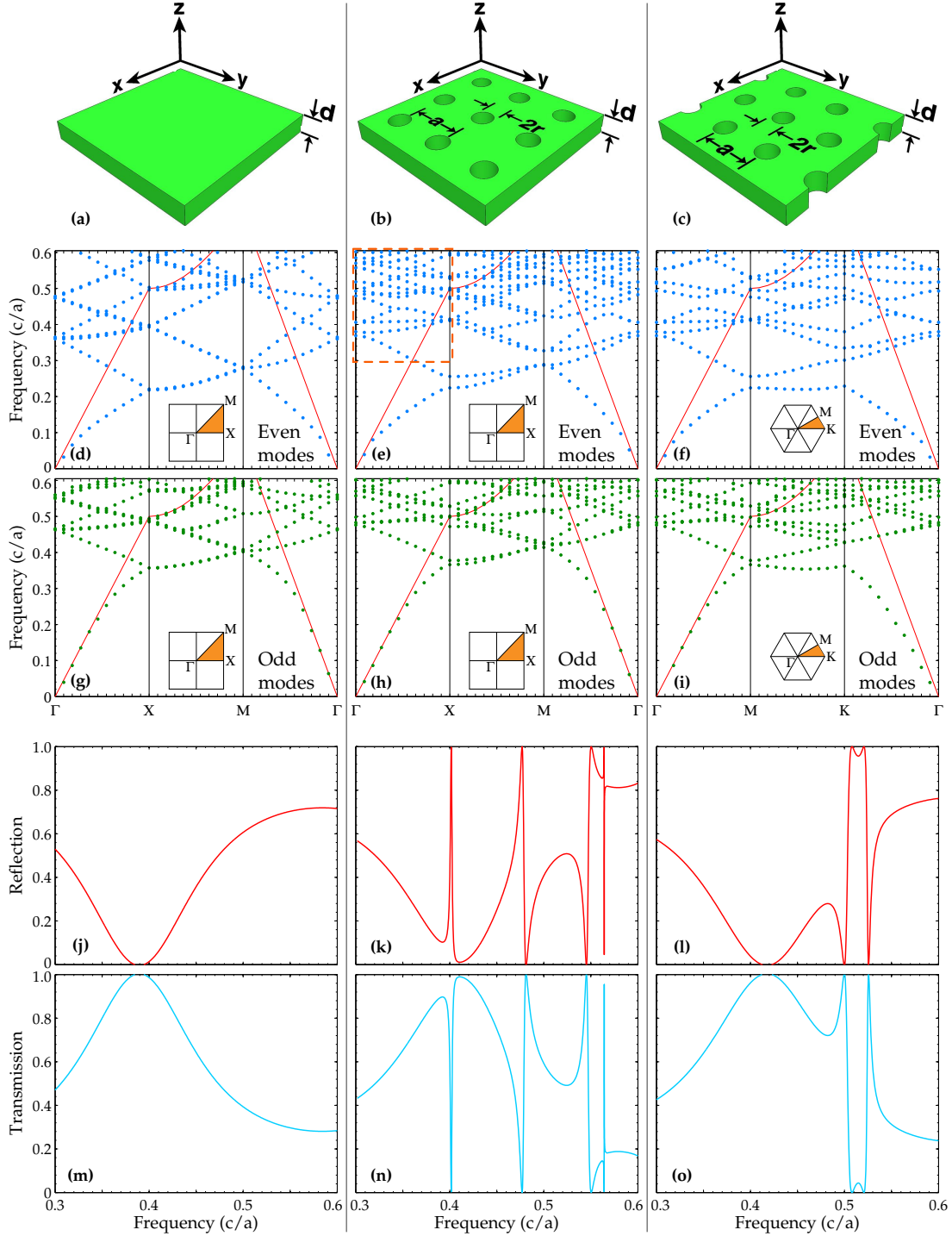


Figure 3.1: Comparison between an unpatterned dielectric slab and the square and triangular photonic crystal slabs. (a), (b) and (c) show a view of each configuration, respectively. (d), (e) and (f) show the photonic band diagrams for the even (TE-like) modes while (g), (h) and (i) show them for the odd (TM-like) modes. The red line in each represents the light line. The inset in each band diagram shows the Brillouin zone, with the irreducible zone shaded in orange. (j), (k) and (l) show the out-of-plane normal reflection spectrum for each structure with the corresponding transmission spectrum shown in (m), (n) and (o). For the band diagrams $d=0.3667a$, $r=0.2a$ and epsilon was 12.25. For the reflection and transmission spectra $a=600$ nm, $d=220$ nm, $r=120$ nm and $n=3.5$ with the electric field polarised along the y -axis.

only need to focus on the region of the band diagram above the light-line, often referred to as the light cone. At the Γ -point, the parallel wavevector component is zero and corresponds to vertical emission, normal from the surface. As the parallel wavevector increases, in either the Γ -X or Γ -M direction, the emission angle increases from normal because the wavevector of the emitted wave now has a parallel component. Therefore, from the band diagram it is not only possible to see what the frequency of each mode is, but equally importantly, it is possible to determine the angular emission properties of each mode.

We begin the comparison by firstly looking at the modes of the unpatterned, uniform dielectric slab with dielectric constant of 12.25 ($n=3.5$), similar to silicon in the near-infrared wavelength range, with a slab thickness d of $0.3667a$ as illustrated in Fig. 3.1a. Vertical confinement of light within the slab is provided by total internal reflection. The band diagrams for the uniform dielectric slab are shown in Fig. 3.1d for the even (TE-like) modes and Fig. 3.1g for the odd (TM-like) modes with the red line the light line. The insets illustrate the first Brillouin zone with the irreducible Brillouin zone shaded in orange. The Brillouin zone is square for both the unpatterned and square lattice and hexagonal for the triangular lattice. The band diagram is calculated along the side of the Brillouin zone Γ -X-M- Γ (Γ -M-K- Γ for the hexagonal lattice), which are the high symmetry points of the lattice.

Due to the use of a reduced-zone scheme the dispersion curves for the uniform dielectric slab case are folded into the first Brillouin zone by the reciprocal lattice vectors. Because of this band folding, it appears that the uniform dielectric slab exhibits quasi-guided modes i.e. mode above the red light line. However, this is not the case, and is only an artefact of the reduced Brillouin zone scheme and the simulation technique used. In order to calculate the band diagram for the uniform slab, a finite square section of the slab, containing no air holes, with a period a is used. Each band diagram is folded at the reciprocal wavevector values, i.e. at the X- and M-points of the band diagram. For the square and triangular hole arrays this folding introduces the guided resonance modes above the light line. Since the uniform slab is also a periodic structure due to the reduced computational domain, the software folds the guided modes at the X- and M-points of the band diagram. Giving the impression that there are modes above the light line, but this is just a consequence of the computation technique employed to calculate the band diagram. The modes of the uniform slab are fully guided and exist below the light line only.

We now look at the two photonic crystal slabs; the square hole array and the triangular hole array with period a , slab thickness $d = 0.3667a$ and radius $r = 0.2a$. In-plane propagation of light in the slab is determined by the crystal lattice, while again the vertical confinement of light within the slab is provided by total internal reflection. The band diagrams for both lattice configurations and for both even and odd modes are shown in Fig. 3.1(e,f,h,i), respectively. These band structures display some similarities to the uniform dielectric slab, but also some very important differences. The similarity is that modes below the red light line are fully guided with the electromagnetic energy completely confined to the slab. However, in the case of the patterned slab, the modes above the red light line can couple to radiation modes and the energy can leak out. The rate of this energy loss or Q-factor varies with frequency and wavevector.

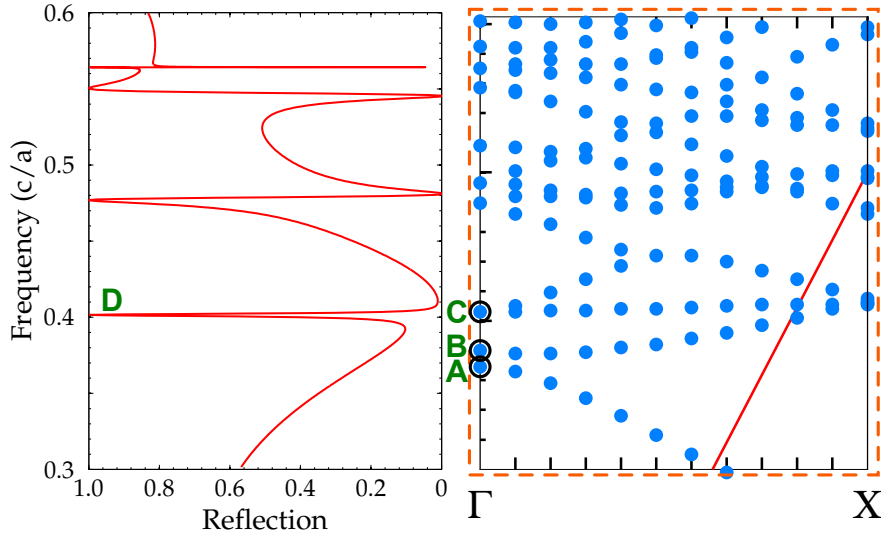


Figure 3.2: Comparison of the band diagram modes near the Γ -point (b) with the sharp resonances of the normal reflection spectrum of the square hole array photonic crystal slab (a). Both images are repeated from Fig. 3.1, (a) is Fig. 3.1k while (b) is Fig. 3.1e (indicated by the inset of the dotted orange box).

Comparing the band diagrams across the three structures, the modes of the unpatterned (uniform) slab split into multiple distinct resonant bands within the square and triangular band diagrams. For example, focus on the the lowest frequency modes at the X-point and the M-point of the uniform slab and compare it to the corresponding modes at the X-point and M-point of the square slab and the M-point and K-point of the triangular lattice. It is easy to see how the single frequency mode of the uniform slab splits up into two modes for the periodic structures. The same behaviour happens throughout the band diagram for the higher frequencies modes also.

The presence of these quasi-guided resonances greatly affects the transmission, reflection and absorption of externally incident light on the photonic crystal. Fig. 3.1(j-o) also compares the reflection and transmission spectra of the three structures for normal incidence light. The finite element software COMSOL was used to calculate these spectra by simulating a single unit cell of the slab suspended in air and illuminating with a plane wave source overhead with period $a = 600$ nm, thickness $d = 220$ nm, radius $r = 120$ nm and index $n=3.5$.

The reflection (transmission) spectrum of the uniform slab shows a slowly varying response due to interference of the reflections from the top and bottom interfaces, i.e. the Fabry-Pérot response of the slab. The square and triangular lattices then introduce additional features; the slowly varying background is still clearly visible, but we observe additional narrow linewidth resonances. These resonances arise from the interaction between the photonic crystal modes and the Fabry-Pérot modes of the slab, and are therefore Fano-type modes. These Fano resonances for the square hole photonic crystal slab are examined in detail in reference [65].

In order to make the connection between the quasi-guided resonances of the band diagram and these sharp reflection (transmission) resonances, we need to consider the modes at the Γ -point of the band diagram. Figure 3.2 illustrates this comparison for the square hole array slab. A section of the even mode band

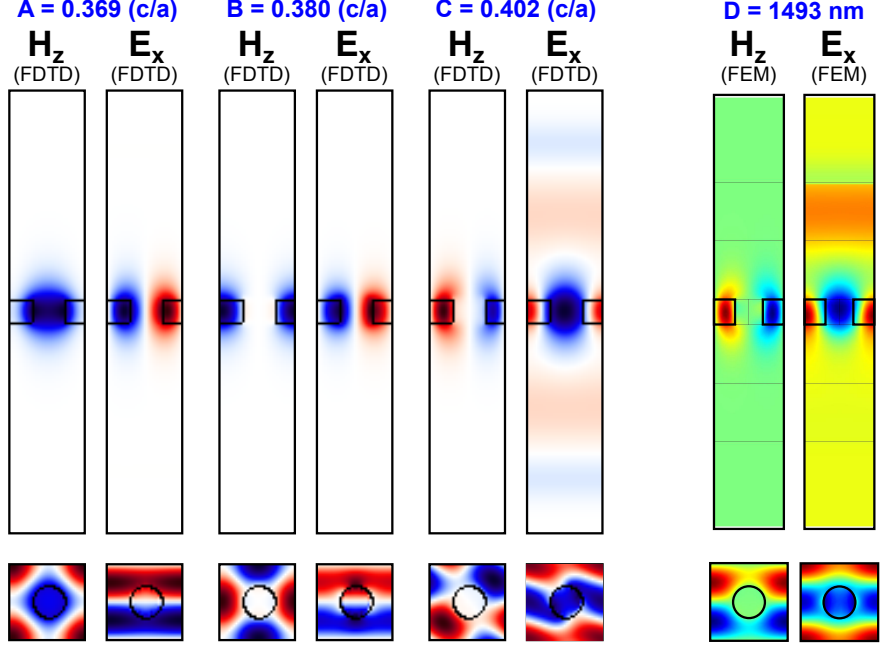


Figure 3.3: Magnetic and electric field profiles of the first three modes at the Γ -point of the band diagram in Fig. 3.2, labelled A,B,C along with the corresponding mode profile for the reflection peak marked D. The field profiles A-C are obtained using MEEP (FDTD), the same computational model as used for the band diagram calculations, while the final mode profile D is obtained from the COMSOL (FEM) model for calculating the normal reflection spectrum. Please note, the modes C and D correspond to the same resonance.

diagram of the square hole lattice (Fig. 3.1e), indicated by the dotted orange box, is taken and compared to the reflection spectrum (Fig. 3.1k) of the same structure. The computational parameters are the same for both. The four sharp Fano resonances of the reflection spectrum in the left hand panel occur exactly at four resonant frequencies where there is a quasi-guided mode of the photonic crystal slab at the Γ -point

The other modes at the Γ -point are not present in the reflection spectrum. This is unusual, as the modes exist within the light cone and are therefore expected to couple to radiation modes. The fact that these modes are not observed indicates that they do not couple to a propagating mode.

Figure 3.3 displays the electric and magnetic field profiles of the three lowest band edge modes at the Γ -point and the reflection peak, labelled A,B,C and D in Fig. 3.2, respectively. Please note, the modes A,B and C are taken from the band diagram, calculated using MEEP, but the mode D is taken from the reflection spectra calculated using COMSOL. The reflection peak at D corresponds to the band diagram resonant mode C. Therefore, the modes C and D are the same resonance calculated separately by two different techniques.

The top images display field in the xy plane and the bottom panels are horizontal cross-sections along the yz plane. The absence of radiative components for the first two modes A and B, is a result of in-phase superpositions of the forward and backward travelling waves, where the in-plane electric field vectors add destructively. This behaviour can be explained using the symmetry mismatch argument. By examining the electric field profile for the three modes; A and B

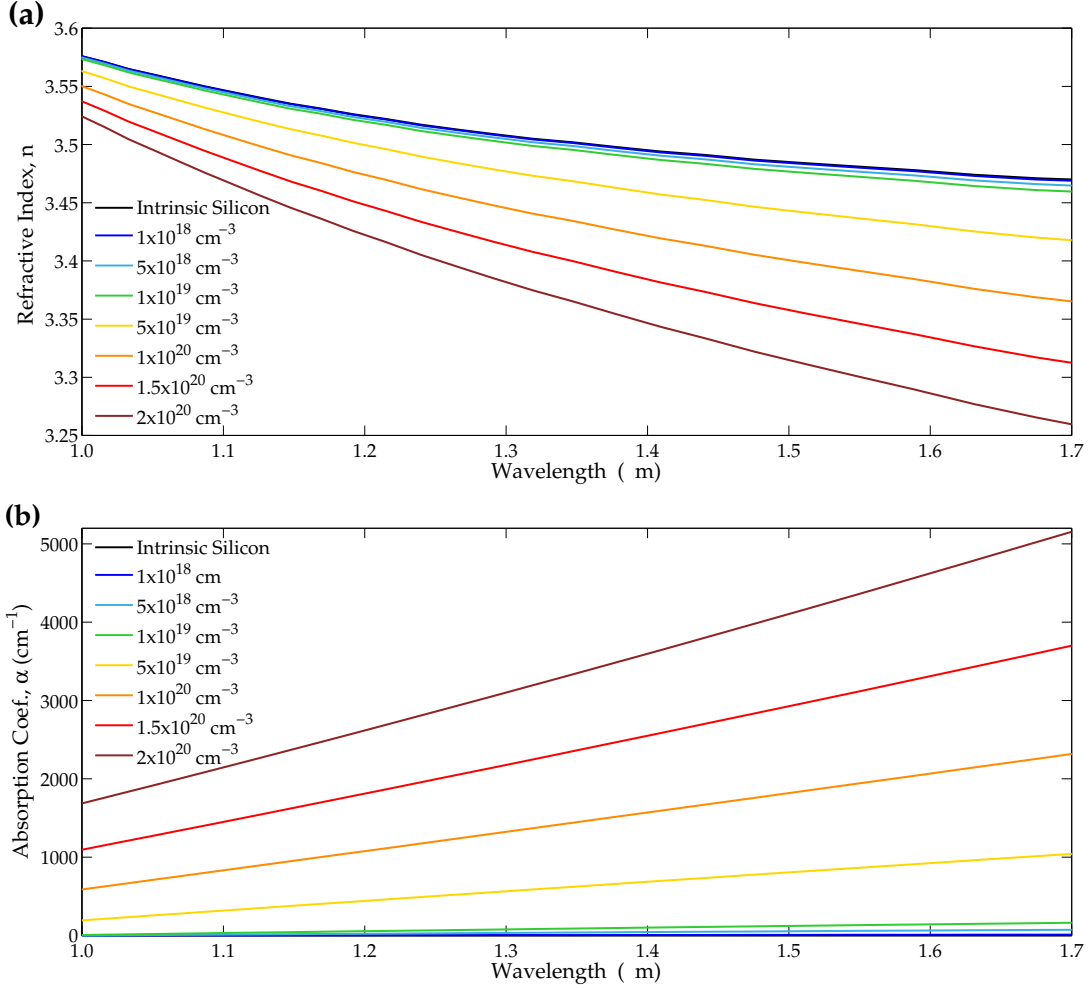


Figure 3.4: Graph of refractive index, n , (a) and adsorption coefficient, α , (b) versus wavelength for intrinsic silicon and seven different n-type doping densities. These graphs were calculated from Eqs. (3.1) to (3.4).

display an uneven electric field profile while for mode C, the field profile is even about the centre of the unit cell. The confined modes, with the anti-symmetric electric field profile, interferes destructively with itself in the far field, therefore no net out-coupling of light. On the other hand, the mode marked C (and D for the reflection spectrum) are symmetric about the centre of the unit cell and therefore vertical emission out of the slab is possible, notice the propagating field profile above and below the slab for C.

3.2.2 Introducing Absorption - Doped Photonic Crystal Slab

The material chosen to fabricate these photonic crystals for controlling thermal emission is silicon. In the infrared wavelength range (above 1 μm) there is practically no absorption of light by silicon, therefore silicon will have very low emission.

A good method to increase the absorption of light in this wavelength region is to increase the carrier concentration through doping of the silicon layer. Using experimental optical absorption spectra of silicon over a large range of doping

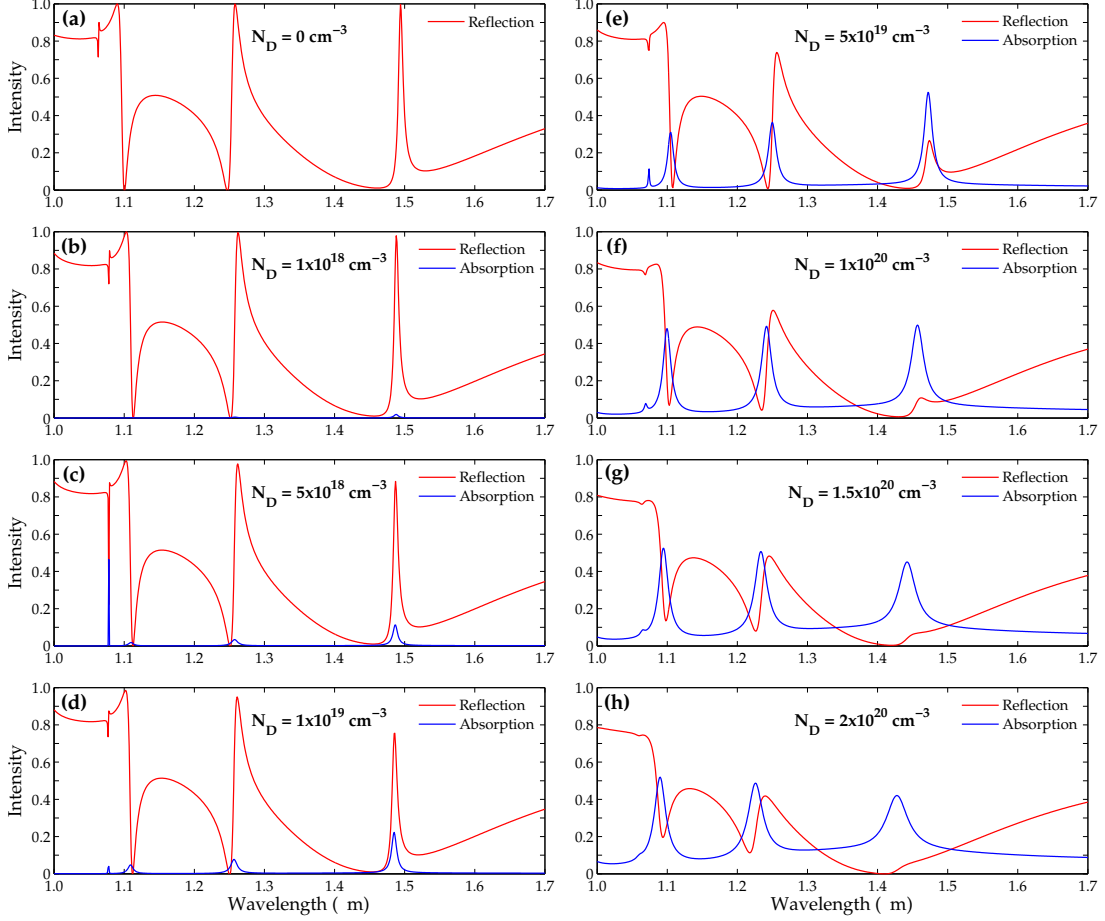


Figure 3.5: Reflection and absorption simulation results of a plane wave incident on a square hole photonic crystal slab, period $a = 600$ nm, thickness $d = 220$ nm, radius $r = 120$ nm, and with increasing doping concentration: (a) is for intrinsic (undoped silicon, no absorption), (b) $1 \times 10^{18} \text{ cm}^{-3}$, (c) $5 \times 10^{18} \text{ cm}^{-3}$, (d) $1 \times 10^{19} \text{ cm}^{-3}$, (e) $5 \times 10^{19} \text{ cm}^{-3}$, (f) $1 \times 10^{20} \text{ cm}^{-3}$, (g) $1.5 \times 10^{20} \text{ cm}^{-3}$ and (h) $2 \times 10^{20} \text{ cm}^{-3}$. Note a slight blue-shift of the resonances with doping, which is due to the corresponding reduction of the refractive index

concentrations, reference [38] derived an empirical expression relating the change in refractive index and absorption coefficient to the change in carrier concentration at both $1.3 \mu\text{m}$ and $1.55 \mu\text{m}$ wavelengths for both p- and n-type doping. Accordingly, all devices presented in this thesis were n-type doped with phosphorous. The expressions describing the change in absorption and refractive index due to the increase in electron concentration are, for $1.3 \mu\text{m}$:

$$-\Delta n = 2.98 \times 10^{-22} (\Delta N_e)^{1.016} \quad (3.1)$$

$$\Delta \alpha = 3.48 \times 10^{-22} (\Delta N_e)^{1.229} \quad (3.2)$$

And for $1.55 \mu\text{m}$:

$$-\Delta n = 5.4 \times 10^{-22} (\Delta N_e)^{1.011} \quad (3.3)$$

$$\Delta \alpha = 8.88 \times 10^{-21} (\Delta N_e)^{1.167} \quad (3.4)$$

where ΔN_e is the change in free electron concentration due to n-type doping, Δn and $\Delta \alpha$ is the change in refractive index and absorption coefficient due to

the doping concentration, respectively. Figure 3.4a and 3.4b show this change in refractive index and absorption coefficient, respectively, for seven different doping concentrations ranging from $1 \times 10^{18} \text{ cm}^{-3}$ to $2 \times 10^{20} \text{ cm}^{-3}$ over the wavelength range of $1 \mu\text{m}$ to $1.7 \mu\text{m}$ by interpolating and extrapolating around the two data points at $1.3 \mu\text{m}$ and $1.5 \mu\text{m}$.

Taking the very same square lattice photonic structure as described in the earlier part of this section, we can now include the optical losses induced by doping the silicon layer. The computational model is the same three dimensional model used earlier. By examining the reflection (R) and transmission (T) spectra of the doped slab, the absorption (A) of the slab can be easily calculated using $R+T+A=1$.

Figure 3.5 shows how the reflection and absorption spectrum of the square lattice slab change as the doping concentration is increased. Figure 3.5a is the reflection spectrum for the intrinsic (undoped) silicon case. This is identical to the reflection spectrum discussed earlier (Fig. 3.1k) except that the x-axis parameter has changed to wavelength instead of frequency, which results in the spectrum being plotted the other way around. I chose wavelength as the parameter because the doping induced absorption is strongly wavelength dependent and so dispersion has to be taken into account.

Figures 3.5(b-h) shows the reflection and absorption spectra of the square hole photonic crystal slab for an increasing range of doping concentrations going up to $2 \times 10^{20} \text{ cm}^{-3}$. Figure 3.5 clearly shows that the absorption spectra are amplified at the position of each of the reflection resonances (compared to the background off resonance absorption) for each doping concentration. The off-resonance background absorption of the photonic crystal slab continuously increases as the doping concentration increases. However, for example, examining the resonantly enhanced absorption peak at around $1.5 \mu\text{m}$, the absorption continually increases up to a doping concentration of $5 \times 10^{19} \text{ cm}^{-3}$. As the doping concentration increases further, the enhanced absorption peak begins to decrease again. Naively, one might expect that the higher the doping concentration, the greater the absorption but clearly, the presence of the resonance complicates matters somewhat. To help explain this, we use temporal coupled mode theory.

3.3 Temporal Coupled Mode Theory

In the previous section, we noted that the maximum absorption value of the photonic crystal slab, at normal incidence, was 0.5 for each of the resonantly enhanced absorption peaks. Increasing the absorption coefficient by increasing the carrier concentration didn't push this value above 0.5. Why does the absorption saturate at 0.5? To explain and understand why the photonic structures exhibit this behaviour, we will examine the quasi-guided resonances of the structure in more detail and identify how the physical parameters of the system relate to the photonic crystal behaviour within the framework of temporal coupled mode theory [68].

Coupled mode theory is a perturbation analysis of a system of coupled resonators. Coupled mode theory is used in a range of applications, and in more recent times, has been used widely to model optical resonant systems such as

laser cavities, optical nonlinearities and photonic crystal slabs. Coupled mode theory is based on looking at two types of components; (i) localised modes and (ii) propagating modes. The interactions of these components are analysed under very general principles such as the conservation of energy and result in a universal description of the system and device. In our case, the localised mode is one of the Fano resonances of the photonic crystal slab and the incident and outgoing plane waves are the propagating modes. The principle of coupled mode theory is based on a number of very general assumptions:

- Weak coupling
- Linearity
- Time invariance (materials and/or geometry doesn't change)
- Conservation of energy
- Time reversal invariance

The key most important assumption here is the weak coupling condition. Weak coupling assumes that the resonant mode is well confined and only very slowly leaks energy out of the resonance structure. All of these assumptions are valid for all of the photonic structures studied in this thesis.

3.3.1 Symmetric Photonic Crystal Slab

To formulate the analysis we consider our structure as one resonator coupled to two input/output ports, that is, the single photonic crystal resonant mode can only couple to just one plane wave travelling upward and one plane wave travelling downward. The system is depicted in Fig. 3.6a. We will derive a set of equations that describes the coupling between the photonic resonant mode and the two input/output channels. To begin, we start by assuming that the amplitude of the field in the resonator is proportional to some variable A and that $|A|^2$ is equal to the electromagnetic energy stored in the cavity and ω_0 is the resonant frequency of this isolated photonic crystal mode. The amplitudes of the incoming (outgoing) fields at each side of the slab are expressed as S_{u+} (S_{u-}) and S_{d+} (S_{d-}) respectively, and are normalised such that the absolute value of the fields squared is the power travelling in the upward or downward direction. The subscripts u and d refer to the upper and lower (downward) side of the slab, respectively. The resonant mode decays into the upward and downward direction with lifetimes of τ_u and τ_d , respectively and this is typically referred to as radiation loss, see Fig. 3.6a. Firstly, consider the isolated resonant Fano mode of the photonic crystal slab itself with no input power from either side. The mode in the crystal will decay very slowly and assume a complex frequency $\omega_c = \omega_0 - i/\tau_{rad}$, where τ_{rad} is the net lifetime of the field which is related to the upward and downward decay rates as

$$\frac{1}{\tau_{rad}} = \frac{1}{\tau_u} + \frac{1}{\tau_d} \quad (3.5)$$

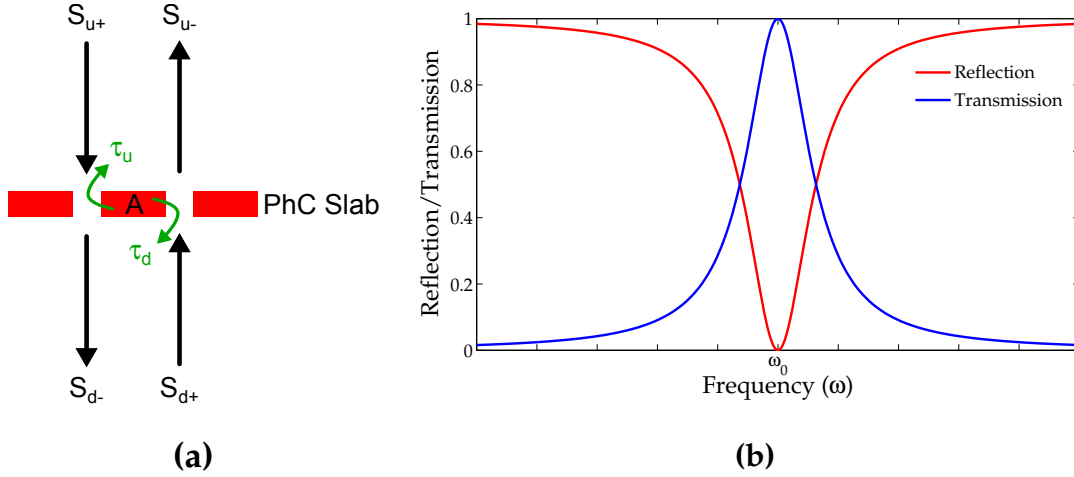


Figure 3.6: (a) A schematic illustrating the coupling between a single photonic crystal slab resonance (A) and the upward and downward radiation channels. (b) Plot of the reflection (Eq. 3.12) and transmission (Eq. 3.13) around the resonant frequency ω_0 , for an incident plane wave on the upper surface of the photonic crystal slab.

The amplitude of the field A varies with time as $A(t) = A_0 e^{i\omega_0 t} e^{-\frac{t}{\tau_{rad}}}$ with the first exponent describing the harmonic oscillatory part of the field and the second the total exponential decay of the field out of the resonator, including both the upward (S_{u-}) and downward (S_{d-}) radiation loss channels. The dynamic equation for A is

$$\frac{dA}{dt} = i\omega_0 A - \frac{A}{\tau_u} - \frac{A}{\tau_d} \quad (3.6)$$

Consider a plane wave with angular frequency ω on the upper-side of the slab with field amplitude (S_{u+}). With no input from the lower half, (S_{d+}) = 0, the set of coupled mode equations describing the coupling of the input plane wave to the resonant slab and the coupling of that energy back out to radiation modes in the upper and lower directions are:

$$\frac{dA}{dt} = i\omega_0 A - \frac{A}{\tau_u} - \frac{A}{\tau_d} + \sqrt{\frac{2}{\tau_u}} S_{u+} \quad (3.7)$$

$$S_{u-} = -S_{u+} + \sqrt{\frac{2}{\tau_u}} A \quad (3.8)$$

$$S_{d-} = \sqrt{\frac{2}{\tau_d}} A \quad (3.9)$$

The derivation of these dynamic equations can be found in [28]. These equations describe the excitation of the slab resonator mode by a single incident wave. The resonator mode is described by three parameters, i.e. the resonance frequency, ω_0 and the two decay rates of the field from the resonator into the upward and downward direction, τ_u and τ_d . These equations are derived with no reference to the geometry of the system. Exact rigorous three dimensional simulations are needed to determine the values of ω_0 and $\tau_{u,d}$, or at least a two dimensional simulation to get a good estimate of these values. If the frequency of the incoming plane wave source is ω , then due to the linearity of the system, the response of

the resonator is also at the same frequency i.e. the field everywhere will oscillate as $e^{i\omega t}$, therefore

$$\frac{dA}{dt} = i\omega A \quad (3.10)$$

Substituting Eq. (3.10) into the left hand side of Eq. (3.7), we obtain the steady state equation for A

$$A = \frac{\sqrt{\frac{2}{\tau_u}} S_{u+}}{[i(\omega - \omega_0) + (\frac{1}{\tau_u} + \frac{1}{\tau_d})]} \quad (3.11)$$

We can now compute the reflection ($R(\omega)$) and transmission ($T(\omega)$) coefficients of the slab resonator, as a function of the input frequency ω . The reflection coefficient of the resonator in a steady state is obtained from (3.8) and (3.11) and has a minimum value at $\omega = \omega_0$

$$R(\omega) = \frac{|S_{u-}|^2}{|S_{u+}|^2} = \frac{(\omega - \omega_0)^2 + (\frac{1}{\tau_u} - \frac{1}{\tau_d})^2}{(\omega - \omega_0)^2 + (\frac{1}{\tau_u} + \frac{1}{\tau_d})^2} \quad (3.12)$$

Similarly, the transmission coefficient is obtained using (3.9) and (3.11) and has a maximum value at $\omega = \omega_0$

$$T(\omega) = \frac{|S_{d-}|^2}{|S_{u+}|^2} = \frac{\frac{2}{\tau_d} |A|^2}{|S_{u+}|^2} = \frac{\frac{4}{\tau_u \tau_d}}{(\omega - \omega_0)^2 + (\frac{1}{\tau_u} + \frac{1}{\tau_d})^2} \quad (3.13)$$

The reflection and transmission equations describe a Lorentzian resonance with each plotted in Fig. 3.6b around the resonant frequency ω_0 . With a little algebra, it can be easily shown that $R(\omega) + T(\omega) = 1$.

It is often useful to write the decay rate in terms of the dimensionless figure-of-merit quantity called the Quality factor (Q), instead of τ , as τ has a unit of time. The Q-factor is defined as

$$Q = \frac{\omega_0 \tau}{2} \quad (3.14)$$

Now we can rewrite the dynamic equation for A in terms of Q-factors as

$$\frac{dA}{dt} = i\omega_0 A - \frac{\omega_0}{2Q_u} A - \frac{\omega_0}{2Q_d} A + \sqrt{\frac{\omega_0}{Q_u}} S_{u+} \quad (3.15)$$

$$S_{u-} = -S_{u+} + \sqrt{\frac{\omega_0}{Q_u}} A \quad (3.16)$$

$$S_{d-} = \sqrt{\frac{\omega_0}{Q_d}} A \quad (3.17)$$

Where, Q_u and Q_d are the Q-factors of the resonant slab mode by radiation in the upper and lower direction respectively.

$$\frac{1}{Q_{rad}} = \frac{1}{Q_u} + \frac{1}{Q_d} \quad (3.18)$$

3.3.2 Symmetric Photonic Crystal Slab with Absorption

Next, we consider the exact same square lattice photonic crystal structure but now we include material absorption loss in the system. This loss of amplitude via absorption is viewed as another output port, i.e. a third loss mechanism, coupled to the resonator and similar to the radiative decay channels. Figure 3.7a illustrates the addition of this extra loss channel to the resonator system, with the blue arrows indicating the internal loss of energy due to the material absorption. The decay rate of the mode is modified because the power not only escapes through radiation losses but now also dissipates internally due to the added material absorption, ($Q_{abs} = \omega_0\tau_{abs}/2$).

$$\frac{1}{Q_{tot}} = \frac{1}{Q_u} + \frac{1}{Q_d} + \frac{1}{Q_{abs}} \quad (3.19)$$

The additional terms and equations due to the absorption loss channel are highlighted in blue. The dynamic equation (3.15) is modified to take this extra loss channel of absorption into account

$$\frac{dA}{dt} = i\omega_0 A - \frac{\omega_0}{2Q_u} A - \frac{\omega_0}{2Q_d} A - \frac{\omega_0}{2Q_{abs}} A + \sqrt{\frac{\omega_0}{Q_u}} S_{u+} \quad (3.20)$$

$$S_{u-} = -S_{u+} + \sqrt{\frac{\omega_0}{Q_u}} A \quad (3.21)$$

$$S_{d-} = \sqrt{\frac{\omega_0}{Q_d}} A \quad (3.22)$$

$$S_{abs-} = \sqrt{\frac{\omega_0}{Q_{abs}}} A \quad (3.23)$$

Where S_{abs-} is the amplitude of the field in the absorption loss channel. Again in steady state,

$$A = \frac{\sqrt{\frac{\omega_0}{Q_u}} S_{u+}}{i(\omega - \omega_0) + \omega_0 \left(\frac{1}{2Q_u} + \frac{1}{2Q_d} + \frac{1}{2Q_{abs}} \right)} \quad (3.24)$$

From (3.20), we can derive an equation for the absorptivity, (α), for an incident plane wave on the upper surface of the resonant slab structure, taking into account both radiation loss and material absorption loss

$$\alpha_u(\omega) = \frac{|S_{abs-}|^2}{|S_{u+}|^2} = \frac{\frac{1}{Q_u Q_{abs}}}{(\omega - \omega_0)^2 + \left(\frac{1}{2Q_u} + \frac{1}{2Q_d} + \frac{1}{2Q_{abs}} \right)^2} \quad (3.25)$$

The total Q-factor is

$$\frac{1}{Q_{tot}} = \frac{1}{Q_{rad}} + \frac{1}{Q_{abs}} \quad (3.26)$$

Due to symmetry of the slab in the vertical z-direction $Q_u = Q_d$, the radiation decay rates in the upper direction are equal to the decay rate in the lower direction, and thus (3.18) becomes

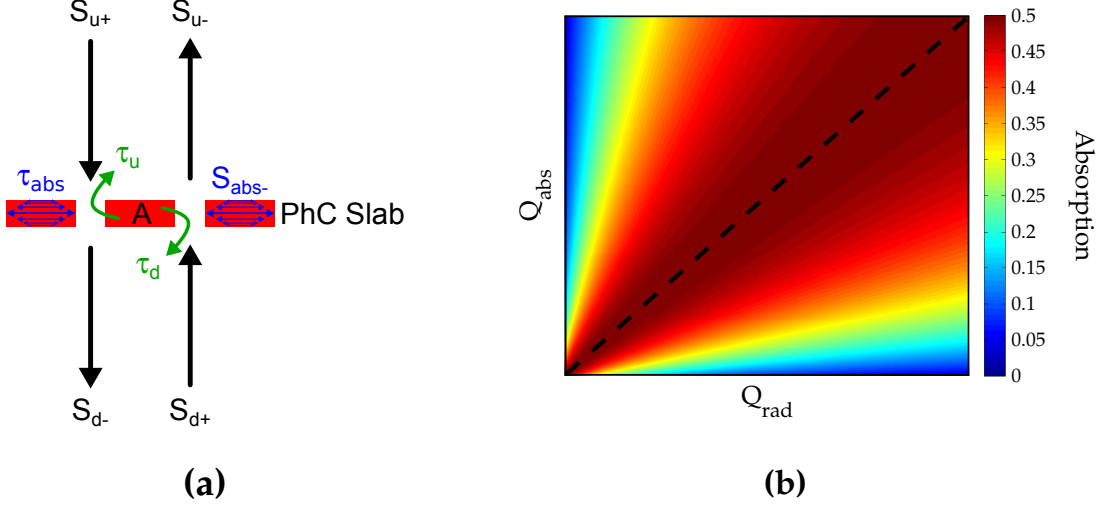


Figure 3.7: (a) A schematic illustrating the coupling between a single photonic crystal slab resonance and the upward and downward radiation channels, including the third loss channel due to material absorption. (b) A contour plot of the absorption (Eq. 3.29) graphically showing that the maximum value of the equation is 0.5, and that to reach this maximum value, both the radiative Q-factor and the absorption Q-factor need to be equal. The inset black dotted line in (b) indicates this maximum regime.

$$\frac{1}{Q_{rad}} = \frac{2}{Q_u} \quad (3.27)$$

Substituting (3.18) and (3.27) into (3.25) gives

$$\alpha_u(\omega) = \frac{\frac{1}{2Q_{rad}Q_{abs}}}{(\omega - \omega_0)^2 + \left(\frac{1}{2Q_{rad}} + \frac{1}{2Q_{abs}}\right)^2} \quad (3.28)$$

And on resonance with $\omega = \omega_0$ becomes

$$\alpha_u(\omega_0) = \frac{1}{\left(\frac{1}{2Q_{rad}} + \frac{1}{2Q_{abs}}\right)^2} \quad (3.29)$$

Figure 3.7b plots equation (3.29) on a two dimensional contour map. From this plot, the maximum of (3.29) is achieved when $Q_{rad} = Q_{abs}$, along the black dotted line on the plot. Therefore the maximum value of the absorptivity of the slab from a single incident plane wave is when the total radiation decay rate is equal to the decay rate due to the material absorption, and when $Q_{rad} = Q_{abs}$, $\alpha_u(\omega_0) = 0.5$. So, in conclusion, the maximum possible value of absorptivity is 0.5, which is in full agreement with what we saw with the three dimensional finite element simulations for the photonic structure in the previous section in Fig. 3.5. This case of $Q_{rad} = Q_{abs}$ is also referred to as the “critical coupling condition” [68].

3.3.3 Q-matching Doped Photonic Crystal Slab

To examine this Q-matching condition $Q_{abs} = Q_{rad}$, we look at the square hole array photonic crystal slab. We re-examine the even mode band diagram of the square hole array lattice at the Γ -point, Fig. 3.2k. As already discussed, the band

Table 3.1: Radiative Q-factors for the square hole array photonic crystal slab.

Γ -Point Frequency (c/a)	Reflection Wavelength (μm)	Radiative Q-factor (Q_{rad})	Slab Overlap (%)
0.4063	1.494	194	93.2
0.4933	1.253	141	86.3
0.5571	1.096	118	94.5
0.5680	1.054	7500	94.5

diagram shows many modes at the Γ -point, yet the normal reflection spectrum shows only four distinct resonances. We will calculate the radiative Q-factor (Q_{rad}) of each of these four distinct modes at the Γ -point of the band diagram which can be done using the FDTD simulation software, MEEP.

To accurately calculate the Q-factors, one must use a full three dimensional computational domain so that the correct thickness of the slab is taken into account. The computational domain and boundary conditions are exactly the same as those used to calculate the band diagram consisting of a single square unit cell of the square hole slab suspended in air with periodic boundary conditions in the directions perpendicular the slab and with PML layers at the top and bottom of the domain. The structure has side length period a , hole radius $0.2a$ and slab thickness of $0.3667a$. A point source and a monitor point are placed within the slab. Initially the source is switched on and pumps the slab. The energy couples to all the available modes of photonic structure within the bandwidth of the source. The position of the source within the slab is critical in order to ensure that all available modes are being excited.

To ensure coupling to all possible modes, the position of the source is varied within the slab. Please note, that this source is not trying to simulate thermal emission, it is used to excite and determine all the possible resonant modes for a given photonic crystal slab structure. For example, the band diagrams presented in Fig. 3.1 contain many dots, each dot corresponds to a mode which was excited and coupled to by the point source within the slab. However, typically, the complete band diagram is not generated from one position, only a partial diagram is created. This is because at some positions the source will be at a null point of some of the modes and therefore, unable to excite it. By varying the position of the source throughout the slab it is possible to build up the complete band diagram. I used approximately 10 different positions within the slab, keeping away from the centre slab region and the edges of the computational domain. Due to so many positions, many of the modes will appear more than once, but this method ensures that all available resonant modes are identified.

To improve the accuracy of the Q-factor calculation, a narrow-bandwidth source centred around the frequency value of interest is used. Once the source is switched off the monitor point measures the decay rate of the field within the slab. This radiative Q-factor measurement takes into account energy lost from the slab mode to the upward and downward direction. Due to the periodic boundary conditions perpendicular to the slab, the slab appears infinite, so no

Table 3.2: Absorption Q-factor for different doping concentrations for the square hole array photonic crystal slab at 1.494 μm .

Doping Concentration (cm^{-3})	Absorption Q-factor (Q_{rad})
5×10^{18}	2900
1×10^{19}	1286
5×10^{19}	193
1×10^{20}	85

energy is lost in that direction.

Table 3.1 shows the calculated radiative Q-factor values for the four resonant modes corresponding to the four reflection resonances for the intrinsic undoped silicon case ($n=3.5$). All the other modes at the Γ -point had negative or unrealistically large values of radiative Q-factor indicating that these resonances are unstable or are “dark” modes of the structure.

The absorption Q-factor, which indicates the rate at which energy is lost due to material absorption, is calculated using

$$Q_{abs} = \frac{\epsilon_r}{\epsilon_i \sigma} \quad (3.30)$$

Where $\epsilon_{r,i}$ are the real and imaginary parts of the dielectric function, both are wavelength dependent, and σ is the fraction of modal energy within the slab. A COMSOL three dimensional model of the slab structure, very similar to the one used to calculate the reflection spectrum, was used to calculate the percentage of modal energy in the slab. Using the eigenfrequency solver, the resonant modes of the structure are examined and at each resonant frequency, the time averaged electric and magnetic energy density [34] is calculated for the entire computational domain, then for the slab itself.

We now consider the absorption Q-factor for various doping densities. To simplify things, we examine only one resonant mode, i.e. the lowest frequency mode of frequency 0.4063 c/a (1.494 μm). Table 3.2 shows the value of the absorption Q-factor for four different doping concentrations at wavelength 1.494 μm ; $5 \times 10^{18} \text{ cm}^{-3}$, $1 \times 10^{19} \text{ cm}^{-3}$, $5 \times 10^{19} \text{ cm}^{-3}$ and $1 \times 10^{20} \text{ cm}^{-3}$.

With a doping density of $5 \times 10^{19} \text{ cm}^{-3}$, an absorption-limited Q-factor of 193 is achieved, which matches the radiative Q-factor of 194 almost exactly. At this Q-matching condition, the peak absorptivity should be 0.5 for this doping density. Looking back at Fig. 3.4e, which shows the simulated absorption spectrum for the same structure with a doping density of $5 \times 10^{19} \text{ cm}^{-3}$, we see that the peak absorptivity is indeed 0.5 at 1.474 μm .

Finally, one point to consider is the decrease of the refractive index of the silicon due to the doping and the resulting loss of confinement. This decrease in the silicon refractive index results in a decreases in the effective index of the mode which in turn blue shifts the resonant wavelength and changes the radiative Q-factor. Here, the resonant wavelength changed from 1.494 μm (with $n=3.5$) to 1.474 μm (with $n=3.448$) at $5 \times 10^{19} \text{ cm}^{-3}$. With very little change in the

percentage of modal energy within the slab, the absorption Q-factor at this wavelength (1.474 μm) increases to 208. The radiative Q-factor is now very slightly reduced to 192, so in conclusion, even with such large doping concentrations of $5 \times 10^{19} \text{ cm}^{-3}$ and change in effective index, the Q-matching of ($Q_{rad} = Q_{abs}$) is still sufficiently fulfilled and the maximum absorption condition is met.

3.3.4 Vertically Asymmetric Photonic Crystal Slab with Absorption

In Section 3.3.2 (Symmetric Photonic Crystal Slab with Absorption), we derived the equation for the absorptivity and found that the maximum possible value for the slab structure is 0.5, which directly relates to the simulations of the structure that yielded a maximum emissivity value of 0.5. For a thermal emitter device, one of the main aims is to achieve a narrowband thermal emitter with an emissivity equal to 1 or at least very close to that value, yet with symmetric structures, we immediately lose half of the generated light to the lower side of the slab.

If we take another look at the equation for the absorptivity (3.25) of a plane wave, we note that on resonance, it is maximised when $Q_{abs} = Q_{rad}$. Therefore, in (3.25), replace Q_{abs} with (3.18) and simplify to

$$\alpha_u(\omega_0) = \frac{\frac{1}{Q_u}}{\frac{1}{Q_u} + \frac{1}{Q_d}} \quad (3.31)$$

The absorptivity (emissivity) of the upper surface can be further increased by maximising the ratio of upward to downward radiation ($\frac{1}{Q_u}$)/($\frac{1}{Q_d}$) while keeping Q_{rad} fixed. A possible method of increasing this ratio is to add asymmetry to the slab structure in the vertical direction. To do this, I looked at not etching the holes of the photonic crystal all the way through, and to leave a layer of silicon at the base of each of the holes to see what effect this would have. A schematic illustrating this method is shown in Fig. 3.8a where there is a layer of silicon at the base of the crystal holes. Figure 3.8b shows a theoretical plot of Eq. 3.31, the absorptivity (emissivity) on resonance of the upper surface of the photonic crystal slab against the ratio of ($\frac{1}{Q_u}$)/($\frac{1}{Q_d}$). The blue dotted line inset in the plot shows the symmetric case where the two decay rates are equal and the max absorptivity is 0.5. As the ratio increases, the absorptivity (emissivity) increases and asymptotically approaches unity.

Coupled mode theory has now taken us as far as it can. To accurately determine what the actual absorptivity values for this asymmetric structure are, we need to look at the full three dimensional doped structure. To begin, we will look at the symmetric structure studied in the previous sections and add the silicon layer to the bottom of each hole, using a square hole array photonic crystal slab: period 600 nm, radius 120 nm and slab thickness 220 nm with doping concentration of $5 \times 10^{19} \text{ cm}^{-3}$. The thickness of the silicon layer at the bottom of each crystal hole, t , was varied from 20 nm to 100 nm. The calculations were carried out using the same COMSOL three dimensional finite element model that was used with the symmetric crystal case.

To fully test the structure, the absorption of a plane wave incident both on the upper and the lower surface needs to be calculated. Figure 3.9a shows the

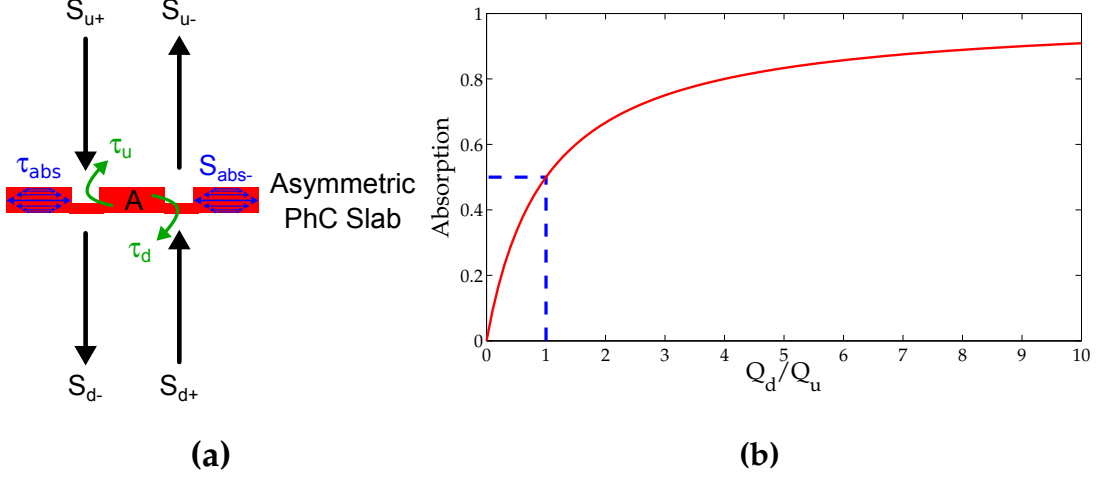


Figure 3.8: (a) A schematic illustrating the coupling between a single asymmetric photonic crystal slab resonance and the upward and downward radiation channels, including the third loss channel due to material absorption. (b) A plot of Eq. 3.31, the absorptivity of the upper surface of the asymmetric photonic crystal slab plotted against the ratio $(\frac{1}{Q_u})/(\frac{1}{Q_d})$. The blue dotted line shows the symmetric case with the maximum possible absorptivity of 0.5

simulated absorption results for a doping concentration of $5 \times 10^{19} \text{ cm}^{-3}$. The top panel displays the absorption for a plane wave incident on the upper surface, i.e. the “top-down” configuration. The bottom panel of Fig. 3.9a shows the absorption results for a plane wave incident on the lower surface, i.e. the “bottom-up” configuration. By calculating the absorption on both surfaces, the emissivity from these surfaces is also directly calculated. By examining the absorption, we can see what the emission profile will look like when the same structure is heated.

Overall, there is no major change in the spectrum compared to the absorption spectrum of the symmetric case, Fig. 3.5e, and the familiar four absorption peaks are still present. However, there is an overall red shift of the absorption peaks as the thickness t is increased from 20 nm to 100 nm, which is due to the increasing amount of silicon present which increases the effective index of each mode and in turn shifts the resonance wavelength to a larger value.

Considering each resonance individually of Fig. 3.9a and comparing the absorption value of the top-down to the bottom-up configuration for each of these resonances, it is clear that the one with the greatest difference in absorption is the second resonance in the $1.1 \mu\text{m}$ to $1.2 \mu\text{m}$ wavelength range. In the top down configuration, it reaches a maximum absorption value of 0.616 with $t = 70 \text{ nm}$ and the same thickness in the bottom-up approach reaches a maximum value of 0.082. The other two resonances hover around an absorption value of 0.5 in both configurations, showing no great change in their absorption properties even with the presence of the extra silicon layer in the air holes.

Returning to the enhanced absorption peak at $1.176 \mu\text{m}$, the total absorption at this wavelength is 0.698, obtained by summing the top-down and bottom-up absorption values. At the critical coupling condition, the absorption of both surfaces should reach a total of 1. This is evident from the symmetric case, where on the upper surface, the maximum absorption value of 0.5 is achieved when the correct doping concentration is reached. This makes the total absorption equal

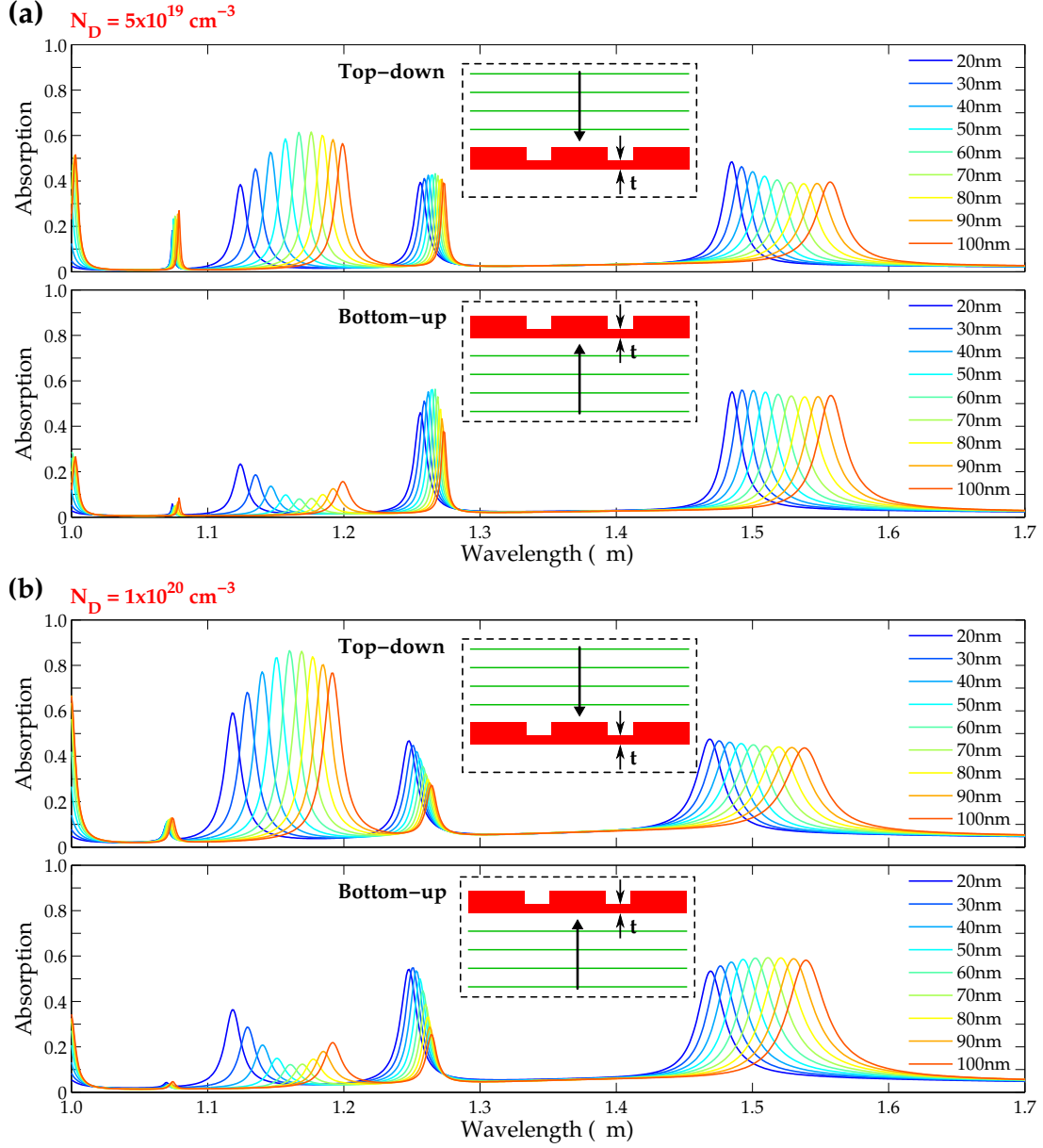


Figure 3.9: Simulated absorption spectra for the asymmetric photonic crystal slab with period $a = 600 \text{ nm}$, hole radius $r = 120 \text{ nm}$ and total slab thickness $d = 220 \text{ nm}$. The absorption of the upper and lower surface was simulated for a range of values of t from 20 nm to 100 nm . (a) shows the results for a doping concentration of $5 \times 10^{19} \text{ cm}^{-3}$ and (b) shows the results for an increased doping concentration of $1 \times 10^{20} \text{ cm}^{-3}$.

1 when both surfaces are considered. So in the asymmetric case, it is possible that further enhancement of the absorption on the upper surface is possible. To investigate the possibility the doping concentration of the slab was increased to $1 \times 10^{20} \text{ cm}^{-3}$ and the same simulations were run with the same structural parameters. The corresponding results are plotted in Fig. 3.9b.

Comparing the top and bottom panels, it is immediately obvious that the resonance for $t = 70 \text{ nm}$ (now at $1.169 \mu\text{m}$ wavelength) shows a maximum absorption value in the top-down configuration of 0.862 with a corresponding value in the bottom-up case of 0.123, their total value being 0.985, almost equal to total possible absorption of 1. This observation confirms that with this higher doping density, we have almost reached the critically coupled condition of $Q_{abs} = Q_{rad}$ for this structure.

3.4 Device Fabrication

Following on from these design considerations, a set of devices was fabricated in silicon-on-insulator (SOI). A schematic of the device is shown in Fig. 3.10 along with a cross-sectional view of the crystal structure in the inset. The entire top layer of silicon is n-type doped. The square hole array photonic crystal is in the center of the device flanked by two aluminium contact pads. The doped layer of silicon provides the material absorption for the device to operate as a good thermal emitter. The doping has a secondary function which is to reduce the electrical resistance of the top silicon layer and to allow current injection into the top silicon layer, thereby resistively heating the photonic crystal. To improve the thermal insulation, i.e. to reduce the heat loss of the crystal structure to the substrate, the photonic crystal is suspended in air. As will be explained in detail later, it is difficult to achieve a large area membraned photonic crystal, as the structure collapses as the size is increased. To solve this problem, a system of oxide support structures were implemented that keep the membrane suspended, as illustrated in the inset in Fig. 3.10.

The fabrication starts with a SOITEC silicon-on-insulator wafer with 220 nm silicon layer and a $2 \mu\text{m}$ buried oxide layer. From this wafer, a suitably sized piece is cleaved. This size is limited by the size of the furnace tube and is approximately $20 \times 15 \text{ mm}$. The first step of the process is to dope the entire top silicon layer. Before doping, the sample needs to be rigorously cleaned using what is known as a RCA clean [69].

The RCA-1 clean which is sometimes known as the “standard clean-1”, (SC-1), is a cleaning procedure to remove any organic residue and films from silicon wafers. The process works by sequential oxidative desorption and complexing with $\text{H}_2\text{O}_2\text{-NH}_4\text{OH-H}_2\text{O}$. During this process the surface of the silicon is oxidised and a thin oxide remains on the surface of the wafer, which is later removed.

The RCA-1 solution contains: 5 parts water (H_2O), 1 part 27% ammonium hydroxide (NH_4OH) and 1 part 30% hydrogen peroxide (H_2O_2). To begin the procedure, the water along with the ammonium hydroxide are placed in a beaker and heated to $70 \text{ }^\circ\text{C}$ on a hotplate. The solution is then removed from the hotplate and the hydrogen peroxide is added. The solution vigorously bubbles, indicating it is ready for use. The piece of SOI wafer is placed in the solution and soaked for 10-15 minutes to remove any organic contaminants. When finished,

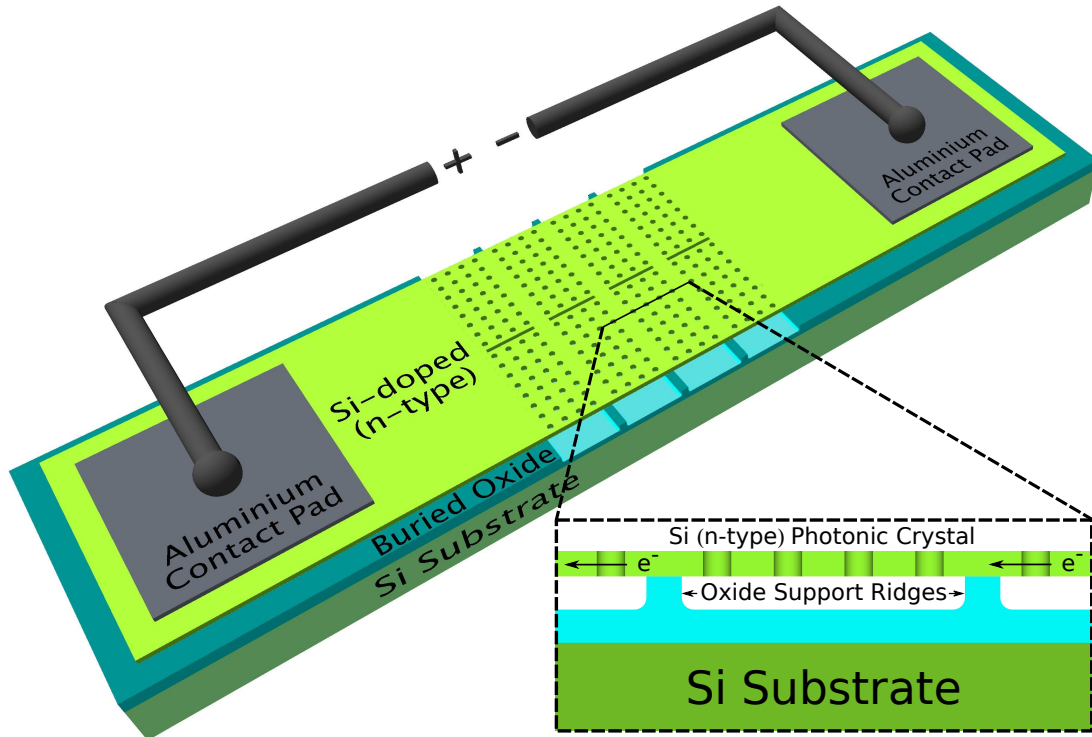


Figure 3.10: Schematic of the entire thermal emission device. Showing the doped silicon layer on the oxide and silicon substrate. The photonic crystal structure is in the centre with aluminium contact pads at either side. The inset shows a cross-section of the crystal. The crystal was membraned to increase its thermal insulation and reduce heat loss to the substrate. Due to the increased carrier concentration the crystal was resistively heated by applying a bias across the device [57].

the wafer sample is thoroughly rinsed in running deionised (DI) water, still water can contain organic residue and re-contaminate the surface. Finally, to remove the residual oxide layer, the SOI chip is placed in a solution of DI water and HF (5:1) for 1 minute.

3.4.1 N-type (Phosphorus) Diffusion Doping

To dope the top layer of the SOI wafer, we use a solid source diffusion method. The basic process and concept of this phosphorus diffusion doping procedure are illustrated in Fig. 3.11. The phosphorous source is a ceramic wafer and consists of an active component Silicon Pyrophosphate (SiP_2O_7) carried on an inert silicon carbide (SiC) substrate (Phosphorus Grade PH-950, Saint-Gobain Ceramics, USA).

Figure 3.11b shows how the SOI sample and the phosphorus source are mounted vertically in the furnace. It is important that they are placed as closely as possible without touching. They are mounted on a quartz boat with the phosphorus source placed upstream in the nitrogen flow. At the high diffusion temperature, the active component of the silicon pyrophosphate decomposes to the form phosphorus pentoxide glass vapour (P_2O_5), which evaporates from the source by direct volatilisation and then condenses on the silicon wafer. This thin layer of P_2O_5 provides elemental phosphorus for the diffusion into the silicon via

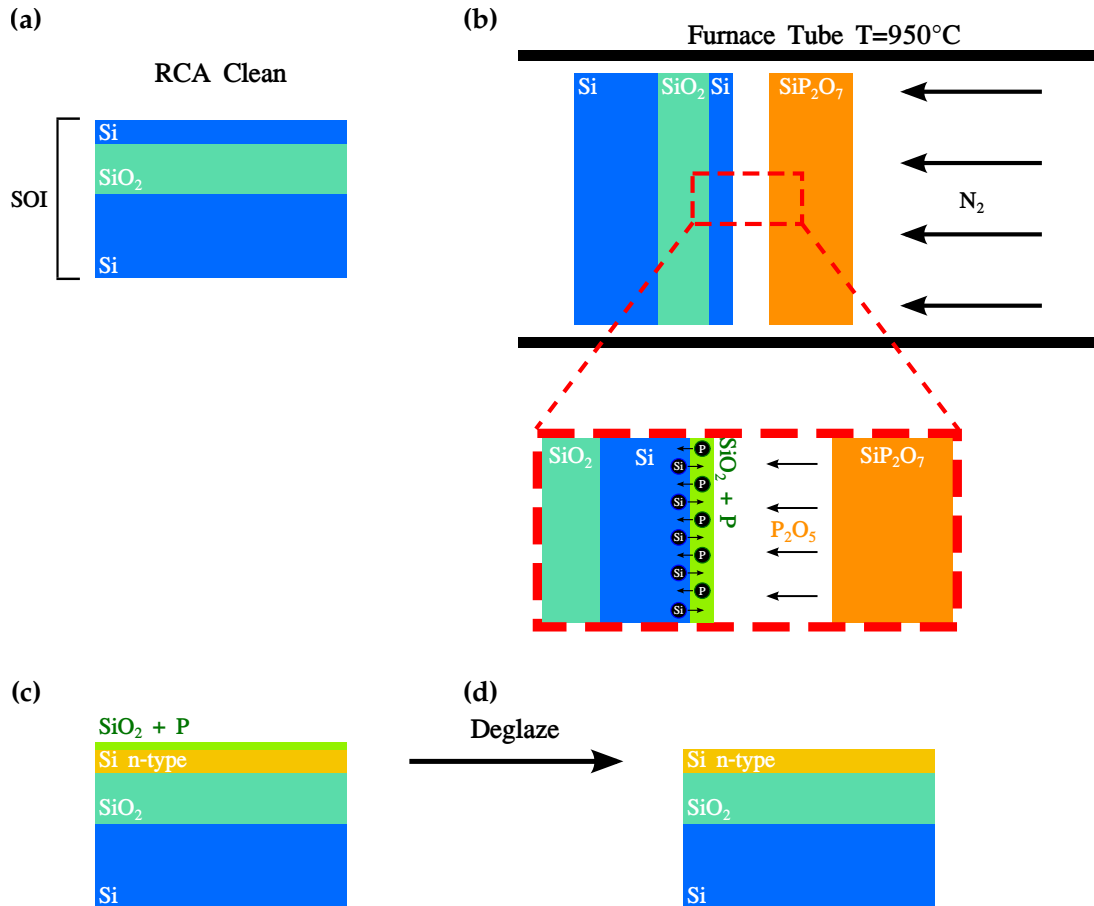


Figure 3.11: Solid source phosphorus diffusion doping procedure. (a) Firstly, the piece of SOI is clean using the RCA protocol. (b) The SOI sample is loaded along with the phosphorus source in the furnace tube. Where at a temperature of 950 °C the doping is carried out. The inset schematic simply illustrates the silicon atoms diffusing to the top while the phosphorus atoms fill the silicon vacancies and dope the silicon. (c) After the procedure the thick oxide layer is removed from the surface in a deglaze step using a solution of HF and DI water.

the reaction $2P_2O_5 + 5Si = 4P + 5SiO_2$. At these high temperatures, the silicon atoms diffuse to the surface to form silicon dioxide (SiO₂), leaving behind silicon vacancies. The phosphorous atoms then diffuse into the silicon layer and occupy the vacant sites left by the silicon.

To begin the process, the furnace is first slowly heated to 950 °C at a rate of 5°/min. Once the furnace has reached an equilibrium state, the quartz boat with the SOI wafer and the phosphorus source are first placed at the edge of the furnace tube, and left for two minutes. The boat is then slid into the centre of the furnace tube and left for another two minutes. Finally, the furnace itself is placed over the centre of the tube and the doping time begins. The entire process is carried out in a 100% nitrogen environment, with a gas flow rate of 0.5 slpm. To obtain a doping concentration of $5 \times 10^{19} \text{ cm}^{-3}$, the boat is left for approximately 45 minutes. The repeatability of the process is not excellent, even with parameters such as the temperature, gas flow rate and doping time all under control, as other factors such as the shape and uniformity of the source and any tilt of the sample in the quartz boat also play a role in the doping process. These

factors are difficult to control but it is possible to obtain a doping concentration reasonably close to target each time, within $\pm 15\%$.

After doping the unload procedure is the same as the loading: the furnace, still at 950 °C, is pulled away and after two minutes, the boat is pulled back to the edge of the tube; then wait another two minutes before finally removing the quartz boat. The excess unreacted dopant glass and the silicon dioxide are removed with a deglaze step of HF and DI water solution (1:5) for 1 minute.

3.4.2 Fabrication of Photonic Crystal

The sample is now ready for the fabrication of the photonic crystal structures in the top 220 nm layer of doped silicon. The photonic crystal fabrication procedure is detailed in Fig. 3.12. After the deglazing step, the sample is cleaned in acetone and IPA. A layer of electron beam (e-beam) resist, ARP 6200.13 (ALLRESIST, Germany), is spun on the sample at 5000 rpm, giving a 350 nm-thick layer and baked for 2 minutes at 180 °C (Fig. 3.12b). The ARP is a high resolution positive resist; where the exposed part is developed away, so the required pattern (i.e. the lattice of holes) is exposed.

The exposure is done using a state-of-the-art electron beam lithography machine Voyager (Raith) with an acceleration voltage of 50 kV. The pattern exposed in the resist is the square lattice of holes and the 5 μm wide isolation trench which runs around the crystal pattern. To ensure complete electrical isolation from the rest of the chip (Fig. 3.12c). As the exposing beam of electrons propagate through the resist layer, the electrons experience forward scattering. This results in the actual exposed area being larger than the written area. To compensate for this effect, the hole size is modified in the design pattern by reducing the radius of each hole by 10 nm compared to the required radius. For the isolation trench, this size reduction is not important as the trenches are large and their exact size is not critical.

To remove the exposed resist and leave the photonic crystal pattern behind, the sample is developed in the e-beam resist developer (AR 600.546) for 1 minute and 30 seconds at room temperature. To quench the development, the sample is rinsed in DI water (Fig. 3.12d). The pattern is transferred to the underlying doped silicon layer by reactive ion etching (RIE) (Fig. 3.12e). This is a dry etch process and is a combination of two etching mechanisms. The radio frequency plasma of the RIE system generates ions and free radicals, which are the two etching components. The dry etch process has two components; physical and chemical. The physical component is the etching done by the accelerated ions. This process is anisotropic and mills the exposed silicon. The second component is the etching done by the reactive radicals, which is isotropic. The goal of the process is to etch vertical walls, which requires a balance between the physical and chemical. The gas composition is a 1:1 ratio of $\text{ChF}_3:\text{SF}_6$ at a pressure of 4.4×10^{-2} mBarr. To completely etch away the full 220 nm layer of silicon, the plasma is maintained for 1 minute and 55 seconds. The final step is to remove the remaining layer of resist by placing the sample in 1165 solvent at 60 °C (Fig. 3.12f). Figure 3.12g,h shows two scanning electron micrographs (SEM) of the fabricated square lattice photonic crystal.

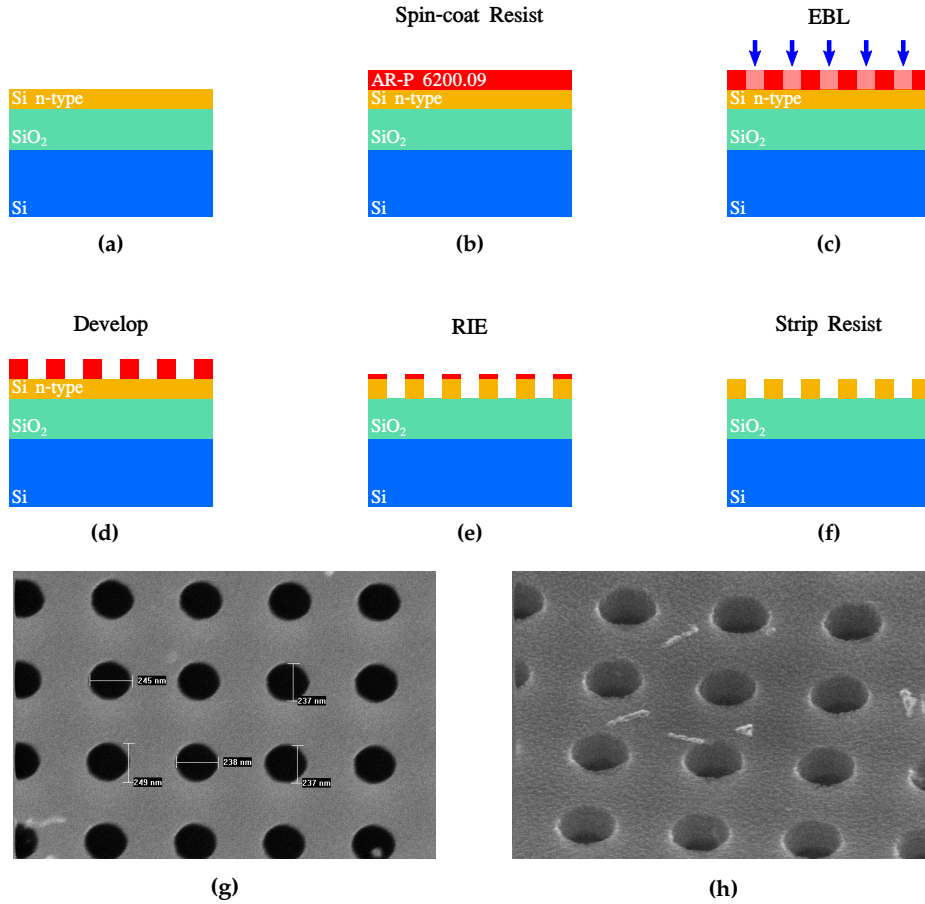


Figure 3.12: Schematic of the fabrication steps for the fabrication of photonic crystals. (a) The SOI substrate with the top silicon layer previously doped with the method described in Fig. 3.11. (b) The e-beam resist ARP 6200.09 (ALLRESIST, Germany) is spun on the sample. (c) Electron beam lithography (EBL) defines the pattern of the photonic crystal in the e-beam resist. (d) The resist is developed for 1 minute and 30 seconds. (e) The pattern in the ARP mask is transferred to the silicon layer via a dry etch process in the reactive ion etcher (RIE). (f) The remaining ARP mask is removed with heated acetone. (g) and (h) show examples of fully fabricated photonic crystals.

3.4.3 Aluminium Contact Pads

The next part of the fabrication process following the fabrication of the crystal pattern is the deposition of the aluminium contact pads. The contact pads are used to inject current into the doped silicon (and through the crystal structure) using electrical needle probes. A double resist layer lift-off procedure is implemented for the fabrication of the pads. The lift-off procedure is an alternative to etching and allows one to achieve patterns with materials that may otherwise be difficult to etch.

The complete lift-off and deposition procedure is outlined in Fig. 3.13. The contact pads are deposited after the etching of the isolation trench and the photonic crystal lattice. The bilayer e-beam resist (Fig. 3.13b) is made up of two different resists. One is a high molecular weight resist (950PMMA) and is spun on top of a slightly more sensitive bottom layer resist with a lower molecular weight (495PMMA).

For our particular application, we require a thick layer of aluminium due to

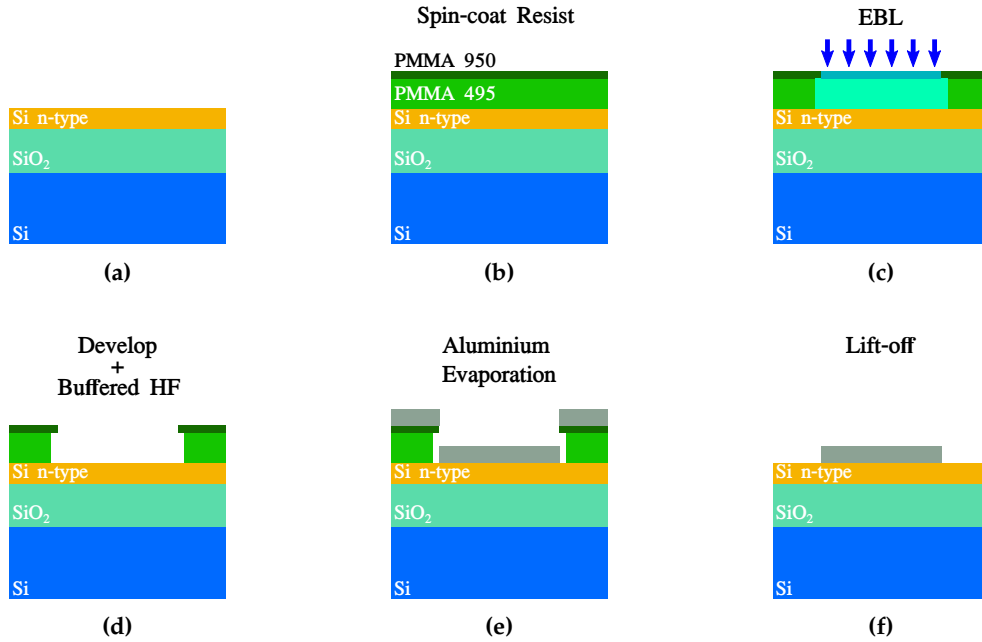


Figure 3.13: Fabrication of aluminium contact pads by lift-off: (a) The sample which has been doped and had photonic crystal already etched is cleaned in acetone and IPA. (b) Two layers of 495PMMA followed by a single layer of 950PMMA, diluted with xylene, are spin coated on top of the sample. (c) The contact pad pattern, in this case simply large squares, is exposed using e-beam lithography. (d) Sample is developed in a solution of IPA and H₂O 7:3, followed by a 60 second dip in buffered HF solution (HF:NH₄F at 1:6) to remove the native surface oxide. (e) Aluminium is deposited over the entire sample. (f) The sample is placed in heated acetone to dissolve the PMMA resist and lift-off the top layer of aluminium.

the relatively high currents passing through the sample. Thin aluminium layers (≈ 100 nm) melted and disintegrated very easily due to this high current density at the tip of the needle probe. An aluminium layer of approximately 600 nm was required. For a successful lift-off, the recommendation is that the first layer of resist be about 2-3 times thicker than the required metal thickness. This ensures a clean break between the metal layer deposited on the silicon and the layer deposited on the resist.

To achieve a thick bottom resist layer, two layers of the resist, 495PMMA, were spun. Each at 1500 rpm (≈ 400 nm thick) and each layer baked at 180 °C for 2 minutes. The top resist layer ideally needs to be as thin as possible, 100 nm. So the 950PMMA is diluted with xylene with a ratio of 1:1 and spun at 5000 rpm and baked at 180 °C for 5 minutes, bringing the combined thickness of the three layers to about 1 μ m.

The desired pattern, in this case is simply large squares $450 \times 450 \mu$ m, were exposed using the e-beam lithography system (Fig. 3.13c). The sample is developed in a solution of IPA:H₂O at a ratio of 7:3. Due to the difference in molecular weight and the sensitivity of the two resists, the exposed area is wider in the two bottom resist layers (495PMMA) than the top 950PMMA layer. After development an undercut in the bottom layer is visible, Fig. 3.13d. It is this undercut that makes this lift-off procedure so successful.

Before the metal deposition, the sample is dipped into a solution of hydroflu-

oric acid (HF, 1:1 with H₂O) and ammonium fluoride (NH₄F) 1:6, known as buffered HF, for 60 seconds. Buffered HF removes the thin native oxide layer on the surface of the silicon where the contact pads are going to be and ensures good electrical conduction from the pad to the silicon layer. This step is done just before loading the sample into the metal evaporator where it is quickly pumped down to vacuum. The buffered HF solution is used in preference to the standard HF because the standard HF attacks and damages the PMMA resist layer where the buffered solution doesn't damage the resist and only very slowly attacks the PMMA.

The aluminium is thermally evaporated and a layer with a thickness of about 600 nm is deposited across the entire sample (Fig. 3.13e). The undercut between the two resist layers ensures that the metal layer on top of the resist is not connected to the bottom metal layer on the silicon and can be easily removed. Finally, to carry out the lift-off process, the sample is placed in acetone to dissolve the PMMA layers. Heated acetone and gentle agitation in an ultra sonic bath speeds up the process. After all the PMMA is dissolved, all that remains on the sample are the contact pads (Fig. 3.13f).

3.4.4 Photonic Crystal Membrane

The final step of the thermal emitter device fabrication is to under-etch the crystal structure to increase the thermal insulation of the layer. By reducing the heat loss to the substrate, a much greater membrane temperature is possible for the same input electrical power. The thermal conductivity of silicon dioxide is around 0.8-0.93 Wm⁻¹K⁻¹ compared to 0.024 Wm⁻¹K⁻¹ for air, which is more than 30 times lower. The high thermal conductivity of the buried silicon dioxide layer was very evident in early experiments where the oxide layer wasn't removed. When heating the silicon layer, no light emission, either visible or infra-red, was detected and this was simply down to the silicon layer not being able to get hot enough due to the massive heat loss to the oxide layer beneath. Also, removing the oxide layer improves the light confinement in the photonic crystal slab by increasing the index contrast for the confined modes.

To remove the oxide layer, a buffered HF acid solution, same as before (HF:NH₄F at 1:6) of a ratio of 1:6, was used to dissolve the oxide layer. The aluminium contact pads need to be protected during this step, as the HF acid reacts with aluminium, even though only slightly, but it does result in pitting of the contact pads.

To protect the aluminium contact pads, a layer of photo resist S1818 (Shipley) is spin coated on the sample at 4000 rpm and baked at 100 °C for 2 minutes (Fig. 3.14b). Using a photo mask with a window slightly wider than the crystal pattern, the resist was exposed with ultraviolet (UV) light (Fig. 3.14c). To open up the HF windows, the sample was developed in S1818 developer, MF319 for 40 seconds (Fig. 3.14d). The sample is then placed into the buffered HF solution for 5 minutes to remove the oxide layer (Fig. 3.14g) and finally the remaining resist was stripped in acetone and the sample rinsed in IPA. Fig. 3.14g,h show two SEM images of the HF undercut beneath the crystal structure. Since the wet etch is isotropic, the oxide layer beneath the unpatterned silicon is also etched.

There were many issues with the early fabrication attempts of these devices.

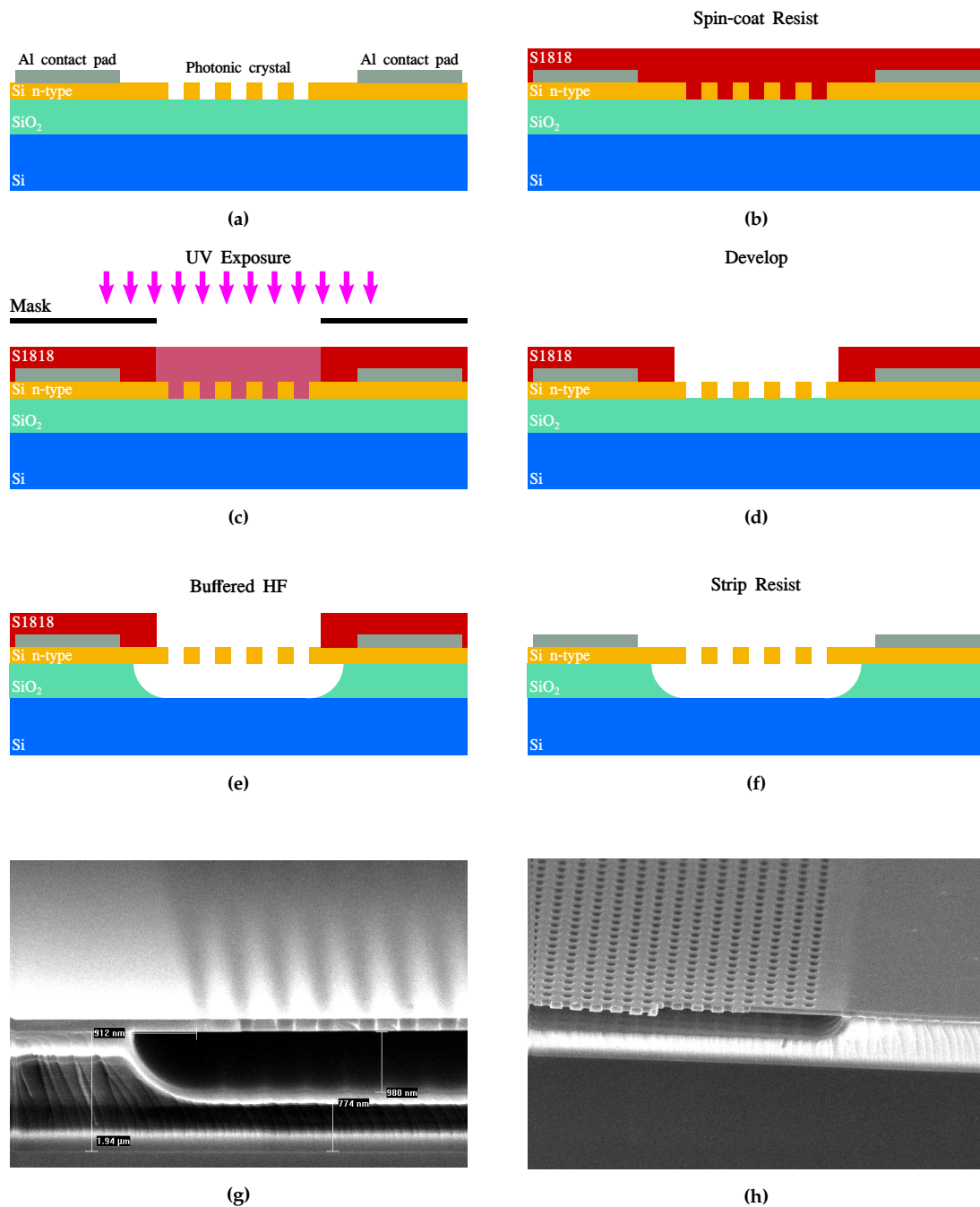


Figure 3.14: Phonic crystal under-etching process flow: (a) The complete device so far is depicted here with the photonic crystal flanked at either side by the aluminium contact pads. (b) The photo resist S1818 is spun onto the sample. (c) Sample is exposed with UV light through a photo mask. (d) The HF windows are opened up by developing the sample in MF319 developer. (e) the sample is placed in buffered HF solution (HF:NH₄F at a ratio of 1:6), etching the oxide. (f) The remaining resist is stripped using acetone and rinsed in IPA. (g), (h) Two SEM images showing the under-etched photonic crystal.

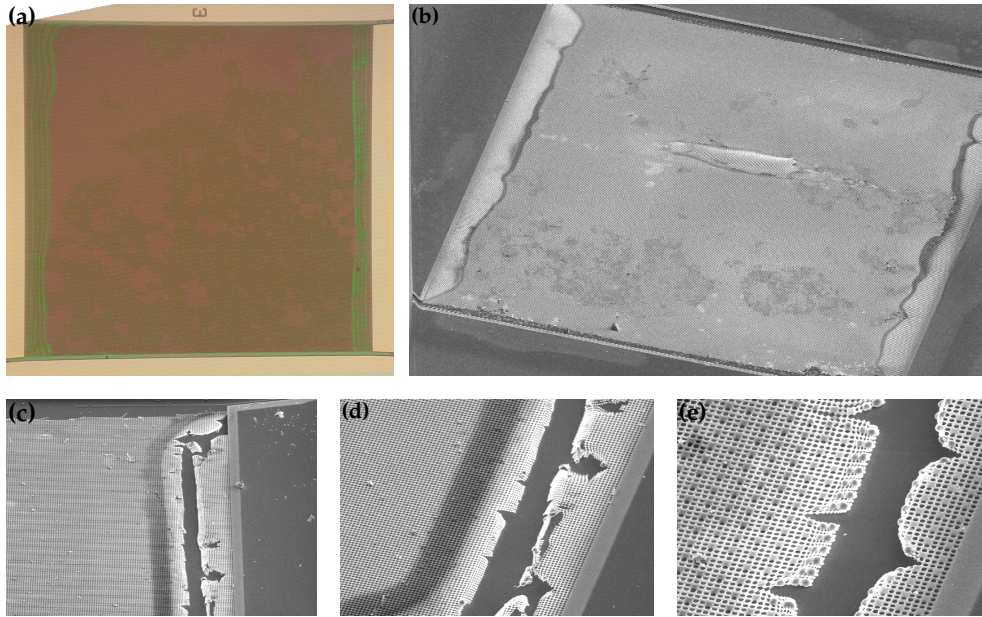


Figure 3.15: (a) Optical microscope image of a collapsed membrane, $200 \times 200 \mu\text{m}$. (b) SEM image of a collapsed membrane also $200 \times 200 \mu\text{m}$. (c)-(e) SEM images of collapsed membranes with melted crystal lattices due to over heating at the point where the membrane meets the unpatterened supported silicon.

The main issue was that the doped silicon membranes did not heat up uniformly, which was obvious from the uneven distribution of light emission from the crystal. Also, the membranes melted and were destroyed very easily due to hot spots i.e. small areas of intense heat with high intensity emission. The reason for these failures was not immediately obvious and through detailed investigation, it was discovered that these large area membranes (around $200 \times 200 \mu\text{m}$) had actually collapsed after the removal of the oxide layer and were in contact with the silicon substrate beneath. Figure 3.15a shows an overhead optical microscope image of a collapsed membrane and Fig. 3.15b shows a SEM image of a collapsed membrane. From the SEM image, the photonic crystal membrane has completely collapsed in the centre, making contact with the silicon substrate below. Two very short pieces at each end of the crystal have not collapsed where the membrane meets the unpatterened silicon. Comparing this SEM image to the optical image, it is easy to understand what the green dark and bright fringes at each end of the crystal pattern are. These fringes are the result of interference between the light reflected from the 220 nm membrane layer and the silicon substrate because the separation between the two changes from nothing up to $2 \mu\text{m}$ where the crystal membrane goes from the substrate up to the silicon on the oxide. This interference pattern phenomena is known as Newton's rings. Fig. 3.15c-e show where this piece of membrane heats so much that the silicon melts completely across the crystal.

Typically, photonic crystal waveguides and cavity structures are suspended in air to improve the Q-factor of the resonances by giving a greater index contrast and improving the light confinement. These structures have membranes that span 10 to $20 \mu\text{m}$ in length. For our out-of-plane thermal emission we need a membrane structure in the order of $100\text{s } \mu\text{m}$ in size to increase the amount of

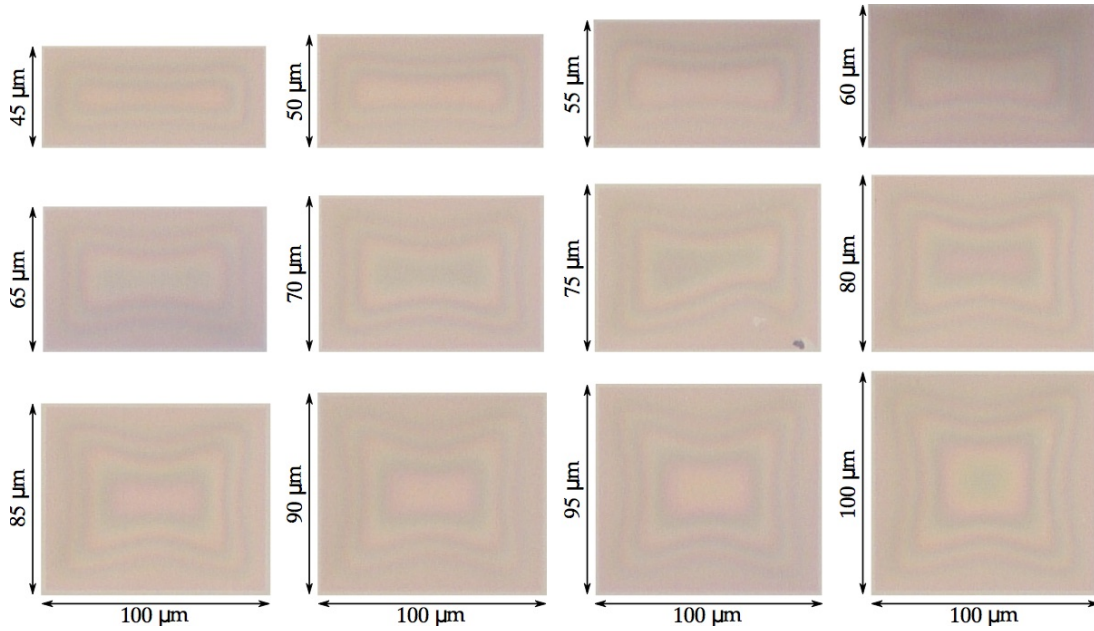


Figure 3.16: Optical microscope images of different sized photonic crystal membranes ranging from $45 \mu\text{m}$ to $100 \mu\text{m}$ in length. The interference fringes (or Newton's rings) suggest that the membrane has bowed and maybe totally collapsed and in contact with the silicon substrate below.

light produced. According to the Stefan-Boltzmann law, the power emitted is directly related to area of the emitter. As these devices are thermal emitters and we are examining them in the $1 \mu\text{m}$ to $1.7 \mu\text{m}$ wavelength range, we are operating in the tail of the blackbody curve, so low light level signal is expected. By increasing the membrane size, we can increase the amount of light that can be collected and coupled to the spectrometer.

To investigate the cause of the collapse of these large membranes, a comparison was carried out where the size of the membrane was varied. The same square hole array lattice was used and for each of these crystal patterns the width was kept at $100 \mu\text{m}$ and the length was varied from $5 \mu\text{m}$ up to $100 \mu\text{m}$. All the structures were underetched using the buffered HF solution. Fig. 3.16 shows an array of optical microscope images looking at these structures from the top. Only structures from $45 \mu\text{m}$ to $100 \mu\text{m}$ are shown here. Each of the images clearly displays a pattern of interference rings around the crystal pattern. This is the first indication that the crystal membrane may have collapsed or at least is strongly bowed and deflected. It is no longer flat, as these interference fringes are caused by the separation between the membrane and the silicon substrate varying along the crystal i.e. if the crystal was perfectly flat there would be no fringe pattern.

Next, we cleaved through these crystal membranes and examined them in the scanning electron microscope, looking edge-on. Figure 3.17 shows the edge-on view of each crystal membrane from a $5 \mu\text{m}$ to $100 \mu\text{m}$ wide span. The SEM images for $5 \mu\text{m}$ to $40 \mu\text{m}$ span are taken at a magnification of 2027 times while the larger membrane span images are taken at 1032 times magnification. Examining the SEM images, even with a span of $15 \mu\text{m}$, the crystal membrane begins to deflect and bow down and this collapsing gradually increases as the



Figure 3.17: SEM images looking edge on at the photonic crystal membrane. The crystal span length varies from $5 \mu\text{m}$ wide up to $100 \mu\text{m}$. Note that it is the width of the actual crystal that is indicated in each SEM image, however, the total span length will be a little wider due to undercutting of the oxide, approximately $2 \mu\text{m}$ at each side.

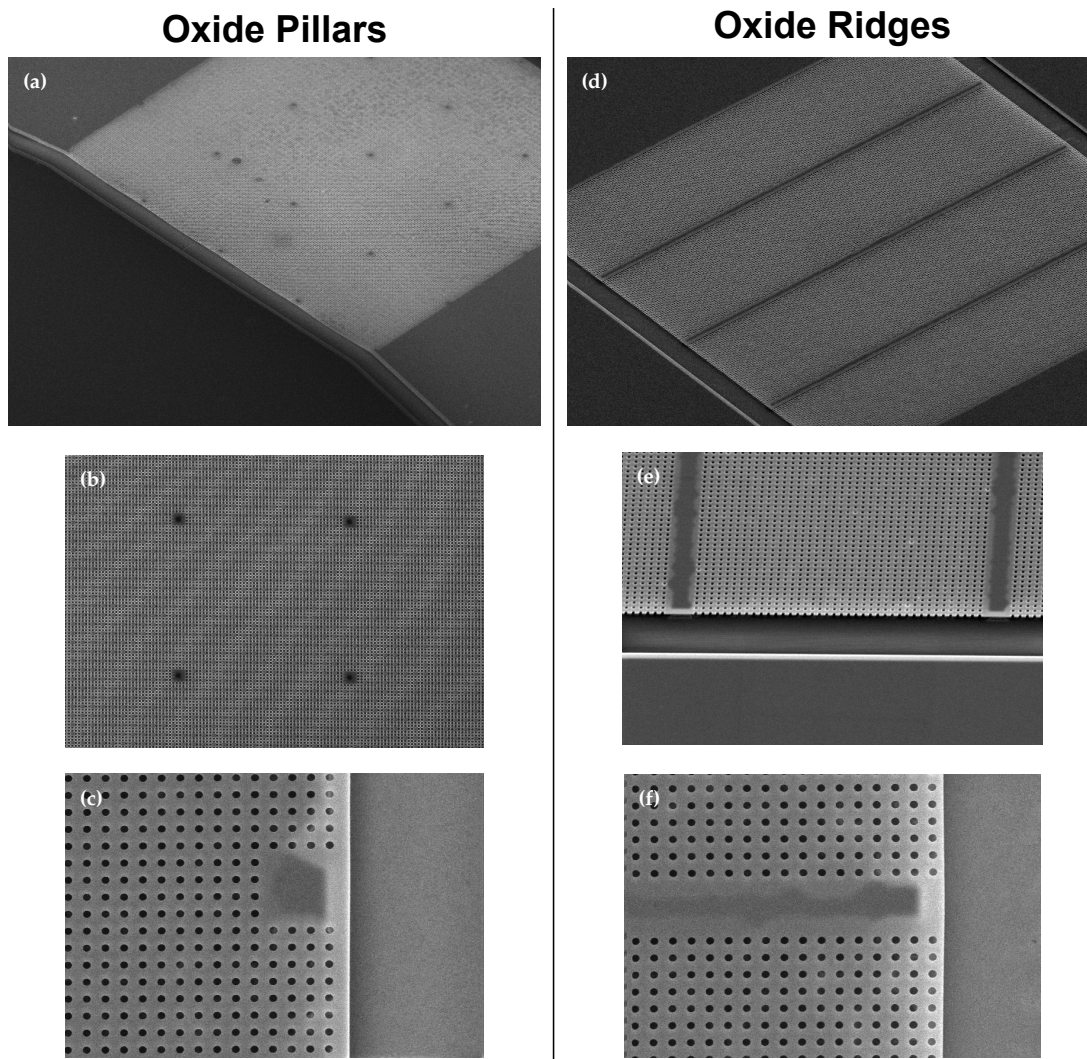


Figure 3.18: SEM images of two possible solutions to the collapsing membranes. On the left-hand side are images ((a) - (c)) of the oxide pillars and on the right-hand side ((d) - (f)) are the corresponding images for the oxide ridges. The oxide supports beneath the silicon membrane are achieved by removing holes from the square lattice to protect and mask the oxide from the HF wet etch.

span length increases. However, it is not until $85 \mu\text{m}$ span that the membrane actually makes contact with the silicon substrate. Also note that the numbers in the dimensions in the figure correspond to the crystal width. Following the HF oxide under cut, however, the actual span length of the silicon membrane is a little larger, approximately by $2 \mu\text{m}$ at each side.

This bowing and deflection of the membrane is not a big surprise as during the fabrication process of the SOI and the wafer bonding there is a lot of compressive stress in the 220 nm silicon layer. So when this layer is released from the oxide layer beneath, the membrane layer will start to bow due to this built in compressive stress. The membranes shown here all bow down but in some cases they can deflect up, for span lengths up to $40 \mu\text{m}$. As the membrane size is increased, the membrane starts to sag down and eventually totally collapses and makes contact with the silicon substrate for lengths above $80 \mu\text{m}$.

This sag and collapse of the membrane is not due to the internal compressive

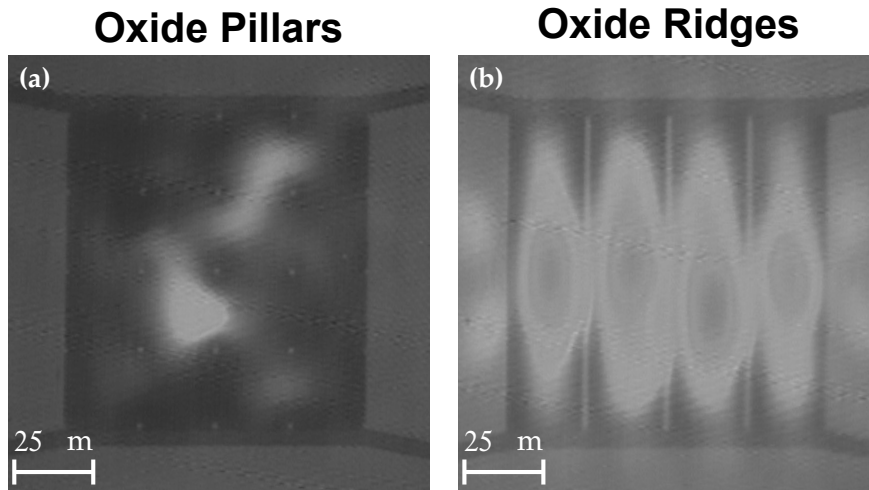


Figure 3.19: Infrared camera images of the membraned photonic crystal light emission with a bias applied. (a) Membrane supported with the oxide pillars and (b) the membrane supported with the oxide ridges. A much more uniform and even light emission distribution is visible from the oxide ridge system compared to the two emission hot spots in oxide pillar case.

stress but maybe due to a number of other factors. One possible reason is that the membrane is simply too large to support itself, coupled with the perforation of air holes, it becomes like a net and the membrane begins to sag under its own weight. Another possible reason for the collapse is the drying of the sample. By blowing drying the sample with nitrogen to remove the isopropyl alcohol (IPA), the capillary forces between the membrane and the substrate may force the membrane down and in contact with the substrate. Van der Waals forces then attract and keep the membrane bonded to the substrate. A possible solution would be to use a critical point dryer to remove the IPA or even to use vapour HF to under etch the membrane, removing the need for liquid altogether. However, having such large membranes is not necessarily a good thing. For large membranes other issues such as thermal expansion and heat distribution start to come in to play. A smaller area membrane allows for greater control of the structure when heated and provides a much more robust device.

This bowing and collapsing of the membrane for any span length greater than $10\ \mu\text{m}$ and $80\ \mu\text{m}$, respectively, poses the same problem as before, namely the loss of thermal energy to the oxide layer and the substrate. To solve this problem, a method to support such large membranes was developed using oxide ridges and pillars. The idea involves leaving narrow pieces of buried oxide layer behind to act as supports and prop up the large crystal membrane.

Experiments were carried out with both pillars of oxide and complete ridges of oxide across the crystal membrane. To protect the oxide beneath the crystal in the areas where the supports are needed holes were removed from the crystal lattice. This automatically acted as a mask for the oxide from the HF wet etch. Figure 3.18 shows examples of both implementations. The SEM images show where the lattice holes have been removed. The support structures are indicated by the dark spots (strips) in the images. The spacing between two neighbouring oxide pillars and oxide ridges was chosen to be $25\ \mu\text{m}$. This size span was chosen as it showed minimal bowing while still being a reasonably good size crystal

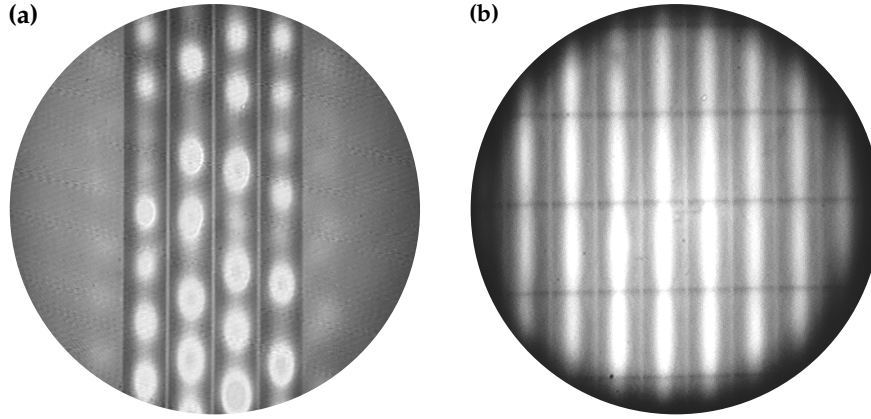


Figure 3.20: Infrared camera images of heated photonic crystal membranes with oxide ridge supports. (a) Does not contain any thermal expansion slots. Notice the uneven light emission profile, compared to (b) where thermal expansion slots (dark horizontal lines) are etched into the crystal here notice the very uniform light emission profile along the crystal.

width.

The oxide pillars are by far the most attractive option as they effect the lattice the least by removing fewer holes compared to the ridge option which removes an entire row of holes. However, as shown in the infrared camera images in Fig. 3.19, the membranes supported with oxide pillars heat unevenly, which is evident from the uneven light emission pattern, Fig. 3.19a. The reason for this uneven heat distribution maybe the fact that these membranes have too many degrees of freedom i.e. too many deflection options and membrane modes and so can too easily form hot spots in the crystal membrane. In comparison, the oxide ridge system behaves much better. Each strip of crystal expands into a single mode shape, deflecting either upwards or downwards along the crystal and producing a very uniform distribution of light emission, Fig. 3.19b.

One final issue with the photonic crystal membrane was encountered when the crystal was increased in size from $200 \times 200 \mu\text{m}$ to $500 \times 500 \mu\text{m}$. In the direction along the oxide ridges we noted a very non-uniform emission pattern and hotspots (Fig. 3.20a).

These high intensity emission points are due to the thermal expansion and thus the bowing of the crystal membrane as it heats up. The longer crystal membrane (greater than $200 \mu\text{m}$) has more degrees of freedom for expansion and forms patterns along the crystal lattice. These patterns then form places of high heat intensity and so we see the greatest amount of light emission from these areas. To relieve this thermally induced stress, slots were etched into the crystal, perpendicular to the oxide ridges, at $50 \mu\text{m}$ intervals. Fig. 3.20b shows an infrared camera image of the same crystal as (a) but this time including the thermal expansion slots etched along into crystal (dark horizontal lines). The crystal now expands very evenly when heated with a very even and stable light emission profile. The centre of the crystal is emitting more light than the areas next to the oxide ridges, which is expected as the centre will be much hotter than the cooler areas next to the oxide.

Finally, the complete fabricated thermal emission device is presented in Fig. 3.21. The optical image shows a top-down view of the device. There is a large

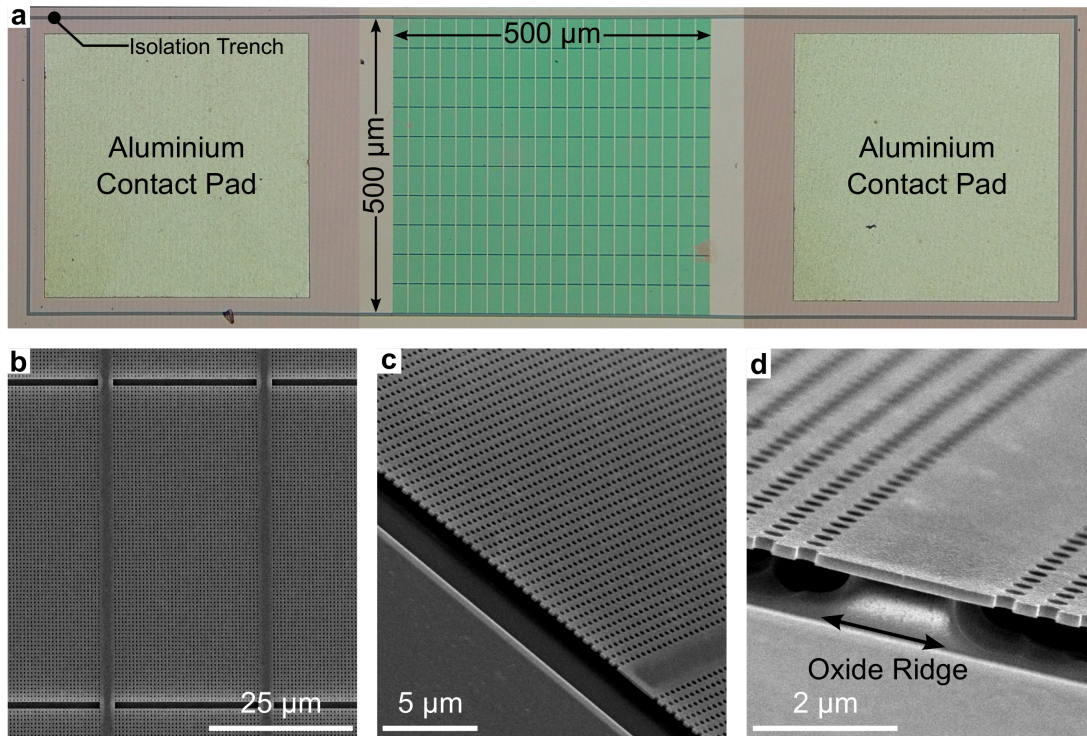


Figure 3.21: Optical and SEM images of the completely fabricated thermal emitter device. (a) Top-down view of the fabricated device. The image shows the deposited aluminium contact pads on both sides of the photonic crystal structure along with the isolation trench around the entire device. (b) SEM image of the photonic crystal structure, showing missing rows of holes in the vertical direction for the support ridges and the gaps in the horizontal direction to allow for thermal expansion of the crystal area. (c) SEM image showing the photonic crystal slab suspended above the substrate. (d) Zoomed-in SEM image showing the oxide support ridge beneath the photonic crystal slab [57].

area photonic crystal membrane in the centre of the image, of $500 \times 500 \mu\text{m}$ size, flanked by two aluminium contact pads. Figure 3.21b is an SEM image showing the missing rows of holes in the vertical direction along with the thermal expansion slots in the horizontal direction. Figure 3.21c is another SEM image showing the photonic crystal slab suspended above the silicon substrate. Finally, Fig. 3.21d is a close up SEM image of the oxide support ridge beneath the crystal slab.

3.5 Device Characterisation

This section contains both the passive characterisation of the photonic crystal slabs and the thermal emission from the devices. The reflection and emission properties are examined for the square hole array photonic crystal slab for a high doping density. A novel temperature estimation technique using the thermo-optic effect of silicon is implemented to calculate the operating temperature of the membrane.

3.5.1 Passive Characterisation - Reflection

Passive characterisation is performed by looking at the reflection spectrum of the photonic crystal structures and by comparing the results with those expected from simulation.

The design and properties of the reflection measurement setup are explained in detail in Section 2.6. In principle, the measurement system for the reflection and the emission characterisation is the same. For the case of the reflection measurement, the light source is external and is imaged directly onto the sample. The reflected light is collected and coupled into the spectrum analyser. For the thermal emission, the light source is the chip itself and the same light collection principles are applied. The light source is a broadband tungsten-halogen source with a wavelength range of 300 - 2600 nm.

The setup has two different methods of light illumination and collection. The first of these two modes is referred to as setup-A (Fig. 2.9). For reflection, the light source is focused down onto the sample and the reflected light is collected and coupled into the multimode fibre connected to the optical spectrum analyser (OSA). This reflected light is collected over a cone extended around the normal to the sample. The collected light from the sample is imaged with a 1:1 magnification ratio onto the facet of the multimode fibre. Therefore, the core size of the fibre and its numerical aperture (NA) determine the size of the cone of collected light and over what area the light is collected from. In our case, the multimode fibre has a core diameter of 105 μm and an NA of 0.22 corresponding to a collection cone with an angle of $\approx 12^\circ$ to normal.

The second method, setup-B (Fig. 2.10), introduces two extra lenses to the optical setup. This system illuminates the sample with near-plane waves of light. This is in contrast to setup-A where the sample is illuminated with focused wavefronts. For light collection, either reflection or emission, the system only images the plane wave emission or reflection from the sample onto the facet of the fibre. The nice feature of setup-B over setup-A is that the plane wave illumination provides a very accurate representation of the plane wave illumination in the COMSOL 3D simulations, therefore allowing a good comparison between the simulated behaviour and the real device behaviour. The disadvantage, however, is that the intensity is strongly reduced, by approximately a factor of 10.

Firstly, to calibrate the system and the OSA, the reflection spectrum of an unpatterned and undoped SOI sample is measured. The emission spectrum of the light source is taken into account prior to measuring. The SOI contains two layers, 220 nm silicon layer on top of a 2 μm oxide layer. The reflection spectrum, measured using both setup configurations, is shown in Fig. 3.22a and b. Due to the multilayer nature of the sample, the reflection spectrum is not a simple Fabry-Pérot response but a combination of the interference between the two layers. The simulated normal reflection response of the SOI is shown in both panels of Fig. 3.22 in red. The refractive index of silicon was taken from [70] to include the correct dispersion of silicon over the wavelength range. The refractive index of the oxide layer was taken as 1.47. Very good agreement between the measured and simulated spectrum is achieved for both measurement setups. The poor signal to noise ratio of setup-B compared to setup-A is obvious, due to the lower intensity. For the simulation, the thickness of the SOI was reduced to 215 nm to obtain the very good agreement. This thickness is within the wafer

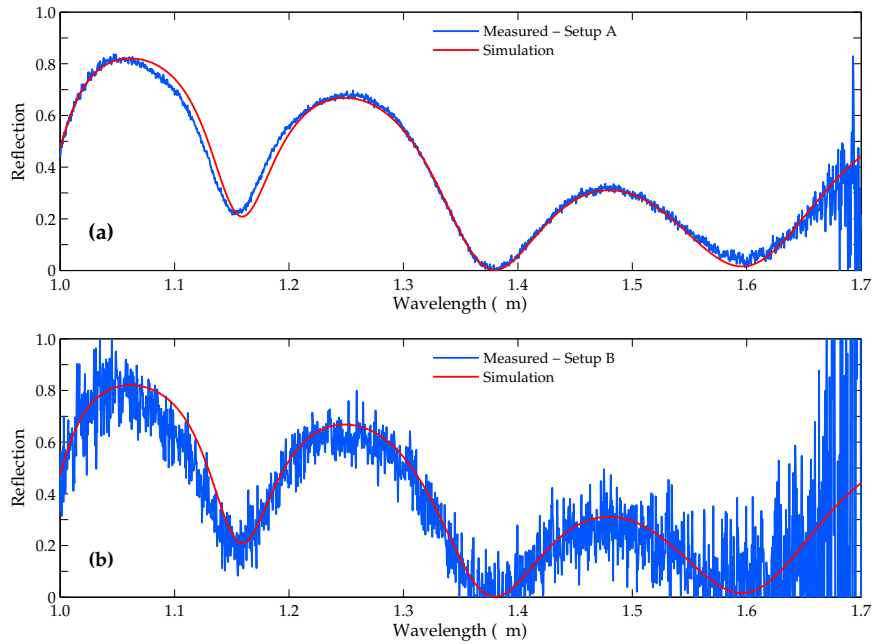


Figure 3.22: Reflection measurements from an unpatterned and undoped SOI sample. (a) Measured reflection spectrum using measurement setup-A and (b) using measurement setup-B. The simulated normal reflection spectrum in each panel is the same and is computed using the 3D COMSOL model using a silicon slab thickness of 215 nm.

manufacturers tolerance on the silicon device layer thickness of ± 5 nm.

Since a very good agreement between the simulated and measured reflection spectrum of the SOI sample was achieved, this became the reference measurement for the setup. Often it is suggested to use metallic mirrors for calibration and reference, however their performance over a broad wavelength range may not be flat and consistent. With the SOI sample we accurately know all the optical properties and thicknesses of the the three layers so it is a much better reference structure.

We examine the optical behaviour of the square hole array photonic crystal slab by measuring the reflection spectrum. To measure the reflection spectrum, ideally one would like to have the slab perfectly flat and completely suspended in air with no defects or rows of holes missing along the crystal. Then, using plane wave illumination, obtain the reflection spectrum from the structure. This method would allow one to compare the measured results with the expected reflection spectrum as shown in Fig. 3.5a. Unfortunately, getting a perfectly flat photonic crystal suspended completely in air is quite difficult. As shown previously, even to get a relatively large piece of photonic crystal suspended across a SOI wafer is not possible. To solve these issues and make the characterisation of the slabs possible, the crystal pattern was etched into the silicon layer and the oxide layer was not removed, hence measuring the reflection spectrum of the photonic crystal on top of an oxide layer. This way, all the parameters are known and the crystal is completely flat and without defects or missing rows of holes.

Figure 3.23a shows the measured reflection spectrum for the crystal on oxide, taken with setup-A measurement configuration and Fig. 3.23b is taken with setup-B configuration. The simulated spectrum in both plots is the same and is

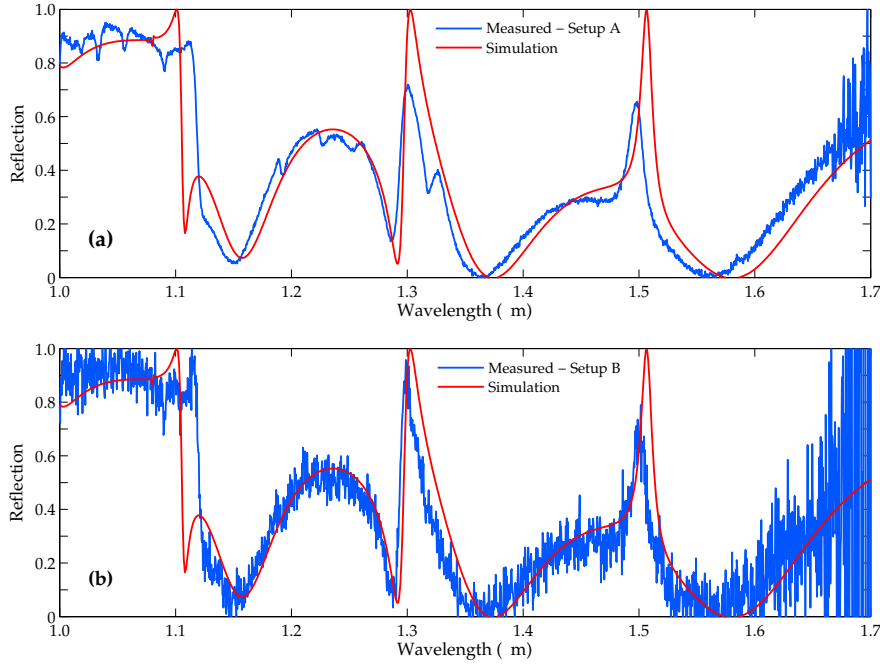


Figure 3.23: Reflection measurements for a square hole array undoped photonic crystal slab; period 600 nm, hole radius 120 nm, on 2 μm oxide layer on a silicon substrate. (a) Measured reflection spectrum using measurement setup-A and (b) using measurement setup-B. The simulated normal reflection spectrum in each panel is the same and is computed using the 3D COMSOL model using a silicon slab thickness of 215 nm.

the normal reflection spectrum for the square hole array photonic crystal slab, period 600 nm, hole radius 120 nm and silicon thickness 215 nm on 2 μm oxide on a substrate of silicon calculated using the 3D COMSOL model. Very good agreement between the measured and simulated reflection results is achieved for both measurement configurations. However, a closer examination of the measured reflection spectrum from setup-A reveals a second peak at 1.325 μm . This peak is not present in the spectrum measured with setup-B. This peak is present because the light in setup-A is collected over a cone of angles compared to the plane wave collection of setup-B. Therefore, setup-B is the more accurate method and achieves better agreement to the simulation results. The only disadvantage is that the signal level is much lower and the noise is a lot more prevalent in the measurements for setup-B.

The above characterisation is with a large crystal lattice and no rows of missing holes. Very good agreement with the expected reflection behaviour is achieved. However, looking at the real thermal emitter, what effect does removing 4 rows of holes every 25 μm have on the crystal performance? Maybe the real question is, how the 25 μm crystal span compare to the propagation distance of the photonic crystal resonances. To do full 3D simulations to examine and investigate these properties is very difficult, because the computational domain would be too large and is simply not feasible. In fact, it is easier to fabricate the structures and to measure the reflection spectrum. The experiment will not give us all the information about the propagation distances or the modes, but it will give us a very accurate indication of the effect it has on the reflection spectrum.

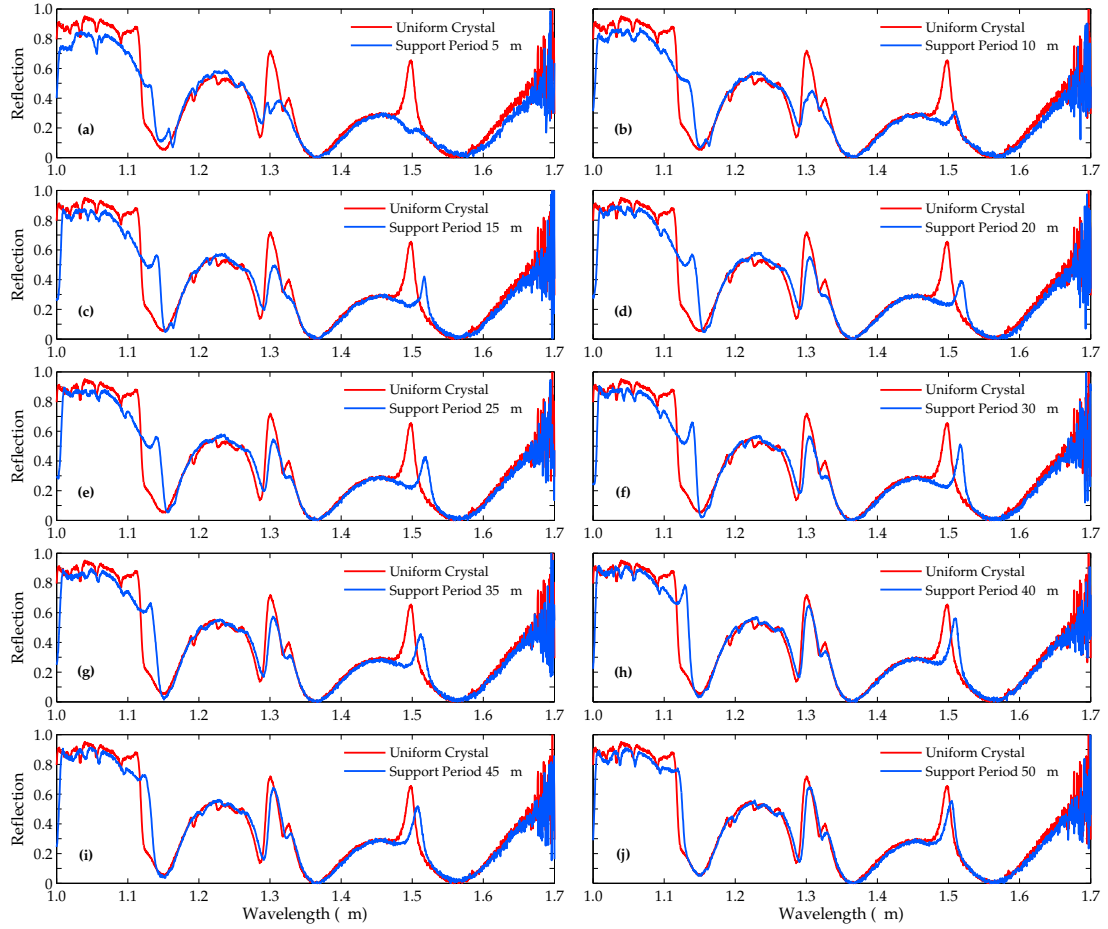


Figure 3.24: Examining the effect of four missing rows of holes on the square array photonic crystal slab. The period between the missing rows of holes is varied from 5 μm to 50 μm , (a) - (j) The reflection spectrum (measured using setup A), each for a different period, along with reflection spectrum for the uniform crystal are plotted.

A series of crystal patterns were fabricated on undoped SOI and the oxide was not removed. These lattices contained strips of four missing rows of holes. The period between these strips was varied from 5 μm up to 50 μm . For each the reflection spectrum was measured using setup-A (light collected over a cone of angles around the normal). The results are presented in Fig. 3.24 where each reflection spectrum is plotted along with the uniform crystal reflection spectrum (in red) of Fig. 3.23b.

The results show that there is indeed a deviation in the reflection spectrum for smaller lattice sizes. For the larger periods of 45 μm to 50 μm , the spectra almost completely agree with the uniform lattice. As the period between the missing rows of holes increases from 5 μm , the resonance peaks slowly take shape. The peak at 1.5 μm seems to be most affected by the missing rows of holes. Firstly the position of the peak has shifted to longer wavelengths suggesting the resonance sees the extra unpatterned silicon as this increases the effective index and so shifts the resonance to longer wavelengths. On the other hand, the resonance around 1.3 μm stays in the same location with no real wavelength shift.

3.5.2 Temperature Estimation Procedure

Determining the temperature of the photonic crystal membrane is more difficult than it appears at first sight. Conventional spectral methods cannot be used as these assume a blackbody emission spectrum, which the photonic crystal clearly doesn't emit. Alternatively, the fragile membrane cannot be touched by a thermocouple as this would potentially cause a short-circuit, also provide a cooling effect and certainly damage the crystal. Even the substrate temperature cannot be used, as it is not directly heated and it has very different thermal emission properties compared to the patterned photonic crystal membrane.

In order to obtain an accurate estimation of the temperature of the photonic crystal membrane, we exploited the thermo-optic effect of silicon. The thermo-optic effect is the change in a material's refractive index due to a change in temperature. The wavelength of the resonant modes of the photonic crystal slab depend on the effective index of the mode which is related to the refractive index of the doped silicon. Therefore, any change in the index of the silicon changes the effective index of the mode and thus the wavelength of resonant mode. This effect provides a very nice dependency between the temperature of the silicon and the wavelength of the resonance. However, this relationship does need to be calibrated and has a different dependency for each of the different resonant modes as the percentage overlap of the mode and the silicon is specific for each mode.

Due to the nature of the material (doped silicon) and the high temperatures that the membrane is expected to reach (≈ 1000 K) data on the temperature dependent refractive index for doped silicon is not available. This prevented the use of simulations to calibrate the temperature dependent wavelength position of each of the resonances. An alternative procedure is to take the device and heat it up on an external hot plate and measure the reflection spectrum at each increment of temperature change. This way the temperature of the entire device will be known and can be related to the spectral position of the resonance as the temperature changes.

To execute this procedure the sample was placed onto an external heater and the surface temperature of the chip was measured using a thermocouple attached to the surface placed away from the actual photonic crystal membrane. By placing the sample on a heater of high thermal mass, we can assume that the entire sample, including its surface, is in thermal equilibrium. The maximum surface temperature we were able to reach using the external heater was 740 K. We measured the reflection spectrum at each step of the heating process and tracked the spectral position of the reflection resonance at $\approx 1.2 \mu\text{m}$. The reflection spectra were measured using the setup-A configuration.

Figure 3.25 shows the measured reflection spectrum of the photonic crystal membrane (period 605 nm and hole radius 120 nm) for the resistively heated membrane with an applied bias range from 0 V to 78 V. The reflection measurement for the chip on the external heater is very similar and so is not included. As the photonic crystal membrane heats up, the refractive index of the silicon increases and so does the effective index of the resonance mode, so the mode shifts to longer wavelengths. Each of the reflection curves shows a strong reflection peak at $\approx 1.2 \mu\text{m}$. The peak is a superposition of multiple Lorentzian resonances i.e. there are two resonant peaks visible at the room temperature spectrum, 0

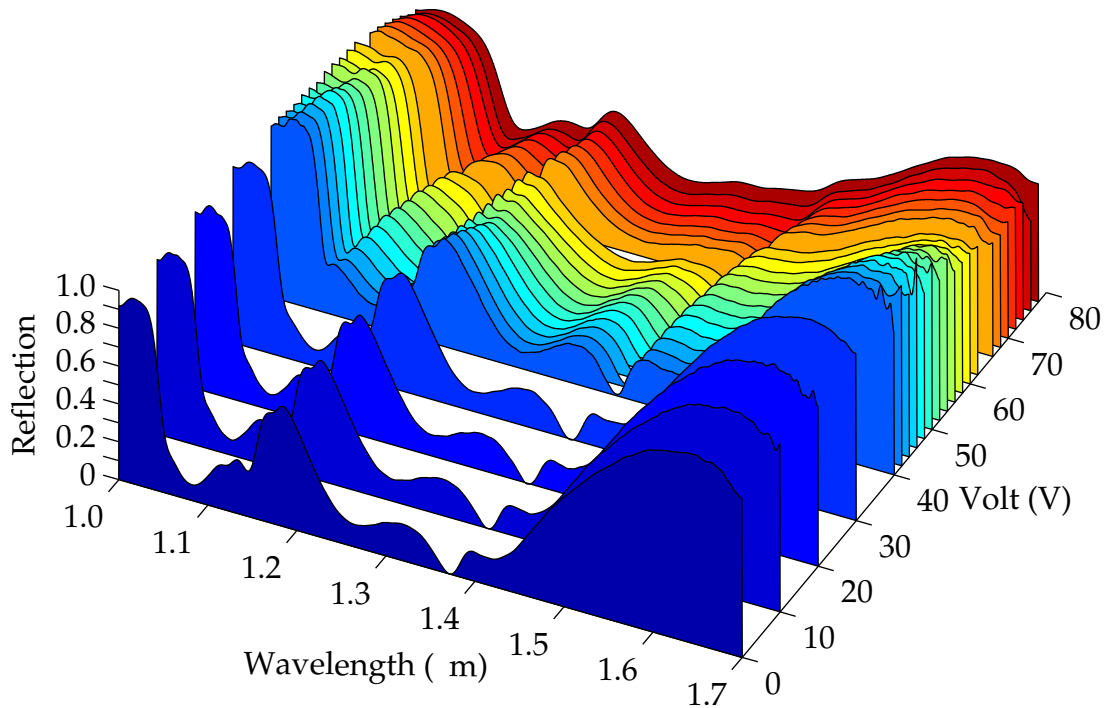


Figure 3.25: Measured reflection spectra of the photonic crystal membrane for a range of applied voltages: 0 V, 10 V, 20 V, 30 V, 40 V, 42 V, 44 V, 46 V, 48 V, 50 V, 52 V, 54 V, 56 V, 58 V, 60 V, 62 V, 66 V, 68 V, 70 V, 72 V, 74 V, 76 V, 78 V. The measurements were done using setup-A measurement configuration.

V, because the measurement spectra are taken using setup-A and so collect light from a cone of angles. Also these reflection spectra are a little different to the ones shown in Fig. 3.23 (completely uniform crystal slab on oxide) and Fig. 3.24e (crystal slab on oxide with four missing rows of holes every $25 \mu\text{m}$) because these measurements are made on the fabricated device, which is suspended with oxide ridge supports, so the reflection properties have changed somewhat.

Two Lorentzian curves are fitted to accurately track the position of the two resonant wavelengths at $1.2 \mu\text{m}$. The fit is shown in Fig. 3.26a, where a narrower wavelength range and a select number of reflection resonances are replotted from the 3D plot in Fig. 3.25. The two fits for the room temperature (0 V) and the high bias (76 V) spectra are shown. The same fitting procedure was applied to the reflection data measured with the device on the external heater, not included here. This method allows us to determine the relationship between the temperature of the photonic crystal membrane and the resonant reflection wavelength. The black solid line in Fig. 3.26b shows this relationship with a measured thermal coefficient of 0.07 nm/K for the short wavelength resonance (the magenta Lorentzian fit) for the sample measured on the external heater. Since we were unable to achieve surface temperatures higher than 740 K with the available heater, we extrapolated the line to higher temperatures as a very good linear fit to the data was achieved, the dotted segment of the plot in Fig. 3.26b.

Figure 3.26 shows the measured reflection spectrum for the photonic crystal slab resistively heated, to make the graph readable only seven of the applied

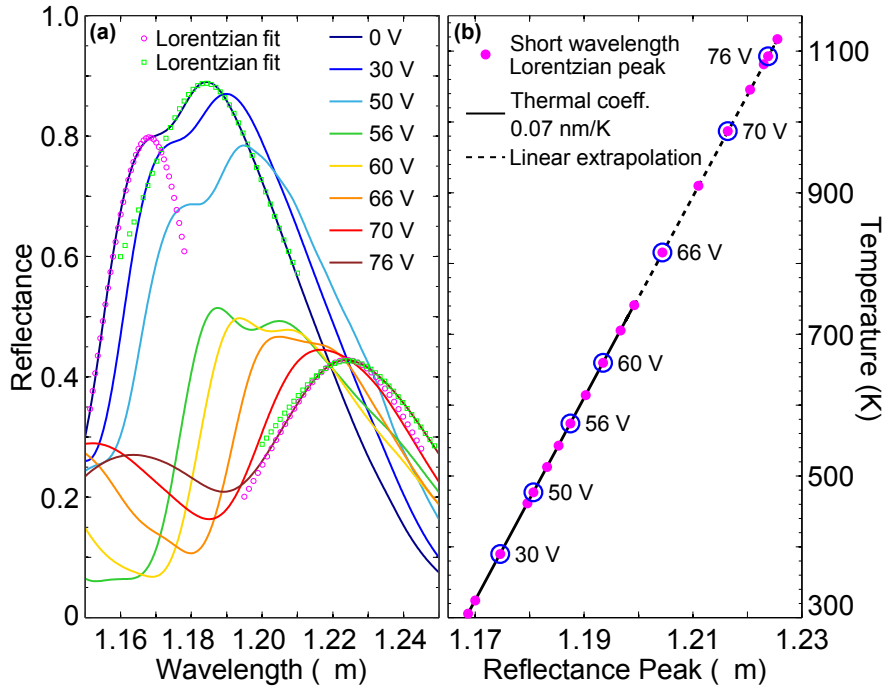


Figure 3.26: (a) Measured reflection spectrum for the resistively heated photonic crystal membrane, at room temperature (0 V) and for seven different applied voltages: 30 V, 50 V, 56 V, 60 V, 66 V, 70 V and 76 V. Two Lorentzians are fitted to the reflection resonances (shown here for the case of room temperature and one of the higher obtained temperature with a voltage of 76 V) in order to track the peak wavelength of the resonances accurately. (b) The black solid line represents the thermal coefficient (0.07 nm/K) for the photonic crystal membrane which was calculated using an external heater that reached a maximum surface temperature of 740 K. The linear extrapolation of this coefficient to higher temperatures is also shown. The solid magenta dots represent the peak position of the left hand (short wavelength) reflection resonance (indicated with the magenta Lorentzian fit in panel (a)) as the voltage increases, with the seven reflection resonances from panel (a) highlighted. Using the calculated (and extrapolated) thermal coefficient value, the applied voltage can be accurately mapped onto the corresponding temperature value [57].

voltages are plotted: 30 V, 50 V, 56 V, 60 V, 66 V, 70 V and 76 V. For the high voltage case of 76 V, the two Lorentzians almost completely overlap and hence have very similar resonant wavelengths. Figure 3.26b shows how the temperature for each reflection measurement is determined by using the peak of the reflection resonance for the short wavelength Lorentzian fit mapped onto the thermal coefficient line, with each of the reflection resonances shown in panel (a) individually marked in (b).

I would like to comment on the linear extrapolation in Fig. 3.26b, on its accuracy and is any deviation from the linear behaviour expected at the high temperatures. The linear fit to 740 K represents how the peak wavelength of the optical resonance in the slab shifts as the temperature increases. Up to 740 K the relation is very linear with an almost perfect linear fit achieved with the measured data, however, what happens beyond this?

The resonant wavelength of the mode depends on a number of things; the refractive index of the material (and also the surrounding medium), the thick-

ness of the slab, the period of the structure and the hole radius. If any of these parameters change the resonant wavelength will shift. By heating the structure all of these parameters will change but with varying magnitudes. The thermo-optic effect relates how a material's refractive index changes as the temperature changes. For intrinsic bulk silicon the refractive index shift from room temperature to 750 K is approximately linear [71]. No data is available for highly doped silicon material. The thermal expansion of the silicon material will increase the size of the structural parameters; slab thickness and period. The crystal lattice constant for intrinsic bulk silicon also increases approximately linearly with temperature to over a 1000 K [72].

Although these trends point to a linear response at high temperatures, it is difficult to isolate how each parameter change contributes to the resonant wavelength shift as the temperature increases and would require investigation via simulation. However, what I can say is that I expect the behaviour to be closely linear and that there will be, at least, no major deviations from a linear-like response. For there to be a significant deviation from linear behaviour there would need to be a significant change with one of the parameters where the mode profile and/or mode confinement changes suddenly, e.g. when the material softens or starts to melt. At this point the linear relationship will most certainly be gone. For the devices used here no such behaviour was observed, the material and the crystal structure did not degrade at the high temperatures. The optical response of the heated structure was re-examined at room temperature after heating and the resonance wavelength had not changed. Therefore, it is safe to say that the material and photonic crystal structure are stable at the high temperatures. Finally, I would like to point out that this technique is used as an estimation procedure and to give a ball park figure of the operating temperature.

3.5.3 Active Characterisation - Thermal Emission

Finally, I present the thermal emission spectra for the doped square hole array photonic crystal slab. For this device the doping concentration was $\approx 2.5 \times 10^{20} \text{ cm}^{-3}$; much larger than the optimal of $5 \times 10^{19} \text{ cm}^{-3}$. The reason behind such high doping was to ensure that the conductivity of the silicon layer was large enough to make sure it was possible to electrically pump and heat the device. Furthermore, the period of the thermal emitter presented here is slightly larger at 605 nm, with a hole radius of 120 nm.

Such high doping densities are beneficial for resistive heating as it allows an electric current to easily pass through the crystal structure. The disadvantage, however, is that it limits the Q-factor of the emission peak, high doping means more losses and ultimately a broader (low Q) resonance. To achieve a high Q thermal emitter, firstly, requires a high Q optical resonance. A simply way to increases the Q of the square hole array photonic crystal slab is to decrease the hole radius. Next, to optimally Q-match the absorption Q-factor to such a high optical Q requires a a much lower doping density. Then the high Q optical resonance coupled with the lower doping density will result in a high Q thermal emitter.

The problem now is how to efficiently heat the device, as resistively heating may no longer be a viable option. One option is to place high doped regions (or

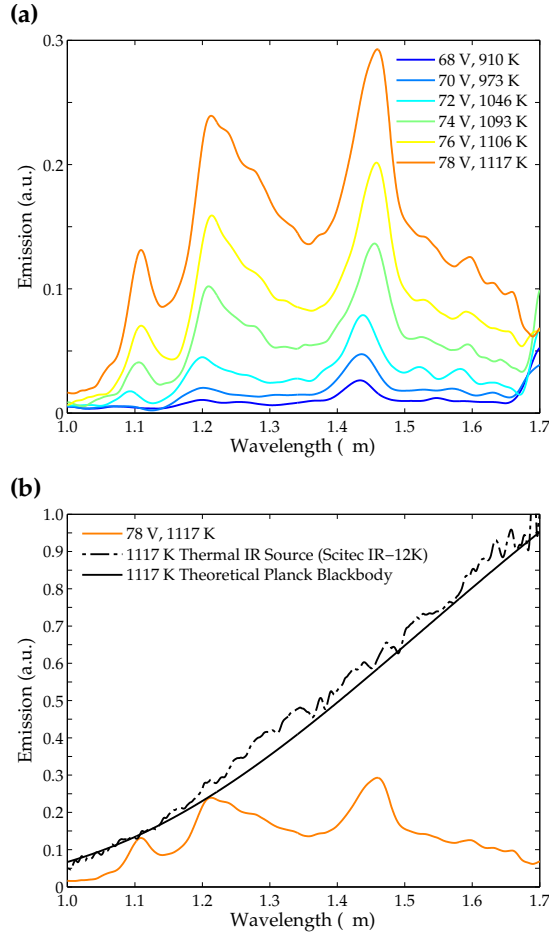


Figure 3.27: (a) Measured thermal emission spectra with a bias of 68 V, 70 V, 72 V, 74 V, 76 V and 78 V (b) Emission spectra for 1117 K replotted with a blackbody reference curve, which was obtained from an infrared thermal source (Scitec IR-12K) heated to 1117 K. The light emission was collected over an angle of $\approx 12^\circ$ around the normal for both devices. The theoretical Planck blackbody emission at 1117 K is also included.

pads) at either side of the low doped crystal pattern. The high doped pads can be resistively heated and through conduction, heat up the neighbouring crystal structure. Other alternatives might include placing metal heaters directly on top or underneath the crystal pattern.

Figure 3.27a shows six emission spectra with a bias of 68 V, 70 V, 72 V, 74 V, 76 V and 78 V. The estimated temperature of each spectrum is 910 K, 973 K, 1046 K, 1093 K, 1106 K, and 1117 K, respectively. Figure 3.27b compares the highest temperature emission spectrum (1117 K) to a blackbody curve at the same temperature. The black dashed curve is a measured blackbody radiation curve at ≈ 1117 K taken for reference from an infrared thermal source, while the solid black line indicates a theoretical Planck blackbody curve at 1117 K [1]. Each emission spectra clearly show three distinct emission peaks, matching the three peaks shown in the simulation results in Fig. 3.5. To analyse the spectral position of the three peaks we compare the spectrum at 1117 K to the square hole array photonic crystal slab band diagram Fig. 3.28. The band diagram is reduced as we are only interested in the area around the Γ -point i.e. vertical emission (Fig.

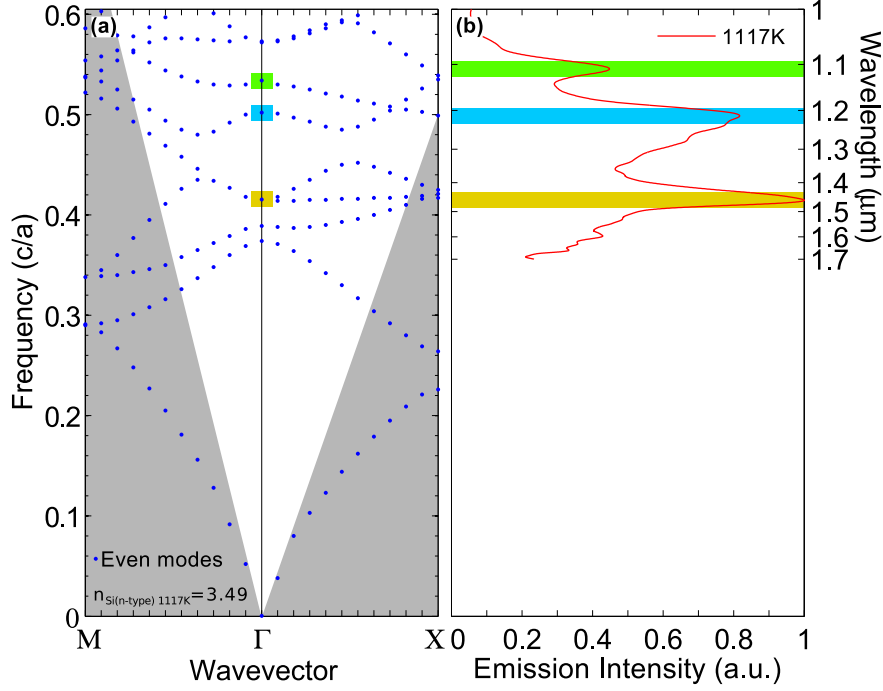


Figure 3.28: Comparison of the emission spectrum at 1117 K (b) to the corresponding band diagram (a). The band diagram takes into account the index reduction due to the high doping levels and also the index increase due to the high operating temperature. The spectrum on the right hand side is the same as that shown in Fig. 3.27a for 1117 K [57].

3.28a). This band diagram represents the highly doped photonic crystal structure at high temperature (1117 K); in contrast to the band diagram presented in Fig. 3.1, it takes both index reduction due to doping and index increase due to temperature into account. In fact, the reduction in refractive index due to doping ($\Delta n_{doped} = -0.19$, at $1.40 \mu\text{m}$) and the refractive index increase due to heating ($\Delta n_{thermal} = +0.18$, at $1.46 \mu\text{m}$, 1117 K) are of very similar magnitude. The three emission peaks (Fig. 3.28b) correlate excellently with the three band diagram resonances highlighted in Fig. 3.28b. The Q-factor of the peak at $1.46 \mu\text{m}$ is ≈ 18 , with a FWHM of $\approx 80 \text{ nm}$.

The blackbody reference curve was obtained with an infrared thermal source (Scitec IR-12K) heated to 1117 K. Comparing this curve with the three emission peaks at, $1.11 \mu\text{m}$, $1.21 \mu\text{m}$ and $1.46 \mu\text{m}$ at the same temperature of 1117 K, we note that the emissivity is 0.5 at the $1.46 \mu\text{m}$ resonance as expected, while the emissivity of the shorter wavelength peaks is almost 1. For such high doping density, all emission peaks should have an emissivity value of 0.5. I associate this apparent discrepancy with the temperature estimation technique. In actual fact, the operating temperature of the device may be higher than calculated. If this is the case, then the two lower wavelength peaks could potentially have an emissivity value ≈ 0.5 and the one at $1.46 \mu\text{m}$ would be much lower. Then it is possible to explain the low emissivity of the long wavelength peak with the results presented in Fig. 3.24. Where we see that for a photonic crystal span length of $25 \mu\text{m}$ long the wavelength resonance is distorted and therefore, could potentially alter emission properties at that wavelength with the two lower wavelength peaks remaining unchanged.

Consider the Stefan-Boltzmann law (Eq. 1.16), the temperature is proportional to the fourth root of the emitted power. In order to achieve an emissivity of 0.5 for the two shorter wavelength emission peaks (Fig. 3.27b), the power emitted by the corresponding blackbody emitter needs to double, i.e. the blackbody curve in Fig. 3.27b needs to effectively double in height. Approximately, to double the emission power the temperature needs to increase by a factor of 1.18. In this case that leads to a temperature increase of ≈ 200 K, which is feasible and therefore, may explain the discrepancy with the emissivity values.

Unfortunately, no other thermal emission devices were successfully fabricated. Due to the difficult nature of the fabrication process, there was no time remaining to explore and push the device further. One parameter to explore in the future is the doping concentration and examine the critical coupling point by varying the doping density. Furthermore, the asymmetric structure is certainly a promising design improvement that can be made which ultimately improves the efficiency of the device. Finally, a more accurate temperature calculation scheme is needed. I propose the use of the temperature dependence of the resistance as a possible alternative to the thermo-optic approach I presented here. The key advantage of this approach is the temperature calibration. The oxide layer beneath the crystal does not need to be removed to measure the electrical resistance of the doped silicon crystal. Therefore, a more accurate value of the crystal is obtained compared to the thermo-optic approach where the air gap beneath the crystal in the end leads to some uncertainty in the true temperature value.

Chapter 4

Metallic Thermal Emitter

4.1 Introduction

In this chapter, I present two different thermal emitter designs that are both based on metallic structures, with a strong emphasis on examining the angular emission properties of the devices.

The use of metals in the designing of thermal emitters is an obvious choice due to the intrinsic broadband absorbing properties they possess. Metals are naturally absorbing materials in the visible, however, in the near- and mid-infrared wavelength range they absorb relatively weakly [37]. By adding a photonic structure, the absorption can be resonantly enhanced. This absorption enhancement, which usually occurs over narrow wavelength ranges, results in an enhancement of the emission, according to Kirchhoff's law of thermal radiation [5].

There are many examples in the literature of thermal emission devices with metals as the primary emission material. These devices cover a wide range of emission wavelengths, from the visible to the mid-infrared. One of the most common metals used is tungsten [8, 10, 54, 73]. Tungsten is often chosen as the material to use in a selective thermal emitter because of its high thermal stability; it is well suited for temperatures up to 2000 K. Gold is also a very popular metal for thermal emission devices, especially in the visible and near-infrared wavelength range due to its suitable absorption properties [6, 11, 74]. The problem, of course, is its low melting point, which limits high temperature operation. The photonic structures fabricated using these materials range from simple one dimensional surface gratings [6, 10] to two dimensional arrays of holes [11, 75] and even up to fully metallic three dimensional structures [9, 54, 76].

Many of the experiments and analyses carried out in this range of devices are based on thermal emission in near-normal direction (perpendicular to the surface), because it is easy to measure. However, to fully understand and characterise the efficiency of the device, it is necessary to determine the emission of the photonic crystal into all angles i.e. to examine how the emissivity and wavelength changes away from normal. From Kirchhoff's law, we know that for a given structure, in thermal equilibrium, the emissivity is equal to the absorptivity. However, the absorption (A) is not only a function of wavelength but also a function of incident angle, $A(\lambda, \theta, \phi)$, where θ is the angle to normal and ϕ is the rotational, azimuthal angle. And of course the emission (E) will mirror this same behaviour, $E(\lambda, \theta, \phi, T)$, which includes its temperature dependence (T).

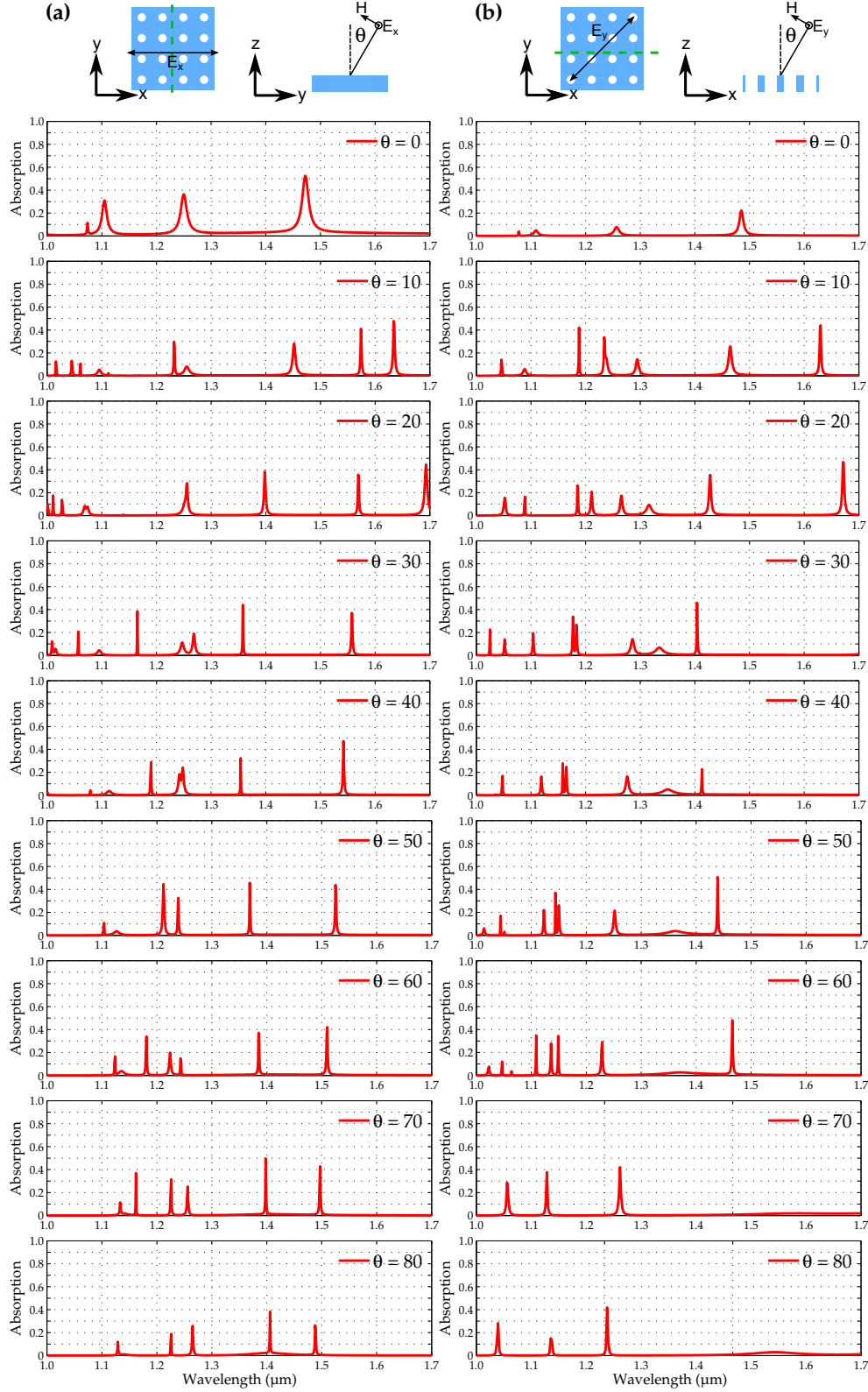


Figure 4.1: Absorption spectrum for the doped square hole array photonic crystal slab, as discussed in Chapter 3. Period 600 nm, hole radius 120 nm slab thickness is 220 nm and doping concentration of $5 \times 10^{19} \text{ cm}^{-3}$. Absorption simulated for normal to 80° incidence and both electric field polarisations; (a) (left-hand column) E_x and (b) (right-hand column) E_y . The two schematics at the top of each column indicate the electric polarisation and the angle of incidence θ relative to the slab.

One method to examine the angular dependence of the emission from a structure is to look at the corresponding band diagram. For the square hole array photonic crystal slab presented in Chapter 3, it is possible to see the angular behaviour of each of the resonances by examining the band diagram in Fig. 3.1e. The band diagram relates the resonant frequency to the in-plane wavevector. The in-plane wavevector is a function of incident angle, therefore, the band diagram gives information of how the resonance wavelength (frequency) changes with the incident angle.

The band diagram gives information about the resonances in the slab, but it gives no information about absorption. To further examine the angular emission properties, the absorption profile for off-normal incident light needs to be calculated. Figure 4.1a shows the simulation results of the absorption profile for the square hole array against incident angle. The computation was completed with the same COMSOL 3D model as in Chapter 3. The electric field was polarised along the row of holes and at 45° to the lattice (see insets for correct orientation) and the doping density of the slab was 5×10^{19} with a period of 600 nm and a hole radius of 120 nm. It is clear that the absorption, and thus the emission, wavelength changes with increasing angle from normal i.e. the resonant position changes and the other peaks are introduced. This means that the emission wavelength changes with angle. This angle dependence is not a very attractive quality, as it is desirable to have a monochromatic narrowband light source, with the same emission wavelength in all directions.

This angular dependence is a fundamental property of periodic structures. In this chapter, I present two structures that show a very strong angular **independence** on the resonant wavelength over a large solid angle range, almost to 90° . The first device is based on a metamaterial structure consisting of a patterned metal layer positioned above a metallic ground plane with a dielectric spacer (insulator) layer in between. This type of structure is primarily used as a very good absorber of incident radiation. The second device is based on a 1D binary biharmonic grating structure, constructed by combining two gratings with different periods, etched into a thick layer of gold.

4.2 Metal-Insulator-Metal

4.2.1 Introduction

Another range of materials that may have beneficial attributes for thermal emission control are metamaterials. Metamaterials are artificial electromagnetic materials usually composed of a periodic array of metallic elements, where the collective behaviour of these elements represents a material with properties which are difficult to attain with natural materials. Research into metamaterials has grown enormously since the 2000s focusing on many novel phenomena such as negative refractive index [77,78], invisibility cloaks [79] and perfect lenses [80,81].

One very interesting use of metamaterials has been their development as “perfect absorbers” and their ability to obtain near unity absorption at nearly any wavelength range [82–84]. One class of these perfect absorbers are known as metal-insulator-metal (MIM) resonators [85–88]. Some of these devices even claim omnidirectional absorption for any polarisation i.e. the same resonant ab-

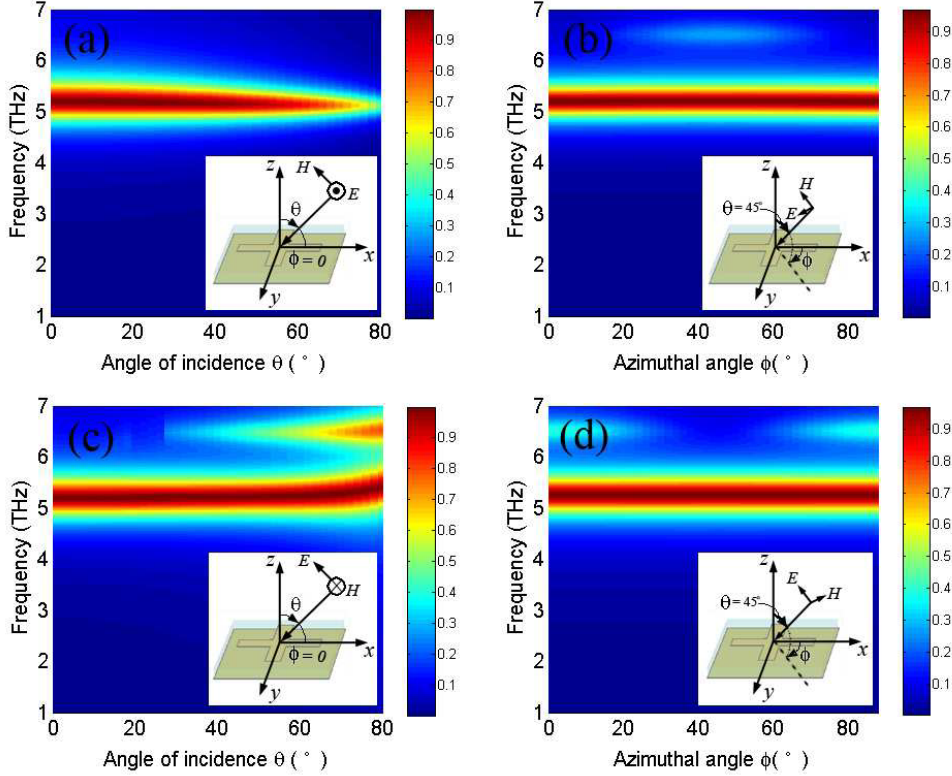


Figure 4.2: Absorption spectra as a function of incident angle θ for (a) TE polarization and (c) TM polarization, when azimuthal angle $\phi = 0$. The absorption spectra as a function of azimuthal angle ϕ for (b) TE polarization and (d) TM polarization, when incident angle $\theta = 45^\circ$. Reprinted with permission from [86].

sorption wavelength over a very large incident angle range [86,89]. Reference [86] shows an example of such a trilayer structure consisting of a thick gold ground plane, acting as semi-infinite mirror, a thin polymer layer separates it from an array of gold nano wires (or crosses). This structure is designed to operate in the THz frequency range, which is around 30 to 100 μm in wavelength. The structure has achieved nearly omnidirectional high absorption of light for both TE and TM polarisations. Figure 4.2 summaries some of the simulation results taken from the publication.

The unit cell of the MIM device is shown insets of Fig. 4.2. The cavity between the two metal layers acts as a resonator, this resonance increases the light interaction with the lossy gold and increases absorption. An incoming photon excites an electric dipole resonance in the nanowire. This localised surface plasmon mode is coupled to its own image in the ground plane, which oscillates 180° out of phase, this causes a resonant dip in the reflection spectrum. By tuning the separation distance between the two metal layers near perfect absorption at the resonance wavelength is achieved due to strong confinement within the MIM structure.

It is obvious how well the device in [86] works as an absorber over such a large incident angle range of up to 80 degrees off normal. This type of omnidirectional absorption behaviour is very attractive for a thermal emitter. In principle, a perfect absorber will radiate light as described by its absorptivity, therefore sharp, high Q-factor, angular intolerant resonances are possible with

very high emissivity. However, we ideally want the resonant wavelength to be within the near-infrared wavelength range, around $1.5 \mu\text{m}$. As the resonant wavelength is proportional to the length of the nanowire, it is possible to resize the structure and scale it down to operate in the near-infrared range.

To keep things simple, I only considered the gold nano wire (dipole) arrays and not the cross dipole structures. This allowed me to restrict the model to a single polarisation. Reference [86] used a gold dipole of $16 \mu\text{m}$ length, which yields a resonant wavelength of around $60 \mu\text{m}$. By rescaling the size, a dipole length in the range of 300-400 nm is required to achieve a resonant wavelength of around $1.5 \mu\text{m}$. The other parameters are tuned commensurately; the dipole width is reduced from $3 \mu\text{m}$ to 75 nm and the period of $22 \mu\text{m}$ down to 550 nm. The thickness of the metal dipoles is also reduced from 200 nm to 40 nm, as it is important to keep it thicker than the skin depth. The polymer spacer layer is not so easily scaled down. In the reference, a lossy polymer with an index of 1.87 is used. I replaced this with a flowable oxide (FOx 15) layer, with index around 1.47, therefore, the exact thickness required to achieve maximum absorption will require some tuning.

The proposed method of heating the device was to pass a current through the ground metal plane and then resistively heat it, and in turn heat up the entire structure. With this purpose in mind, the ground plane of gold was replaced with platinum. Platinum has a very high melting temperature around 2000 K and is therefore very suitable for this kind of application. The real components of the dielectric function for platinum and gold behave similarly in the near-infrared wavelength range, although the real part is more negative for gold than for platinum. The device performance should not be altered too much by this substitution.

Simulations were carried out to investigate how the combination of gold nanowires on a insulating layer of FOx, all on a platinum ground plane, behaved in the near-infrared wavelength range. The simulations were performed with a 3D COMSOL model. The model measured the reflection (R) of an incident plane wave on a single unit cell of the structure. Periodic boundary conditions flanked the unit cell on all sides, with PMLs placed on the top and bottom of the computational domain. Due to the ground plane being optically thick, i.e. no transmission, the absorption (A) of the structure can be calculated directly from the reflection spectrum, $A = 1 - R$. The optical properties of the gold were taken from [37] while the properties of platinum were obtained from [90] and the refractive index of the oxide layer assumed to be 1.47. The simulation results are presented in Fig. 4.3. Due to the large amount of computational resources required to compute the reflection for a 3D model, it was not feasible to do a large parameter sweep as that presented in [86], extracted and shown here in Fig. 4.2. However, since we expect the behaviour to be very similar, it is sufficient to look at a limited number of structure parameters and then examine the reflection for a range of incident angles and confirm that the performance is as expected.

The length of the nano wire is tuned from 280 nm to 360 nm, with the minimum in reflection at $\approx 1.5 \mu\text{m}$ for 320 nm (Fig. 4.3a). The thickness of the oxide spacer layer was optimised to increase the absorption to near unity (Fig. 4.3b), with a 60 nm thickness producing 100% absorption. Finally, with the parameters tuned and optimised for normal incidence, the incident angle was

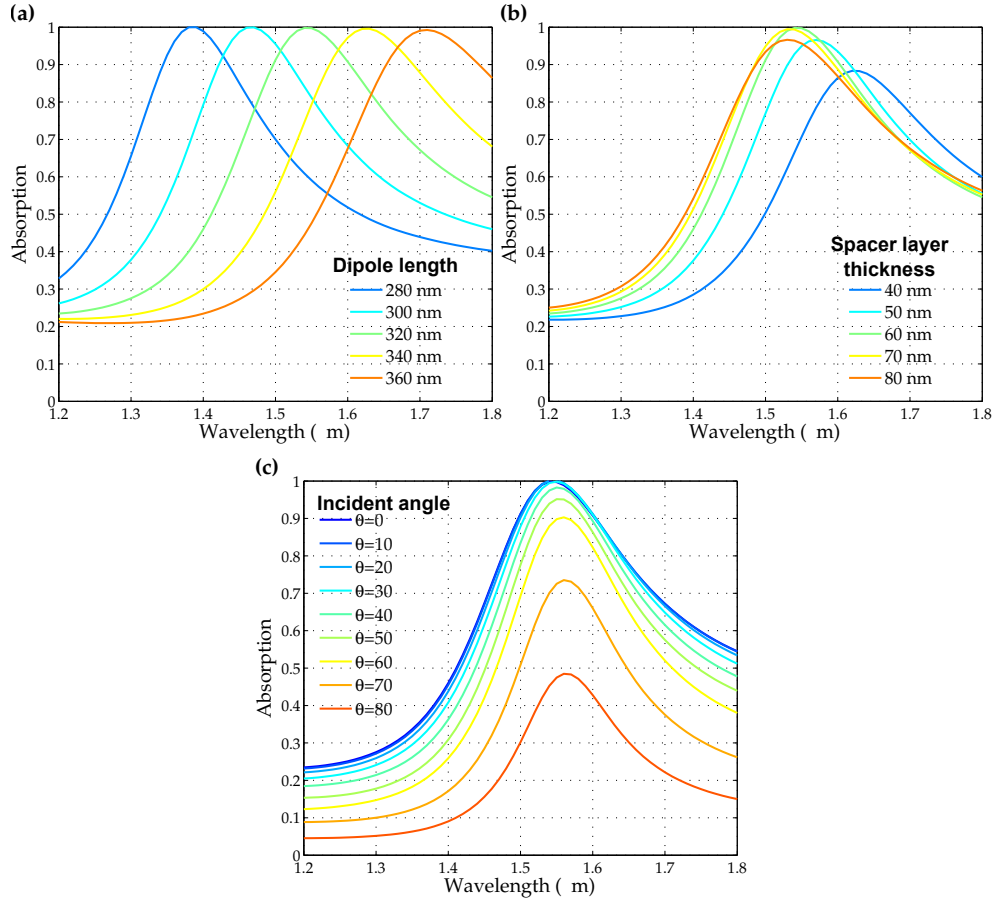


Figure 4.3: Simulated absorption spectra for the MIM structure of gold dipoles on a FOx insulator layer all on a platinum ground plane. The dipole width of 75 nm and thickness of 40 nm remains constant. (a) The dipole length is tuned from 280 nm to 340 nm, (b) the spacer layer thickness is tuned from 40 nm to 80 nm (for a dipole length of 320 nm) and (c) taking the optimal parameters; the dipole length of 320 nm and spacer layer thickness 60 nm, the incident angle (θ) is tuned from 0° to 80° . All for TE polarisation with the electric field parallel to the long side of the dipole.

changed in steps of 10° for the electric field polarisation along the length of the dipole, the results are shown in Fig. 4.3c. Overall, the behaviour is as expected and matches that of the THz omnidirectional absorber. One aspect to note is the width of the resonance. It has a rather large FWHM of approximately 200 nm which is very broad although it does show the angular insensitivity as expected.

4.2.2 Metal-Insulator-Metal Fabrication

The MIM structure consists of a number of fabrication steps; a general overview of the device fabrication is presented in Fig. 4.4. To begin, a thick layer of platinum is deposited on a glass substrate (Fig. 4.4a). To ensure the platinum layer adheres to the glass, a very thin (5 nm) layer of chrome is firstly deposited on the glass. Since the melting point of platinum, and chrome, is high (1768°C and 1907°C , respectively) an electron beam evaporator (Edwards Auto 306 FL 400) was required to perform the deposition.

As already mentioned, heating the structure will be achieved by passing a

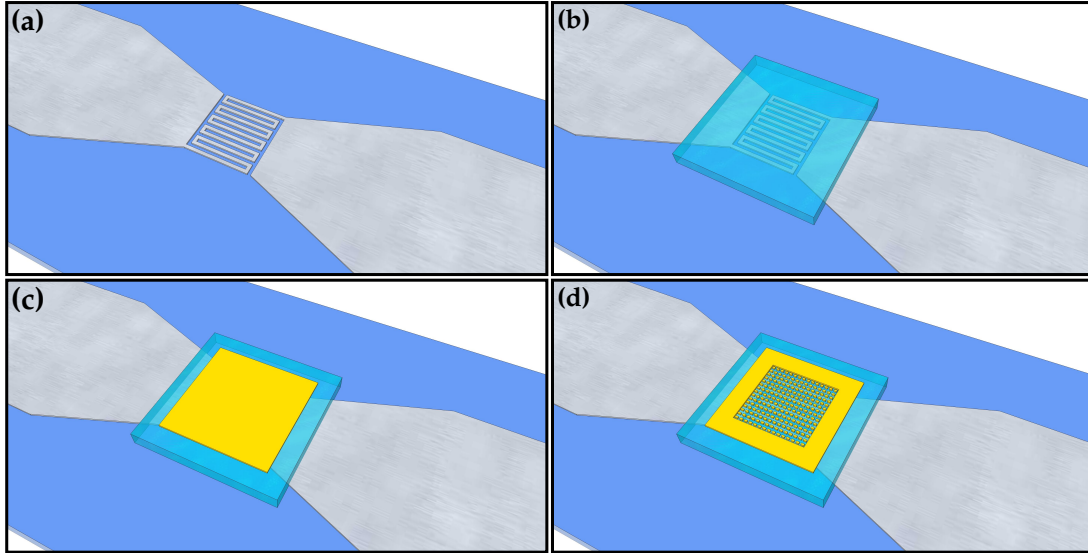


Figure 4.4: Diagrams illustrating the main steps in the fabrication of the MIM structure. (a) The platinum ground plane is deposited on a glass substrate, an isolation trench and heater pattern are dry etched using a RIE (Ar:SF₆, 3:1) into the platinum layer. A 5 nm chrome layer is first deposited to facilitate adhesion of the platinum layer to the glass. (b) A layer of FOx 15 (diluted with MIBK, 1:2) is spin-coated (5000 rpm, ≈60 nm) onto the sample. The region above the platinum heater is exposed using e-beam lithography. After development (TMAH), the written area (negative resist) remains. (c) Using the lift-off technique, a 40 nm layer of gold is deposited on top of the FOx layer. (d) Finally, the dipole pattern is etched into the gold layer using Ar as the etch gas in the RIE.

current through the ground plane. To improve the heating ability, the resistance of the area beneath the array of dipoles was increased by etching a “snake” like heater pattern into the platinum layer (Fig. 4.4a). The total area is $200 \times 200 \mu\text{m}$ and the width of the heater was reduced to $2 \mu\text{m}$. An isolation trench around the device and the region where the electrical needle probes will make contact, was also etched to improve the electrical isolation.

The dry etching of the platinum, and gold layers, was not trivial and proved quite difficult. To begin, the snake heater pattern and isolation trench was defined using electron beam (e-beam) lithography and ZEP 520A resist. The standard ZEP recipe was used with a spin speed of 3700 rpm. However, it was not possible to bake at the usual $180 \text{ }^\circ\text{C}$, as the ZEP resist ‘bubbled’ off the metal layer due to what appeared to be wetting issues. To solve this problem, the resist was baked at the lower temperature of $140 \text{ }^\circ\text{C}$ for twice as long i.e. 20 minutes. The exposed resist was developed in xylene at $23 \text{ }^\circ\text{C}$ for 45 seconds.

The etching of metals, e.g. platinum and gold, is usually carried out by physical sputtering. In our system, Ar gas is used in a reactive ion etcher (RIE). The Ar ions literally mill the material and etch it away. The ZEP resist usually withstands this mechanical etching process very well. For platinum, however, the etch rate is very low, even at high powers and pressures, with basically no etching occurring at all. To increase the etch rate, research in the literature suggests that the etching of platinum is enhanced by including a chemical etching component alongside the physical one [91,92]. With the addition of halogen-based radicals

(either fluorine or chlorine) to the etch plasma, platinum fluoride (or chloride) compounds are formed. These compounds, especially the platinum fluorides, are known to be very unstable and highly volatile and decompose and desorb from the surface readily.

The addition of fluorine ions to the Ar gas mixture was achieved by adding SF₆ gas into the process. The ratio of the two gases (Ar:SF₆) required some tuning. Using a 1:1 ratio, the chemical component was much too strong and it completely etched away all of the ZEP resist mask. As with all RIE etching processes, a balance needs to be struck between the chemical (isotropic) etching component and the physical (anisotropic) etching. A ratio of 3:1 proved to be a good gas mixture, with the resist comfortably surviving the process and a platinum etch rate of 20 nm/min was achieved.

After the etching of the platinum, the next step is the spacer layer of FOx. To achieve the required thickness of the insulating layer of ≈ 60 nm, the FOx 15 was diluted with methyl isobutyl ketone (MIBK), 1:2, spun at 5000 rpm and baked at 180 °C for 5 minutes. To avoid the electrical contact area being insulated by this layer of FOx, the region above the platinum heater, and some of the surrounding area, was exposed using the e-beam. Since FOx is a negative resist the area written will remain after the resist is developed in tetramethylammonium hydroxide (TMAH), for 1 minute. Figure 4.4b illustrates the pad of FOx directly over the platinum heater.

The final step is the fabrication of the gold dipoles on top of the FOx layer. I firstly deposited a 40 nm thick, uniform layer of gold on top of the FOx pad using the lift-off process (Fig. 4.4c). The lift-off procedure has already been explained in detail in Chapter 2 with an example of Al contact pad deposition given in Chapter 3. The process uses two different PMMA e-beam resists to provide an undercut after exposure and development. After the metal deposition, this ensures a clean break between the gold layer on the FOx and the gold layer on the resist. By only depositing gold on the FOx layer, again, the platinum electrical contact area is protected.

To develop the gold etching recipe, I began by looking at etching simple linear ridges of gold (i.e. gratings) before focusing on the smaller dipole pattern. As the final dipole pattern will have feature sizes in the range of 150 to 400 nm, the e-beam resist ZEP was chosen for its high resolution properties. A layer of the resist was spin coated, at 3700 rpm (≈ 400 nm, baked at 140 °C for 20 minutes), onto a thick layer of gold already deposited on a blank silicon substrate for testing. A grating pattern was exposed using the e-beam system with a period of 300 nm and an exposed trench width of 100 nm. Figure 4.5a shows a SEM image of this grating pattern in the resist layer after exposure and development in xylene (at 23 °C) for 45 seconds. All of the exposed resist down to the gold layer, which has a slightly grainy texture, has been removed.

RIE was used to transfer the grating pattern into the gold layer beneath using an Ar-only plasma etch. This type of etching plasma is a purely physical process with the Ar ions bombarding the surface of the gold and physically milling it. Figure 4.5b shows a SEM image of the resist and the gold pattern directly after etching. The resist withstands the physical etching very well and the etch rate of the gold is reasonable at 6 nm/min, here etching for 9 minutes. However, after the removal of the resist in the solvent 1165 (at 60 °C for 40 minutes) it became

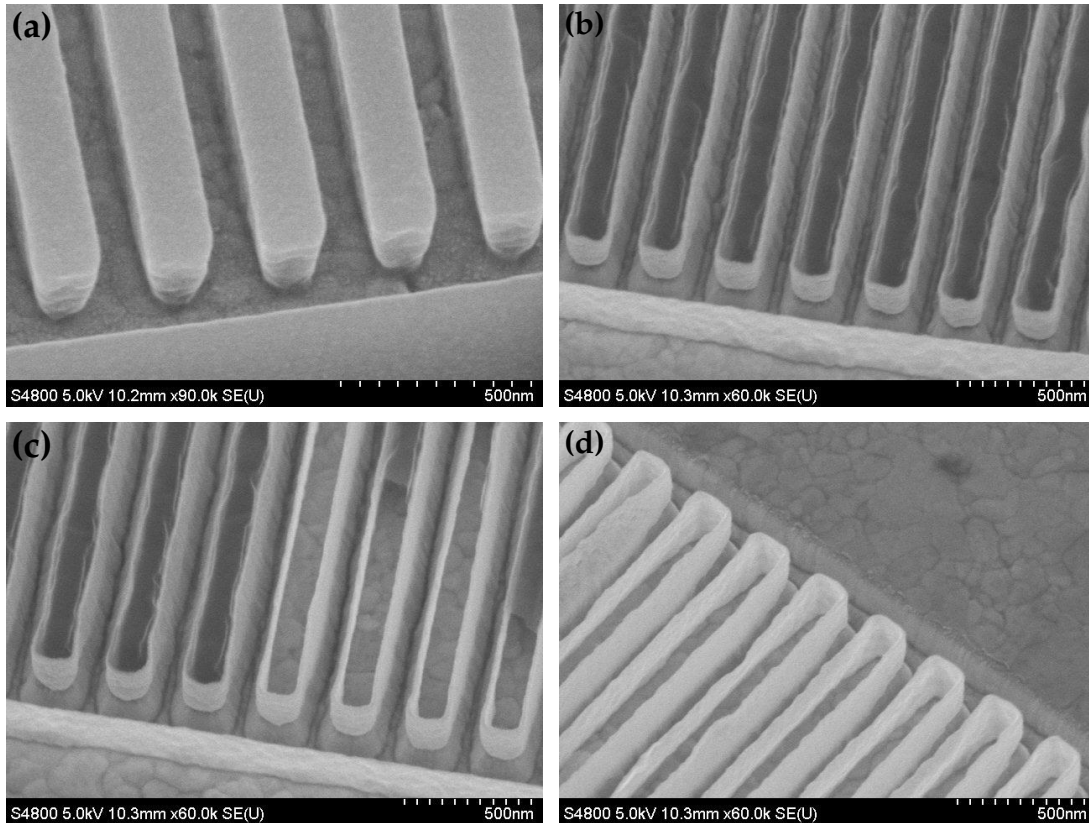


Figure 4.5: SEM images showing various steps of etching gold gratings. (a) The e-beam resist (ZEP) on top of a layer of gold, after the resist has been exposed and developed. The grainy pattern of the gold is visible between the ridges of the resist. (b) Directly after etching in the RIE with Ar gas. The resist is visible on top of the gold ridges. (c) Partial removal of the e-beam resist. Here the redeposited gold on the sides of the resist is visible. (d) After complete removal of the resist, the tall thin side walls of redeposited gold are clearly visible.

obvious that the etching process was not as clean as expected. Tall thin walls of what appears to be redeposited gold remain behind (Fig. 4.5c). These thin walls of redeposited gold are formed around the resist during the etching and stand on top of the etched grating, see the SEM image Fig. 4.5d. The etching of the grating underneath looks good, the side walls are smooth although they do appear to have a slight taper, as expected with an anisotropic physical etching process.

In the literature, this redeposition of etch debris is a known issue for the dry etching of gold. A gas composition of CF_4 (carbon tetrafluoride) + CCl_4 (carbon tetrachloride) [93] or CF_4 + CCl_2F_2 (dichlorodifluoromethane) + O_2 [94] are recommended to prevent redeposition and to increase the etch rate. The addition of chlorine radicals plays the same role as the fluorine for the platinum, as they bind with the gold to form gold chlorides which desorb from the surface and reduce the redeposition. Unfortunately, we did not have access to chlorine gas or any of its compounds, so were unable to improve on the etch quality. Attempts to remove the thin side walls were carried out using O_2 plasma etch, but ended up damaging the grating structure as well. I tried high power ultrasonic agitation in acetone to see if the structures would be broken off but again, this was not

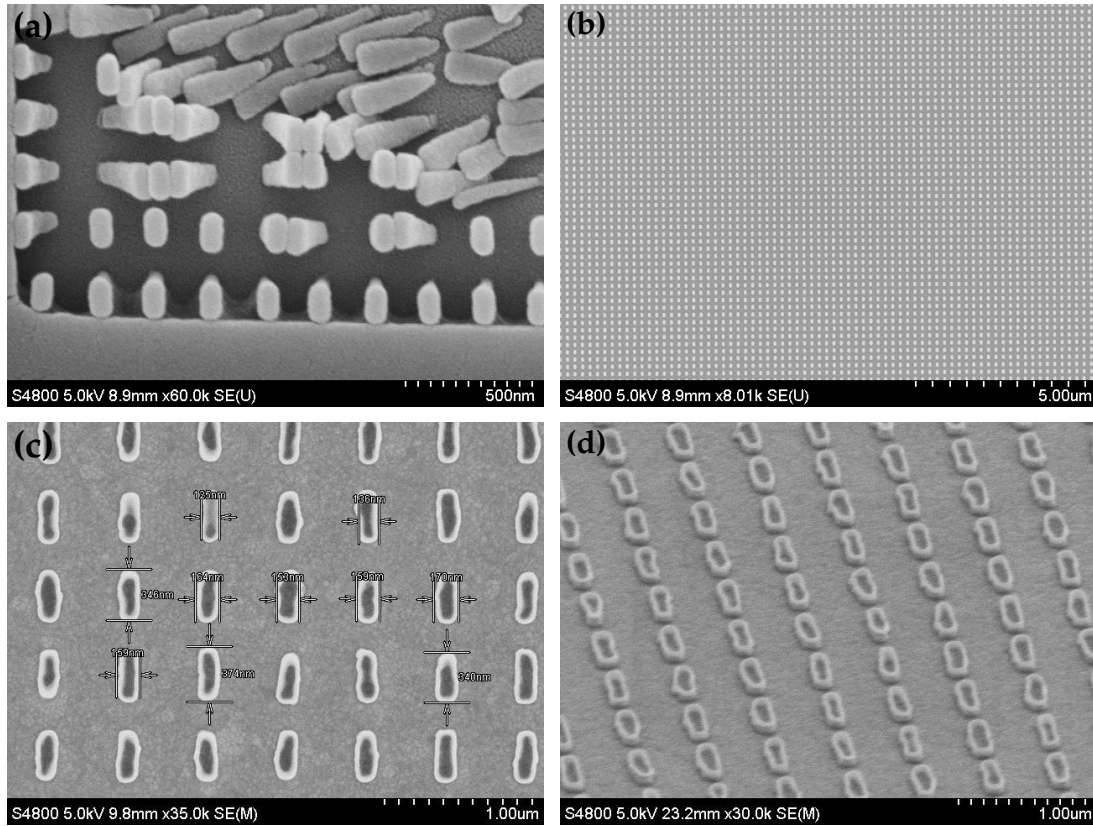


Figure 4.6: SEM images of the dipole pattern in the resist and gold layers. (a) Top view of array of dipoles written in a layer of e-beam resist (ZEP) ≈ 400 nm thick. The thin base of the dipole pillars is obvious this is because of the forward scattering of the electrons as they propagate through the thick resist. The thin base is unable to support the tall pillars. (b) By reducing the ZEP thickness down to 180 nm a very robust array of dipole patterns were written. (c) The dipole pattern is transferred into the gold substrate. The average shape of the dipole is reasonably good, with an average length of 340 nm and width of 140 nm. (d) A tilted view of the same dipole pattern as in (c). Here it is possible to see the redeposited side walls on top of the gold dipoles, as in Fig. 4.5d.

successful. Therefore, we decided to proceed with the etch recipe we had as it did give good metal structures, and see what effect, if any, these extra thin side walls of gold would have on the performance of the dipole structure.

In order to pattern the dipoles into the 40 nm layer of gold, we use ZEP resist, mainly for its excellent etch resistance. Please note, however, that ZEP is a positive e-beam resist, so it is the area around the dipole and not the dipole itself that is exposed. Using the standard thickness of 400 nm, the resist mask was prone to falling over and collapsing. The base of each of the resist pillars was too narrow to support the tall dipole, see Fig. 4.6a.

Reducing the thickness of the resist layer will improve the stability of the dipoles. The thinner the resist, the less e-beam forward scattering and therefore the less undercut of the dipoles. The ZEP was diluted with anisole, ratio 1:1, and spun at 5000 rpm, giving a thickness of 180 nm, with the same baking procedure; 140 °C for 20 minutes. After exposure and development in xylene for 45 seconds, the array of dipoles in the resist were very stable and much more robust, see Fig.

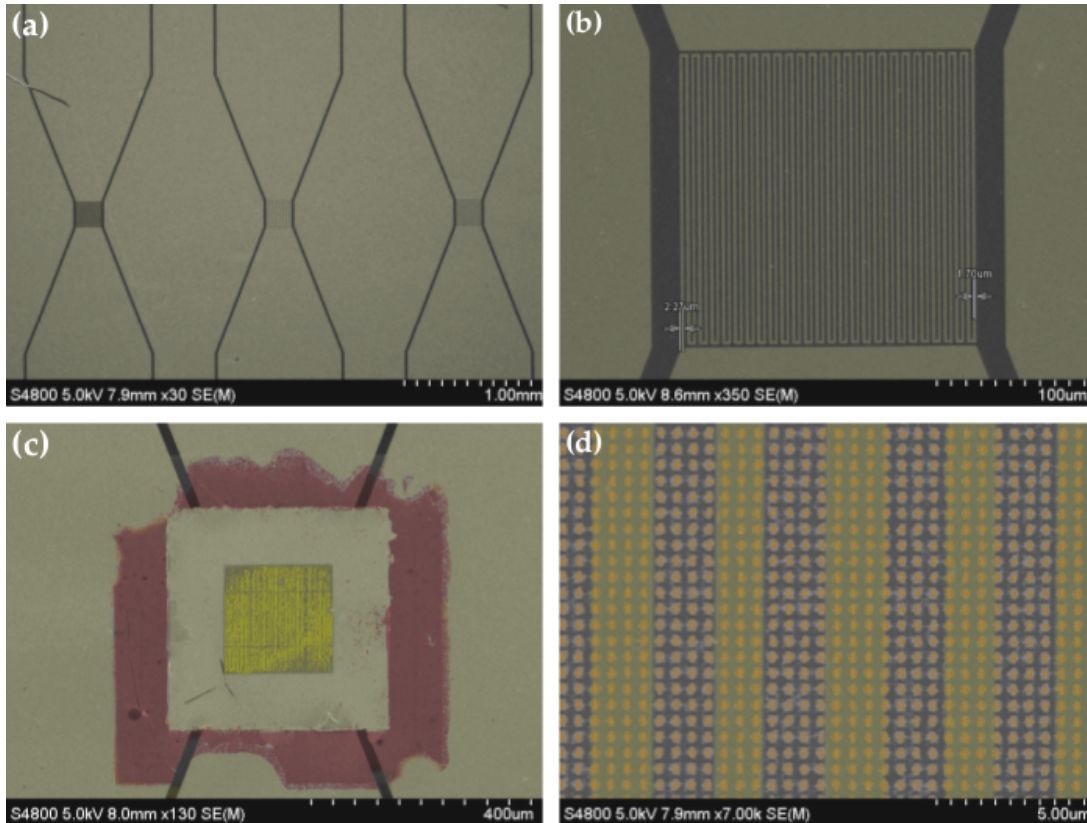


Figure 4.7: SEM images (with false colouring) of the complete final MIM device. (a) A view of the platinum layer with three heater patterns surrounded with isolation trenches. (b) A zoomed in image of one of the platinum heater patterns. (c) The complete fabricated structure. The FOx layer is coloured in red with the gold dipole array coloured in yellow in the centre. (d) A zoomed in image of the gold dipole array. The stripes in the background are the platinum ground plane heater beneath the FOx layer.

4.6b.

With the dipole etch mask now stable, the gold was etched using RIE with Ar as the plasma etch gas. The etched dipoles are shown in the SEM image in Fig. 4.6c. The overall average shape is good, the length of the dipoles are about 350 nm (target 320 nm), the width is about 140 nm, wider than the target of 75 nm. The increased width dimension has little effect on the overall performance, as it is the length of the dipole that is critical for obtaining the correct resonant wavelength. The dipoles do suffer from the extra side wall redepositon, however, which is visible after the removal of the resist layer (Fig. 4.6d).

A quick summary of the fabrication procedure and SEM images of the fabricated device are presented (with false colouring) in Fig. 4.7; (1) A thick platinum layer is deposited on a glass substrate. Isolation trenches and a “snake” heater pattern are etched into the platinum layer using ZEP as the etch mask and Ar and SF₆ as the etch gases, see Fig. 4.7a,b. (2) A layer of FOx 15 (diluted with MIBK) is spin-coated onto the sample and the area above the platinum heater region is exposed using e-beam lithography. After development in TMAH, a patch of FOx remains above the platinum heater, as indicated by the red-coloured region in Fig. 4.7c. (3) A layer of gold is deposited on top of the FOx layer using

the lift-off process, Fig. 4.7c. (4) Finally, the dipole pattern is written into a thin layer of ZEP (diluted with ansiole) and transferred to the gold pad via RIE dry etching using Ar gas, see Fig. 4.7d. In Fig. 4.7d, the stripe pattern beneath the array of gold dipoles is the platinum ground plane heater. Overall, the condition of the fabricated structure is good, with the only real issue being the quality of the gold dipoles, the etching being a little rough and the redeposited side walls not being ideal.

Unfortunately, these devices did not perform as expected. The platinum heaters did not heat up when a voltage was applied across the device. Different heater patterns were fabricated with different heater arm widths. The resistance of each pattern was designed to be different, yet, when the resistance was measured it did not change at all. Through further investigation it was also discovered that each device was not electrically isolated from the other devices on the same chip. We noticed that while the complete layer of platinum was etched through the etching of the adhesion layer of chrome was not considered. It was assumed that this thin (5 nm) layer would etch away easily. In reality, the opposite was true, and we realised that very thin layers of chrome are notoriously difficult to etch away completely. Therefore, even after the etching of the isolation trench and the heater, the current could still escape through the thin chrome layer and therefore it was impossible to heat the device.

No more of these devices were fabricated and not just because of the issues with the chrome dry etching. A very obvious solution to the problem is to use lift-off technique to deposit the chrome and platinum layers, thereby ensuring complete electrical isolation. The main issue, however, were the optical properties of the fabricated devices; the fabricated structure showed no optical resonances when measured in reflection. This can be explained by the poor quality of the gold dipoles and the redeposited walls of gold. This poor quality coupled with the fact that the emission resonance will be very broad anyway, led to the decision that no further devices were fabricated and this type of resonant structure was no longer pursued.

4.3 Binary Biharmonic Gold Grating

4.3.1 Introduction

The second metallic structure that I studied and designed as a potential thermal emission device is a binary biharmonic grating structure. This grating is not a standard single period structure but, it is constructed by adding two grating profiles (biharmonic), with different periods, together. The resonant behaviour of the structure is based on the excitation of surface plasmon resonances. By varying the relative amplitude and phase of the two gratings, very interesting resonant behaviour is observed, e.g. a very wide band gap in the frequency range of the excited surface plasmon polaritons (SPPs).

This very wide band gap produces a flat resonance response in the SPP dispersion curve [95]. Incident electromagnetic radiation will excite surface plasmons and lead to an enhancement of the absorption over a range of incident angles for the same narrow wavelength range. According to Kirchhoff's law, the emissivity of a surface is equal to its absorptivity, therefore, the reverse process is also

possible; thermally excited surface plasmons couple with free space electromagnetic waves, with the same narrow emission wavelength spectrum over a range of emission angles.

This section begins with some background and fundamentals of surface plasmons, before progressing on to designing the binary biharmonic structure. The design begins by looking at purely sinusoidal profile gratings before converting it to a two level binary structure. The first grating generates the band gap and is called the Bragg grating. The period of this grating is half of the resonant wavelength. Bragg scattering occurs where the forward and backward travelling waves interfere and produce standing waves, thereby opening up an energy band gap which is similar from a Bragg mirror. Two standing waves are created, generating an energy band gap where surface plasmon polariton with frequencies within this range are no longer allowed to propagate along the surface.

These standing and propagating waves are all bound to the surface i.e. their momentum is greater than that of the same frequency free space photon. To couple them out, a surface corrugation is required which can provide additional momentum. This is achieved by adding a second grating, called a coupler grating. The period of this grating is equal to the resonant wavelength and provides the momentum needed to get the Bragg resonances out and coupled to free space photons.

The simulations of the optical properties of the metallic gratings, i.e. the reflection (R), have been performed using the rigorous coupled-wave analysis (RCWA). Since the structure is etched into bulk, there is no transmission and the absorption (A) is calculated from $A=1 - R$.

Tuning the ratio of the amplitudes of the two gratings allows tuning of the band gap width. By making the band gap width wider, the dispersion bands flatten even more. However, this method has its limitations. The band gap width is also dependant on the grating groove depth and by increasing the grating depth, very large band gaps are obtained with very flat dispersion curves and little change in the resonant frequency up to angles of 90° each side of normal.

4.3.2 Fundamentals of Surface Plasmon Polaritons

Surface plasmons polaritons can be broadly classified into two types: localised and propagating plasmon polaritons. Localised plasmon polaritons occur as a result of the interaction between light and metallic particles and they form the basis for the resonances of the metal-insulator-metal structure discussed in the previous section. Here we are interested in propagating surface plasmon polaritons (SPPs).

SPPs are electromagnetic excitations at the interface of a metal (conductor) and a dielectric. Similar to light guided in a dielectric waveguide, the light is confined to the interface and propagates until it is totally absorbed by the metal or scatters from the surface. The field has an intensity maximum at the interface and decays exponentially into the metal and dielectric regions. The wave involves charge motion (electrons) in the metal (“surface plasmon”) and electromagnetic waves in the dielectric (“polariton”) [96].

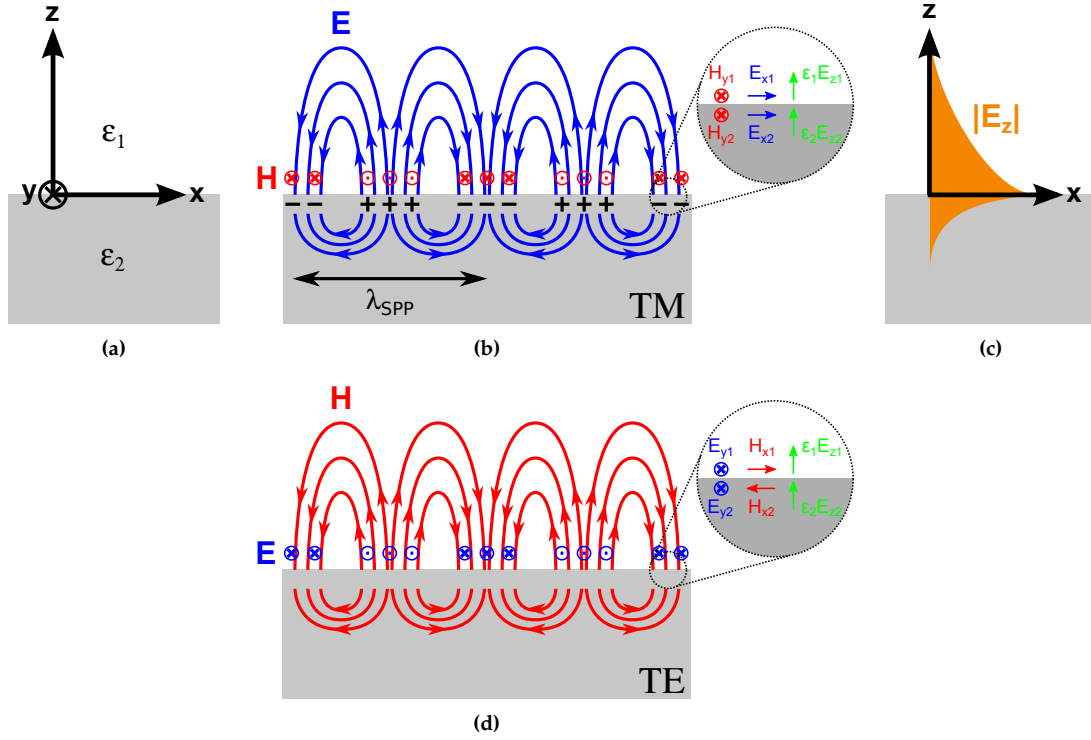


Figure 4.8: (a) Coordinate system for the two material system; ϵ_1 is the dielectric and ϵ_2 is the metal layer. (b) Electric and magnetic field distributions for a propagating SPP along a metal surface for TM polarisation. The three boundary conditions for the electric, magnetic and displacement fields are shown in the inset. Note that all three conditions are fulfilled. (c) The exponential dependence of the electric field intensity away from the surface. The field projects much further into the dielectric medium. (d) Electric and magnetic field distributions for a SPP with TE polarisation. Examining the three boundary conditions illustrated in the inset, the parallel components of the Magnetic (\mathbf{H}) field at the interface have opposite directions making this SPP distribution physically impossible.

4.3.2.1 Surface Plasmon Polariton Dispersion Relation

Figure 4.8 shows a flat interface between dielectric and metallic half spaces with the coordinated system detailed in Fig 4.8a. This is the most simple geometry for sustaining SPPs. The permittivity of the dielectric material, ϵ_1 is real (no absorption) and positive. On the other hand, the permittivity for metals behaves differently and is defined as $\epsilon_2 = \epsilon_{2r} + i\epsilon_{2i}$, where ϵ_{2r} and ϵ_{2i} are the real and imaginary parts of the permittivity, respectively. This difference in the real part of the permittivities is essential to maintaining the SPP oscillations.

Figure 4.8b shows the field distributions of a propagating SPP, with TM (transverse magnetic) polarisation, propagating in the x-direction. The electric fields, by definition, originate on the positive charges and terminate on the negative ones; the magnetic fields oscillate in the y-direction (TM polarisation). The electric (\mathbf{E}) and magnetic (\mathbf{H}) fields of the propagating wave in both regions can be described as follows:

$$\mathbf{E}_j = (E_{xj}, 0, E_{zj})e^{i(k_{xj}x \pm k_{zj}z - \omega t)} \quad (4.1)$$

$$\mathbf{H}_j = (0, H_{yj}, 0)e^{i(k_{xj}x \pm k_{zj}z - \omega t)} \quad (4.2)$$

The \pm and j index depend on the media; it is “+” and $j = 1$ for $z > 0$ (dielectric region), and “-” and $j = 2$ for $z < 0$ (metal region). k_{zj} is an imaginary wave vector component and describes the decay of the field away from the interface in both media. This exponential dependence of the E-field intensity is illustrated in Fig. 4.8c, where k_{xj} is the wave vector component parallel to the surface and in the direction of the propagating SPP. For a propagating wave solution at the interface, the following relations need to be continuous at the boundary, namely the parallel electric and magnetic field components as well as the electric displacement field ($D_j = \epsilon_j E_{zj}$), see inset of Fig. 4.8b, i.e.

$$E_{z1} = E_{z2} \quad (4.3)$$

$$H_{y1} = H_{y2} \quad (4.4)$$

$$\epsilon_1 E_{z1} = \epsilon_2 E_{z2} \quad (4.5)$$

From Eq. 4.3 and 4.4, the x component of the wave vector is the same in both media

$$k_{x1} = k_{x2} = k_x \quad (4.6)$$

and we redefine k_x as the SPP wave vector; $k_x = k_{SPP} = 2\pi/\lambda_{SPP}$ where λ_{SPP} is the wavelength of the plasma oscillations (see Fig. 4.8b).

Together with the description of the electromagnetic fields and the continuity boundary relations, Maxwell’s equations (Chapter 1) are solved for an electromagnetic wave on a plane surface of a semi-infinite metal ($\epsilon_2 = \epsilon_{2r} + i\epsilon_{2i}$) adjacent to a dielectric medium (ϵ_1)

$$\frac{k_{z1}}{\epsilon_1} + \frac{k_{z2}}{\epsilon_2} = 0 \quad (4.7)$$

and

$$k_x^2 + k_{zj}^2 = \epsilon_j \left(\frac{\omega}{c}\right)^2 \quad (4.8)$$

where ω and c are the frequency and speed of the light, respectively. Solving Eqs. 4.7 and 4.8, the dispersion relation for a SPP propagating on the surface is obtained;

$$k_{SPP} = \frac{\omega}{c} \sqrt{\frac{\epsilon_1 \epsilon_2}{\epsilon_1 + \epsilon_2}} \quad (4.9)$$

The derivation of Eq. 4.9 is detailed in a number of very good literature publications such as [97, 98].

It is a well known property that SPPs can be excited only with TM polarised electromagnetic fields. If we do look at the TE (transverse electric) case, the electromagnetic field situation is illustrated in Fig. 4.8d. The boundary requirements for the fields are the same; the components of the electric and magnetic field parallel to the boundary must be continuous. The TE case contradicts this, because the magnetic field component has opposite field directions at the interface, as illustrated in the inset of Fig. 4.8d. The discontinuous field distribution, therefore prevents the excitation and existence of TE polarised SPPs on metal-dielectric interfaces [99].

Note that, for the perpendicular electric displacement field, $D_j = \epsilon_j E_{zj}$, to be continuous at the interface, the real part of the permittivity values have to have different signs. This is the reason why the SPPs occur at metal-dielectric interfaces and not at dielectric-dielectric interfaces.

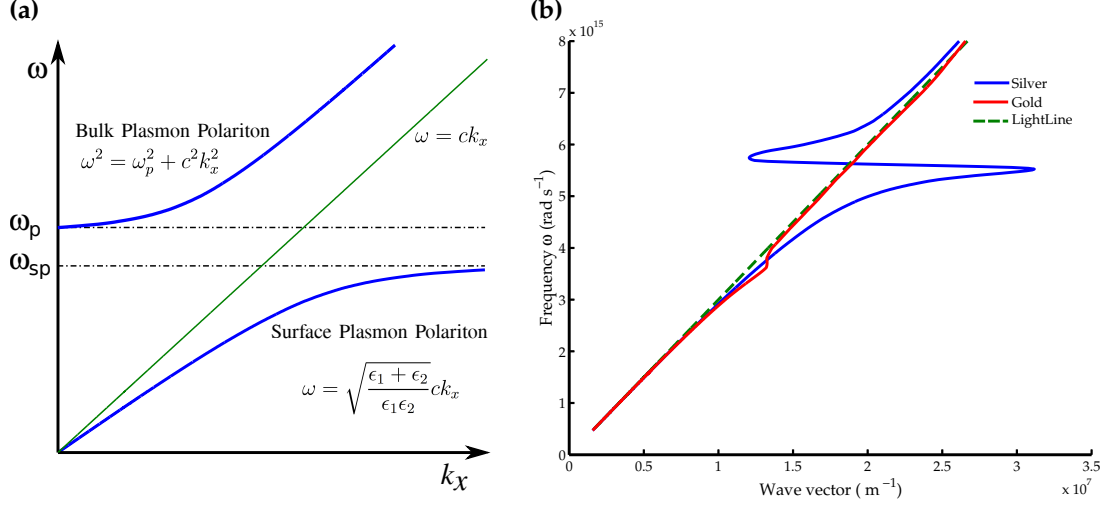


Figure 4.9: (a) Dispersion curve for a SPP propagating along a Drude metal-air interface. The light line ($\omega = ck_x$) is in green. The dotted lines show the position of the plasma frequency (ω_p) and the surface plasmon frequency (ω_{sp}). The SPP curve is below this light line and the transparency region with propagating bulk plasmons illustrated above the light line. (b) Dispersion relation for a SPP propagating on a gold-air (red line) and a silver-air (blue line) interface. The dotted green line is the light line. The silver dispersion curve is included as it better resembles the theoretical Drude metal behaviour compared to the gold.

To examine the SPP dispersion relation in detail, we firstly look at a metal with negligible damping as described by the Drude model [100,101]. In the Drude model, the optical behaviour of the metal is explained using a plasma model, where the free electrons form a gas of particles moving in a fixed background of solid positive ions. The permittivity of the metal with no attenuation is then described as

$$\epsilon_2(\omega) = 1 - \frac{\omega_p^2}{\omega^2} \quad (4.10)$$

where ω_p is the plasma frequency of the free electron gas and ω is the frequency of the light. A full derivation and description of this model can be found in [98]. Figure 4.9a plots Eq. 4.9 for the Drude metal in air ($\epsilon_1 = 1$). The SPP excitations correspond to the area of the dispersion curve below the light line ($\omega = ck$), hence, as previously mentioned, the SPP are confined and bound to the interface.

For small wave vector values, the SPP behaves almost like a photon with the dispersion very close to the light line. In this regime, the SPP waves extend far into the dielectric region. As the wave vector increases, the SPP dispersion relation asymptotically approaches the characteristic surface plasmon frequency, ω_{sp} ,

$$\omega_{sp} = \frac{\omega_p}{\sqrt{1 + \epsilon_1}} = \frac{\omega_p}{\sqrt{2}} \quad (4.11)$$

Which is derived by inserting the free electron dispersion relation into Eq. 4.9. In this regime, as the wave vector approaches infinity and the frequency approaches ω_{sp} , the behaviour of the surface wave changes. The mode is now a collective oscillation of electron plasma near the surface of the metal and is non-propagating. It has an electrostatic character and is known as a surface plasmon.

For larger frequencies above the free electron plasmon frequency (ω_p), the metal becomes transparent and radiative bulk plasmon modes are observed. In this region, the metal acts as a dielectric and the dispersion for these volume plasmon polaritons is described as $\omega^2 = \omega_p^2 + c^2k^2$, for the free electron gas model (Fig. 4.9a). In this thesis, we focus exclusively on the bound SPP below the light line.

Next, we examine the case for a real metal. Figure 4.9b shows two dispersion curves, one for a SPP travelling at a gold-air interface and the second for a SPP travelling along a silver-air interface. Note that, all results and discussions in this chapter are solely based on a gold-air interface structure. The dispersion relation of a SPP on a silver-air interface is included because it resembles the theoretical Drude metal dispersion relation better than gold, therefore, it is included for illustration purposes. The dielectric functions of the gold and silver are obtained from Babar and Weaver [102]. If we compare the real dispersion of gold and silver to the Drude, undamped, dispersion in Fig. 4.9a, we note that the damping suppresses the large k -vectors and so the bound SPP reaches a finite wave vector at the surface plasmon frequency. Also, the evanescent part of the dispersion curve between ω_{sp} and ω_p is now allowed, in contrast to the Drude case where the real part of the wave vector was zero in this region. This reason for the alteration from the Drude case is due to the free electron and interband damping in the real metal that the Drude model does not take into consideration. Therefore, ϵ_2 is complex, making k_{SPP} also complex and the dielectric response of the metal plays a crucial role in the dispersion relation of the SPP.

4.3.2.2 Excitation of Surface Plasmon Polaritons

The SPP dispersion relation clearly illustrates the confined nature of the surface wave. The dispersion curve lies below the light line ($\omega = ck$) with the propagation wave vector, k_{SPP} , greater than the wave vector in air. This means that there is a momentum mismatch between the SPP and the free space photon of the same frequency. This mismatch inhibits the excitation of a SPP on a flat metallic surface by an incoming photon. To achieve coupling between the incident light and the SPP, special techniques for momentum-matching are employed.

There are a number of methods commonly used to overcome this momentum mismatch and to couple light into SPPs; prism coupling, grating coupling, highly focused beam coupling, near-field coupling, end-fire coupling and step-gap leakage coupling. A summary of all these methods is presented in [103].

A very popular method amongst these is to periodically pattern the metal surface with shallow grating grooves or holes, thereby creating a grating coupler. Grating coupling was first observed by Wood in 1901, when he studied the reflection of an incandescent lamp from a ruled metal grating and noticed dark and bright bands in the spectra where the light had coupled to SPPs [104].

We consider a simple 1D grating as in Fig. 4.10a with a period Λ_{cplr} (the use of the subscript ‘‘cplr’’ is somewhat arbitrary but will be used later on to label the period of the ‘‘coupler grating’’; for consistency, it is introduced from the beginning, and an incoming plane wave at an angle θ to the surface normal. The incident radiation will scatter from the grating, increasing or decreasing the component of its wave vector that is parallel to the grating by integer multiples of the grating vector K_{cplr} ($K_{cplr} = 2\pi/\Lambda_{cplr}$). This gives rise to diffracted orders,

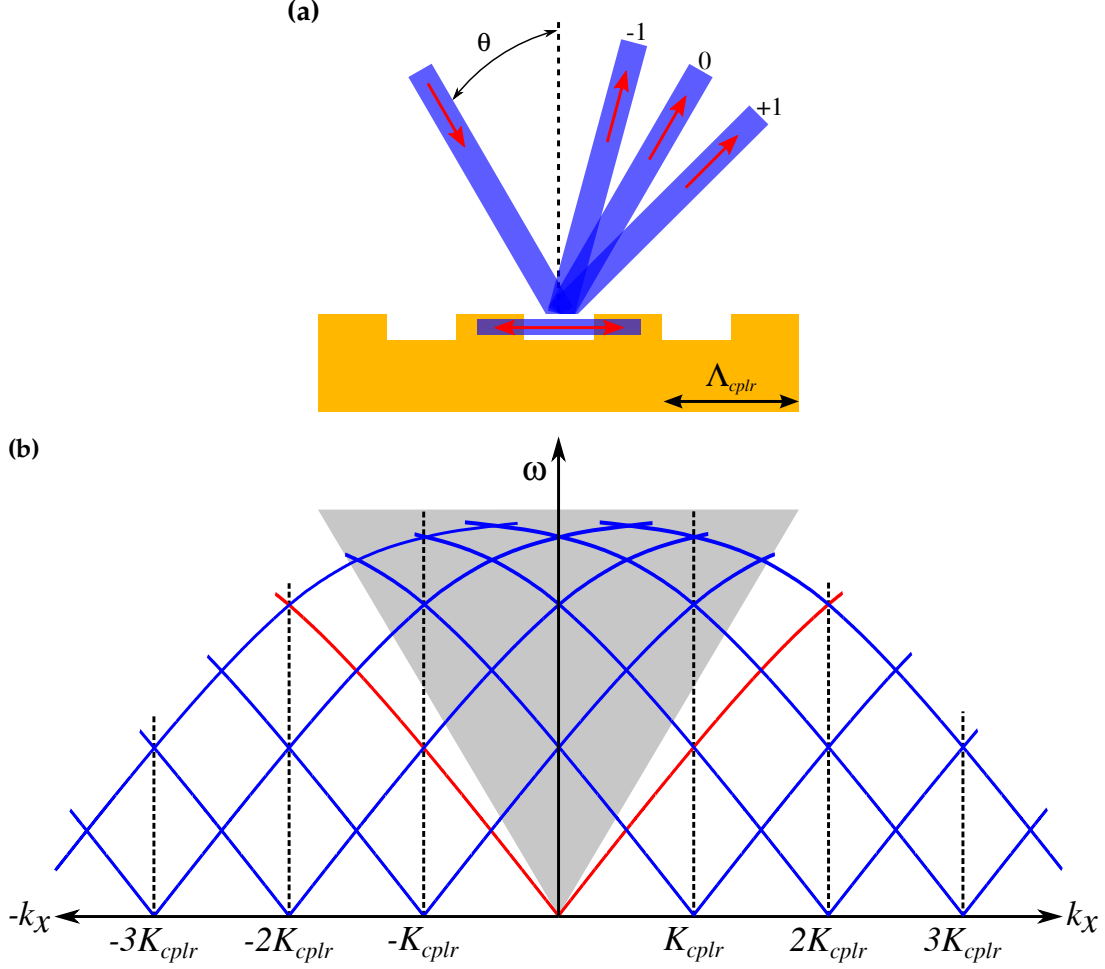


Figure 4.10: (a) Illustration of light incident on a metallic grating structure, period Λ_{cplr} . Depending on the parallel wave vector component of the incident light, it can diffract into propagating orders or into higher evanescent orders that couple to the grating and excite a SPP. (b) The dispersion relation curve for SPPs propagating along a metal grating, the SPP dispersion along a flat surface is highlighted in red, with a period Λ_{cplr} ($K_{cplr} = 2\pi/\Lambda_{cplr}$). Parts of the scattered dispersion curves now lie within the light cone (shaded region) and can be radiately coupled to with external photons.

see Fig. 4.10a. When the resulting wave vector matches the wave vector of the SPP, light can couple according to the following resonant coupling condition

$$k_x = n_1 k_0 \sin\theta \pm m K_{cplr} \quad (4.12)$$

where k_x is the wave vector component within the grating, n_1 is the refractive index of the incident medium (in our case its air, $n_1 = 1$), m is an integer (1,2,3...) corresponding to the diffraction order and k_0 is the wave vector on the incident light in vacuum. The \pm option is because the periodic corrugation can add or subtract integer values of the grating vector K_{cplr} .

Figure 4.10b illustrates how the SPP dispersion relation curve changes with the addition of a grating coupler. The original SPP dispersion curve for propagation on a flat metal surface is shown in red. The periodicity of the structure represents a 1D lattice with each of these lattice points a scattering centre for incident radiation. They can add or subtract momentum in integer multiples of

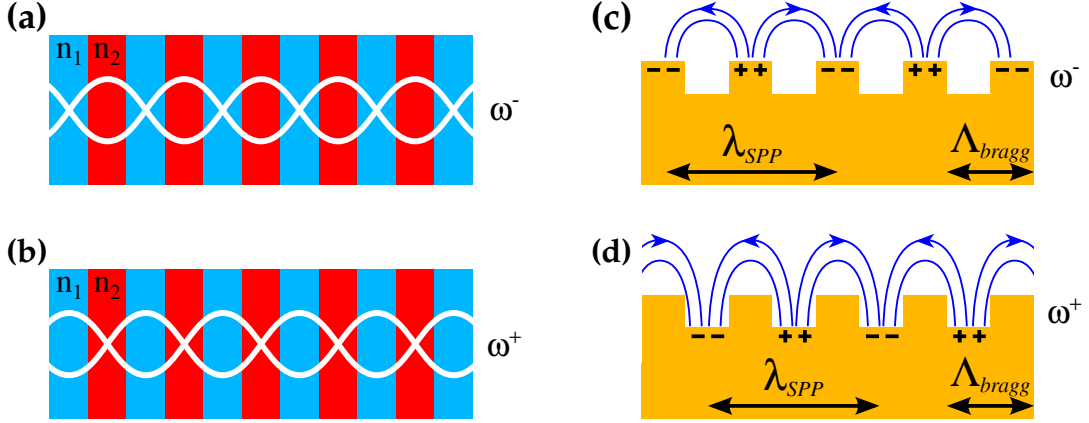


Figure 4.11: Schematic representations of the standing wave solutions of the fields in a dielectric stack, (a) and (b), and for a metallic grating, (c) and (d). The lower frequency mode has the field largely localised within the high index region of the dielectric stack (a) and from ridge-to-ridge of the metal grating (c). The higher frequency mode is the opposite, with the field concentrated in the low index region (b) and from groove-to-groove of the grating (d). (Note that the fields drawn are only a sketch and do not represent the real distribution, as in practice they will not be sinusoidal but be more tightly squeezed into the high/low regions.)

K_{cplr} . As a result, there are now diffracted regions of the SPP dispersion curve within the light cone (shaded grey region). Therefore, it becomes now possible to couple TM polarised light to SPP modes along the metal grating i.e. with the grooves of the grating perpendicular to the plane of incidence and the electric field in the plane of incidence.

4.3.3 Binary Biharmonic Grating Structure

On closer inspection we note that the dispersion relation for the coupler grating presented in Fig. 4.10b is not entirely accurate. Instead, the correct dispersion relation for SPPs propagating along a grating splits at each crossing point of the SPP curves and the periodicity results in an energy band gap opening up at each crossing point. The first order band gap is below the light line and is inaccessible to external photons. A method of extracting photons from this part of the dispersion curve to free space is to include a second grating component (biharmonic structure). I will discuss how to design such a biharmonic structure.

Furthermore, I will look at ways of increasing the band gap size and how to produce very flat bands in the dispersion diagram. A flat dispersion curve indicates angular-independent absorption, which is desirable both for filters and for thermal emitters

Firstly, we will take a step back and consider a simple quarter wave dielectric stack. The stack consists of alternating layers of low (n_1) and high (n_2) refractive index dielectrics, see Fig. 4.11(a,b). Consider a wave propagating perpendicularly to the alternating layers. At each boundary where the light scatters, forward propagating light is scattered backwards. When the periodicity of the stack is half of the effective wavelength of the light, both the forward and backward travelling waves interfere constructively and form a standing wave. Figure 4.11(a,b) shows the two possible configurations the standing wave can take. By using simple

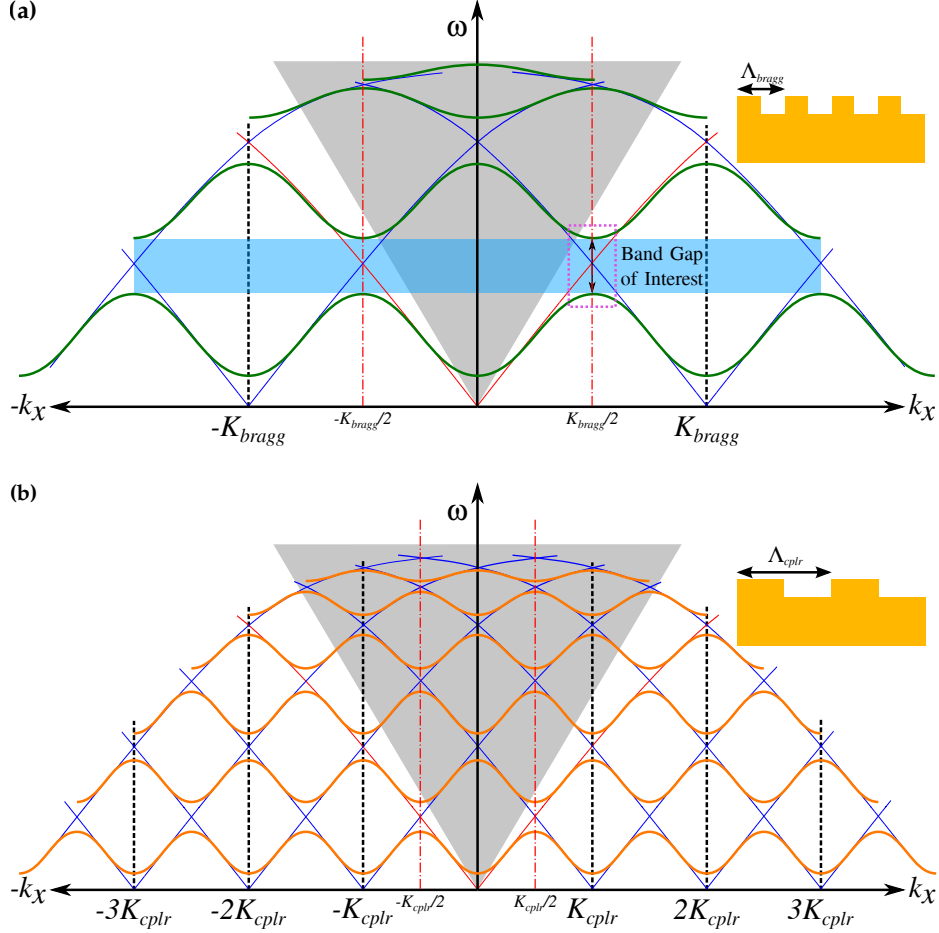


Figure 4.12: Dispersion curves for a SPP propagating along a metal grating for two different periods; (a) period is Λ_{bragg} and (b) period is Λ_{cplr} which is twice Λ_{bragg} . The grey shaded region is the light cone. The original dispersion curves of a SPP propagating along a smooth surface are the solid red lines, the solid blue lines represent the SPP dispersion and each scattering location. At each crossing point of these SPP dispersion curves a band gap in frequency opens up. The edges of the Brillouin zone are indicated in each case with dot-dashed lines at (a) $\pm K_{bragg}/2$ and (b) $\pm K_{cplr}/2$. The inset in each figure shows the geometry of the structure.

symmetry arguments, it can be shown that the forward and reflected waves become in-phase at the middle of the low index region and the middle of the high index region. Since the two regions have different refractive indices, the two modes have different energies and therefore different frequencies. The high index region is analogous to a lower potential in a electronic crystal, therefore, the low energy configuration corresponds to modes localised in the high index medium (ω^-) and conversely, the high energy mode is with the majority of the field in the low index material (ω^+). The frequencies between these two energies ($\omega^+ < \omega < \omega^-$) consequently destructively interfere and are unable to propagate through the structure, thereby, producing a photonic band gap.

We now extend the same analysis to metallic gratings. Here, rather than the refractive index contrast, the ridges of the grating are the scattering points of the structure. Similar to the dielectric stack, if the ridges are spaced by half the SPP wavelength, standing waves form. Again, the two standing wave solutions

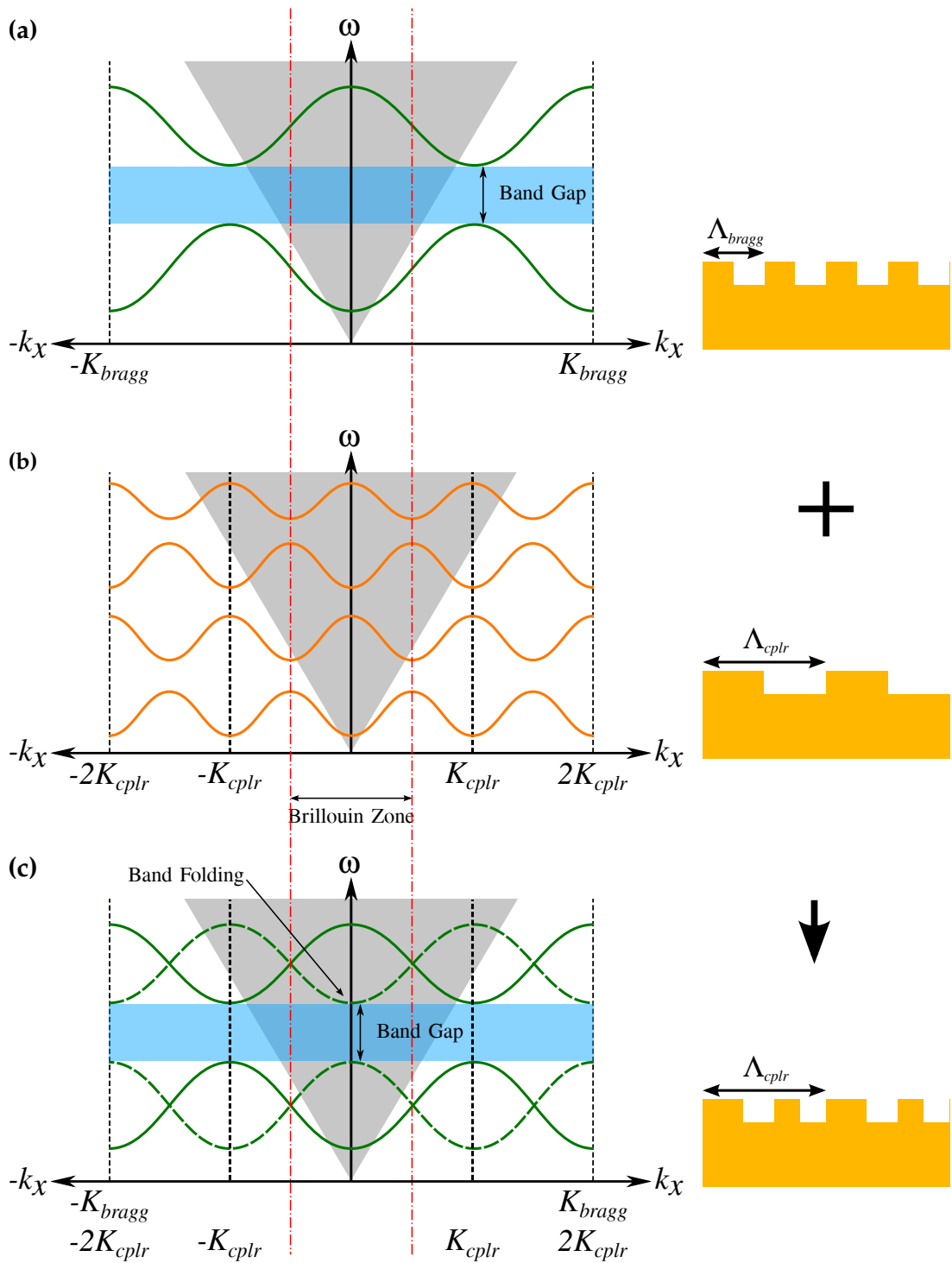


Figure 4.13: Combining the Bragg and coupler gratings to create a biharmonic structure. (a) and (b) show a reduced section of the Bragg and coupler SPP dispersion diagrams, respectively. (c) Shows the resultant dispersion diagram. Effectively, the Bragg dispersion diagram is folded along the edge of the Brillouin zone of the coupler grating and shifts the Bragg band gap in (a) into the light cone as illustrated with the green dotted line in (c).

take different positions with respect to the ridges and the grooves of the grating, see Fig. 4.11c,d. For the low energy configuration, the free charges are pushed to the ridges (Fig. 4.11c), and for the high energy mode, the opposite is the case, with the free charges localised in the grooves and the fields originate from there (Fig. 4.11d). In the high frequency case, the distortion in the field lines increases the energy of that mode compared to the lower energy mode, which has a more confined behaviour.

Let us consider the propagation of a SPP along the surface of a metallic grating in terms of wave vectors. When the grating vector, ($K_{bragg} = 2\pi/\Lambda_{bragg}$) is twice the SPP wave vector (k_{SPP}), then energy band gaps open up in the dispersion plot, see Fig. 4.12a. The band gap of interest is highlighted in blue. This dispersion plot is similar to the one presented in Fig. 4.10b, except that at each crossing point, a band gap opens up.

We will refer to this grating structure as the Bragg grating, $\Lambda_{bragg} = \lambda_{SPP}/2$. However, it is not possible to observe this particular band gap with radiative photons as it is confined outside the light cone, $k_{SPP} > k_0$. A common solution to allow access to modes outside the light cone is to include a second modulation, as already shown in Fig. 4.10b. We can employ the same method to access the band gap formed by the Bragg grating by simply including a second grating, which is called the coupler grating. The coupler grating has a period twice that of the Bragg grating i.e. $\Lambda_{cplr} = 2\Lambda_{bragg}$ (or $K_{cplr} = K_{bragg}/2$). Figure 4.12b shows the dispersion diagram for such a coupler grating.

If we examine both dispersion diagrams in Fig. 4.12, there are also band gaps at higher frequency regions and even one within the light cone (shaded region, when $k_x=0$). These higher frequency band gaps are a result of weaker, higher order, scattering events and are much less probable compared to the first order Bragg scattering band gap. For example, the second order band gap in the centre of the dispersion curve within the light cone of the Bragg structure (Fig. 4.12a) is achieved by the SPP scattering from two consecutive K_{bragg} scatters with $\lambda_{SPP} = \Lambda_{bragg}$. Therefore, we should also note that a single grating structure can perform both tasks; gap creation and coupling. However, the second order process is weaker than the direct K_{bragg} scattering and is not considered here.

Figure 4.13 illustrates the combination of the two different gratings and how the overlap of the band diagrams allows access to the Bragg band gap outside the light cone. Figure 4.13a and Fig. 4.13b shows the dispersion diagram for the Bragg and coupler gratings, respectively, and Fig. 4.13c shows the Bragg band gap within the light cone (dotted green line). The second order band gap of the coupler grating is at the same frequency range as the Bragg first order band gap, and it provides coupling of the Bragg band gap to radiative photons.

A method of constructing a biharmonic grating is presented in [105] where a purely sinusoidal structure is considered. However, for ease of simulation and ultimately, fabrication, a binary structure is much preferred. Reference [95] presents a method of converting the biharmonic sinusoidal structure to such a binary grating pattern. To begin, consider two sinusoidal grating profiles and simply add them together. The resulting grating profile $s(x)$ is described as

$$s(x) = A_1 \sin(K_{cplr}x) + A_2 \sin(K_{bragg}x + \phi_2) \quad (4.13)$$

Remembering that $K_{cplr} = K_{bragg}/2$, A_1 and A_2 are the amplitudes of the Bragg

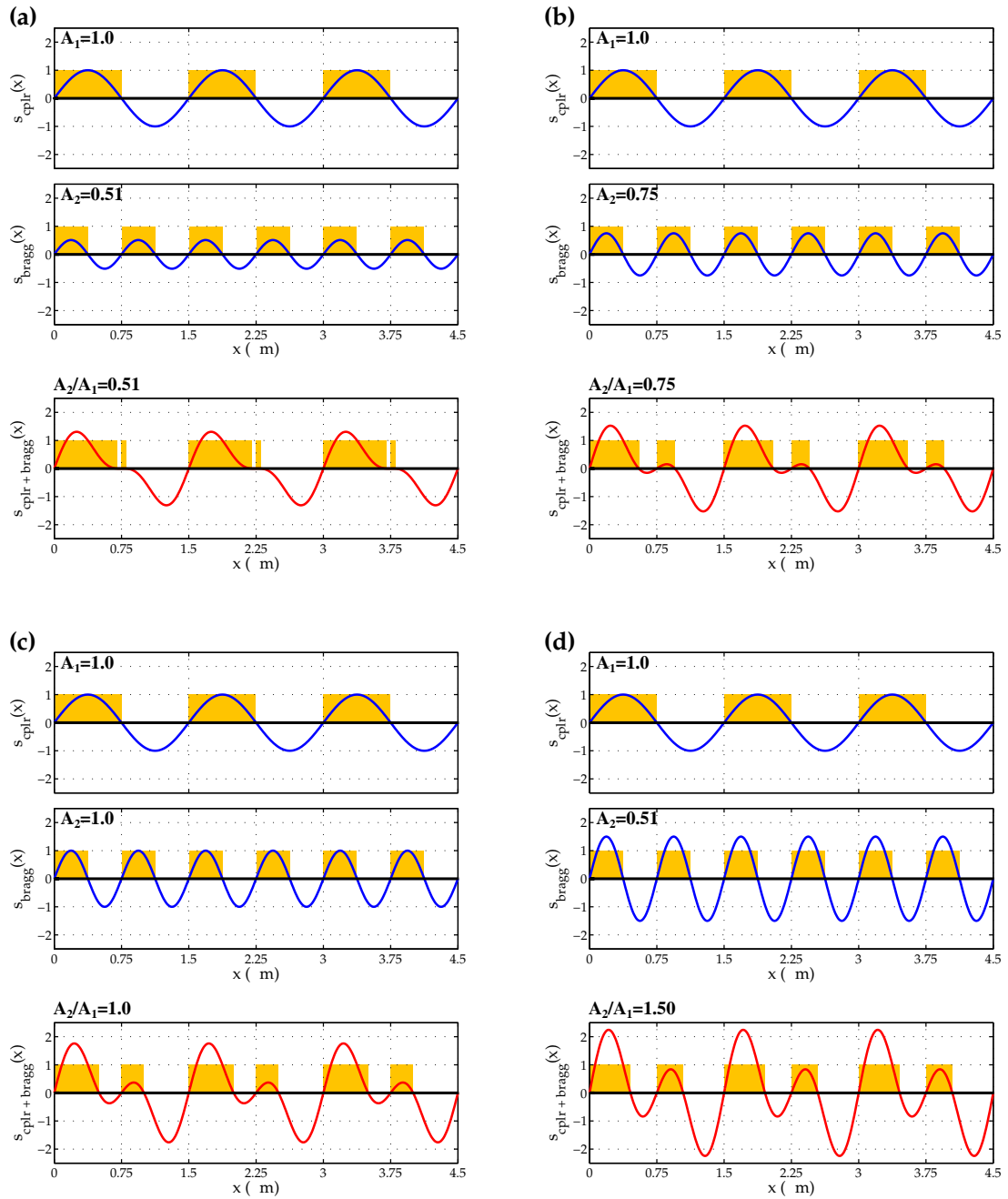


Figure 4.14: Schematic representation of, firstly, the construction of the biharmonic grating profile and secondly, the binarisation of this profile. The relative amplitude between the two sine components are varied; (a) $A_2/A_1 = 0.51$, (b) $A_2/A_1 = 0.75$, (c) $A_2/A_1 = 1.0$ and (d) $A_2/A_1 = 1.5$. The yellow binary grating profile is obtained by constructing a threshold whenever the sinusoidal profile crosses the zero amplitude line.

and coupler grating, respectively, and ϕ_2 is the relative phase between the two components. For the moment we chose the relative phase to be zero. Four examples of a sinusoidal biharmonic grating profile are presented in Fig. 4.14. The relative amplitudes (A_2/A_1) of the two harmonics are varied; (a) $A_2/A_1 = 0.51$, (b) $A_2/A_1 = 0.75$, (c) $A_2/A_1 = 1.0$ and (d) $A_2/A_1 = 1.5$. The first two panels in each show the individual sine component of the Bragg and coupler grating, plotted in blue. The third panel shows the biharmonic profile, plotted in red.

To convert these sinusoidal grating profiles to a binary structure, reference [95] operates the Heaviside step function on the sinusoidal grating profile. I employed a more basic thresholding approach, which was easier to implement. Both techniques achieve a similar binary, rectangular shaped, grating profile. Whenever the biharmonic sine wave crosses the average amplitude line, it corresponds to an edge of the grating profile. When that section of the sine wave is positive it is a ridge and when it is negative it corresponds to a groove, this is arbitrary as the fill-factor is always 50% anyway. All the panels in Fig. 4.14 illustrate how this procedure is implemented. We should also note, that the grating profiles discussed here are not suspended in air but are actually patterned on bulk gold.

4.3.4 Optical Characterisation of the Binary Biharmonic Structure

To characterise the behaviour and simulate the reflection spectra of these binary biharmonic structures we used rigorous coupled wave analysis (RCWA). Firstly, we need to choose the period of the coupler grating, which will determine the centre frequency of the band gap. We want the centre of the band gap region in the near-infrared wavelength range, around $1.5 \mu\text{m}$. Consider normal incidence, $\theta = 0$, Eq. 4.12 becomes

$$k_{SPP} = \pm d K_{cplr} \quad (4.14)$$

where k_x has been replaced with k_{SPP} . Equivalently, from Eq. 4.9

$$\frac{\omega}{c} \sqrt{\frac{\epsilon_1 \epsilon_2}{\epsilon_1 + \epsilon_2}} = \pm d \frac{2\pi}{\Lambda_{cplr}} \quad (4.15)$$

$$\Lambda_{cplr} = \lambda_0 \sqrt{\frac{\epsilon_1 + \epsilon_2}{\epsilon_1 \epsilon_2}} \quad (4.16)$$

where ω/c has been replaced with $2\pi/\lambda_0$ and λ_0 is the free space wavelength. With the grating in air, $\epsilon_1 = 1$, for gold the dispersion is wavelength dependent, at $1.5 \mu\text{m}$, $\epsilon_2 = -100.05 + i3.5545$ [102]. Taking the real part of Eq. 4.16 one gets $\Lambda_{cplr} = 1.492 \mu\text{m}$. To make things simple, we will use a period of $1.5 \mu\text{m}$ (SPP wavelength of $1.508 \mu\text{m}$) which corresponds to a Bragg grating period of $0.750 \mu\text{m}$.

To begin, we first look at the reflection spectra for the Bragg and coupler gratings individually for four different groove depths; 50 nm, 100 nm, 150 nm and 200 nm. Each has a 50% fill-factor and the wavelength range is $0.5 \mu\text{m}$ to $2.5 \mu\text{m}$. The reflection spectra are calculated for a complete range of incident angles; from normal to 90° for TM polarisation. The results are presented in Fig. 4.15 where the x-axis is the parallel wave vector component of the incident light,

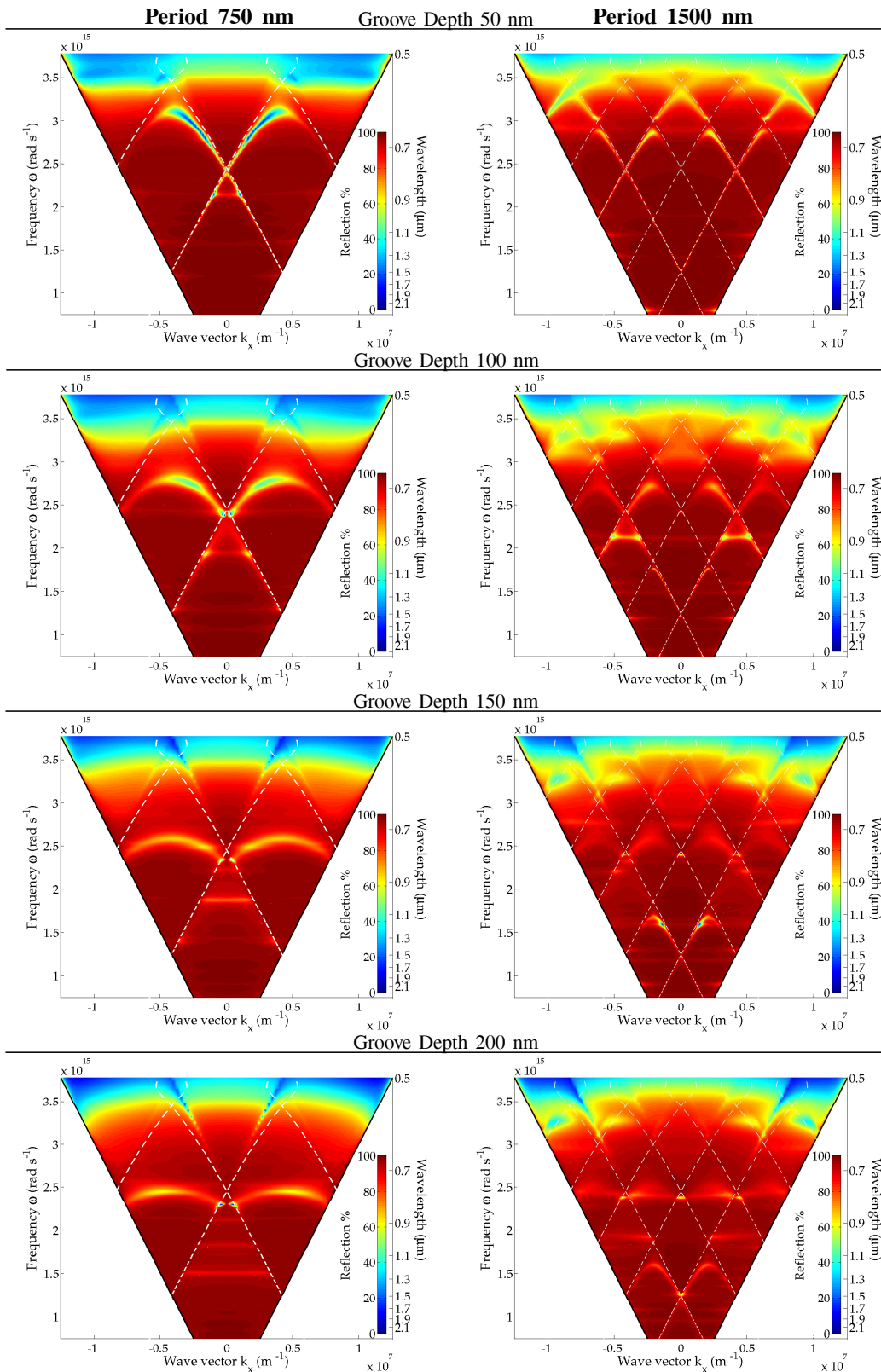


Figure 4.15: Calculated reflection spectra for the Bragg and coupler grating structures with respective period values of 750 nm and 1500 nm. Both structures have a fill-factor of 50% with the incident radiation TM polarised. The grating groove depth is varied; 50 nm, 100 nm, 150 nm and 200 nm. The dispersion of a SPP along a gold-air interface is plotted over the reflection spectra at each of the grating wave vector scattering points as a white dashed line.

$k_x = k_0 \sin(\theta)$, the left hand y-axis is the angular frequency while the right hand y-axis is the wavelength of the light. These graphs represent the complete light cones as shown previously in Figs 4.10, 4.12 and 4.13. In each of the plots the dispersion relation of a SPP propagating along a gold-air interface is overlaid as a white dashed line.

Good agreement is achieved between the shape of the reflection bands and the overlaid SPP dispersion relation and the behaviour is as expected from Fig. 4.12, i.e. the reflection bands should follow the SPP dispersion and curved away as they approach a crossing point. The blue region (very low reflectivity) at the top of each plot corresponds to the wavelength region where the gold is naturally very lossy and so the light is strongly absorbed there. For both grating structures the position of the bands is clear, but, the coupling is very weak i.e. the reflectivity is relatively high which corresponds to low absorption. The band gaps at the crossing points are small and not distinct. Although the bands do appear to get “flatter” as the groove depth is increased.

Of course, the band gap of interest is outside the light cone of the 750 nm period grating (not visible with the single period grating structure). The other area of interest is the second order band gap of the coupler grating (1500 nm) i.e. the first crossing point in the centre region of the dispersion plot. This is where the band gap of the biharmonic structure will be. The band gap produced by the the single period structure is very small and the coupling is very weak.

Next we examine the reflection spectra for the biharmonic structure where the Bragg and coupler grating have been combined. For this, we look at a slightly narrower wavelength range i.e. from 1 μm to 2.5 μm , in order to zoom in on the band gap region. The same full angle range is covered to 90° along with the same four groove depths; 50 nm, 100 nm, 150 nm and 200 nm and of course, all for TM polarisation. Four different amplitude ratios of the coupler to Bragg grating are covered; $A_2/A_1 = 0.51, 0.75, 1.0$ and 1.5 . The simulation results are presented in Fig. 4.16 with the groove depth increasing down the columns and the A_2/A_1 ratio increasing across the rows. Along with the sixteen reflection dispersion plots, the four reflection plots of the coupler grating ($A_2/A_1 = 0$) are replotted from Fig. 4.15 in the first column of the figure for easy reference and comparison.

Firstly, for an amplitude ratio of 0.51, the behaviour is not too unlike that of the coupler grating in the first column. The overall shape of the bands is similar, but, the biharmonic structure does exhibit stronger coupling in places. This similar behaviour is expected as the biharmonic grating profile is very close to that of the single period coupler structure with only a very narrow groove in the grating being the difference (Fig. 4.14a). For all the other dispersion plots, a band gap is easily resolved although only the, low frequency, arm of the gap is clearly obvious.

The higher frequency arm of the gap is very weakly coupled and its presence is not easily resolved in the reflection plots due to the large colour range. By examining the reflection spectra directly, the coupling of the higher frequency modes can be seen.

The general trend in Fig. 4.16 is that increasing the amplitude ratio A_2/A_1 increases the size of the band gap, as expected from [95]. The band gap width is also proportional to the groove depth; for shallow gratings (50 nm) no band gap

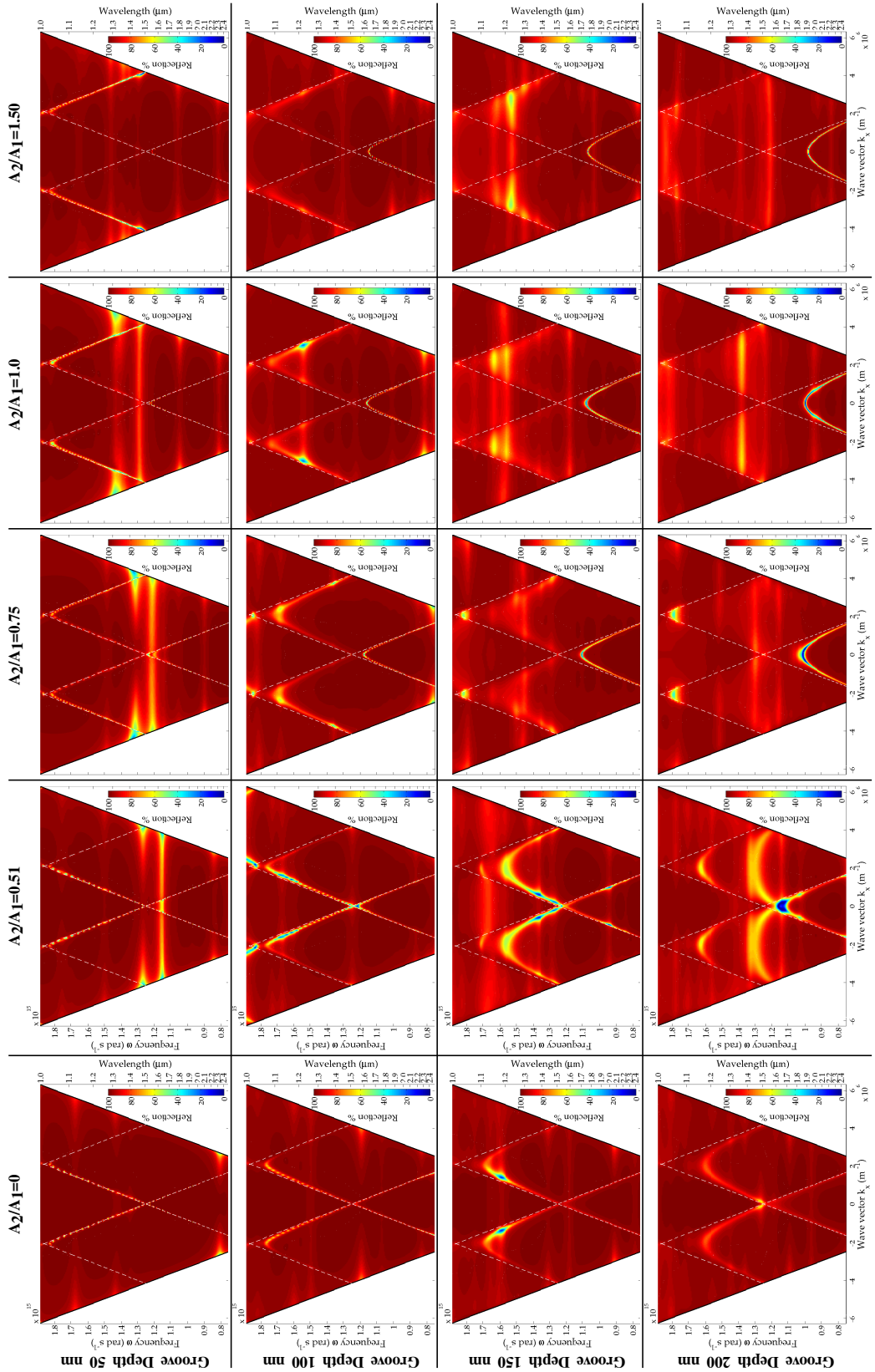


Figure 4.16: Reflection dispersion plots for the binary biharmonic grating structure for a range for of groove depths (50 nm, 100 nm, 150 nm and 200 nm) and a for range of A_2/A_1 amplitude ratios (0.51, 0.75, 1.0 and 1.5). The first column of images are the same as the second column of Fig. 4.15 i.e. the dispersion plots for the coupler grating plotted here with a slightly narrower wavelength range.

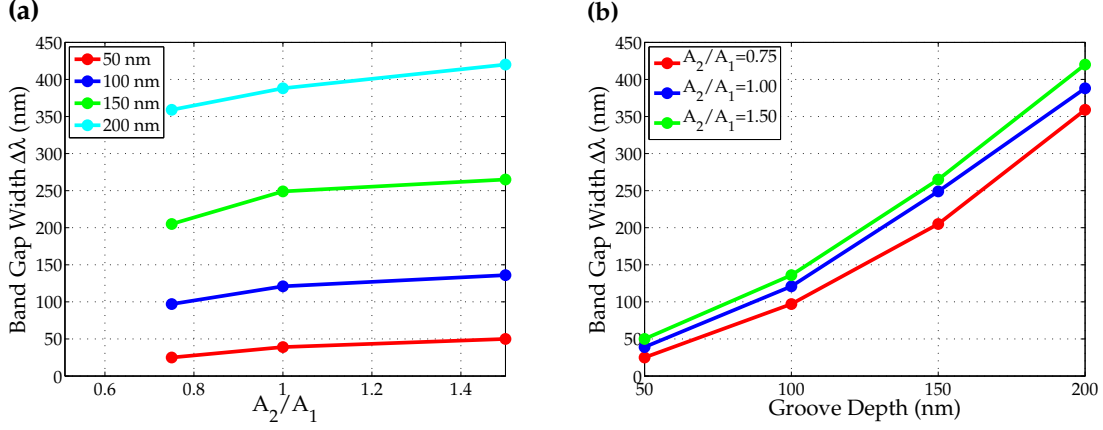


Figure 4.17: Summary of how the band gap width of the biharmonic structure, at normal incidence, varies with increase in amplitude ratio (A_2/A_1) (a) and increase in groove depth (b).

appears. A summary of these two trends is presented in Fig. 4.17. Figure 4.17a shows how the band gap width changes as A_2/A_1 increases for each of the groove depths. The band gap is measured in terms of wavelength for normal incidence and is in units of nanometres. Figure 4.17b examines the same band gaps but shows how the band gap increases as the groove depth increases.

If we compare the biharmonic structure to the single period case of the coupler grating in the first column of Fig. 4.16, a significant difference becomes apparent and the coupling to the first order Bragg band gap via this coupler grating is evident. As the band gap widens, the dispersion of the localised modes flattens. We are interested to see how far can this be pushed i.e. how flat the band can get and over what angular range. From the summaries presented in Fig. 4.17, it is apparent that increasing the grating depth has a significant effect on increasing the band gap size, while increasing the amplitude ratio has less effect. Considering the two trends, further increasing the groove depth should achieve flatter bands.

One thing worth noting is as the band gap increases, the low frequency arm shifts to lower frequencies i.e. larger wavelengths. To compensate for this shift away from the near-infrared wavelength range, the period of the structure needs to be reduced. Through a variety of simulation experiments, it was observed that a period of 550 nm for deep grating shifts the localised modes of the low frequency arm of the band gap into the near-infrared wavelength range around $1.5 \mu\text{m}$, as described.

The results for a biharmonic grating structure, with a Bragg-coupler amplitude ratio of 0.75, and for three different groove depths (600 nm, 800 nm and 1000 nm), are presented in Fig. 4.18. The plots only show the low frequency arm of the band gap. It is very clear that all three groove depths produce very flat dispersion bands, with the groove depth of 800 nm (Fig. 4.18b) producing the flattest band at $1.5 \mu\text{m}$. Therefore, an incident wave couples to the same resonant wavelength regardless of the incident angle. This behaviour is quite extraordinary and not typical for periodic structures. For example, Fig. 4.15 shows how sensitive the resonant wavelength of a single period grating structure is to the angle of incidence. However, here we have designed a periodic structure

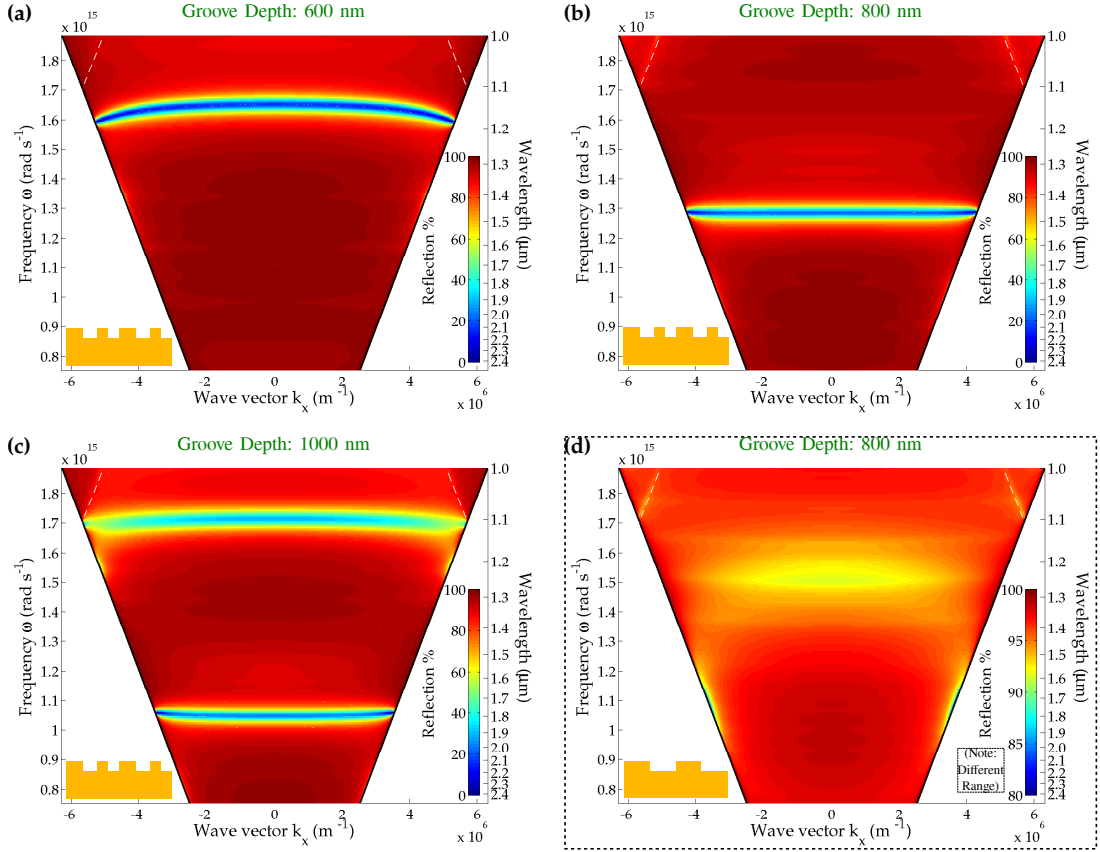


Figure 4.18: Reflection dispersion plots for a biharmonic structure with amplitude ratio of 0.75 for three very deep groove depths; (a) 600 nm, (b) 800 nm and (c) 1000 nm. (d) Is a reflection dispersion diagram for the single period coupler grating structure with a groove depth of 800 nm and fill-factor of 50%. Note the change in the colour scale range.

that is completely angularly insensitive over the full half space of angles from normal to 90° .

To prove that this effect is not purely a deep grating groove effect I have included the reflection dispersion diagram for the equivalent coupler grating with period 550 nm, groove depth 800 nm and fill-factor of 50%, Fig. 4.18d, for all of the biharmonic structures the fill-factor is 50%. The colour range has been changed to make it easier to see the resonant features. A flat, but very broad resonant feature exists at $1.250 \mu\text{m}$ for the coupler grating. It shows how weak the second order scattering can be when compared to the first order Bragg coupling of the biharmonic structure and proves the importance of including both.

Figure 4.19a shows the absorption spectra for the biharmonic structure of Fig. 4.18b, groove depth 800 nm and $A_2/A_1 = 0.75$, for an incident angle range of 0° to 45° . Since there is no transmission through the grating, the absorption is the inverse of the reflection, $A=1-R$. The absorption spectra are plotted in steps of 1° from normal incidence and are stacked up on top of each other, to truly appreciate how flat the dispersion of the structure and how large the free spectral range is. The average linewidth is approximately 50 nm. In Fig. 4.19b the amplitude ratio is increased to 1 and the absorption is pushed up to

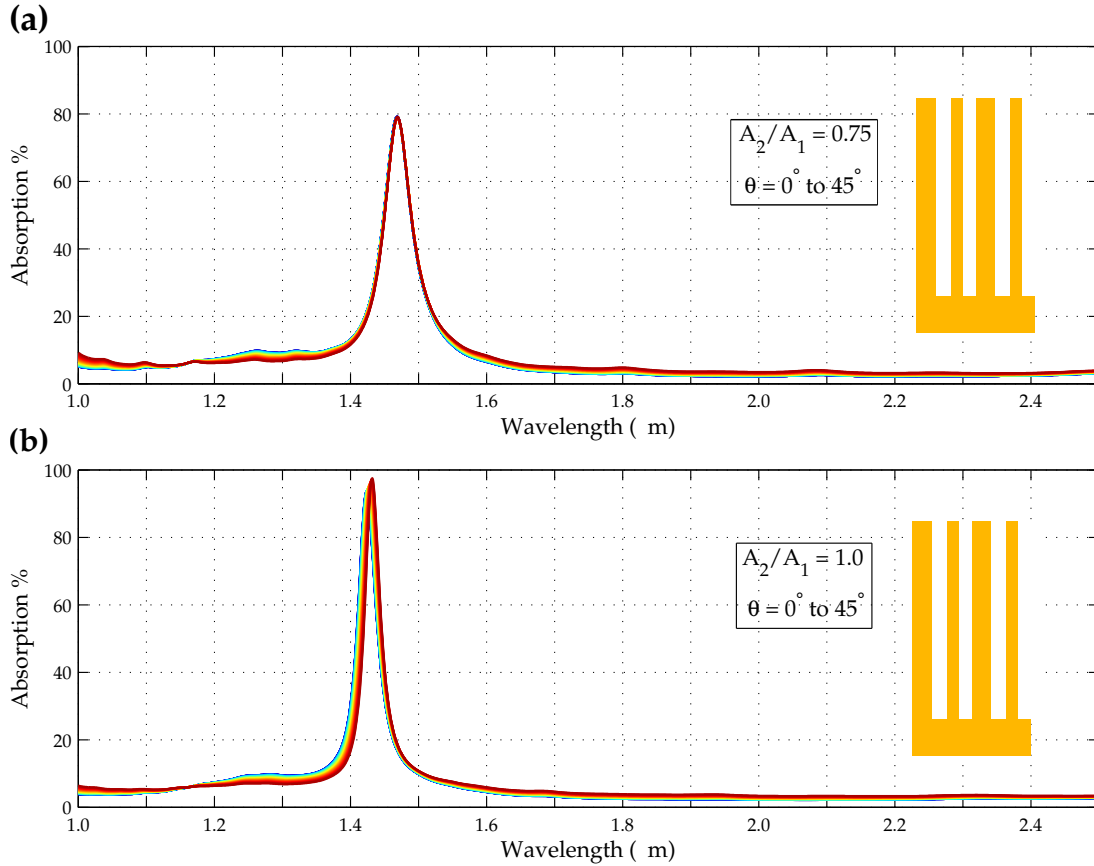


Figure 4.19: Absorption spectra for light incident on the same biharmonic structure as in Fig. 4.18b with period 550 nm, groove depth 800 nm and $A_2/A_1 = 0.75$ (a) $A_2/A_1 = 1.0$ (b). The incident angle ranges from normal to 45° in steps of 1° . In both plots the absorption spectra are plotted stacked on each other, note the rainbow of colours from blue to red.

almost 100%. Therefore, from Kirchhoff's law of thermal radiation, this type of structure will make an excellent thermal emission device. When the structure is heated, the thermally excited SPP will couple to propagating photons via the deep biharmonic gratings and the emission wavelength over the entire half space will be the same, with an emissivity value of almost 1.

A key aspect to consider is the fabrication of such a binary biharmonic structure, however. Unfortunately, I was not able to fabricate these structures during my thesis work. The two insets in Fig. 4.19 show just how high an aspect ratio the grating profile has for such a deep grating (800 nm) with a period of 550 nm. The etching of deep narrow grooves like this into a metal layer like gold is not easy. To relieve the issue it may not be required to etch such a deep grating. Depending on the application, shallower groove depths still produce very flat dispersion bands with strong coupling, although, over a reduced angle range, see Fig. 4.18a. Using the RIE etching recipe presented in the earlier part of this chapter is an option, but, the redeposition of the etched gold is a serious problem. An alternative method to RIE etching process is focused ion beam milling.

Chapter 5

Coupled Cavity Array Thermal Emitter

5.1 Introduction

In Chapter 3, we saw how a square hole array photonic crystal slab achieve narrow band thermal emission through resonant enhancement. The focus in Chapter 3 was completely on the Γ -point resonant modes, i.e. normal emission from the surface, with little attention paid to the off-normal (away from the Γ -point) behaviour of the structure. However, by examining the resonant modes in the band diagram of the square hole array slab (Fig. 3.1e (TE modes)), it is clear that, overall, they are not flat in k-space i.e. the resonant wavelength changes with the wave vector. Furthermore, in the opening section of the previous Chapter (Chapter 4), the off-normal spectral absorption behaviour for the same square hole array photonic crystal slab was presented (Fig. 4.1). The simulation results show that the resonant wavelength shifts and other resonant modes appear as the incident angle is increased from 0° (normal) to 80° . This behaviour is not desirable as typically narrowband monochromatic sources are required, not sources where the emission wavelength changes as a function of angle.

In the previous chapter, two resonant structures with angularly independent resonant behaviour were introduced and designed; the metal-insulator-metal resonator and the binary biharmonic structure. They both exhibited flat dispersion bands with no change in the resonant wavelength against incident angle. However, because the emission material is gold, the resonances are broad and the devices are difficult to fabricate. In contrast, by using silicon as the emission material (Chapter 3), higher Q resonances are achieved and the devices are easier to fabricate. Therefore, we require a structure which exhibits flat dispersion while maintaining narrow linewidth resonances and that can be fabricated from a material such as doped silicon.

In recent years, photonic crystal coupled cavity waveguides (CCWs) have generated interest in the field of slow-light engineering [106]. Basically, the structure consists of a string of resonators, where light is coupled through the waveguide by evanescently coupling to each resonator. The system exhibits slow-light behaviour but also demonstrates flat dispersion bands over large regions of their transmission spectrum. This type of structure shows promising behaviour.

In this chapter, I extend the analysis to a 2D photonic crystal coupled cav-

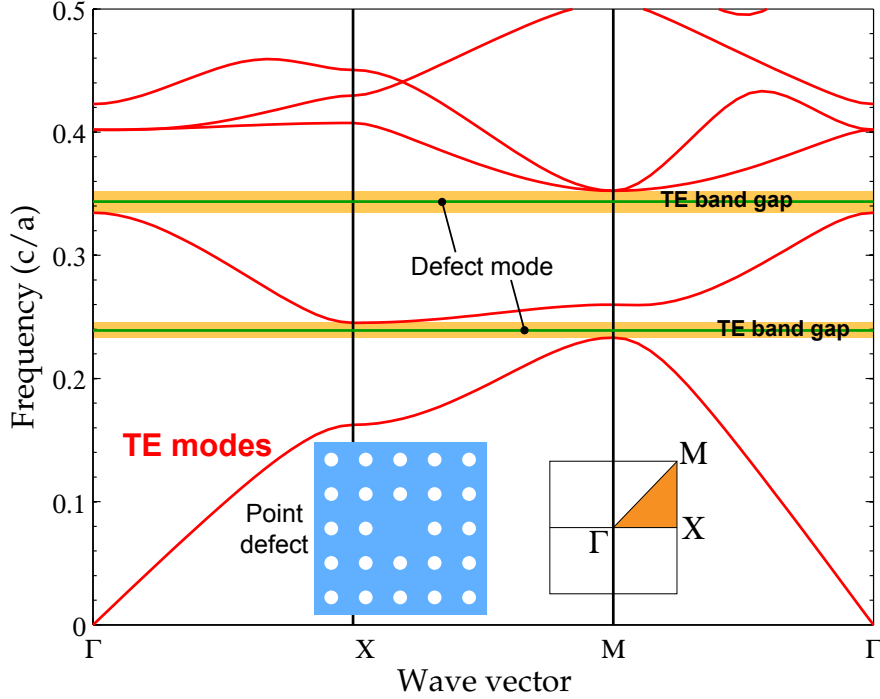


Figure 5.1: Two dimensional photonic band diagram for a square array of holes in silicon ($n=3.5$) with period a hole radius of $0.35a$, TE modes only. The left inset shows a cross-sectional view of the with a single hole, point defect. The right inset show the first Brillouin zone, with the irreducible Brillouin zone highlighted in orange. The yellow regions indicate the complete TE band gaps. A green horizontal line has been added to each band gap schematically to indicate the position of the single defect cavity mode.

ity array (CCA), which exhibit extremely flat dispersion bands. The structure consists of a typical photonic crystal of air holes in a dielectric slab like silicon. To create the cavity array, a hole is removed periodically across the 2D array of holes (e.g. every third hole removed). Each hole creates a defect and the light is trapped within the defect by the surrounding lattice, and therefore, forms a cavity. The coupled cavity mode typically falls within the band gap region of the photonic crystal lattice. CCAs have already demonstrated reasonable flat band behaviour for a square hole array photonic crystal lattice [107, 108], and have been used to achieve ultra-fast nanocavity photonic crystal lasing [109, 110].

Here, we further advance the design of the structure and achieve much flatter dispersion bands across the entire wave vector range. A triangular lattice of holes is used instead of the square array because it produces a larger band gap and so a larger free spectral range. 2D and 3D band diagrams are calculated for the structure. The number of holes between the defect cavities is altered to examine the coupling strength and to alter the dispersion relation. Finally, the material absorption is added by doping the silicon. The corresponding absorption spectra are calculated for normal incidence and, in steps of 10° , upto an incident angle of 80° for both polarisations.

5.2 Defect Modes Inside the Band Gap

5.2.1 Single Point Defect

We begin our discussion by firstly examining the square hole array photonic crystal. A band diagram for such a structure has already been presented in Chapter 1, Fig. 1.6. The crystal is infinite in the out-of-plane direction and it is 2D periodic in the plane, i.e. it is not a slab structure but a pure 2D photonic crystal with infinite columns of air in silicon. The same band diagram is repeated here (for the TE-modes only) in Fig. 5.1, with hole radius $0.35a$ and a refractive index of 3.5.

The TE modes experience two complete photonic band gaps. Within these band gaps, no modes exist and light waves are not allowed to propagate in any direction with any wave vector within the plane. The modes within the band gap are complex and the fields decay exponentially inside the structure. However, if the perfect lattice of air holes is disrupted by the presence of a defect e.g. by removing a single hole from the lattice (point defect), a localised mode is created with a frequency inside the forbidden band gap. This defect mode cannot propagate within the crystal as it is surrounded by a complete band gap, effectively a Bragg mirror in every direction. Such modes decay exponentially from the defect into the surrounding lattice and therefore, the mode is strongly localised in the defect. With no direction for the photons to propagate, the defect becomes a cavity for the photons. The left inset of Fig. 5.1 shows a square lattice with one hole removed to create a point defect. The defect mode appears as a single line (schematically added green lines) within the band gap of the background lattice of modes. It has a flat dispersion across all wave vector values.

5.2.2 Two Dimensional Defect Array

We now extend the analysis to an array of defects and create a coupled cavity array. Firstly, we examine the band gaps for the square and triangular hole array photonic crystals. The band diagrams for these 2D structures are calculated using the MIT Photonic-bands software package (MPB), using the plane wave expansion method. The boundary conditions for the software are periodic in all directions. The disadvantage of using MPB is that it assumes an infinitely thick slab, therefore, the frequency ranges and values are not entirely accurate when comparing to the finite thickness slab case. For the finite slab, the effective index for each mode changes as the field profile extends into the air region and also, light will be lost vertically out of the slab. MPB does, however, allow for an excellent qualitative analysis. The band diagram shape and the band gap positions are very accurate. The computation time of the program is relatively very quick and therefore it is a great tool to start the design process; it is easy to sweep through a large range of structural parameters and to develop good understanding, without the need for rigorous 3D computational analysis.

Fig. 5.2a and Fig. 5.2b show the gap map for the square and triangular lattice photonic crystals (no defects), respectively, both for TE modes, i.e. the electric field is parallel to the direction of periodicity. The gap map is created by varying the hole radius of each lattice and plotting any band gaps. Fig. 5.2c and Fig.

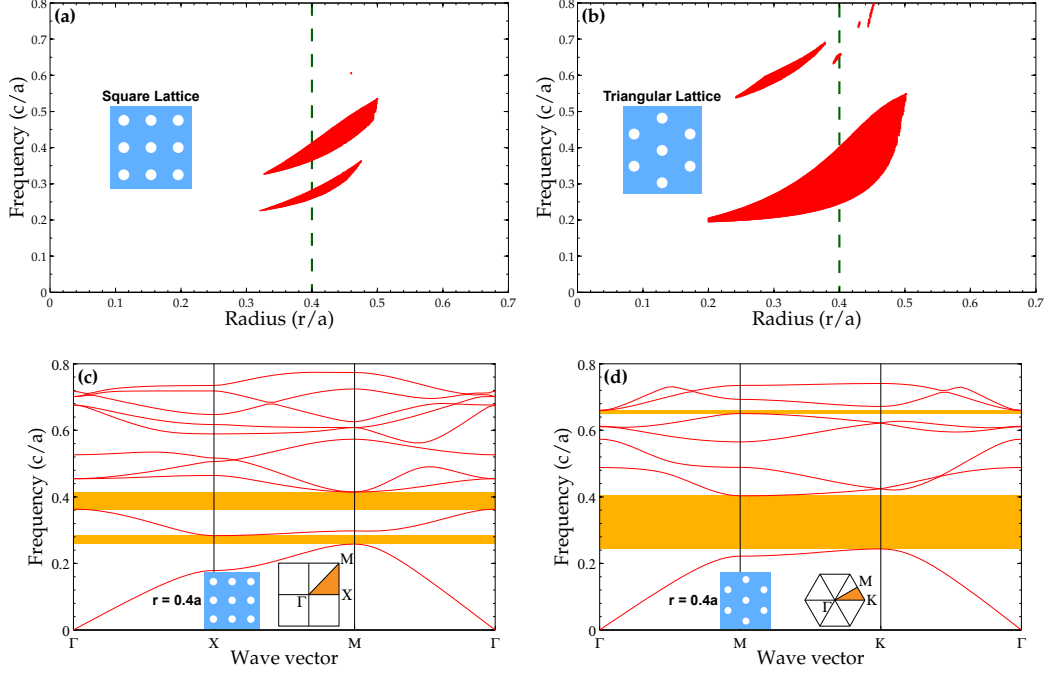


Figure 5.2: Gap map for a square (a) and triangular (b) lattice of air holes in a dielectric, $n=3.5$ (silicon), for TE modes. Band diagram for a square (c) and triangular (d) hole array photonic crystal, with hole radius $0.4a$, for TE modes. Each band diagram is a slice of the gap map diagram at the green dashed line. In (c) and (d) the right inset is the first Brillouin zone, with the irreducible Brillouin zone highlighted in orange. The band gap regions are marked in yellow.

5.2d show the complete band diagram for hole radius of $0.4a$ for both the square and triangular lattices, respectively. The left inset in each shows a cross-section of the geometry while the right inset shows the first Brillouin zone of each lattice, with the high symmetry directions labelled. It is very clear that the triangular lattice offers a much wider band gap over a larger range of hole radii. Therefore, it potentially allows for a much larger free spectral range when a defect mode is added to the band gap. With this considered, we will continue looking at the triangular lattice photonic crystal only.

The first coupled cavity array we will examine is a “ 3×3 ” array, i.e. the period of the defect (hole removal) is three lattice periods, so every third hole along the lattice high symmetry directions (Γ -K and Γ -M) is removed, see inset of Fig. 5.3a. The gap map for the CCA is recalculated and shown in Fig. 5.3a. The large band gaps are broken up into smaller band gaps, within each are the defect cavity modes. Fig. 5.3(b-d) each show a slice through the gap map and look at the actual band diagrams for hole radius of $0.3a$, $0.35a$ and $0.4a$, respectively. It is clear that there are now a number of extra bands above and below the band gap region. The structure in the computational domain has a period of $3a$. Therefore, the Brillouin zone is three times smaller than the original lattice with period a . At the edge of the Brillouin zone the modes (or bands) are folded back onto themselves. Due to the decreased size of the Brillouin zone, the bands are folded more often, therefore, they repeat across the band diagram many times. However, we are not interested in these modes as our focus is on the band gap region, highlighted in yellow.

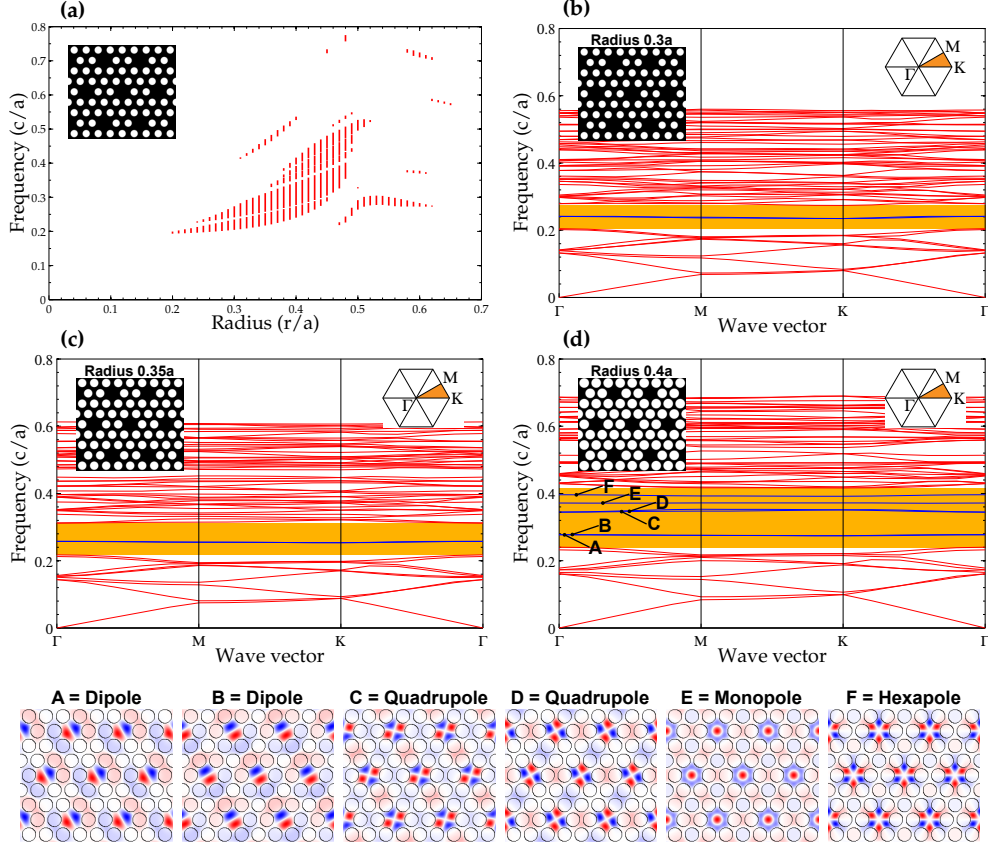


Figure 5.3: (a) Gap map for the CCA photonic crystal, as shown in the inset, for TE modes. The solid vertical lines of Fig. 5.2b are broken up into smaller bands due to the presence of the defect modes. Band diagrams for the CCA with hole radius $0.3a$ (b), $0.35a$ (c) and $0.4a$ (d) are presented. The left inset shows the corresponding structure in each band diagram while the right inset is the first Brillouin zone, with the irreducible Brillouin zone highlighted in orange. The band gap regions are marked in yellow with the CCA modes within this region are coloured blue. The six cavity modes within the band gap for hole radius of $0.4a$ (d) are labelled A-F. The bottom row of images show the magnetic field profile for each of the six cavity modes at the Γ -point. The dielectric in all cases has an index of 3.5 (silicon).

For the hole radius of $0.3a$ and $0.35a$, there is clearly one mode within the band gap, coloured in blue, and for the radius $0.4a$, there are what initially appears to be four defect bands. However, by taking a closer look at the bands, we note a total of six bands, labelled from A-F from low to high frequency. The magnetic field in the z direction (cross-section through the lattice) is shown for these six modes (A-F) at the Γ -point at the bottom of Fig. 5.3. The first two are two dipole modes, the second two are two quadrupole modes, next is a monopole mode and lastly a hexapole mode. It is clear from all the mode profiles that the defect modes are cavity based modes. The light is strongly confined to the defect regions while decaying into the surrounding lattice. The bands or dispersion curves of the defect modes have a sinusoidal oscillating shape. We know from CCWs that the period of this sinusoidal dispersion curve is determined by the CCA periodicity and the amplitude is given by the coupling strength [106, 111, 112].

Focusing on the band diagram of $0.4a$ with the six defect modes, the coupled

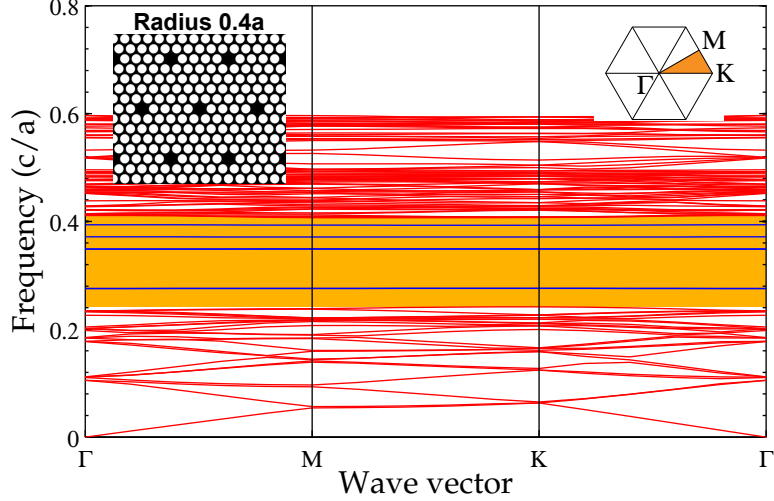


Figure 5.4: Band diagram for a CCA with a cavity period of $5a$ i.e. where every fifth hole is removed (see left inset), for a hole radius of $0.4a$ and refractive index 3.5 (silicon). The right inset shows the first Brillouin zone, with the irreducible Brillouin zone highlighted in orange. The band gap region is marked in yellow with the CCA modes coloured in blue. Notice that the amplitude of the dispersion for these six modes is reduced when comparing to the $3a$ coupled cavity period structure in Fig. 5.3a; increasing the cavity separation increases the 'flatness' of the CCA modes.

cavity period was increased to $5a$. The corresponding band diagram is shown in Fig. 5.4. Again, the number of bands above and below the band gap region have increased because the Brillouin zone of the computational cell has further decreased (now has a period of $5a$), hence more band folding. Looking at the CCA modes in the band gap region, the amplitude of the dispersion curve has decreased and the bands appear to be almost completely flat, as expected from [106]; as the coupling strength is reduced the amplitude of the dispersion band decreases.

5.2.3 Coupled Cavity Array Slab

So far, the analysis has focused on the 2D lattice. In order to get a truly accurate picture of the behaviour of the coupled cavity structure, it is important to take into account the finite size of the slab thickness. Each cavity mode is strongly confined within the plane of the crystal, but, they are inherently lossy in the vertical direction i.e. they can radiate. To obtain an accurate band diagram for the CCA slab, a 3D FDTD solver (MEEP) was implemented [67]. In Chapter 3, MEEP was used to calculate the band diagrams of the square hole array photonic crystal slabs. As with MPB, the parameters are normalized to the period a , but, instead of periodic boundary conditions in all three directions, MEEP can also use perfectly matched layers (PMLs). Therefore, a 3D computational domain consisting of a finite slab with an air region above and below is constructed; PMLs are placed outside the air regions and periodic conditions at the boundary of the unit cell. Unlike the MPB calculations, for the 3D MEEP an actual value for the period, hole radius and slab thickness are taken into account in order to calculate the resonance wavelength from the band diagram directly using $\lambda_{res} = a/\omega_{MEEP}$. The structure considered is a triangular lattice with hole radius of $0.4a$ and with a cavity period of $3a$. The parameters used are: period,

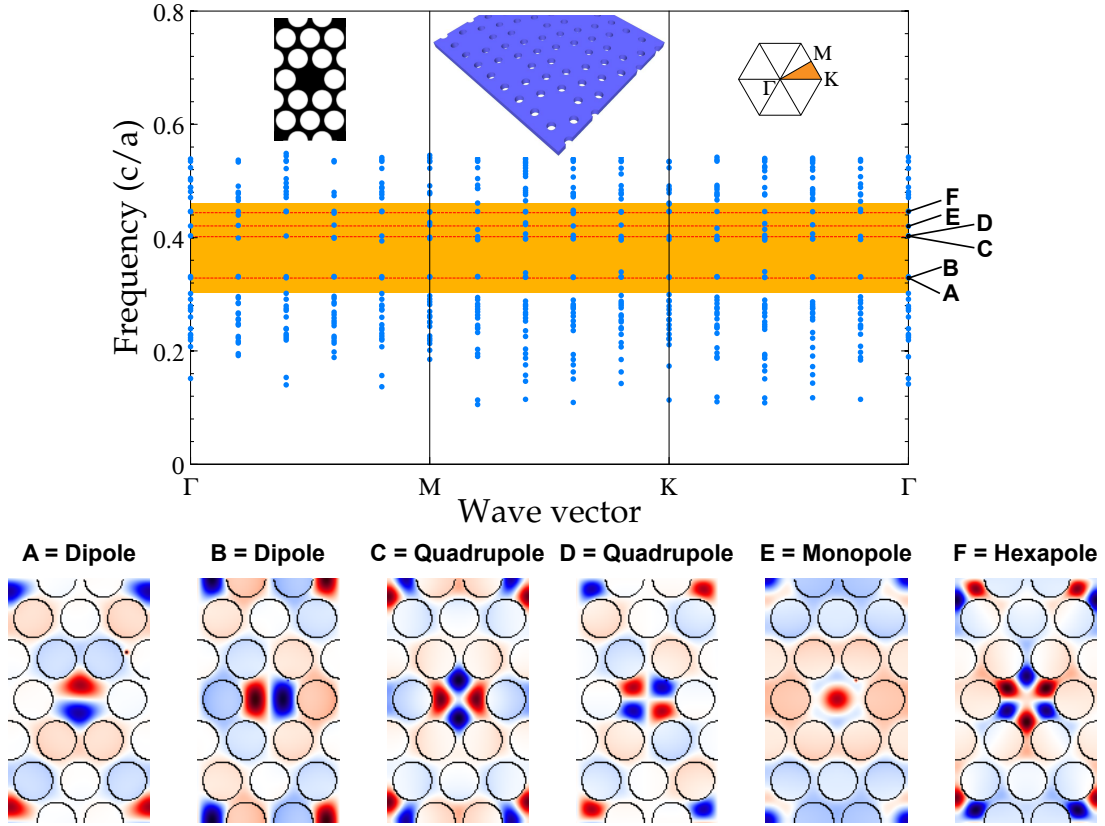


Figure 5.5: Band diagram for a CCA slab calculated using 3D MEEP. The left inset shows a cross-section through the centre of the computational domain. The cavity period is $3a$, hole radius $0.4a$ and the slab thickness is $0.5238a$ with a refractive index of 3.5 (silicon), see centre inset for a schematic of the structure. The right inset shows the first Brillouin zone, with the irreducible Brillouin zone highlighted in orange. The resonant frequencies are discretely calculated, therefore, the mode positions are marked as dots and not bands like in MPB generated diagrams. The band gap is marked in yellow, with horizontal dashed red lines indicating the positions of the six CCA modes, each labelled A-F. The bottom array of magnetic field profiles, are cross sections through the centre of the slab for each of the cavity modes at the Γ -point.

$a = 420$ nm; radius, $r = 0.4a = 168$ nm; slab thickness, $d = 0.5238a = 220$ nm and refractive index, $n=3.5$ (silicon). The cross-sectional view of the CCA unit cell is shown in the left inset of Fig. 5.5.

Fig. 5.5 shows the band diagram calculated for the 3D finite slab CCA structure using MEEP. To calculate, a point source was placed within the slab. To ensure sufficient coupling to all available modes, the position of the source was varied within the slab. However, due to the large computational domain, only a sparse band diagram was calculated with sixteen wave vector values, and the frequency range focussed around the band gap region. The band gap region is less obvious because MEEP calculates the resonant frequencies discretely and not in bands like MPB, therefore there are a lot of dots to join up to create bands. In order, to identify the position of these cavity bands, the mode profiles at the Γ -point were examined. As before, the six cavity modes are identified, labelled A-F, and the corresponding magnetic field profiles are shown below the diagram. Not all cavity modes were successfully excited at every wave vector position. To

Table 5.1: Radiative Q-factors and resonant wavelengths of the six CCA band gap modes labelled A-F in Fig. 5.5.

Mode	frequency (c/a)	λ_{res} (nm)	Q_{rad}
Dipole	0.3310	1269	318
Dipole	0.3317	1266	321
Quadrupole	0.3971	1058	366
Quadrupole	0.4029	1042	94
Monopole	0.4234	991	79
Hexapole	0.4470	940	1375

generate a complete band diagram would simply require more calculations with the source in various positions. However, there are still enough points to get an accurate picture of the behaviour. And it is easy to see that the dispersion of the cavity modes across the entire band diagram is flat and in agreement with the previous 2D MPB results.

5.3 Coupled Cavity Array Slab with Absorption

Now that we have slab structure that exhibits the required flat dispersion, the next step is to examine the absorption and emission properties of the silicon CCA. As shown before in Chapter 3, silicon in the near- and mid-infrared has almost no light absorption properties, therefore it needs to be doped to increase absorption. However, it is not just a case of blindly doping the silicon, there is an optimal doping concentration to achieve maximum absorption while maintaining a narrow linewidth resonance. The process of calculating the correct doping concentration has already been presented in detail in Chapter 3 (Section 3.3) and the process is referred to as “Q-matching” or “critical coupling”. Using coupled mode theory, it was shown that for a single resonant mode within a slab-like structure, the maximum possible value of absorption is 0.5, for a plane wave incident from one side of the slab. It was also proven that to optimally achieve an absorption of 0.5, the Q-factor of the resonant mode (Q_{rad}) and the absorption Q-factor (Q_{abs}) of the material need to be equal, i.e. $Q_{rad} = Q_{abs}$. The radiative Q-factor for each of the six cavity modes at the Γ -point is presented in table 5.1 along with the corresponding resonant wavelength. The Q-factors are calculated using the MEEP software.

The reflection spectrum for the CCA for intrinsic silicon is shown in Fig. 5.6 for a wavelength range of 0.9 μm to 1.7 μm . For both polarisations the reflection spectrum is the same (only shown here for the E_x case), but, each excites a different cavity mode. The reflection spectrum is calculated using the COMSOL Multiphysics software package, as in Chapter 3. The resonance reflection peak at 1.268 μm corresponds to the dipole mode. None of the other cavity modes excited to and the mode profiles did not match those from the MEEP calculations, which

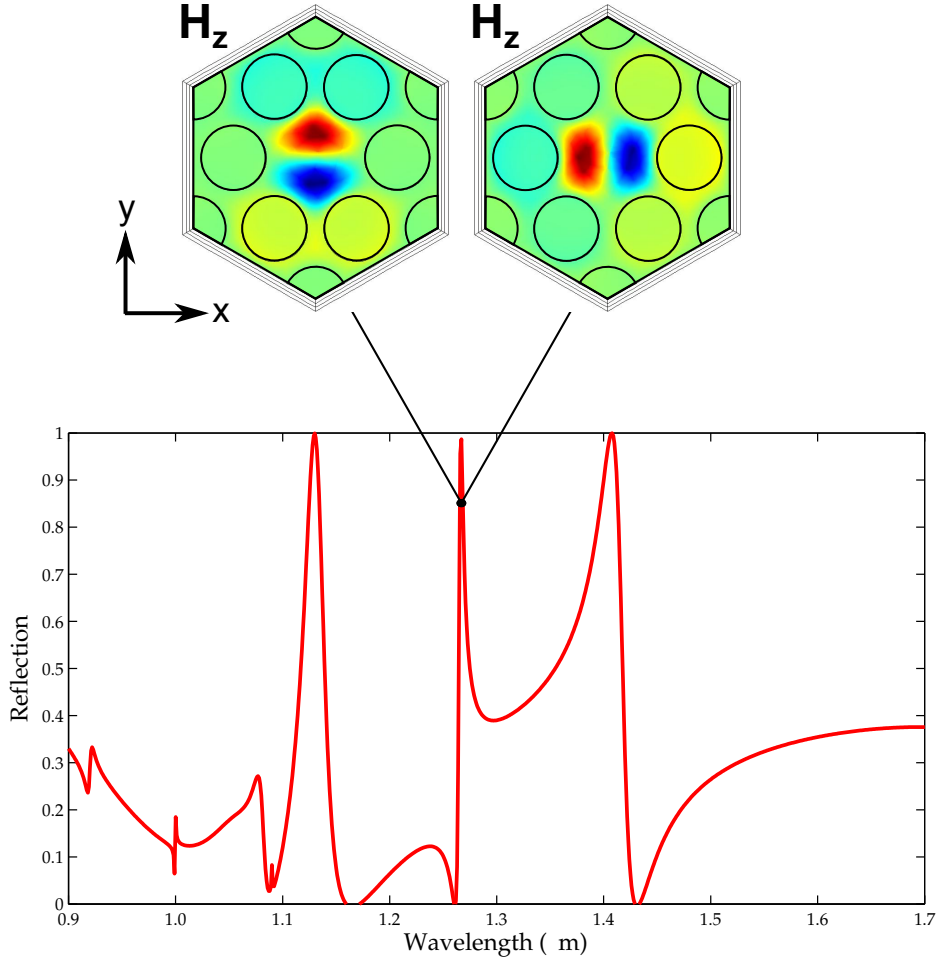


Figure 5.6: Simulated normal reflection spectrum for a CCA slab using COMSOL Multiphysics, with lattice period a equal to 420 nm, a cavity period of $3a$, hole radius 168 nm, the slab thickness is 220 nm and with a refractive index of 3.5 (undoped silicon). The position of the dipole cavity mode is labelled with two magnetic field (H_z) profiles. The two profiles are generated by changing the polarisation of the incident electric field; the left field pattern is generated E_x polarisation while the right is for E_y polarisation.

can not be satisfactorily explained at this point. The magnetic field profile of the dipole cavity mode is shown at the top of Fig. 5.6, with the left for E_x polarisation and and the right for E_y polarisation.

The dipole mode, therefore, appears to be the most suitable cavity mode to pursue. By changing the polarisation of the electric field, both dipole mode orientations are excited. Q_{abs} is calculated using

$$Q_{abs} = \frac{\epsilon_r}{\epsilon_i \sigma} \quad (5.1)$$

Where $\epsilon_{r,i}$ are the real and imaginary parts of the dielectric function, both are wavelength dependent, and σ is the fraction of modal energy within the slab. The fraction of modal energy within the slab is calculated using the COMSOL eigenfrequency solver. The time averaged energy density at the dipole wavelength is calculated for the computational domain and the slab itself with the ratio giving 74%. Following that, a doping density of $n = 6.3 \times 10^{19} \text{ cm}^{-3}$ gives a Q_{abs} -

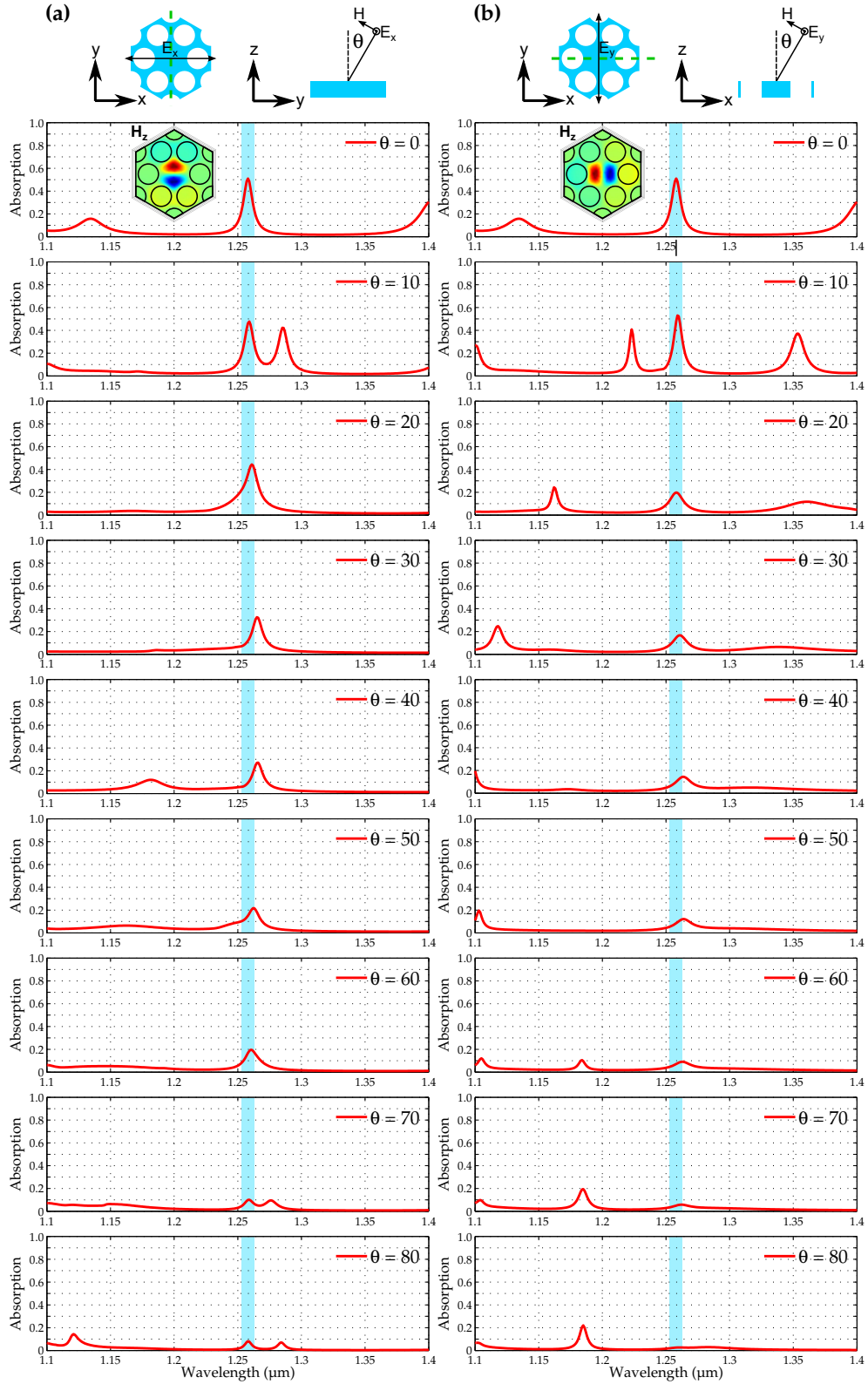


Figure 5.7: Absorption spectrum for the CCA dipole mode, as in Fig. 5.6, for normal to 80° incidence and both electric field polarisations; (a) (left-hand column) E_x and (b) (right-hand column) E_y . The two schematics at the top of each column indicate the electric polarisation and the angle of incidence θ relative to the coupled cavity structure.

factor of 319, almost exactly that of the dipole modes, thereby, achieving the Q-matching condition.

Due to the large computational domain and the computational resources required, only a segment of the spectrum around the dipole mode is simulated, i.e. the wavelength range $1.1 \mu\text{m}$ to $1.4 \mu\text{m}$. Fig. 5.7 shows the spectral absorption for plane wave incident on the doped ($6.3 \times 10^{19} \text{ cm}^{-3}$) CCA array structure. The incident angle is varied from normal ($\theta=0^\circ$) to 80° , in steps of 10° . Fig. 5.7a, i.e. the left column, is for E_x polarisation and Fig. 5.7b, i.e. the right column, is for E_y polarisation. The two insets at the top of each column indicate the direction of polarisation and incident angle relative to the CCA slab. The green dotted line is the cross-section through the slab shown in the right inset of each, for yz (Fig. 5.7a) and xz (Fig. 5.7b) vertical slice.

A maximum absorption of 0.5 is obtained for both polarisations at normal incidence, indicating that reasonably good Q-matching has been achieved. The vertical blue band in each plot indicates the position of the normal incident peak. As the incident angle is increased, for both polarisations, the position of the cavity mode only changes slightly. For the angle range 20° to 50° , it shifts to slightly longer wavelengths before coming back to the original wavelength. The shift is minimal when compared to the large shifts of the square hole array photonic crystal structure. Overall the absorption value decreases with increase in incident angle. Except for the 10° incident angle, there are no other absorption peaks present. These simulation results prove that for a real CCA slab structure, the resonant mode of the dipole cavity is angularly independent for both polarisations i.e. it exhibits flat dispersion properties across all wave vectors. Therefore, for thermal emission, when the doped silicon CCA is heated, it will exhibit a single wavelength, directional emission profile. The peak emission wavelength will not change for off-normal emission and since the absorption decreases with increasing angle, the majority of the light emission will be within $30\text{-}40^\circ$ cone around normal.

Chapter 6

Conclusions and Outlook

The main objective of the project was to theoretically and experimentally investigate the thermal light emission properties from nanophotonic structures, with the overall aim of producing a narrowband monochromatic light source in the near-infrared wavelength range.

To pursue these objectives, I developed four individual photonic resonant structures; (1) square hole array photonic crystal slab, (2) triangular lattice coupled cavity array, (3) metal-insulator-metal resonator and (4) the binary biharmonic grating structure. Each structure showed controlled narrowband thermal emission behaviour, as confirmed by simulations. However, only the photonic crystal slab device was successfully fabricated and experimentally demonstrated narrowband thermal emission.

I believe the body of work in this thesis provides an excellent platform for constructing and engineering the next generation of thermal emission devices. The framework of the thesis covers all aspects of the design and the experimental process. Beginning from a relatively fundamental level, the entire development procedure is presented in detail i.e. starting with theory and simulation, through all the fabrication techniques and accurate device characterisation. Furthermore, a comprehensive analysis of a range of optically resonant structures, each based on a different resonant phenomenon, is carried out.

For the square hole array photonic crystal slab, the complete design, fabrication and measurement procedure is presented in this thesis. At the design stage, a large portion of simulation work was carried out examining the band diagrams and the out-of-plane reflection/absorption spectra. A very clear and detailed understanding of the resonances of the square hole array photonic crystal structure was developed. It led to the accurate determination of the radiative Q-factors for the structure and to very accurate Q-matching with the absorption Q-factor of the material. Using coupled mode theory I showed that the maximum possible value of absorption for an incident plane wave at one side of the structure was 0.5. Initially, this realisation was not good news, as it meant that the maximum possible emissivity value for light emission from one surface of the structure is 0.5. To immediately lose half of the emitted light power is not an attractive quality, especially when efficiency for these devices is a very important parameter.

In an attempt to improve this, and increase the vertical emission from the upper surface of the structure, an asymmetric photonic crystal slab structure

was examined. Improved vertical emission behaviour was demonstrated, where a vertical emissivity value of 0.86 was achieved, however, only for one of the resonant modes. Of course, like any photonic crystal structure, by changing the period, hole size and thickness the resonant mode can be shifted to operate at any wavelength. In conclusion, the vertical asymmetric structure shows some very promising behaviour, it has the ability to increase the vertical emission and ultimately, it will lead to a significant increase in the efficiency for these types of devices.

The fabrication of the device was very challenging and involved many steps, each of which required full recipe development. The membrane support structures are the highlight of the photonic crystal slab fabrication work. With this technique it is, in theory, possible to fabricate any size of photonic crystal membrane or thermal emitter structure.

The bespoke optical measurement setup allows for very accurate device characterisation. What is especially noteworthy about this setup is its setup-B configuration. In the setup-B configuration it is possible to illuminate the device with plane waves of light, in contrast to focusing light down onto the sample. Allowing one to directly compare the simulation results which have been calculated using plane wave sources to the measured spectra. This is very advantageous and removes any guess work when trying to identify resonant features. The highlight of the passive characterisation was the measurement of the reflection spectra of the square hole array photonic crystal slab using this setup-B configuration, almost perfect agreement between experiment and simulation was achieved.

For the metal-insulator-metal resonator, the omnidirectional concept is attractive, but in practice the resonance is just too broad for any real benefit and the device itself has too many critical fabrication steps for such a light source to be worth it. The main challenge in the fabrication is the repeatability of the gold nanoantenna array. However, altering this device to operate in the mid-infrared wavelength range by increasing the structural dimensions may have its advantages. With increased dimensions the fabrication demands are reduced. Therefore, the lift-off technique may become a more viable alternative to etching for the fabrication of the gold dipole arrays.

The other metallic structure, the binary biharmonic grating, also displays extraordinary flat band angular independent emission properties, along with relatively narrow linewidth and a very large free spectral range, which makes this device very attractive. However, due to the large aspect ratio for the grating trenches the device is extremely difficult to fabricate. Gold is also notoriously difficult to etch and achieving the required deep trenches in gold is near impossible. On the other hand, one can trade-off the range of flat dispersion against groove depth; if the application only requires flat dispersion over a smaller angular range, then such a device is more feasible as a reduced groove depth will suffice.

Another approach would be to replace the gold entirely with a dielectric material such as heavily doped silicon, or a refractory plasmonic material such as TiN [113]. For example, the propagation of surface plasmon polaritons along highly doped silicon ($1 \times 10^{20} \text{ cm}^{-3}$) has been demonstrated [114] for wavelengths in the mid-infrared range. Using silicon would greatly reduce the fabrication difficulties, as smooth-walled deep trenches in doped silicon are readily obtainable,

therefore making the BBS structure a viable option to proceed with.

The triangular lattice coupled cavity array displayed some very interesting resonant features. The flat dispersion bands initially looked very promising, with the band diagrams showing flat bands for a number of different localised cavity modes. However, examining the out-of-plane properties of the structure and it appears that only the dipole mode efficiently couples to external radiation. The dipole mode has a relatively small Q-factor and so the absorption (emission) peak is relatively broad. One promising feature about the CCA and the dipole mode is that the absorption (emission) is maximum in the 20-30 ° cone around normal and decays in intensity rapidly outside this range. This strong forward emission is an attractive feature as it will potentially improve the efficiency of the device because in most cases it is the forward projected light signal that is of any use, where as light emitted at large angles is a waste of energy.

The doped silicon membrane coupled with a photonic crystal structure remains the most feasible platform for further device development, since the photonic crystal slab has already demonstrated its ability to achieve narrowband thermal emission. Some steps to improve the emission performance are required, such as introducing the coupled-cavity array for angularly independent resonances. However, there are still issues with the free spectral range, i.e. it would be desirable to have a single resonant mode only within the emission spectrum, so more work on novel structures is required to further improve the performance.

The ideal case would be a photonic crystal coupled cavity array, which would feature the desirable angular insensitivity, where one of the coupled cavity modes has a very large Q-factor compared to the adjacent resonances. To optimally Q-match the absorption Q-factor of the material to this resonance, a relatively low doping density would be required. Such a low doping density, or large absorption Q-factor, would couple very weakly to the surrounding lower Q resonances. Therefore, when the structure is heated, very high Q emission with near-unity efficiency would be achieved for the high Q resonance mode, while the remaining resonances will only emit weakly and display much lower emissivity.

Adding vertical asymmetry to the slab would be another step to increase the upward emissivity of the high Q mode. This would address the issue with a symmetric slab, namely the fact that 50% is radiated up and 50% towards the substrate. Accurate determination of the device efficiency is an important parameter that needs to be measured, so that these narrowband thermal emitters can be compared to the alternative LED sources. For the narrowband thermal emitters to be a viable alternative they need to atleast match and if not better the performance of the already existing LED solutions.

The final point is that the field has matured sufficiently to consider realistic application(s) for these thermal emitters. Parameters such as the target wavelength, bandwidth, emission power, angular tolerance and free spectral range can all be identified. These parameters will help help inform the best device and parameters to choose. Generally, for photonic crystals and due to the linearity of Maxwell's equations, the structures are scalable and could be resized to operate at any wavelength as long as the material parameters, which are not necessarily scalable, allow it.

Bibliography

- [1] M. Planck, *The Theory of Heat Radiation*. Dover Publication, 1914.
- [2] P. C. Sorcar, *Energy saving lighting systems*. New York: Van Nostrand Reinhold, 1982.
- [3] B. Bitnar, W. Durisch, J. C. Mayor, H. Sigg, and H. R. Tschudi, “Characterisation of rare earth selective emitters for thermophotovoltaic applications,” *Solar Energy Materials and Solar Cells*, vol. 73, no. 3, pp. 221–234, 2002.
- [4] H. Wang, H. Ye, and Y. Zhang, “Preparation and performance evaluation of Er₂O₃ coating-type selective emitter,” *Science China Technological Sciences*, vol. 57, no. 2, pp. 332–338, 2014.
- [5] G. Kirchhoff, “On the relation between the radiating and absorbing powers of different bodies for light and heat,” *Annalen der Physik*, vol. 109, p. 275, 1860.
- [6] M. Kreiter, J. Oster, R. Sambles, S. Herminghaus, S. Mittler-Neher, and W. Knoll, “Thermally induced emission of light from a metallic diffraction grating, mediated by surface plasmons,” *Optics Communications*, vol. 168, pp. 117–122, 1999.
- [7] D. L. C. Chan, M. Soljacić, and J. D. Joannopoulos, “Thermal emission and design in 2D-periodic metallic photonic crystal slabs,” *Optics express*, vol. 14, no. 19, pp. 8785–96, 2006.
- [8] I. Celanovic, N. Jovanovic, and J. Kassakian, “Two-dimensional tungsten photonic crystals as selective thermal emitters,” *Applied Physics Letters*, vol. 92, 2008.
- [9] M.-L. Hsieh, J. Bur, Y.-S. Kim, and S.-Y. Lin, “Direct observation of quasi-coherent thermal emission by a three-dimensional metallic photonic crystal,” *Optics Letters*, vol. 38, no. 6, pp. 911–3, 2013.
- [10] M. Laroche, C. Arnold, F. Marquier, R. Carminati, J. J. Greffet, S. Collin, N. Bardou, and J. L. Pelouard, “Highly directional radiation generated by a tungsten thermal source,” *Optics Letters*, vol. 30, no. 19, pp. 2623–2625, 2005.
- [11] R. Biswas, D. Zhou, I. Puscasu, E. Johnson, A. Taylor, and W. Zhao, “Sharp thermal emission and absorption from conformally coated metallic

- photonic crystal with triangular lattice,” *Applied Physics Letters*, vol. 93, pp. 2008–2010, 2008.
- [12] I. Puscasu and W. L. Schaich, “Narrow-band, tunable infrared emission from arrays of microstrip patches,” *Applied Physics Letters*, vol. 92, no. 23, 2008.
- [13] J. A. Mason, S. Smith, and D. Wasserman, “Strong absorption and selective thermal emission from a midinfrared metamaterial,” *Applied Physics Letters*, vol. 98, no. 24, 2011.
- [14] C. Wu, B. Neuner III, J. John, A. Milder, B. Zollars, S. Savoy, and G. Shvets, “Metamaterial-based integrated plasmonic absorber/emitter for solar thermo-photovoltaic systems,” *Journal of Optics*, vol. 14, no. 2, p. 024005, 2012.
- [15] T. Inoue, M. D. Zoysa, T. Asano, and S. Noda, “Realization of narrowband thermal emission with optical nanostructures,” vol. 2, no. 1, pp. 27–35, 2015.
- [16] B. J. Lee, C. J. Fu, and Z. M. Zhang, “Coherent thermal emission from one-dimensional photonic crystals,” *Applied Physics Letters*, vol. 87, no. 7, 2005.
- [17] M. De Zoysa, T. Asano, K. Mochizuki, A. Oskooi, T. Inoue, and S. Noda, “Conversion of broadband to narrowband thermal emission through energy recycling,” *Nature Photonics*, vol. 6, pp. 535–539, 2012.
- [18] B. Gesemann, S. L. Schweizer, and R. B. Wehrspohn, “Thermal emission properties of 2D and 3D silicon photonic crystals,” *Photonics and Nanostructures - Fundamentals and Applications*, vol. 8, no. 2, pp. 107–111, 2010.
- [19] H. Sai, H. Yugami, Y. Akiyama, Y. Kanamori, and K. Hane, “Spectral control of thermal emission by periodic microstructured surfaces in the near-infrared region,” *Journal of the Optical Society of America. A*, vol. 18, no. 7, pp. 1471–1476, 2001.
- [20] J. S. Yu, S. R. Darvish, A. Evans, J. Nguyen, S. Slivken, and M. Razeghi, “Room-temperature continuous-wave operation of quantum-cascade lasers at $4\mu\text{m}$,” *Applied Physics Letters*, vol. 88, no. 4, p. 041111, 2006.
- [21] C. L. Canedy, W. W. Bewley, J. R. Lindle, C. S. Kim, M. Kim, I. Vurgaftman, and J. R. Meyer, “High-power and high-efficiency midwave-infrared interband cascade lasers,” *Applied Physics Letters*, vol. 88, no. 16, p. 161103, 2006.
- [22] A. Krier, “Physics and technology of mid-infrared light emitting diodes,” *Philosophical Transactions of the Royal Society London, A*, vol. 359, pp. 599–619, 2001.
- [23] M. De Zoysa, T. Asano, K. Mochizuki, A. Oskooi, T. Inoue, and S. Noda, “Conversion of broadband to narrowband thermal emission through energy recycling,” *Nature Photonics*, vol. 6, pp. 535–539, 2012.

- [24] J. Meléndez, A. de Castro, F. López, and J. Meneses, “Spectrally selective gas cell for electrooptical infrared compact multigas sensor,” *Sensors and Actuators A: Physical*, vol. 47, no. 1-3, pp. 417–421, 1995.
- [25] A. Kosterev, G. Wysocki, Y. Bakhirkin, S. So, R. Lewicki, M. Fraser, F. Tittel, and R. F. Curl, “Application of quantum cascade lasers to trace gas analysis,” *Applied Physics B: Lasers and Optics*, vol. 90, no. 2, pp. 165–176, 2008.
- [26] A. Catalano, “Thermophotovoltaics: A new paradigm for power generation?,” *Renewable Energy*, vol. 8, no. 1-4, pp. 495–499, 1996.
- [27] Y. X. Yeng, W. R. Chan, V. Rinnerbauer, V. Stelmakh, J. J. Senkevich, J. D. Joannopoulos, M. Soljacic, and I. Čelanović, “Photonic crystal enhanced silicon cell based thermophotovoltaic systems,” *Optics Express*, vol. 23, no. 3, p. A157, 2015.
- [28] J. J. D. Joannopoulos, S. Johnson, J. N. J. Winn, and R. R. D. Meade, *Photonic crystals: molding the flow of light*. 2008.
- [29] E. Yablonovitch, “Inhibited spontaneous emission in solid-state physics and electronics,” *Physical Review Letters*, vol. 58, no. 20, pp. 2059–2062, 1987.
- [30] S. John, “Strong localization of photons in certain disordered dielectric superlattices,” *Physical Review Letters*, vol. 58, no. 23, pp. 2486–2489, 1987.
- [31] S. Noda, “Full Three-Dimensional Photonic Bandgap Crystals at Near-Infrared Wavelengths,” *Science*, vol. 289, no. 5479, pp. 604–606, 2000.
- [32] J. G. Fleming, S. Y. Lin, I. El-Kady, R. Biswas, and K. M. Ho, “All-metallic three-dimensional photonic crystals with a large infrared bandgap,” *Nature*, vol. 417, no. 6884, pp. 52–55, 2002.
- [33] L. Rayleigh, “On the maintenance of vibrations by forces of double frequency, and on the propagation of waves through a medium endowed with a periodic structure,” *Philosophical Magazine Series 5*, vol. 24, no. 147, pp. 145–159, 1887.
- [34] M. Born and E. Wolf, *Principles of Optics*. Pergamon Press, 1999.
- [35] C. Kittel, *Introduction to Solid State Physics*. Wiley, 2005.
- [36] R. Eisberg, R. Resnick, and J. Brown, *Quantum Physics of Atoms, Molecules, Solids, Nuclei, and Particles*. Wiley, 1986.
- [37] P. B. Johnson and R. W. Christy, “Optical Constants of the Noble Metals,” *Physical Review B*, vol. 6, no. 12, pp. 4370–4379, 1972.
- [38] M. Nedeljkovic, R. Soref, and G. Z. Mashanovich, “Free-carrier electrorefraction and electroabsorption modulation predictions for silicon over the 1-14-um infrared wavelength range,” *IEEE Photonics Journal*, vol. 3, no. 6, pp. 1171–1180, 2011.

- [39] P. J. Hesketh, J. N. Zemel, and B. Gebhart, “Organ pipe radiant modes of periodic micromachined silicon surfaces,” *Nature*, vol. 324, no. 6097, pp. 549–551, 1986.
- [40] T. Inoue, T. Asano, M. De Zoysa, A. Oskooi, and S. Noda, “Design of single-mode narrow-bandwidth thermal emitters for enhanced infrared light sources,” *Journal of the Optical Society of America B*, vol. 30, no. 1, p. 165, 2012.
- [41] T. Inoue, M. De Zoysa, T. Asano, and S. Noda, “Single-peak narrow-bandwidth mid-infrared thermal emitters based on quantum wells and photonic crystals,” *Applied Physics Letters*, vol. 102, no. 19, pp. 10–14, 2013.
- [42] T. Inoue, M. De Zoysa, T. Asano, and S. Noda, “Filter-free nondispersive infrared sensing using narrow-bandwidth mid-infrared thermal emitters,” *Applied Physics Express*, vol. 7, no. 1, 2014.
- [43] M. J. Collins, C. Xiong, I. H. Rey, T. D. Vo, J. He, S. Shahnia, C. Reardon, T. F. Krauss, M. J. Steel, a. S. Clark, and B. J. Eggleton, “Integrated spatial multiplexing of heralded single-photon sources.,” *Nature communications*, vol. 4, p. 2582, 2013.
- [44] I. H. Rey, *Active Slow Light in Silicon Photonic Crystals : Tunable Delay and Raman Gain*. PhD thesis, University of St Andrews, 2013.
- [45] T. Shoji, T. Tsuchizawa, T. Watanabe, K. Yamada, and H. Morita, “Low loss mode size converter from 0.3 μm square Si wire waveguides to single-mode fibres,” 2002.
- [46] T. Tsuchizawa, K. Yamada, H. Fukuda, T. Watanabe, J. I. Takahashi, M. Takahashi, T. Shoji, E. Tamechika, S. I. Itabashi, and H. Morita, “Microphotonic devices based on silicon microfabrication technology,” *IEEE Journal on Selected Topics in Quantum Electronics*, vol. 11, no. 1, pp. 232–239, 2005.
- [47] V. R. Almeida, R. R. Panepucci, and M. Lipson, “Nanotaper for compact mode conversion.,” *Optics Letters*, vol. 28, no. 15, pp. 1302–1304, 2003.
- [48] M. Pu, L. Liu, H. Ou, K. Yvind, and J. M. Hvam, “Ultra-low-loss inverted taper coupler for silicon-on-insulator ridge waveguide,” *Optics Communications*, vol. 283, no. 19, pp. 3678–3682, 2010.
- [49] M. Grande, L. O’Faolain, T. P. White, M. Spurny, A. D’Orazio, and T. F. Krauss, “Optical filter with very large stopband (approximately 300 nm) based on a photonic-crystal vertical-directional coupler.,” *Optics Letters*, vol. 34, no. 21, pp. 3292–3294, 2009.
- [50] S. McNab, N. Moll, and Y. Vlasov, “Ultra-low loss photonic integrated circuit with membrane-type photonic crystal waveguides.,” *Optics Express*, vol. 11, no. 22, pp. 2927–2939, 2003.

- [51] M. Boroditsky, R. Vrijen, T. F. Krauss, R. Coccioli, R. Bhat, and E. Yablonovitch, “Spontaneous Emission and Purcell Enhancement from Thin-Film 2-D Photonic Crystals,” vol. 17, no. 11, pp. 2096–2112, 1999.
- [52] M. Fujita, S. Takahashi, Y. Tanaka, T. Asano, and S. Noda, “Simultaneous inhibition and redistribution of spontaneous light emission in photonic crystals,” *Science (New York, N.Y.)*, vol. 308, no. 5726, pp. 1296–1298, 2005.
- [53] X. Liu, T. Tyler, T. Starr, A. Starr, N. Jokerst, and W. Padilla, “Taming the Blackbody with Infrared Metamaterials as Selective Thermal Emitters,” *Physical Review Letters*, vol. 107, pp. 4–7, July 2011.
- [54] S. Y. Lin, J. Moreno, and J. G. Fleming, “Three-dimensional photonic-crystal emitter for thermal photovoltaic power generation,” *Applied Physics Letters*, vol. 83, no. 2003, pp. 380–382, 2003.
- [55] V. Rinnerbauer, Y. X. Yeng, W. R. Chan, J. J. Senkevich, J. D. Joannopoulos, M. Soljačić, and I. Celanovic, “High-temperature stability and selective thermal emission of polycrystalline tantalum photonic crystals,” *Optics Express*, vol. 21, no. 9, pp. 11482–91, 2013.
- [56] J. Y.-T. Huang, D. P. Xu, L. J. Mawst, T. F. Kuech, I. Vurgaftman, and J. R. Meyer, “GaAsSbN-GaAsSb-InP type-II ‘W’ quantum wells for mid-IR emission,” *IEEE Journal of Selected Topics in Quantum Electronics*, vol. 13, no. 5, pp. 1065–1073, 2007.
- [57] B. J. O’Regan, Y. Wang, and T. F. Krauss, “Silicon photonic crystal thermal emitter at near-infrared wavelengths,” *Scientific Reports*, vol. 5, p. 13415, 2015.
- [58] J. Li, L. O’Faolain, I. H. Rey, and T. F. Krauss, “Four-wave mixing in photonic crystal waveguides: slow light enhancement and limitations,” *Optics Express*, vol. 19, no. 5, pp. 4458–4463, 2011.
- [59] A. Di Falco, L. O’Faolain, and T. F. Krauss, “Dispersion control and slow light in slotted photonic crystal waveguides,” *Applied Physics Letters*, vol. 92, no. 8, 2008.
- [60] T. F. Krauss, “Slow light in photonic crystal waveguides,” *Journal of Physics D: Applied Physics*, vol. 40, no. 9, pp. 2666–2670, 2007.
- [61] J. Li, T. P. White, L. O’Faolain, A. Gomez-Iglesias, and T. F. Krauss, “Systematic design of flat band slow light in photonic crystal waveguides,” *Optics Express*, vol. 16, no. 9, pp. 6227–6232, 2008.
- [62] D. M. Beggs, T. P. White, L. O’Faolain, and T. F. Krauss, “Ultracompact and low-power optical switch based on silicon photonic crystals,” *Optics Letters*, vol. 33, no. 2, pp. 147–149, 2008.

- [63] L. O’Faolain, D. M. Beggs, T. P. White, T. Kampfrath, K. Kuipers, and T. F. Krauss, “Compact optical switches and modulators based on dispersion engineered photonic crystals,” *IEEE Photonics Journal*, vol. 2, no. 3, pp. 404–414, 2010.
- [64] A. Ricciardi, S. Campopiano, A. Cusano, T. F. Krauss, and L. O’Faolain, “Broadband mirrors in the near-infrared based on subwavelength gratings in SOI,” *IEEE Photonics Journal*, vol. 2, no. 5, pp. 696–702, 2010.
- [65] S. Fan and J. Joannopoulos, “Analysis of guided resonances in photonic crystal slabs,” *Physical Review B*, vol. 65, pp. 1–8, 2002.
- [66] S.-L. Chua, Y. Chong, a. D. Stone, M. Soljacić, and J. Bravo-Abad, “Low-threshold lasing action in photonic crystal slabs enabled by Fano resonances,” *Optics express*, vol. 19, no. 2, pp. 1539–1562, 2011.
- [67] A. F. Oskooi, D. Roundy, M. Ibanescu, P. Bermel, J. D. Joannopoulos, and S. G. Johnson, “Meep: A flexible free-software package for electromagnetic simulations by the FDTD method,” *Computer Physics Communications*, vol. 181, no. 3, pp. 687–702, 2010.
- [68] H. A. Haus, *Waves and Fields in Optoelectronics*. Prentice-Hall, 1984.
- [69] W. Kern, “The evolution of silicon wafer cleaning technology,” *Journal of Electrochemical Society*, vol. 137, no. 6, pp. 1887–1892, 1990.
- [70] E. D. Palik, “Handbook of Optical Constants,” *Proc. Natl. Acad. Sci. USA*, vol. 2, p. 1096, 1991.
- [71] H. Li, “Refractive index of Silicon and Germanium and its Wavelength and Temperature Derivatives,” *J. Phys. Chem. Ref. Data*, vol. 9, pp. 561–658, 1980.
- [72] W. M. Yim and R. J. Paff, “Thermal expansion of AlN, sapphire, and silicon,” *Journal of Applied Physics*, vol. 45, no. 3, pp. 1456–1457, 1974.
- [73] A. Heinzl, V. Boerner, A. Gombert, B. Blasi, V. Wittwer, and J. Luther, “Radiation filters and emitters for the NIR based on periodically structured metal surfaces,” *Journal of Modern Optics*, vol. 47, pp. 2399–2419, 2000.
- [74] H. J. Lezec, A. Degiron, E. Devaux, R. A. Linke, L. Martin-Moreno, F. J. Garcia-Vidal, and T. W. Ebbesen, “Beaming light from a subwavelength aperture,” *Science (New York, N.Y.)*, vol. 297, pp. 820–2, Aug. 2002.
- [75] W. Zhao, R. Biswas, I. Puscasu, and E. Johnson, “Angular variation of absorption and thermal emission from photonic crystals,” *Journal of the Optical Society of America B*, vol. 26, no. 9, p. 1808, 2009.
- [76] J.-H. Lee, W. Leung, T. G. Kim, K. Constant, and K.-M. Ho, “Polarized thermal radiation by layer-by-layer metallic emitters with sub-wavelength grating,” *Optics Express*, vol. 16, no. 12, pp. 8742–8747, 2008.

- [77] D. R. Smith, W. J. Padilla, D. C. Vier, S. C. Nemat-Nasser, and S. Schultz, “Composite Medium with Simultaneously Negative Permeability and Permittivity,” *Physical Review Letters*, vol. 84, no. 18, pp. 4184–4187, 2000.
- [78] R. A. Shelby, D. R. Smith, and S. Schultz, “Experimental verification of a negative index of refraction.,” *Science (New York, N.Y.)*, vol. 292, no. 5514, pp. 77–79, 2001.
- [79] D. Schurig, J. J. Mock, B. J. Justice, S. A. Cummer, J. B. Pendry, A. F. Starr, and D. R. Smith, “Metamaterial electromagnetic cloak at microwave frequencies,” *Science (New York, N.Y.)*, vol. 314, no. 5801, pp. 977–980, 2006.
- [80] J. B. Pendry, “Negative refraction makes a perfect lens,” *Physical Review Letters*, vol. 85, no. 18, pp. 3966–3969, 2000.
- [81] N. Fang, H. Lee, C. Sun, and X. Zhang, “Sub-diffraction-limited optical imaging with a silver superlens.,” *Science (New York, N.Y.)*, vol. 308, no. 5721, pp. 534–537, 2005.
- [82] N. I. Landy, S. Sajuyigbe, J. J. Mock, D. R. Smith, and W. J. Padilla, “Perfect metamaterial absorber,” *Physical Review Letters*, vol. 100, no. 20, pp. 1–4, 2008.
- [83] H. Tao, C. M. Bingham, a. C. Strikwerda, D. Pilon, D. Shrekenhamer, N. I. Landy, K. Fan, X. Zhang, W. J. Padilla, and R. D. Averitt, “Highly flexible wide angle of incidence terahertz metamaterial absorber: Design, fabrication, and characterization,” *Physical Review B - Condensed Matter and Materials Physics*, vol. 78, no. 24, pp. 2–5, 2008.
- [84] J. Hao, J. Wang, X. Liu, W. J. Padilla, L. Zhou, and M. Qiu, “High performance optical absorber based on a plasmonic metamaterial,” *Applied Physics Letters*, vol. 96, no. 25, pp. 34–37, 2010.
- [85] a. P. Hibbins, W. a. Murray, J. Tyler, S. Wedge, W. L. Barnes, and J. R. Sambles, “Resonant absorption of electromagnetic fields by surface plasmons buried in a multilayered plasmonic nanostructure,” *Physical Review B - Condensed Matter and Materials Physics*, vol. 74, p. 073408, Aug. 2006.
- [86] Y. Ye, Y. Jin, and S. He, “Omni-directional, broadband and polarization-insensitive thin absorber in the terahertz regime,” vol. 1, p. 6, 2009.
- [87] C.-H. Lin, R.-L. Chern, and H.-Y. Lin, “Polarization-independent broadband nearly perfect absorbers in the visible regime.,” *Optics Express*, vol. 19, no. January, pp. 415–424, 2011.
- [88] S. Y. Chou, P. R. Krauss, and P. J. Renstrom, “ λ 3-1000 plasmonic nanocavities for biosensing fabricated by soft UV,” *J. Vac. Sci. Technol. B*, vol. 14, pp. 4129–4133, 2011.
- [89] S. Chen, H. Cheng, H. Yang, J. Li, X. Duan, C. Gu, and J. Tian, “Polarization insensitive and omnidirectional broadband near perfect planar

- metamaterial absorber in the near infrared regime,” *Applied Physics Letters*, vol. 99, no. 25, p. 253104, 2011.
- [90] A. D. Rakic, A. B. Djuricic, J. M. Elazar, and M. L. Majewski, “Optical properties of metallic films for vertical-cavity optoelectronic devices,” *Applied optics*, vol. 37, no. 22, pp. 5271–5283, 1998.
- [91] K. S. Kim, J. M. Lee, J. C. Shin, J. K. Lee, and H. J. Kim, “Reactive ion etching of Pt thin films for fabrication of microcapacitor,” *Journal Of The Korean Physical Society*, vol. 32, pp. S1532–S1534, 1998.
- [92] K. Nishikawa, Y. Kusumi, T. Oomori, M. Hanazaki, and K. Namba, “Platinum etching and plasma characteristics in RF magnetron and electron cyclotron resonance plasmas,” *Japanese Journal of Applied Physics, Part 1: Regular Papers and Short Notes and Review Papers*, vol. 32, no. 12 B, pp. 6102–6108, 1993.
- [93] R. M. Ranade, “Reactive Ion Etching of Thin Gold Films,” *Journal of The Electrochemical Society*, vol. 140, no. 12, p. 3676, 1993.
- [94] R. B. Bass, C. R. Ellis, and W. Lichtenberger, “Anisotropic Reactive Ion Etching of Thick Gold Films for Superconducting Circuits,” 2015.
- [95] I. Balin, N. Dahan, V. Kleiner, and E. Hasman, “Bandgap structure of thermally excited surface phonon polaritons,” *Applied Physics Letters*, vol. 96, pp. 30–33, 2010.
- [96] S. Zeng, D. Baillargeat, H.-P. Ho, and K.-T. Yong, “Nanomaterials enhanced surface plasmon resonance for biological and chemical sensing applications,” *Chemical Society Reviews*, vol. 43, no. 10, pp. 3426–52, 2014.
- [97] H. Raether, *Surface Plasmons on Smooth and Rough Surfaces and on Gratings*. Springer Berlin Heidelberg, 1988.
- [98] S. A. Maier, *Plasmonics: Fundamentals and Applications*. Springer US, 2007.
- [99] A. R. Zakharian, J. V. Moloney, and M. Mansuripur, “Surface plasmon polaritons on metallic surfaces,” *Optics Express*, vol. 15, no. 1, pp. 183–197, 2007.
- [100] P. Drude, “Zur Elektronentheorie der Metalle,” *Annalen der Physik*, vol. 306, no. 3, p. 566, 1900.
- [101] P. Drude, “Zur Elektronentheorie der Metalle; II. Teil. Galvanomagnetische und thermomagnetische Effecte,” *Annalen der Physik*, vol. 308, no. 11, p. 369, 1900.
- [102] S. Babar and J. H. Weaver, “Optical constants of Cu , Ag , and Au revisited,” *Applied Optics*, vol. 54, pp. 477–481, 2015.
- [103] F. Ye, J. M. Merlo, M. J. Burns, and M. J. Naughton, “Optical and electrical mappings of surface plasmon cavity modes,” *Nanophotonics*, vol. 3, no. 1-2, pp. 33–49, 2014.

- [104] R. W. Wood, “On a Remarkable Case of Uneven Distribution of Light in a Diffraction Grating Spectrum,” *Proceedings of the Physical Society of London*, vol. 18, no. 1, pp. 269–275, 1902.
- [105] W. Barnes, T. Preist, S. Kitson, and J. Sambles, “Physical origin of photonic energy gaps in the propagation of surface plasmons on gratings,” *Physical Review B*, vol. 54, no. 9, pp. 6227–6244, 1996.
- [106] A. Yariv, Y. Xu, R. K. Lee, and A. Scherer, “Coupled-resonator optical waveguide: a proposal and analysis.,” *Optics Letters*, vol. 24, no. 11, pp. 711–713, 1999.
- [107] H. Altug and J. Vučković, “Two-dimensional coupled photonic crystal resonator arrays,” *Applied Physics Letters*, vol. 84, no. 2, pp. 161–163, 2004.
- [108] H. Altug and J. Vučković, “Experimental demonstration of the slow group velocity of light in two-dimensional coupled photonic crystal microcavity arrays,” *Applied Physics Letters*, vol. 86, pp. 1–3, 2005.
- [109] H. Altug, D. Englund, and J. Vučković, “Ultrafast photonic crystal nanocavity laser,” *Nature Physics*, vol. 2, pp. 484–488, 2006.
- [110] D. Englund, H. Altug, B. Ellis, and J. Vučković, “Ultrafast photonic crystal lasers,” *Laser and Photonics Reviews*, vol. 2, pp. 264–274, 2008.
- [111] D. Leuenberger, R. Ferrini, and R. Houdré, “Ab initio tight-binding approach to photonic-crystal based coupled cavity waveguides,” *Journal of Applied Physics*, vol. 95, no. 3, pp. 806–809, 2004.
- [112] B. M. Möller, U. Woggon, and M. V. Artemyev, “Bloch modes and disorder phenomena in coupled resonator chains,” *Physical Review B - Condensed Matter and Materials Physics*, vol. 75, no. 24, pp. 1–9, 2007.
- [113] U. Guler, A. Boltasseva, and V. M. Shalaev, “Refractory Plasmonics,” *Science*, pp. 263–264, 2014.
- [114] M. Shahzad, G. Medhi, R. E. Peale, W. R. Buchwald, J. W. Cleary, R. Soref, G. D. Boreman, and O. Edwards, “Infrared surface plasmons on heavily doped silicon,” *Journal of Applied Physics*, vol. 110, no. 12, 2011.

